

# **Structure-Property Correlation of Electron Transport Materials in Organic Devices**

Dissertation

zur Erlangung des akademischen Grades  
eines Doktors der Naturwissenschaften (Dr. rer. nat.)  
im Fach Chemie der Fakultät für  
Biologie, Chemie und Geowissenschaften der Universität Bayreuth

Vorgelegt von

**Mathis-Andreas Muth**

Geboren in Lichtenfels/Deutschland

Bayreuth, 2013



Die vorliegende Arbeit wurde in der Zeit von November 2009 bis März 2013 in der Arbeitsgruppe Angewandte Funktionspolymere am Lehrstuhl für Makromolekulare Chemie I der Universität Bayreuth unter der Betreuung von Prof. Dr. Mukundan Thelakkat angefertigt.

Vollständiger Abdruck der von der Fakultät für Biologie, Chemie und Geowissenschaften der Universität Bayreuth genehmigten Dissertation zur Erlangung des akademischen Grades eines Doktors der Naturwissenschaften (Dr. rer. nat.).

Amtierende Dekanin:	Prof. Beate Lohnert
Dissertation eingereicht am:	08.03.2013
Zulassung durch die Prüfungskommission:	13.03.2013
Wissenschaftliches Kolloquium:	25.06.2013

Prüfungsausschuss:

Prof. Mukundan Thelakkat	(Erstgutachter)
Prof. Anna Köhler	(Zweitgutachter)
Prof. Stephan Förster	(Vorsitz)
Prof. Carlo Unverzagt	



# Table of Content

<b>Summary</b> .....	<b>1</b>
<b>1. Introduction</b> .....	<b>7</b>
1.1 Motivation: Organic Photovoltaics .....	7
1.2 Characterization of Solar Cells .....	10
1.3 Types of Organic Solar Cells .....	13
1.4 Organic Semiconductor Materials .....	20
1.5 Charge Carrier Mobility in Organic Semiconductors .....	33
1.6 Objective of this Thesis.....	47
<b>2. Overview of the Thesis</b> .....	<b>59</b>
<b>3. Unsymmetrical Perylene bisimides: Influence of Substituents on     Crystal Structure and Electron Transport</b> .....	<b>83</b>
<b>4. Liquid Crystalline Perylene Diester Polymers with Tunable Charge     Carrier Mobility</b> .....	<b>113</b>
<b>5. Pendant Perylene Polymers with High Electron Mobility</b> .....	<b>137</b>
<b>6. Correlation of Charge Carrier Mobilities and Solar Cell Parameters     in Polymer:Fullerene Blend Devices</b> .....	<b>161</b>
<b>7. Fullerene-grafted Copolymers exhibiting High Electron Mobility     without Nanocrystal Formation</b> .....	<b>181</b>
<b>8. Annex: Perylene bisimide Blend Solar Cells: Influence of     Substituents on Blend Morphology and Device Performance</b> .....	<b>213</b>
<b>List of Publications</b> .....	<b>227</b>
<b>Danksagung / Acknowledgment</b> .....	<b>229</b>
<b>Erklärung</b> .....	<b>231</b>



## Summary

This dissertation deals with organic semiconductors for applications as electron acceptor (n-type) materials in organic electronic devices such as organic photovoltaic (OPV) cells. Bulk heterojunction (BHJ) solar cells, the most successful type of organic solar cells to date, require an electron donor and an electron acceptor material. The most important parameters which an ideal electron acceptor has to fulfill are strong visible light absorption, sufficient high electron mobility and appropriate energy levels with respect to the donor. Furthermore, the blend morphology of donor and acceptor is crucial for the device performance. Within this thesis, the synthesis and characterization of novel n-type polymers is reported and various techniques to evaluate the above mentioned parameters for n-type small molecules and polymers are presented. The aim was to investigate the impact of chemical structure on the optical and electronic properties and morphology of these semiconductors. Successful strategies how to control and improve light harvesting, electron mobility, blend morphology and solar cell performance were identified. The fundamental question of the charge transport properties of the materials under investigation was addressed by fabricating single carrier devices using the SCLC (space-charge limited currents) method. The morphology was primarily investigated by atomic force microscopy (AFM) and X-ray diffraction (XRD). Optical properties were studied by means of UV/vis and photoluminescence (PL) spectroscopy. Further, differential scanning calorimetry (DSC), temperature-controlled polarized optical microscopy (POM) and cyclic voltammetry (CV) were important characterization techniques in this work. BHJ solar cells were prepared and characterized by external quantum efficiency (EQE) measurements and current density – voltage ( $J$ - $V$ ) characteristics.

The first part of this thesis focuses on perylene imide based small molecules and polymers which represent an important class of n-type semiconductors. In general, these materials have a high tendency for crystallization and aggregate formation which can influence electron mobilities. At the same time, however, large crystalline domains often result in poor device performance when perylenes are used in OPV cells. The side groups of a series of *N*-substituted perylene bisimides (PBI) were found to play a crucial role on crystallinity and charge transport. The nature of the side groups had great impact on the crystalline structure and electron mobility. When hydrophilic oligoethylenglycol (OEG) side groups were present, the perylene molecules aligned in highly ordered hexagonal or lamellar columns and realized high electron mobilities of up to  $7 \cdot 10^{-3} \text{ cm}^2 \text{V}^{-1} \text{s}^{-1}$ , while the perylene derivative with only

---

hydrophobic alkyl chains only showed  $3 \cdot 10^{-5} \text{ cm}^2 \text{V}^{-1} \text{s}^{-1}$ . In addition, the substituents at the perylene core also had a major impact on the blend morphology of OPV devices when these materials were used in combination with a donor polymer. Here, we were able to tune the extent of phase separation between donor and acceptor via hydrophilic-hydrophobic interactions of donor polymer and acceptor side groups. To improve light harvesting of perylene compounds, the  $\pi$ -electron system of PBIs was altered and highly soluble, novel perylene side chain polymers (PPDB and PPDI) were synthesized by nitroxide mediated radical polymerization (NMRP). The pendant perylene moieties were perylene diester benzimidazole (PDB) and perylene diester imide (PDI). Compared to polymers bearing PBI side groups, the visible light absorption of PPDB was broadened and red shifted, whereas a narrower and blue shifted absorption was observed for PPDI. Remarkably, also the electronic nature of the two materials was affected by the modification at the perylene core, as PPDB is an n-type semiconductor and PPDI has a more pronounced p-type character. A comparative study of perylene side-chain polymers synthesized by a combination of NMRP and “click” chemistry revealed that the compound with improved optical properties (PPDEB) exhibited worse charge carrier mobility compared to PPBI. Another striking result was found as an amorphous polymer bearing OEG side chains showed a better electron mobility than the corresponding material with alkyl chains, which was liquid crystalline. A very high electron mobility of  $1 \cdot 10^{-2} \text{ cm}^2 \text{V}^{-1} \text{s}^{-1}$  was measured.

The second part of this dissertation addresses fullerene based acceptor materials, among which Phenyl- $\text{C}_{61}$ -butyric acid methyl ester (PCBM) is the state-of-the-art n-type semiconductor used in OPV. For two fullerene derivatives, Bis-Phenyl- $\text{C}_{61}$ -butyric acid methyl ester (bis-PCBM) and Bis-o-quinodimethane  $\text{C}_{60}$  (bis-oQDMC), exhibiting different substituents at the fullerene core, the LUMO energy levels were higher compared to PCBM. As a result, improved open circuit voltages ( $V_{OC}$ ) in BHJ solar cells with a donor polymer were obtained. The efficiency however did not improve, because of reduced short circuit current densities ( $J_{SC}$ ). We found that for the bis-PCBM system,  $J_{SC}$  was limited by low electron transport, while for the bis-oQDMC system an unfavorable blend morphology hampered the performance. The problem of low electron mobility could be overcome by reducing the thickness of the active layer and higher  $J_{SC}$  and overall device performance could be achieved. A drawback of fullerene small molecules is that diffusion, aggregation and crystallization of these molecules within BHJ blends can often negatively affect the stability of the blend morphology and reduce the device performance. We discovered that aggregate and crystallite formation in novel fullerene side chain polymers could be successfully suppressed, whilst high electron mobility and better film properties were achieved.

Altogether, new insights into structure-property relation of organic electron transport materials are presented in this work. Altering the  $\pi$ -electron system and the substituents attached to the electronically active parts of the respective compounds has been shown to be a powerful tool to improve optical and charge transport properties as well as morphology. Moreover, the detailed analysis of charge transport in OPV blends helped to understand the performance of solar cells and an approach towards active layers with enhanced morphological stability is shown.

## Zusammenfassung

Diese Dissertation befasst sich mit organischen Halbleitern, die als Elektronakzeptor- oder n-typ Materialien in organischen elektronischen Bauteilen, wie z.B. organischen Photovoltaikzellen (OPV), verwendet werden können. „Bulk heterojunction“ (BHJ) Solarzellen, die derzeit den erfolgreichsten Typ von organischen Solarzellen darstellen, benötigen sowohl Elektronendonator- als auch Elektronakzeptormaterialien. Die wichtigsten Parameter, die ein idealer Akzeptor erfüllen muss, sind eine hohe Absorption des sichtbaren Lichts, ausreichende Elektronenmobilität und auf den entsprechenden Donor abgestimmte Energieniveaus. Außerdem hat die Blendmorphologie von Donor und Akzeptor entscheidenden Einfluss auf die Effizienz der Solarzelle. In dieser Dissertation sind die Synthese und Charakterisierung von neuartigen n-typ Polymeren sowie verschiedene Techniken zur Bestimmung der oben beschriebenen Parameter für niedermolekulare und polymere n-typ Materialien beschrieben. Ziel war es, den Einfluss der chemischen Struktur auf die optischen und elektronischen Eigenschaften und die Morphologie dieser Halbleiter zu bestimmen. Erfolgreiche Strategien um Lichtabsorption, Elektronenmobilität, Blendmorphologie und Solarzelleneffizienz zu kontrollieren und zu verbessern, konnten herausgearbeitet werden. Die grundlegende Frage nach dem Ladungstransport der zu untersuchenden Materialien wurde mittels der SCLC- („space-charge limited currents“) Methode beleuchtet. Die Morphologie wurde in erster Linie mittels Rasterkraftmikroskopie (AFM) und Röntgendiffraktometrie (XRD) untersucht. Die optischen Eigenschaften wurden mittels UV/vis- und Photolumineszenzspektroskopie bestimmt. Des Weiteren sind Differentielle Wärmeflusskalorimetrie (DSC), temperaturabhängige Polarisationsmikroskopie (POM) und Cyclovoltammetrie (CV) als wichtige Charakterisierungsmethoden in der vorliegenden Arbeit zu nennen. BHJ Solarzellen wurden

---

angefertigt und mittels Externer Quanteneffizienz (EQE) und Strom-Spannungs- ( $J$ - $V$ ) Kennlinien charakterisiert.

Der erste Teil dieser Dissertation beschäftigt sich mit niedermolekularen Verbindungen und Polymeren auf Perylenimidbasis, die eine wichtige Klasse von n-typ Halbleitern darstellen. Generell haben diese Materialien die Eigenschaft, Kristallite und Aggregate zu bilden, was die Elektronenmobilität stark beeinflussen kann. Große kristalline Bereiche führen jedoch oftmals zu niedrigen Effizienzen, wenn Perylene in OPV Zellen verwendet werden. Bei einer Reihe von  $N$ -substituierten Perylenbisimidinen (PBI) zeigte sich, dass die Art der Seitengruppensubstituenten bedeutenden Einfluss auf die Kristallinität und den Ladungstransport haben. Bei hydrophilen Oligoethylenglycol- (OEG) Seitengruppen, richteten sich die Perylenmoleküle in hochgeordneten hexagonalen oder lamellaren Kolumnen aus, wobei hohe Elektronenmobilitäten von bis zu  $7 \cdot 10^{-3} \text{ cm}^2 \text{ V}^{-1} \text{ s}^{-1}$  erreicht wurden, während das Perylenderivat mit hydrophoben Alkylseitengruppen nur  $3 \cdot 10^{-5} \text{ cm}^2 \text{ V}^{-1} \text{ s}^{-1}$  zeigte. Zudem hatten die Substituenten am Perylengerüst entscheidenden Einfluss auf die Blendmorphologie von OPV Zellen, wenn diese Materialien mit einem Donorpolymer kombiniert wurden. Die Phasenseparation zwischen Donor und Akzeptor konnte hierbei durch die hydrophob-hydrophilen Wechselwirkungen des Donorpolymers mit den Seitengruppen des Akzeptors kontrolliert werden. Um die Lichtabsorption von Perylenverbindungen zu verbessern, wurde das  $\pi$ -Elektronensystem der PBIs variiert und hochlösliche, neue Perylenseitenkettenpolymere (PPDB und PPDI) mit Hilfe der Nitroxid-vermittelten radikalischen Polymerisation (NMRP) synthetisiert. Die Perylenseitenketten bestanden aus Perylendiesterbenzimidazol (PDB) und Perylendiesterimid (PDI). Verglichen mit Polymeren, die PBI- Seitengruppen besitzen, war die Lichtabsorption von PPDB spektral verbreitert und rotverschoben, während eine schmalere und blauverschobene Absorption bei PPDI beobachtet wurde. Bemerkenswerterweise wurden auch die elektronischen Charakteristika der zwei Materialien durch die Modifikation am Perylengerüst beeinflusst, da PPDB ein n-typ Halbleiter ist, jedoch bei PPDI der p-typ Charakter ausgeprägter ist. Eine Vergleichsstudie von Perylenseitenkettenpolymeren, die mittels einer Kombination aus NMRP und „Click“-Chemie synthetisiert wurden, verdeutlichte, dass die Verbindung mit verbesserten optischen Eigenschaften (PPDEB) einen schlechteren Ladungstransport im Vergleich zu PPBI zeigte. Als eine weitere wichtige Erkenntnis gilt, dass ein amorphes Polymer mit OEG Gruppen eine bessere Elektronenmobilität aufwies, als das entsprechende Material mit Alkylketten, welches flüssig-kristallin war. Eine sehr hohe Elektronenmobilität von  $1 \cdot 10^{-2} \text{ cm}^2 \text{ V}^{-1} \text{ s}^{-1}$  wurde gemessen.

Der zweite Teil dieser Dissertation handelt von Fulleren-Akzeptormaterialien. Hierbei ist Phenyl-C<sub>61</sub>-butylsäuremethylester (PCBM) als n-typ Material Stand der Technik bei OPV Anwendungen. Für die beiden Fullenderivate Bis-Phenyl-C<sub>61</sub>-butylsäuremethylester (bis-PCBM) und Bis-o-quinodimethan C<sub>60</sub> (bis-oQDMC), die jeweils unterschiedliche Substituenten am Fullerenegerüst tragen, sind die LUMO Energieniveaus höher als bei PCBM. Infolge dessen konnten höhere Leerlaufspannungen (V<sub>OC</sub>) in BHJ Solarzellen mit einem Donorpolymer erhalten werden. Die Gesamteffizienz verbesserte sich jedoch aufgrund der verringerten Kurzschlussstromdichte (J<sub>SC</sub>) nicht. Wir ermittelten, dass für das bis-PCBM-System die Kurzschlussstromdichte durch einen schlechteren Elektronentransport limitiert war, während bei dem bis-oQDMC-System eine unpassende Blendmorphologie der Grund für eine niedrige Effizienz der Solarzelle war. Das Problem der niedrigen Elektronenmobilität konnte durch Verringern der aktiven Schichtdicke umgangen und somit eine höhere J<sub>SC</sub> sowie eine höhere Gesamteffizienz der Solarzelle erreicht werden. Ein Nachteil niedermolekularer Fullereene ist ihre Diffusion, Aggregation und Kristallisation in BHJ Blends, was häufig die Stabilität der Blendmorphologie und die Effizienz der Solarzelle beeinträchtigt. Wir entdeckten, dass die Aggregat- und Kristallitbildung in neuartigen Fullereneseitenkettenpolymeren erfolgreich unterdrückt, gleichzeitig aber hohe Elektronenmobilitäten und bessere Filmeigenschaften erhalten werden konnten.

Zusammenfassend weist diese Arbeit neue Erkenntnisse über Struktur-Eigenschaftsbeziehungen organischer Elektronenleiter auf. Veränderungen am  $\pi$ -Elektronensystem und an den Substituenten des elektronisch aktiven Teils des Halbleiters haben sich als effektives Mittel zur Verbesserung der optischen Eigenschaften und der Ladungstransporteigenschaften, sowie der Morphologie herausgestellt. Zudem erweiterte die detaillierte Analyse des Ladungstransportes in OPV Blends das Verständnis der Solarzellencharakteristika und deren Effizienz. Schließlich wurde auch ein Ansatz in Richtung morphologisch stabilerer aktiver Schichten aufgezeigt.



# 1. Introduction

## 1.1 Motivation: Organic Photovoltaics

The future supply of energy for humankind is currently a heavily discussed topic in politics and society. While the worldwide energy demand increases and global warming is continuing, the acceptance of traditional energy sources like fossil fuels and nuclear power is shrinking. Hence, providing alternative, environmental friendly and renewable energy in sufficient quantity and at low costs is one of the biggest challenges that our society now faces. Among all “green” energy sources, the solar energy is of special importance due to the huge amount of energy that is provided in the form of irradiation every day. It is worth mentioning that the amount of solar energy reaching the earth surface during 1 h ( $1.4 \cdot 10^{30}$  J) is equivalent to the annual worldwide energy consumption.<sup>1, 2</sup> In a solar cell, the energy of light absorbed by a semiconducting material, can directly be converted into electricity using the photovoltaic effect, which was discovered by Alexandre-Edmond Becquerel in 1839.<sup>3</sup> Today, the most efficient photovoltaic (PV) cells are based on monocrystalline silicon as semiconductor, where power conversion efficiencies (PCE) of 25 % can be reached in single junction devices.<sup>4</sup> The high material and production costs of crystalline silicon cells however limit their wide-scale use at present which is why other PV technologies are emerging. Among the most promising types in this context are organic photovoltaic (OPV) cells. Since the discovery of electrical conductivity in conjugated polymers by Heeger, MacDiarmid and Shirakawa in the 1970s (which was awarded with the Nobel Prize in chemistry in 2000), semiconductors based on organic molecules and polymers have attracted great attention. When compared to inorganic silicon, the key benefit in using organic or polymeric (plastic) semiconductors in PV is its solution processability, which allows for cost efficient, high-throughput, roll-to-roll printing of multilayered structures on a large area. As a consequence, production cost can be minimized significantly. Crucial for the success of a “green” energy technology is the time it takes to get back the energy that was invested during production,

which is known as the energy payback time. For crystalline silicon solar cells, the energy payback time is approximately 1-2 years, whereas for OPV energy payback times of only 1 day can be achieved.<sup>5</sup> In addition, the feasibility of large area printing on flexible substrates opens up new possible applications of portable and light-weight solar power for integration into clothes, bags, etc.. Also, since only very thin films of a few hundreds of nanometers are required as the active layer, semitransparent cells can realize building integrated photovoltaics. Another advantage of OPV is their higher sensitivity at low light intensities, which enables better efficiencies for indoor applications or at diffuse light conditions.<sup>1</sup> Furthermore, the color of the devices, which is also an important factor from a marketing point of view, can be tuned by changing the chemical structure of the materials used. The huge interest in OPV technology is also attested by the growing number of scientific papers being published each year, as illustrated in Figure 1a. An image of a flexible and light weight organic solar panel is shown in Figure 1b.

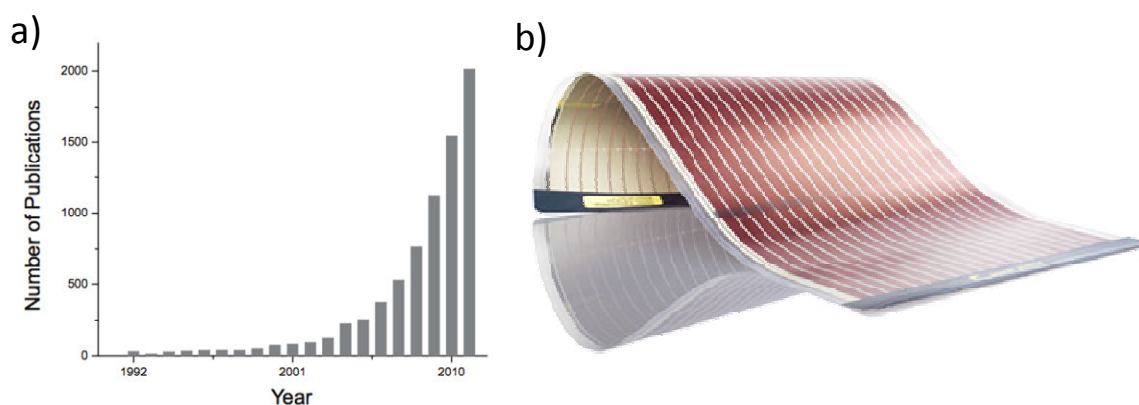


Figure 1: a) Number of publications on organic solar cells since 1992;<sup>6</sup> b) flexible organic solar panel.<sup>7</sup>

### Organic Photovoltaik Concepts

An electrical isolator is roughly defined as a material with a wide band gap ( $E_g$ ) larger than 3 eV. For organic materials, the band gap is given by the difference between the highest occupied molecular orbital (HOMO) and the lowest unoccupied molecular orbital (LUMO). The majority of organic molecules and polymers are considered as isolators. To become

---

semiconducting, a material needs to exhibit the following important features. Organic semiconductors mainly consist of alternating C-C single and C=C double bonds, resulting in  $sp^2$ -hybridization of their carbon atoms. Electrons in the  $p_z$ -orbital of each  $sp^2$ -hybridized carbon atom form  $\pi$ -bonds with neighboring  $p_z$ -electrons, which then results in delocalization of these  $\pi$ -electrons. As a result of  $\pi$ -electron delocalization, the energy levels of the orbitals merge and the band gap energy is reduced. Thus the band gap in organic semiconductors reaches values of approximately only 1-3 eV. Electrons can be excited from the HOMO into the LUMO by thermal excitation or by absorption of light with suitable energy. Therefore, organic semiconducting materials are able to absorb light in the UV/visible region of the solar spectrum and transport electric current.<sup>8</sup> From the onset of the absorption spectrum, one can calculate the optical band gap. An onset at longer wavelengths is equivalent to a band gap decrease. The often used term ionization potential (IP) can be related to the HOMO, electron affinity (EA) refers to the LUMO of a material. Concerning the mechanism of charge transport in organic materials, a direct comparison to the band-like transport in inorganic semiconductors is inaccurate. Since there is no long range order in organic materials, electronic states are localized on individual molecules or segments of molecules and charge carrier mobility is commonly orders of magnitude lower. The implications on charge transport are discussed in more details in Section 1.5. Another important property of organic semiconductors is their high absorption coefficients, which enables efficient light absorption in films with a thickness of only hundreds of nanometers. These intrinsic properties of organic semiconductors dictate the design of OPV cells. In general, organic semiconductors can be classified as donors (p-type) and acceptors (n-type). Further they are divided into polymer and small molecule based materials. Examples for both can be found in Section 1.4.

The fundamental processes of photoinduced charge generation in an organic solar cell, comprise of *absorption* of a photon, formation of an *exciton*, *exciton diffusion*, *charge transfer*, *charge separation*, *charge transport* and *charge collection*, which are outlined in the following. The efficiency of light absorption in the active layer depends on its absorption spectrum, the extinction coefficient and the active layer thickness. Absorption of light within the semiconductor leads to the excitation of an electron from the HOMO into the LUMO of

the material, resulting in an electron-hole pair or exciton. The electron-hole pair is coulombically bound with the exciton binding energy typically being in the range of 0.1-1 eV.<sup>9, 10</sup> At room temperature the binding energy is larger than  $k_B T$  and hence electron and hole cannot dissociate directly.<sup>11</sup> To overcome the exciton binding energy, an electrical field is required, so that charges can separate. Therefore, the exciton needs to diffuse to a region, where such a driving force is provided. Exciton diffusion lengths however, are usually limited to approximately 10 nm due to the short lifetime and slow diffusion coefficient of this state.<sup>12-14</sup> Several ways of providing the driving force for charge separation and avoiding recombination of the exciton will be described for each type of OPV cell below. Once electron and hole are separated, the free charges need to be transported to the respective electrodes, holes to the anode, electrons to the cathode. Finally, charges are collected at the electrodes generating a photocurrent. In an organic solar cell, most of the steps described here compete with various recombination processes, resulting in energy losses. Depending on device architecture and materials used, the reason for recombination can be different. Details will be discussed in the following sections for each kind of OPV device. Understanding the cause and minimizing recombination losses is the focus of extensive studies worldwide in order to improve the efficiency of OPV.<sup>15</sup> Researchers commonly use the following methods to characterize organic solar cells.

## 1.2 Characterization of Solar Cells

The two most important methods for characterizing solar cells in general are the measurement of the current density-voltage ( $J$ - $V$ ) characteristics and the determination of the external quantum efficiency (EQE). Usually,  $J$ - $V$  curves are recorded in dark and under illumination. As a light source, solar simulators are commonly used, the irradiation spectrum of which matches the air mass 1.5 (AM1.5) solar spectrum. For a standard measurement, the light intensity is set to  $1000 \text{ Wm}^{-2}$ , which is equivalent to “1 sun” and the solar cell should be kept at  $25 \text{ }^\circ\text{C}$ . All important parameters of a solar cell, which are short-circuit current density ( $J_{\text{sc}}$ ), open-circuit voltage ( $V_{\text{oc}}$ ), filling factor (FF) and power conversion efficiency (PCE),

can be extracted directly from the  $J$ - $V$  curve. A typical  $J$ - $V$  curve under illumination is depicted in Figure 2a. The current density at zero applied voltage corresponds to  $J_{SC}$  and the voltage where the current density is equal to zero is the  $V_{OC}$ . Both points span a rectangle, which is shaded in Figure 2a. Between those two points along the  $J$ - $V$  curve the solar cell generates power ( $P=J \cdot V$ ). The point, where the product of  $J$  and  $V$  is largest, is denoted as maximum power point (MPP). The corresponding rectangle is also shaded in Figure 2a. The FF is a measure of the “rectangularness” of the  $J$ - $V$  curve and is influenced by charge transport properties, recombination, as well as series and “shunt” resistance.<sup>8</sup> It is a measure of the ratio of  $J_{SC}$  and  $V_{OC}$  that can be used for power generation and is calculated as follows:

$$FF = \frac{J_{MPP} \cdot V_{MPP}}{J_{SC} \cdot V_{OC}}$$

The power conversion efficiency (PCE) is defined as the electrical power produced by the solar cell divided by the power of light irradiating the device:

$$PCE = \frac{P_{OUT}}{P_{IN}} = \frac{J_{SC} \cdot V_{OC} \cdot FF}{P_{IN}}$$

Besides recording  $J$ - $V$  curves, measuring the external quantum efficiency (EQE) spectrum (also called *Incident Photon to power Conversion Efficiency*, *IPCE* spectrum) is important for characterizing a solar cell. The EQE is defined as the fraction of incident photons that produced free electrons collected at the device electrode at a certain wavelength  $\lambda$ , and is calculated according to the following equation:

$$EQE = \frac{h \cdot c}{q} \cdot \frac{J_{SC}(\lambda)}{P(\lambda)\lambda}$$

with  $P(\lambda)$  being the monochromatic incident optical power,  $h$  the Plank’s constant,  $c$  the speed of light,  $q$  the elementary charge and  $J_{SC}(\lambda)$  is the short circuit current density at wavelength  $\lambda$ .

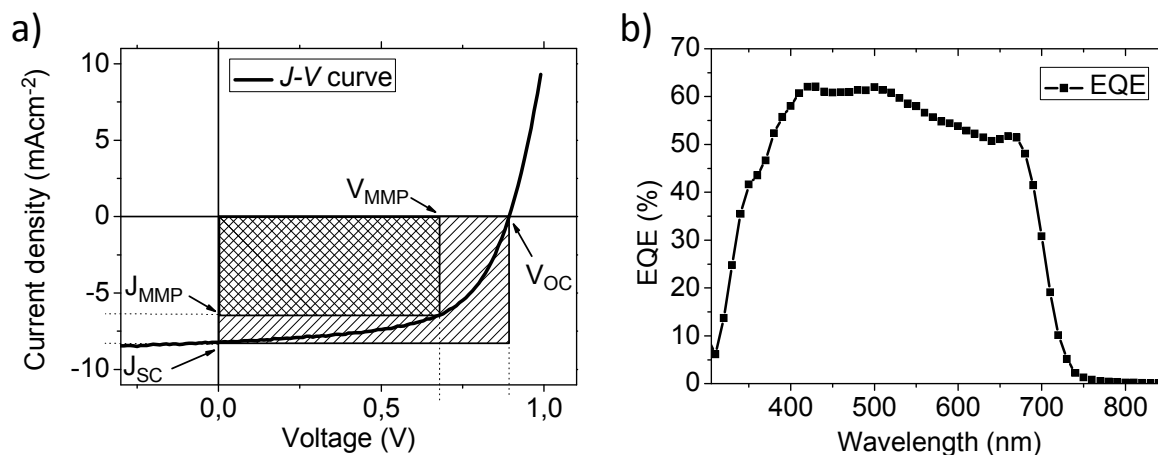


Figure 2: a) Typical J-V characteristics of an organic solar cell under illumination where the intersections with the abscissa and the ordinate are  $V_{OC}$  and  $J_{SC}$ , respectively; the maximum power point (MPP) is determined where the product of voltage and current density is maximal ( $V_{MPP} \cdot J_{MPP}$ ); b) external quantum efficiency (EQE) spectrum of an organic solar cell.

To measure the EQE spectrum, the photovoltaic device is irradiated with monochromatic light of known intensity and the photocurrent that is generated is detected for each wavelength, commonly in the UV/visible and near IR part of the spectrum. One can calculate the  $J_{SC}$  of a cell by integrating its EQE spectrum over the AM1.5 solar spectrum:<sup>1,16</sup>

$$J_{sc} = \frac{q}{hc} \int_{\lambda(1)}^{\lambda(2)} P(\lambda) EQE(\lambda) \lambda d\lambda$$

where  $\lambda_1$  and  $\lambda_2$  are wavelength limits of the incident spectra.<sup>17</sup> A typical EQE spectrum of an organic solar cell is shown in Figure 2b. If the total amount of photons actually absorbed by the active layer or reflection losses are known, the internal quantum efficiency (IQE) can be determined from EQE. These standardized methods are essential for characterizing and comparing any kind of solar cell. In the following, a brief overview of different OPV concepts is given.

### 1.3 Types of Organic Solar Cells

#### Single layer solar cells

Organic single layer solar cells were the first organic photovoltaic devices tested.<sup>18</sup> A semiconductor, which is used for light harvesting, is sandwiched between two electrodes with different work functions. The schematic of such a device is shown in Figure 3a. Indium tin oxide (ITO), deposited on a substrate such as glass, is used as a transparent anode, a p-type semiconductor as active layer and the low work function metal aluminium as cathode. For a qualitative understanding of the basic principle, typical Schottky and p/n-junction models, originally developed for inorganic semiconductors, are applied here for organic semiconductors (Figure 3b).

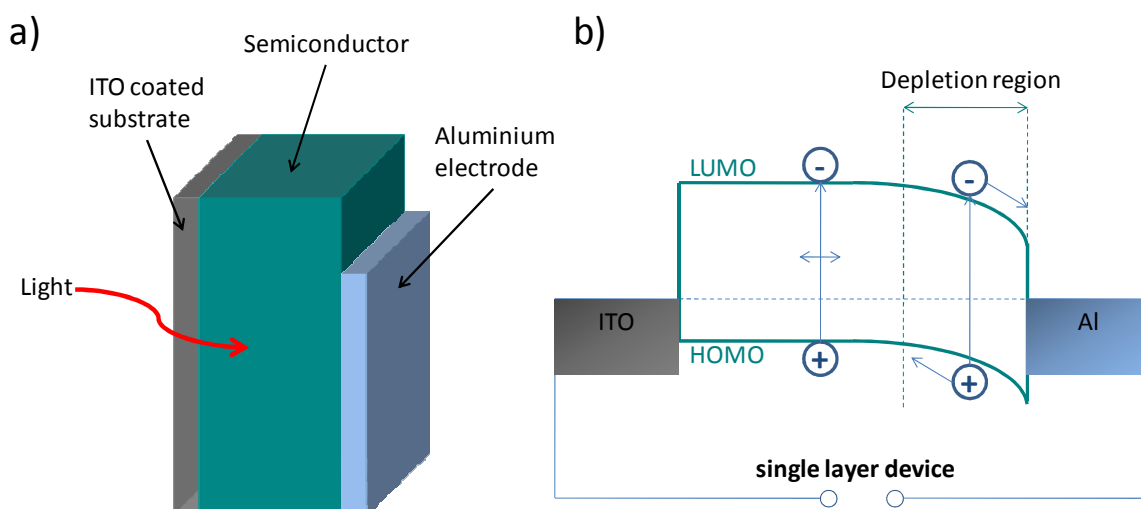


Figure 3: a) Device architecture of an organic single layer solar cell with indium tin oxide (ITO) as transparent electrode, a p-type semiconductor as light absorbing layer and aluminium top contact; b) schematic energy band diagram of a single layer solar cell; photogenerated excitons can only be dissociated into free charges in the depletion region, formed by the Schottky-contact, which limits efficient charge separation and hence PCE.<sup>8, 21</sup>

It is worth mentioning, that this is only an approximation of the solid-state properties of these materials. When a semiconductor is brought into contact with another material having a different work function (in this case a p-type semiconductor with high work function and aluminium with low work function), the different electrochemical potentials or Fermi levels

equilibrate. As a consequence of this so called band bending, a space-charge or depletion region (Schottky-contact) is built up close to the interface.<sup>19</sup> To operate this device as a solar cell, a photogenerated exciton created somewhere in the active layer has to diffuse to the depletion region. Only then, the electric field is strong enough to overcome the coulomb interaction of hole and electron. As mentioned above, exciton diffusion length is limited to several nanometers, which is why organic single layer solar cells are commonly not very efficient. PCEs reported were usually far below 0.1 %, however for merocyanine dyes a PCE of 0.7 % was achieved in the late 1970s.<sup>20</sup>

### **Bilayer heterojunction solar cells**

A more efficient charge separation and higher PCEs were realized with bilayer heterojunction solar cells, where an electron donor (p-type or hole transporting material) and electron acceptor (n-type or electron transporting material) are stacked together thereby forming a planar interface. An example of such a device was given by Tang in 1986, who reported a remarkable efficiency of 1 % for a two-layer organic photovoltaic cell consisting of copper phthalocyanine as donor and a perylene derivative as acceptor.<sup>22</sup> The device setup and schematic of charge photogeneration in a bilayer heterojunction solar cell are depicted in Figure 4. Possible band bending at the semiconductor/metal interface is neglected here. A suitable energy offset between LUMO of donor and LUMO of acceptor, as well as HOMO of donor and HOMO of acceptor is crucial, so that a potential drop arises and a heterojunction is formed, when both materials are brought in contact. If an exciton is created in the donor, the electron which now resides in the LUMO of the excited donor state may be transferred to the LUMO of the acceptor. The requirement for this photoinduced electron transfer to happen is that the energy offset is bigger than the coulomb binding energy of the exciton.<sup>23</sup> Hence, Coulomb interaction may be overcome and the exciton can be separated into free charges. The same applies for the reverse hole transfer from an acceptor excited state. The exciton needs to be created close to the donor-acceptor interface to reach the heterojunction within the exciton diffusion length.<sup>24</sup> Once the exciton is separated, the free charges can be transported to the electrodes, whereby holes travel within the donor and electrons within the

acceptor. A great advantage of this concept is that recombination is minimized at this stage, when holes and electrons are separated. To efficiently extract the charges, electrodes should match the donor HOMO and the acceptor LUMO.<sup>8</sup> Vacuum-deposited copper phthalocyanine/ $C_{60}$  films were shown to give 3.6 % PCE (under 1.5 suns illumination) with this device architecture.<sup>25</sup> The drawback of this concept is that exclusively excitons that are in proximity to the heterojunction can contribute to the charge generation, which ultimately limits the device performance. Another drawback is that orthogonal solvents are required for solution processing of two organic layers, which limits its applicability. Hence most bilayer devices are fabricated by thermal evaporation processes, which is usually more complicated and expensive compared to solution processing. The bilayer concept, however, has been further developed by Leo *et al.* by introducing doped charge extraction layers in the device stack. PCEs exceeding 8 % were reported.<sup>26</sup>

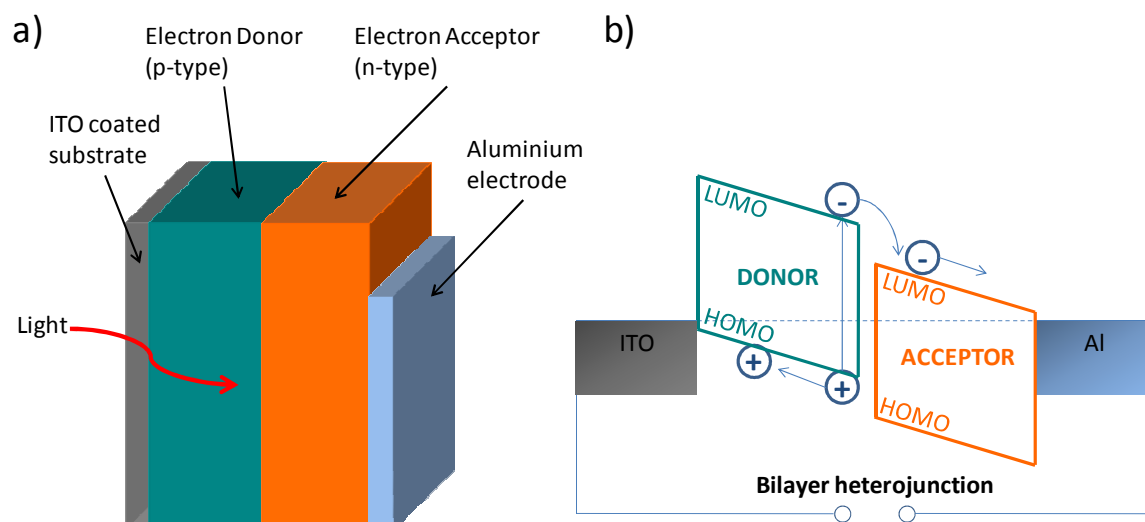


Figure 4: a) Device architecture of an organic bilayer heterojunction solar cell with ITO as transparent electrode, a p-type and n-type semiconductor forming a heterojunction at the interface and aluminium top contact; b) schematic energy band diagram of a bilayer heterojunction cell; photogenerated excitons can only be separated in a thin layer at the donor-acceptor interface; the work functions of the electrodes match the HOMO of donor or the LUMO of acceptor, respectively.<sup>8, 21</sup>

### Bulk heterojunction (BHJ) solar cells

A major breakthrough in OPV was the invention of the bulk heterojunction (BHJ) concept, first realized independently by groups of Heeger and Friend in 1995.<sup>27,28</sup> Donor and acceptor material are intimately mixed to form a three dimensional interpenetrating network. The majority of the BHJ devices comprise of at least one component which is a polymer semiconductor, usually a conjugated polymer. An illustration of a BHJ solar cell is given in Figure 5a. Ideally, the bicontinuous network is organized on a nanometer scale resulting in a large interface area, so that every exciton created can reach a donor acceptor interface within its diffusion length. This decreases the probability of geminate recombination, resulting in higher  $J_{sc}$ .

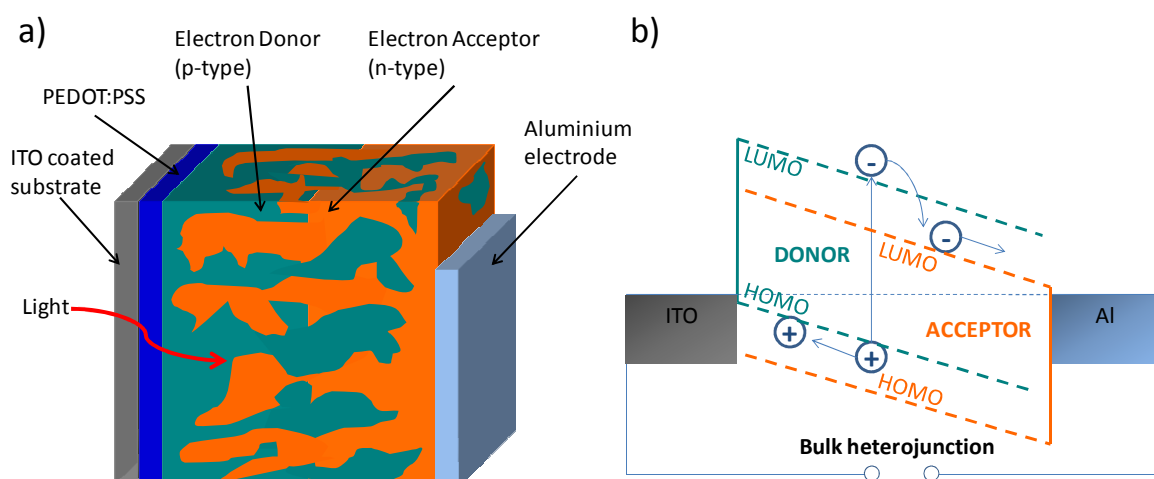


Figure 5: a) Device architecture of an organic bulk heterojunction (BHJ) solar cell with ITO as transparent electrode, a PEDOT:PSS buffer layer, a p-type and n-type semiconductor forming an interpenetrating network and aluminium top contact; b) schematic energy band diagram of a BHJ cell; ideally, due to nanoscale phase separation of donor and acceptor and the resulting large interface area, charges can be generated throughout the whole active area.<sup>21</sup>

Compared to a bilayer device, the massive increase in interface area enables a very efficient photoinduced charge transfer. A recent review by Durrant and co-worker gives insights into the charge photogeneration in organic BHJ solar cells.<sup>15</sup> Using the example of a polymer:PCBM blend, charge dissociation is explained in Figure 6. An exciton created in the polymer phase can undergo an electron transfer from the polymer to the acceptor (PCBM). Even though being located on different materials, the electron-hole pair does not necessarily

dissociate into free charges directly. A so called interfacial charge-transfer (CT) state may form, which then thermally relaxes with an electron-hole separation distance (thermalization length)  $a$ . The CT state can now undergo geminate recombination back to the ground state or to a triplet exciton state. Alternatively, free charge carriers can form and the charges can migrate towards the respective electrodes. According to Onsager theory the probability of the desired dissociation into free charge carriers depends on the ratio between  $a$  and the Coulomb capture radius  $r_c$ .

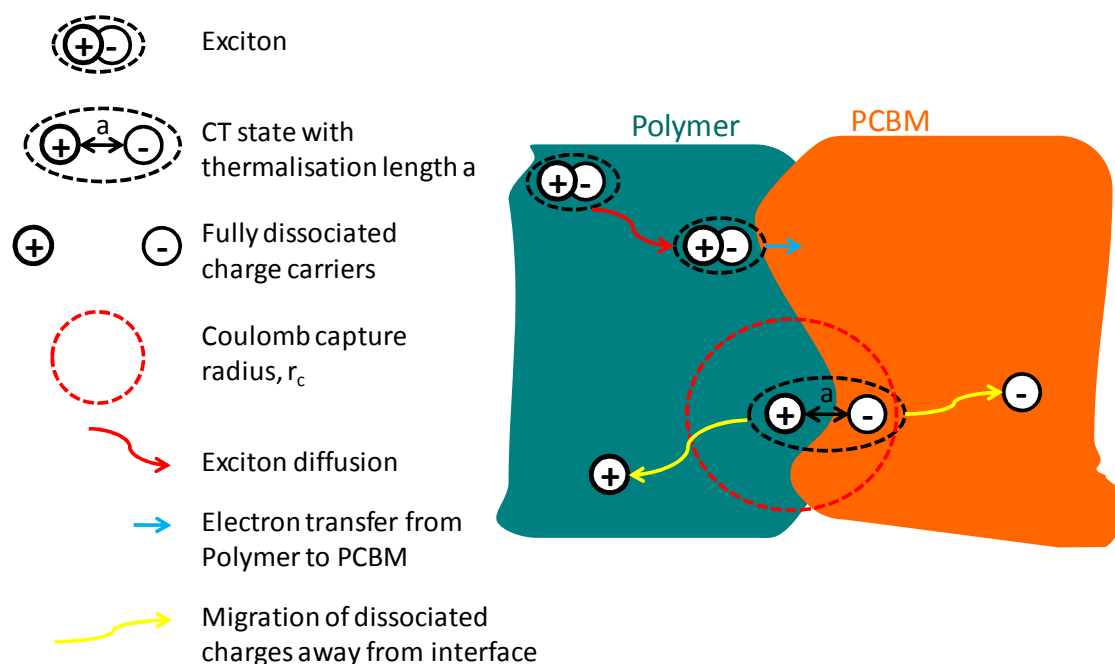


Figure 6: Schematic of charge dissociation: after exciton diffusion and generation of the charge-transfer (CT) state, the dissociation into free charges depends on the ratio between  $a$  and the Coulomb capture radius  $r_c$ , which is drawn as spherical for simplification.<sup>15</sup>

A bigger domain size favors CT-state dissociation, but can also lead to less efficient exciton diffusion to the interface. Also, steric interactions at the donor acceptor interface in the case of nonfullerene OPV devices were found to be of major importance for the energy of the CT state.<sup>29</sup> Depending on the size and bulkiness of solubilizing substituents at the polymer backbone, the CT state can be raised in energy, which decreases the barrier for charge separation. These findings demonstrate, that molecular design has a direct impact on both morphology and charge photogeneration.

In addition to a high interface area, sufficient percolation pathways for the continuous flow of generated charge carriers within the donor and acceptor phase towards the respective electrodes are crucial to avoid bimolecular (non-geminate) recombination losses. In fact the morphology of the bulk heterojunction has significant influence on device performance, which points out that controlling and tuning the morphology plays a crucial role.<sup>30, 31</sup> In addition to morphology, the interfaces of the organic material and electrodes are decisive as well. Buffer layers (e.g. PEDOT:PSS as electron blocking layer and TiO<sub>2</sub> or ZnO as hole blocking layers) should be introduced to avoid that charge carriers reach the opposite electrode and to maximize  $V_{OC}$ .<sup>32</sup> For the realization of highly efficient OPV cells, an understanding of the complex interplay of material design, processing conditions and morphology is essential.

Apart from high donor acceptor interface area, another key benefit of BHJ cells compared to bilayer devices is the ease of processability from solution. Solution processed bilayers require orthogonal solvent systems, in order not to dissolve the underlying layer during processing, which limits the choice of materials one can use. In BHJ devices, the active layer can be deposited from one solution. Several film deposition techniques like spin coating or doctor blading are commonly used on a laboratory scale. For large scale production of OPV films by roll to roll printing, slot-die coating or screen printing are the methods of choice.<sup>5, 33</sup> The film drying process, among other factors, influences the morphology of the bulk heterojunction. It is desirable to obtain a morphology where donor and acceptor material phase segregate on a nanometer scale. From a thermodynamic point of view, usually demixing of both compounds is preferred. In consequence, a bulk heterojunction often suffers from poor morphological stability due to increasing phase segregation of the two compounds over time, resulting in device degradation. Extensive studies on the morphology of BHJ devices can be found in literature.<sup>29, 31, 34-39</sup> In the following, a survey of the most important methods for controlling (from a device processing point of view) and characterizing morphology in OPV blends is given.

Thermal annealing<sup>31, 40, 41</sup> and solvent annealing<sup>42</sup> are widely used methods to alter the morphology of e.g. archetypal P3HT:PCBM blends (see sections below for structural details). The heat treatment as postproduction method for BHJ devices was shown to enhance  $V_{OC}$ , FF

and  $J_{SC}$ . Here, better  $V_{OC}$  and FF are presumably due to less series and high shunt resistance in the device. The improved  $J_{SC}$  on the other hand is often attributed to a reorientation and better packing of the material, leading to improved charge carrier mobilities.<sup>43</sup> Also, thermal annealing has been suggested to enhance phase separation due to the formation of distinct (pure) donor and acceptor phases, which can to some extent improve device performance.<sup>41</sup> A controlled solvent evaporation rate during solvent annealing could lead to higher charge carrier mobility and balanced charge transport in the device.<sup>30</sup> These methods presented result in higher mobility of polymer-chains or small molecule diffusion, so that the blend morphology is not “frozen”, but molecules can reorient. Similarly, the use of mixed solvents systems or co-solvents for film deposition also showed improved device efficiency in many cases.<sup>44-46</sup> Especially adding small amounts of high boiling point solvents like 1,8-octanedithiol was shown to increase polymer crystallinity, because the film drying speed is reduced and the polymer chains have more time to stack and form crystallites. For solution processed small molecule blends, overall domain sizes could be reduced from 20-30 nm to 15-20 nm by using only 0.25 %v/v of 1,8-diiodooctane as a co-solvent, which lead to significantly improved PCE.<sup>47</sup> Another powerful tool to tune the film morphology is solvent vapor annealing, which can be applied at room temperature without causing thermal damage to the film.<sup>48, 49</sup> This post production technique can help optimizing and stabilizing the blend morphology.<sup>50</sup>

All these methods have been proven useful for individual blend systems, but they cannot be seen as general tools to improve any BHJ solar cell. For every new material combination, finding the optimum conditions is crucial. The above mentioned methods can also have a negative impact on the devices performance depending on the material used. To gain a better understanding on how the blend morphology influences the solar cell characteristics, several techniques for the characterization of the BHJ are commonly used.

Among the most commonly used microscopy techniques for morphology examination of thin films is Atomic force microscopy (AFM), Scanning electron microscopy (SEM) or Transmission electron microscopy (TEM). High resolution information about surface topography and the surface distribution of donor and acceptor can be obtained by AFM.<sup>34</sup> For Polymer:Fullerene blends, the mapping of different domains of the two compounds could be

used to gain information about nanoscale phase separation across the bulk of the blend by imaging cross-sections with SEM<sup>51</sup> and TEM<sup>38</sup>. A vertical gradient in blend composition of BHJ films has been detected with Variable-angle spectroscopic ellipsometry (VASE)<sup>39</sup> and X-ray photoelectron spectroscopy<sup>52</sup>. Structural properties within an OPV blend like size and orientation of semicrystalline regions with respect to the substrate can be investigated by grazing incidence X-ray diffraction (GIXRD).<sup>53</sup>

Furthermore, UV/vis spectroscopy is an efficient and relatively simple method to probe microstructure of thin films. Excitonic coupling, intrachain order and fraction of crystalline domains for polymer samples,<sup>54</sup> and aggregation pattern of small molecules<sup>55</sup> can be detected. Photoluminescence quenching is a good estimation of the efficiency of charge transfer in donor acceptor blends and can therefore also give valuable information about morphology.<sup>56</sup> Finally transient absorption spectroscopy measurements reveal time resolved dynamics on transfer, recombination and transport mechanisms.<sup>57, 58</sup> To date, the most successful BHJ cells consist of polymers as the donor and small molecules as acceptor part with efficiencies approaching 10 %<sup>4, 16</sup> Nevertheless, polymer-polymer blends and blends of small molecules are also relevant systems.<sup>47, 59</sup> An overview of important donor polymers and acceptor materials used in OPV is given in the next chapter of this introduction.

## 1.4 Organic Semiconductor Materials

### Hole transport materials

Conjugated donor polymers are currently the most promising p-type or hole transport materials for OPV applications because of their potential to combine good film-forming properties, intensive light absorption, suitable HOMO and LUMO levels and high hole mobilities. The number of publications on new polymers synthesized and tested in BHJ solar cells has become tremendously high during the last years. Several recent review articles address this rapidly growing field of research.<sup>6, 35, 60-62</sup> In this section, a brief survey of the

development of p-type polymers as well as important concepts for the design of highly efficient donors for OPV is given. Starting from 1995, the first relevant BHJ devices were built based on poly(phenylene vinylene) (PPV) such as poly[2-methoxy-5(2'-ethylhexyloxy)-1,4-phenylenevinylene] (MEH-PPV) and (poly[2-methoxy-5-(3,7-dimethyloctyloxy)]-1,4-phenylenevinylene (MDMO-PPV) as donor material.<sup>27, 28</sup> In combination with a fullerene acceptor (PCBM, see following section for more details) high PCEs of up to 3.3 % were reported for PPV based BHJ solar cells.<sup>63, 64</sup> The next generation p-type polymer was poly(3-hexylthiophene) (P3HT), with which 5 % PCE can be achieved after optimization.<sup>30, 31</sup> Extensive research has been done on the synthesis of P3HT and optimization of P3HT:PCBM solar cells, which makes this polymer probably the most thoroughly studied material for OPV. Due to the lower band gap compared to PPV and the higher crystallinity which results in improved hole transport, higher  $J_{SC}$  were realized. Apart from processing conditions, regioregularity and molecular weight were found to have a major impact on device performance.<sup>65</sup> Further improvements of both PPV and P3HT based solar cells were limited due to the comparatively large band gap of these materials. In order to increase photocurrent and hence PCE of OPV devices it is inevitable to engineer materials that can absorb more light in the red and infrared region to better utilize the solar spectrum. A redshift of the absorption edge is tantamount to lowering the band gap, which is why the vast majority of novel p-type polymers for OPV are the so-called low band gap polymers. Several factors have an impact on the band gap of a conjugated polymer, which are molecular weight, bond length alternation, planarity of the polymer backbone, aromatic resonance energy, substituents and intermolecular interactions.<sup>35</sup> Engineering HOMO and LUMO levels of polymers is challenging as most of the above mentioned factors are also related to each other and can affect chemical, mechanical and physical properties as well. For example, changing the chain length of the substituents influences the solubility of the polymer in the first place. At the same time, intermolecular interactions, like supramolecular arrangement or aggregation as well as planarity of the polymer chains can be altered.

One approach to decrease the band gap of a conjugated polymer is to increase its quinoid character. In general, there are two possible resonance structures for a conjugated polymer in its ground state: the aromatic and the quinoid form. In the aromatic form each monomer unit

(e.g. thiophene, benzene) keeps its aromaticity with confined  $\pi$ -electrons. Upon delocalization of these  $\pi$ -electrons along the conjugated polymer chain, double bonds are converted into single bonds and *vice versa*. The polymer is in its quinoid form, which is energetically less stable than the aromatic, and thus has a lower band gap caused by a loss in stabilization energy. The bond length alternation (BLA) is a parameter describing the average of the difference in length between adjacent carbon-carbon bonds in the polymer chain. Large values for BLA are obtained for materials mainly in the aromatic form, whereas an increasing quinoid character results in decreasing BLA.<sup>66</sup> One way to promote the quinoid form is to fuse a heterocyclic ring with an aromatic or another heterocyclic ring with higher resonance energy (e.g. benzene, 1.56 eV and thiophene, 1.26 eV), so that the lower resonance energy material is more likely to “dearomatize” to adopt a quinoid structure and reduce the bond length alternation<sup>67,68</sup> (Figure 7a).

Another strategy for lowering the band gap of conjugated polymers is the donor-acceptor concept, which was proposed by Havinga in 1992.<sup>69</sup> A copolymer consisting of alternating “electron-rich” donor and “electron-deficient” acceptor parts leads to mixing of their orbitals with different degrees of intramolecular charge transfer character, which results in a reduced band gap. The hybridization of the molecular orbitals of donor and acceptor unit resulting in a reduced band gap are depicted in Figure 7b. Careful design of donor and acceptor moieties allows for tuning the strength of the intramolecular charge transfer and the band gap.<sup>70</sup> By implementing such a “push-pull” system, electron delocalization and the formation of quinoid character is promoted, which also leads to a smaller band gap. Strong donor-like moieties are usually found for example for aromatic heterocycles containing oxygen or sulfur atoms. Electron acceptors include heterocyclic aromatic systems like quinoline, quinoxaline or benzothiadiazole containing e.g. nitrogen atoms. Examples for such polymers are given in Figure 8. A copolymer consisting of alternating benzo[1,2-*b*:4,5-*b'*]dithiophene and thieno[3,4-*b*]thiophene units (PTB) gave a PCE of over 7 % in OPV devices. The well known donor-acceptor copolymer poly(4,4-dialkyl-cyclopenta[2,1-*b*:3,4-*b'*]dithiophene-*alt*-2,1,3-benzothiadiazole (PCPDTBT) gave up to 5.5 % PCE in standard OPV cells.<sup>44</sup> With poly[*N*-9'-hepta-decanyl-2,7carbazole-*alt*-5,5(4',7')-di-2-thienyl-2',1',3'-benothiadiazole)] (PCDTBT) (see Figure 8), a polymer based on dithienylbenzothiadiazole and soluble carbazole units, a

PCE of 6.1 % and a remarkable IQE of almost 100 % was achieved.<sup>71</sup> All these polymers were combined with fullerenes as acceptors to get high PCE.

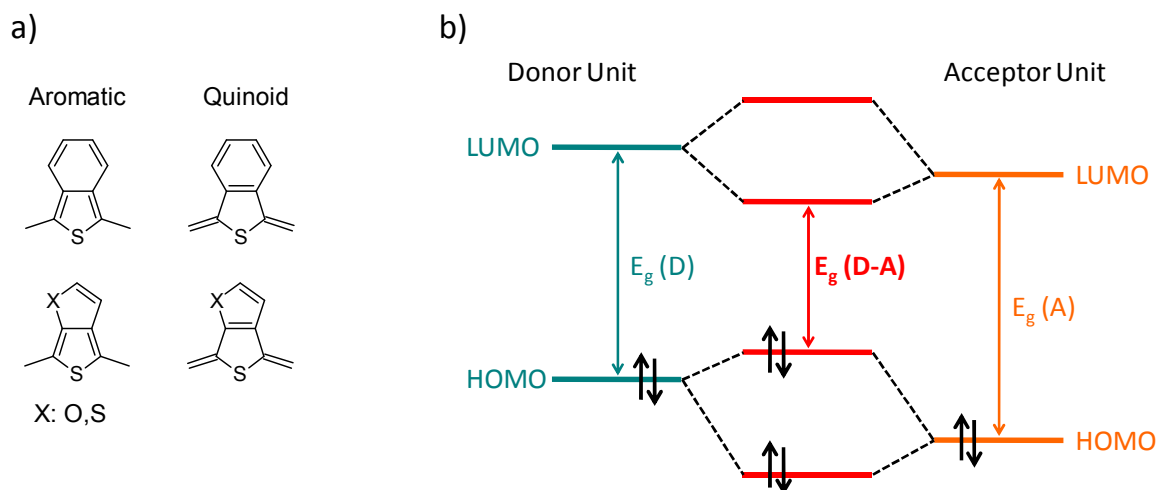


Figure 7: a) Quinoid approach for decreasing the band gap of a conjugated polymer: example of stabilization of quinoid resonance structure by aromatic benzene or thiophene rings; b) donor-acceptor approach: molecular orbital interaction between donor and acceptor units lowers the band gap ( $E_g$ ) of conjugated polymers by the creation of an intramolecular charge transfer.<sup>35</sup>

Finding the optimum ratio and relative strength of donor and acceptor unit is still a remaining question. Not only the band gap, but also the position of HOMO and LUMO levels is crucial for high performance OPV cells. A linear relation of the relative difference of HOMO of the p-type material and the LUMO of the n-type material and the  $V_{OC}$  has been found.<sup>72</sup> Hence, a desired low donor HOMO for good  $V_{OC}$  is in conflict with the request for a small band gap to potentially achieve high  $J_{SC}$ . Lowering both HOMO and LUMO of the donor will only succeed to a limited extent, because, as mentioned earlier, a certain LUMO-LUMO offset of p-type and n-type material is required for efficient charge transfer. It has been demonstrated that individual tuning of HOMO and LUMO levels within a donor-acceptor copolymer should be feasible, because in these materials, the HOMO is mainly localized on the donor part and the LUMO mainly on the acceptor part.<sup>73</sup> Great effort is put on modifying the strength of donor or acceptor moieties in order to gain an understanding of how the energy levels influence device performance.<sup>35</sup>

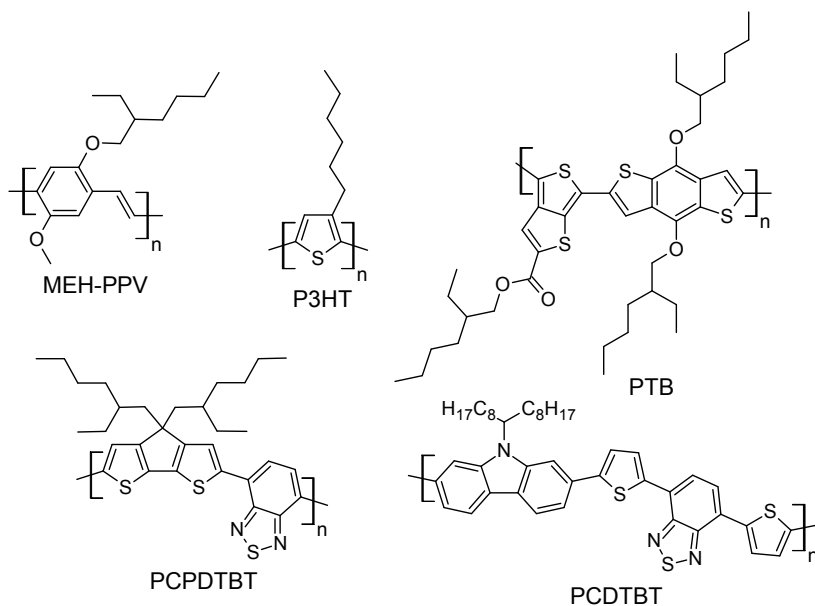


Figure 8: Important p-type conjugated polymers are MEH-PPV ((poly[2-methoxy-5(2'ethylhexyloxy)-1,4-phenylenevinylene]) and P3HT (poly(3-hexylthiophene)), as well as PTB (poly(thieno[3,4-b]thiophene-alt-benzo[1,2-b:4,5-b']dithiophene)), PCPDTBT (poly(4,4-dialkyl-cyclopenta[2,1-b:3,4-b']dithiophene-alt-2,1,3-benzothiadiazole) and PCDTBT (poly[N-9'-hepta-decanyl-2,7carbazole-alt-5,5(4',7'-di-2-thienyl-2',1',3'-benothiadiazole)]) as low band gap polymers.

Another important aspect that needs to be considered when designing new polymers for OPV application is solubility in order to guarantee good processability from organic solvents. Chain length, side groups, backbone rigidity, polymer regioregularity and intermolecular interactions (e.g.  $\pi$ - $\pi$  stacking) are key factors influencing solubility. For example, too strong  $\pi$ - $\pi$  stacking limits processability and can also have an impact on morphology and hence device performance. The choice of solubilizing side groups is therefore crucial for the successful implementation of a polymer in OPV cells.

For the synthesis of alternating donor-acceptor copolymers especially transition-metal-catalyzed cross-coupling reactions have proven to be convenient to create C-C bonds between  $sp^2$ -hybridized carbon atoms. The reaction mechanism starts with a transition-metal-catalyzed oxidative addition of the C-X bond of an organic halide as electrophile. Subsequently transmetalation with a main group organometallic nucleophile takes place, followed by a reductive elimination resulting in the carbon-carbon bond formation, at which the catalyst is also regenerated.<sup>66</sup> Palladium or nickel based complexes are commonly used as

catalysts. Stille coupling, using organotin,<sup>74</sup> or Suzuki coupling, using organoboron<sup>75</sup> monomers as organometallic nucleophiles are currently the most efficient and widely used methods. Both reactions can be realized under mild conditions and are tolerant to a variety of functional groups. Usually higher molecular weights are obtained in Stille polycondensation. Since Stille coupling involves toxic tin compounds, however, Suzuki coupling is the preferred reaction in relation to industrial large scale production.

### **Electron transport materials**

In this section, an overview and recent developments of relevant electron transport or n-type materials for the application as electron acceptor in OPV cells are presented. An “ideal” acceptor should combine good light harvesting properties, high electron mobility and stability under processing and operational conditions. In addition, ease and cost of synthesis are important factors as well. A typical feature of n-type materials is electron deficiency and a low-energy LUMO, which makes them comparatively easy to be reduced. Electron deficient reduced molecules (often radical anions) are less reactive and are therefore more stable to oxygen or water.<sup>76</sup>

#### *Fullerene based acceptors*

Since the discovery of stable, aromatic spherical shaped clusters consisting of 60 carbon atoms in 1985, the so called buckminsterfullerenes<sup>77</sup> have attracted enormous attention as electroactive material. The readily available C<sub>60</sub> (see Figure 9) acts as electron acceptor being able to accept up to six electrons in solution and shows high electron mobility.<sup>78</sup> Because of its limited solubility, vacuum deposition was the predominant deposition technique, where C<sub>60</sub> was successfully used in bilayer heterojunction solar cells with high efficiencies of 3.6 % with a copper phthalocyanine donor.<sup>25</sup> It was in 1995 when Hummelen and coworkers reported the methano-fullerene derivative Phenyl-C<sub>61</sub>-butyric acid methyl ester (PC<sub>61</sub>BM) as a soluble version of C<sub>60</sub>.<sup>79</sup> In a BHJ, efficient charge separation resulting from ultrafast (in the range of

50-100 fs) photoinduced electron transfer from a p-type polymer to PCBM was demonstrated in the same year.<sup>27</sup> These findings boosted the development of organic solar cells. Until now, PCBM has become the most used acceptor in OPV devices. Especially the spherical shape seems advantageous compared to planar semiconductors as it enables 3D electron transport. A drawback of PC<sub>61</sub>BM is its weak visible light absorption. To address this issue, PC<sub>71</sub>BM, the C<sub>70</sub> analogue to PC<sub>61</sub>BM, was developed, which gave higher photocurrent and PCE in OPV cells because of its stronger absorption in the blue region of the solar spectrum.<sup>80</sup> Nowadays, highly optimized solar cells with either PC<sub>61</sub>BM or PC<sub>71</sub>BM are reaching over 8 % PCE with suitable low-band gap polymers.<sup>16, 81</sup> Further improvements, especially regarding V<sub>OC</sub> are envisioned by implementing materials with lower LUMO levels. Attaching solubilizing groups to the fullerene core not only enables solution processing of organic electronic devices but also allows for tuning HOMO and LUMO energy levels. A variety of substituents have been developed and explored. As a consequence of a covalent link between substituent and C<sub>60</sub> core, the resulting C<sub>60</sub> adduct exhibits two less delocalized  $\pi$ -electrons, which reduces its electron affinity by around 50-100 meV per substituent.<sup>76</sup> A variety of mono- bis- and tris adducts (shown in Figure 9) have been synthesized to take advantage of the resulting changes in LUMO energy levels and to achieve higher V<sub>OC</sub> in solar cells. For example, using the Indene-C<sub>60</sub> bisadduct (ICBA) a very high PCE of 6.5 % with P3HT as donor could be realized.<sup>82</sup> This improvement compared to the standard P3HT:PCBM (ca. 5 % PCE) was mainly due to a higher V<sub>OC</sub>. Higher V<sub>OC</sub> were also reported for bis-PCBM, tris-PCBM,<sup>58</sup> Indene-C<sub>60</sub> monoadduct (ICMA)<sup>83</sup> and Bis-o-quinodimethane C<sub>60</sub> (bis-oQDMC).<sup>84</sup> In many cases however, improvements in V<sub>OC</sub> were negatively compensated by lower J<sub>SC</sub>, when higher adduct fullerenes were used.<sup>85</sup> It was found that the morphology of polymer:fullerene blends can change significantly, depending on the fullerene derivative in use. Multiple side groups at the fullerene core can result in poor percolation paths and hence reduced photocurrents. Also, nanoscale morphology is altered when a new fullerene derivative is used because solubility and polymer-fullerene interaction may change. It is therefore necessary to optimize each novel blend system regarding ratio of polymer:fullerene, film thickness, solvents and processing conditions. Diffusion of PCBM within the blend and the formation of PCBM agglomerates has been observed upon heat treatment<sup>86</sup> and is

problematic with respect to long term stability of solar cells, depending on the donor polymer used.

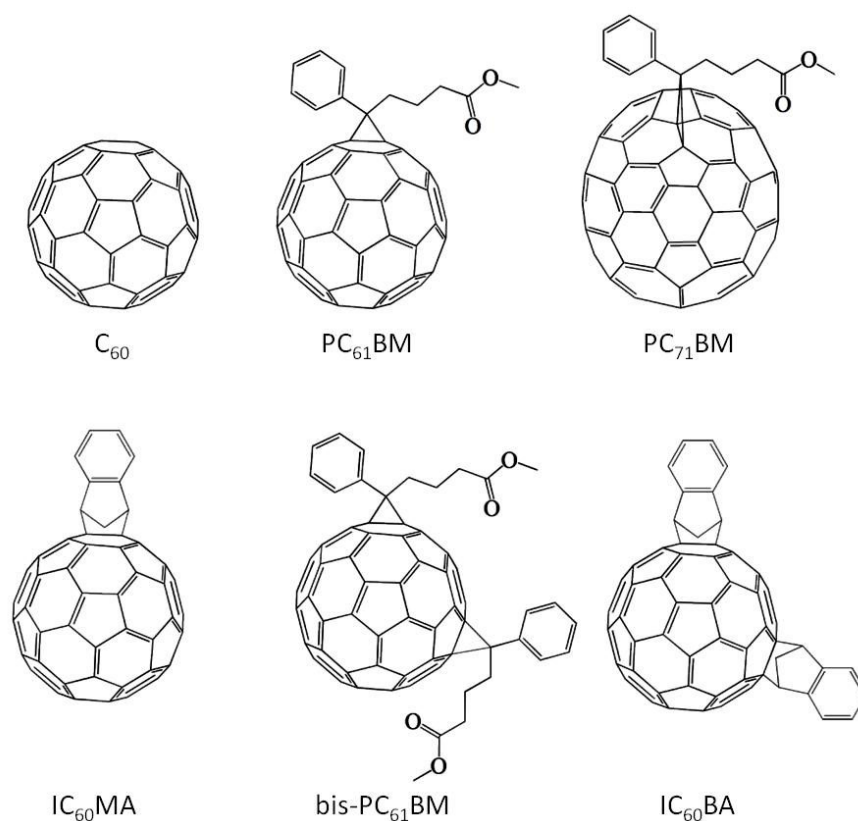
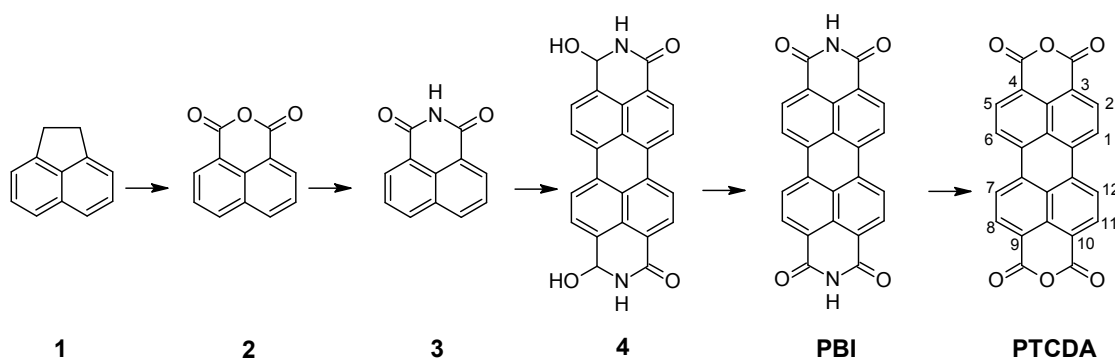


Figure 9: Chemical structures of relevant fullerene derivatives used as electron transport material in OPV (reproduced from Miller et. al<sup>37</sup>).

Altogether, fullerene based acceptors are currently the most successful materials in OPV. Nevertheless, several drawbacks like relatively high production cost, low visible light absorption and limited band gap variability make research and development of other classes of electron transport materials inevitable. Among non fullerene n-type material, perylene based semiconductors are of great interest, which is the subject of the following section.

## Perylene based acceptors

Perylene bisimides (PBIs) and related compounds are a versatile and robust class of n-type semiconductors. Because they can combine high electron affinities, good electron mobilities, strong visible light absorption and chemical, thermal and photostability<sup>76</sup>, they are of particular interest for OPV cells. Starting material for the synthesis of various perylene derivatives is perylene-3,4,9,10-tetracarboxylic acid dianhydride (PTCDA), a red pigment, which can be obtained in a five step synthesis from acenaphthene, a coal tar extract. The synthetic route is described in Scheme 1. Naphthalic acid anhydride **2** is obtained by V<sub>2</sub>O<sub>5</sub>-catalyzed oxidation of acenaphthene **1**. Condensation reaction of **2** with aqueous ammonia gives naphthalimide **3**. In a bimolecular nucleophilic substitution at temperatures above 200 °C and the presence of molten alkali **3** reacts with itself and the reduced (leuco) form of PBI, **4**, is obtained after precipitation into water. Oxidation of **4** gives **PBI**, which can be hydrolyzed to yield the anhydride **PTCDA**.<sup>87</sup> PTCDA is commercially available and inexpensive.



Scheme 1: Synthesis of PTCDA starting from the coal tar extract acenaphthene.<sup>87</sup>

Starting from PTCDA, there are twelve functionizable positions at the perylene core, which is indicated in Scheme 1. Positions 3,4,9 and 10 are known as the *peri*-, 2,5,8 and 11 as the *ortho*- and 1,6,7 and 12 as the *bay*-positions. Li *et al.* gave a good overview about different substitutions at all positions of the perylene core recently.<sup>88</sup> By carefully choosing the position and the sort of substituents, optical, electrochemical and physical properties can be tuned. An overview of important perylene derivatives is given in Figure 10, which is briefly discussed in the following. Symmetrical *N*-substituted PBIs (see Figure 10) are widely used

in optoelectronic devices<sup>36, 89-92</sup>, but also as a colorant in the coating industry, for which “Pigment Red 179” (N,N'-dimethyl-PBI) was developed.<sup>88</sup> It can be readily obtained by imidization reactions of PTCDA with aliphatic amines in high yields.<sup>93</sup> Depending on the length of the aliphatic chain, the solubility of PBI can be tuned. Especially long and branched side chains provide excellent solubility in common organic solvents. Substitution at the imide position (*N*-substitution) does not change the optical properties in solution or energy levels of the material, because the electronic coupling between the PBI core and the imide substituents is negligible due to nodes in the HOMO and LUMO at the imide nitrogen.<sup>94</sup> The substituents not only affect solubility, but also have a major impact on aggregation and self-assembly properties. In general,  $\pi$ - $\pi$  interaction of the perylene cores lead to strong aggregation and crystallinity of PBI molecules, which can be suppressed by choosing bulky substituents. Also, hydrogen bond-directed gelation of PBIs with amid-bearing substituents,<sup>95</sup> and the self-assembly in nanobelt and nanosphere morphologies for linear and branched alkyl substituents<sup>96</sup> was observed for symmetrical *N*-substituted PBIs. Even though being promising as electron acceptor for OPV devices, symmetrical *N*-substituted PBIs usually show poor performance, mainly due to low photocurrents. Two loss channels were found to be responsible, both have their origin in a problematic nanomorphology of the donor-acceptor blend.<sup>97</sup> For finely dispersed PBI in a p-type polymer matrix bimolecular recombination was limiting device efficiency, whereas for highly aggregated PBIs charge transfer between donor and acceptor was the main issue. These findings emphasize the need for controlling the intermolecular interaction and morphology in PBI blend devices. In this context, liquid crystalline (LC) mesophases of organic semiconductors have the potential to combine structural order, easy processing and reduced problems related to excessive crystallization and grain boundaries and hence represent an alternative way to improve morphology. 1D charge transport through the columns of discotic liquid crystals was shown to be very efficient with charge carrier mobilities greater than  $0.1 \text{ cm}^2\text{V}^{-1}\text{s}^{-1}$ .<sup>98</sup> For PBIs, it was demonstrated recently that columnar hexagonal ( $\text{Col}_h$ ) mesophases could be obtained when an unsymmetrical *N*-substitution pattern (see Figure 10) was applied.<sup>99</sup> By implementing various branched alkyl and oligoethylenglycol (OEG) side chains, the phase transition temperatures and the mesophase-width could be tuned. Implementing LC materials in high efficiency solar cells however, has still not been realized yet. Perfect alignment of the

discs within the column is a challenging task, because small defects or disorder in core-core distance can limit charge carrier transport significantly.<sup>100</sup>

As discussed above, symmetrical and unsymmetrical *N*-substituted PBIs exhibit similar absorption spectra and energy levels. For OPV application, an extended light absorption however is desirable in order to harvest more light and increase the photocurrent. In general, absorption and HOMO and LUMO energy levels can be altered by modifying the aromatic  $\pi$ -conjugation system. Extending the  $\pi$ -system results in increased delocalization of  $\pi$ -electrons, which makes less energy needed to excite an electron from the HOMO into the LUMO of the molecule. In other words, a red shift in absorption can be expected for a larger  $\pi$ -conjugation system. In the 1980s, Tang used a perylene derivative fused with two benzimidazole units (perylene bisbenzimidazole, compare Figure 10)) for the first bilayer organic solar cell.<sup>22</sup> Since no solubilizing groups were present in this molecule, the film could only be obtained by vacuum evaporation. A new class of soluble perylene compounds, perylene diester benzimidazoles (see Figure 10), with broad and red shifted absorption compared to PBI was presented recently.<sup>101</sup> The diester functionality allowed for attaching side chain to provide high solubility and the benzimidazole moiety fused to the perylene core improved optical properties. Depending on the choice of side groups, LC mesophases over a broad temperature range, and even at room temperature, could be obtained.

Synthesis and characterization of a PBI with tert-butylphenoxy side groups at the bay positions and acetonaphthopyrazine dicyanide terminal moieties (PERI, Figure 10)) was presented by Mikroyannidis *et al.*<sup>102</sup> They reported a PCE of 3.88 % for a solution processed blend of a p-type small molecule and PERI, which is the highest value reported for a BHJ using a non-fullerene material as acceptor. One of the highest electron mobilities were measured in single-crystal FETs of PDIF-CN<sub>2</sub> (Figure 10)<sup>103</sup>, which achieved up to 3 cm<sup>2</sup>V<sup>-1</sup>s<sup>-1</sup> in ambient and 6 cm<sup>2</sup>V<sup>-1</sup>s<sup>-1</sup> in vacuum. An approach to disrupt crystallinity of PBIs by molecular design was shown by *Rajaram* and co-workers, who covalently linked two PBI *via* their imide groups to form a nonplanar PBI dimer (see Figure 10).<sup>104</sup> As a result of steric hindrance the perylene cores are twisted with respect to each other, which reduces aggregation and  $\pi$ - $\pi$  stacking. A remarkable PCE of 2.77 % in a BHJ solar cell was achieved.

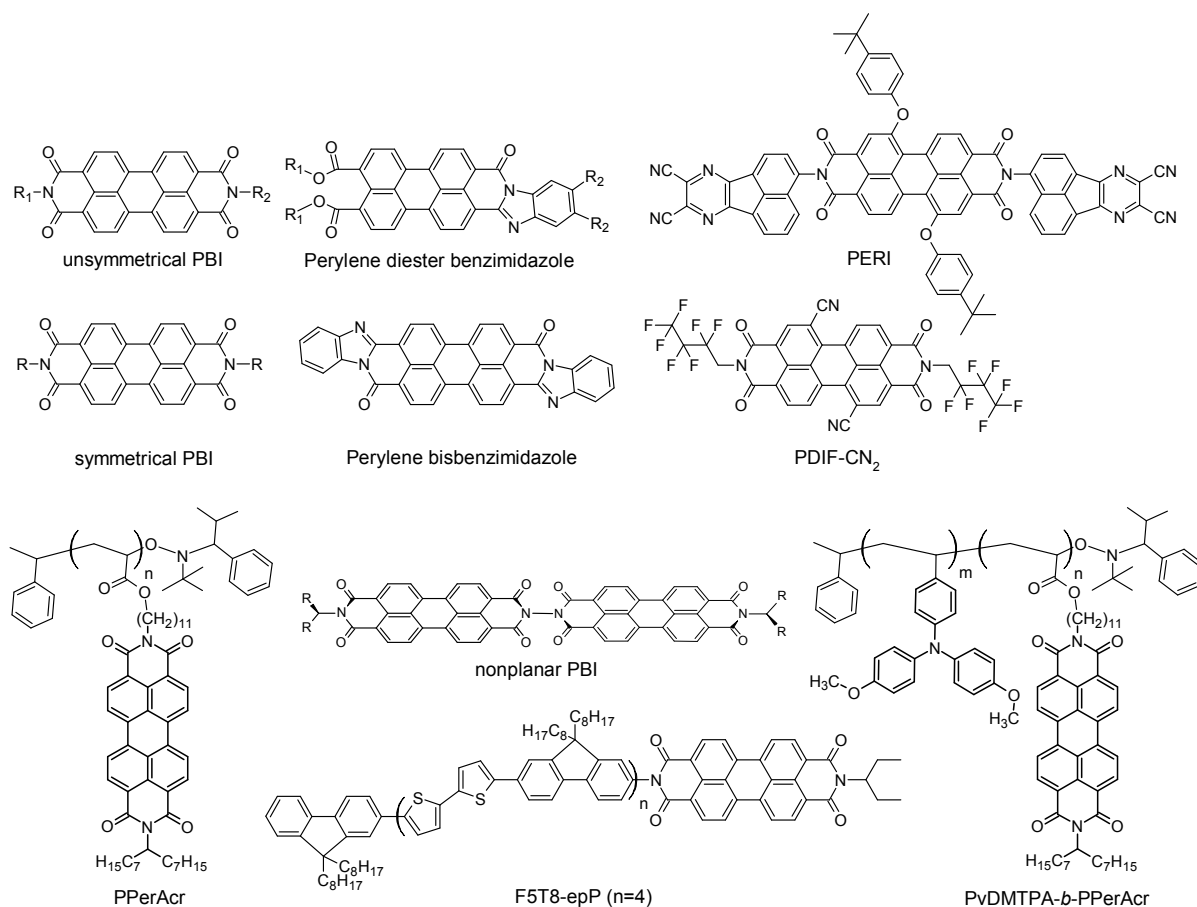


Figure 10: Important perylene based *n*-type materials.

The combination of a donor and acceptor in a co-oligomer was shown recently, where the donor part was formed by oligo(fluorene-*alt*-bithiophene) and the acceptor part by PBI (F5T8-epP, Figure 10).<sup>105</sup> The oligomers can self-assemble into ordered alternating donor-acceptor lamellae with the period being in the range of only 5-10 nm. Photovoltaic devices of this single material gave PCEs of up to 1.75 % after a solvent vapor annealing step. Thin films of a donor-acceptor diblock copolymers (see section below) with the electronically active donor and acceptor moieties as side chains to the polymer backbone (PvDMTPA-*b*-PPerAcr, Figure 10), exhibit nanostructured domains of 15 nm in diameter. The PCE was found to be 0.32 %, but is expected to be significantly higher, if vertical alignment of the domains within the device could be achieved.<sup>106</sup> The corresponding side chain homopolymer PPerAcr in Figure 10 showed good performance in OFET, with a mobility of  $1.2 \cdot 10^{-3} \text{ cm}^2 \text{ V}^{-1} \text{ s}^{-1}$  after thermal annealing.<sup>107</sup> This overview on various perylene based semiconductors

illustrates that many promising concepts exist, and that future research will lead to further improvements towards optimum device operation.

### **Donor-Acceptor diblock copolymers**

To date, the key issue with OPV blend system is that morphology and long term stability of the blend can still not be fully controlled. To overcome these intrinsic problems the use of donor-acceptor diblock copolymers, where donor and acceptor moieties are covalently linked in a polymer, is a promising way forward.<sup>108</sup> Depending on the volume fraction of each block, the Flory-Huggins parameter  $\chi$ , and the degree of polymerization, the self-assembling and equilibrium morphology of the block copolymer can be tuned for a variety of nanostructures.<sup>109</sup> For OPV applications, vertically aligned multicolumn or lamellar morphologies with the domain sizes of 10-20 nm (similar to exciton diffusion length) can be obtained. The domain size can be tuned by adjusting the polymer chain length. An illustration of such an ideal morphology is given in Figure 11a, where a very high interfacial area between donor and acceptor as well as good percolation pathways for charge carriers throughout the whole device are realized. Fully functionalized donor-acceptor diblock copolymers with hole- and electron transport segments exhibiting nanodomains of 15 nm in diameter were demonstrated in solar cells.<sup>106</sup> The chemical structure of the donor-acceptor diblock copolymer, namely poly(bis(4methoxyphenyl)-4'-vinylphenylamine)-*block*-poly(perylene diimide acrylate) is shown in Figure 11b. Furthermore, the performance of a diblock copolymer compared to a blend system of donor and acceptor could be increased by one order of magnitude, because nanometer phase separation was obtained only for the diblock copolymer.<sup>110</sup> Achieving a vertical alignment of the columns with respect to the substrate is not trivial, however this is necessary to exploit the potential of this concept. So far, D-A copolymers show low PCE compared to the best donor acceptor blend devices.

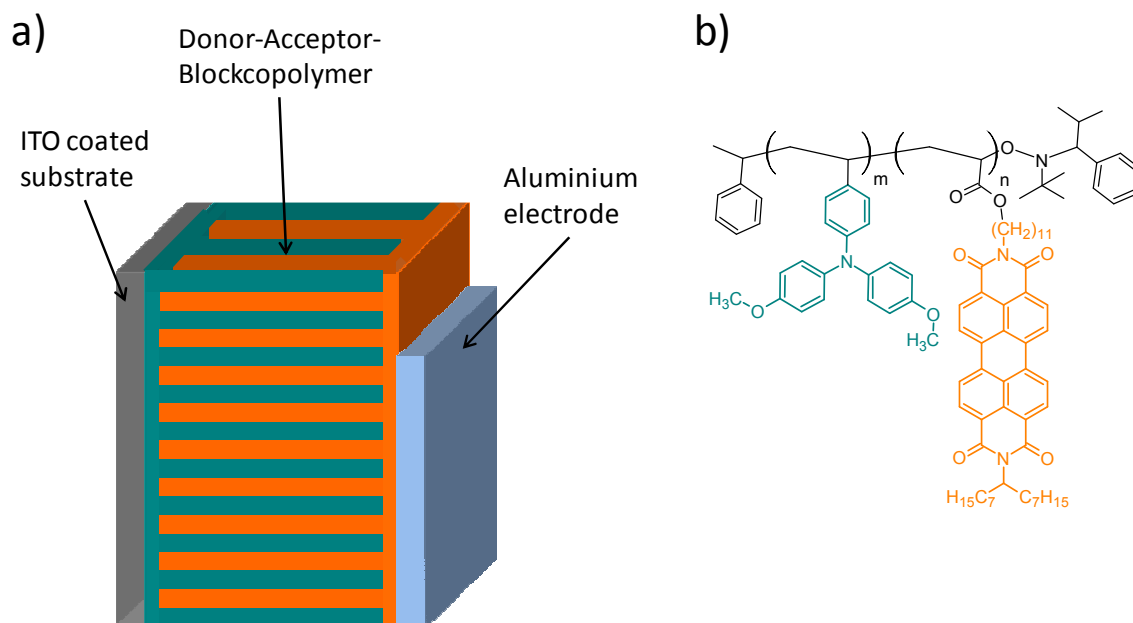


Figure 11: a) Solar cell with a donor-acceptor diblock copolymer as active layer; b) example of a donor-acceptor diblock copolymer.<sup>106</sup>

## 1.5 Charge Carrier Mobility in Organic Semiconductors

The charge transport properties of organic semiconductors are one of the key features which influence the performance of OFETs and OPV devices. An important figure of merit is the charge carrier mobility  $\mu$ , which is defined as

$$\mu = \frac{v}{E}$$

with  $v$  as the drift velocity of the charge carriers and  $E$  the applied electrical field. Mobility times number of charge carriers  $n$  times electronic charge  $e$  gives the electrical conductivity  $\sigma_c$ :

$$\sigma_c = n \cdot e \cdot \mu$$

As mentioned above, organic semiconductors exhibit low charge carrier mobilities, compared to their inorganic counterparts. This is mainly due to their disordered nature, the amount and nature of charge traps, energetic disorder due to inhomogeneity and the resulting differences from the band-like transport of inorganic materials. In inorganic semiconductors, an excited electron has a relatively large average free path in the conduction band of the material. The same applies for the residual hole in the valence band. In contrast, in organic semiconductors, excitons are tightly bound by Coulomb interaction because of the low dielectric constants of organic materials (typically 2-4)<sup>16</sup> and electron-electron and electron-lattice interactions.<sup>111</sup> Excitations are localized on individual molecules due to disorder and weak coupling in organic molecules. Coulomb attraction  $V$ , that an exciton needs to overcome in order to dissociate into free carriers is given by<sup>15</sup>

$$V = \frac{e^2}{4\pi\epsilon_r\epsilon_0 r}$$

where  $\epsilon_r$  is the dielectric constant,  $\epsilon_0$  is the vacuum permittivity and  $r$  is the electron-hole separation distance. Hence, electronic states in organic semiconductors are localized and the band-like charge transport of inorganic materials does not apply. In organic semiconductors, so called hopping processes can occur, where thermally excited charge carriers tunnel between molecular localized sites. Charge transport in organic semiconductors (at ambient temperature) can therefore approximately be considered as a series of thermally activated electron transfers, which allow charges to move from one molecule to another.<sup>76</sup> Besides temperature, the electric field is another parameter influencing the charge carrier mobility, which is considered in the well-known Poole-Frenkel relation:<sup>112</sup>

$$\mu(E, T) = \mu(0, T) \cdot \exp(\gamma(T)\sqrt{E})$$

where  $\mu(0, T)$  is the temperature dependent zero-field mobility and  $\gamma(T)$  is the field activation of the mobility. Expressions for  $\mu(0, T)$  and  $\gamma(T)$  have been developed in various transport models over the past decades in order to explain charge transport in disordered polymers and small molecules, which show good agreement with electrical measurements for some particular systems. For the typical features of polymers, which include twisted and kinked

chains, chemical defects and a variation in the conjugation length, the Gaussian density of states (DOS) model or Gaussian disorder model (GDM) was proposed.<sup>113</sup> It states that instead of two energy bands separated by an energy gap, the charge transport sites are energetically spread. The density of these states is approximately Gaussian shaped, which is depicted in Figure 12 and represents the disorder of the system. Within this model, experimental results could only be explained at high electric fields. On account of this, the model was extended to the correlated Gaussian disorder model (CGDM or CDM), which includes a spatial correlation among hopping sites.<sup>114</sup> Spatial correlations can be explained by long-range charge-dipole interaction in the material.<sup>115</sup> The electric field dependency can be understood in the sense that an external electric field lowers the barrier for upward energy hops. The field dependence becomes more important, as the extent of energetic disorder grows.<sup>116</sup>

In conclusion, the two Gaussian DOS models can describe the temperature and field dependent charge carrier mobility of OPV or organic light emitting diodes. Another theoretical model proposes an exponential distribution of DOS. This model is more relevant for the description of organic field effect transistors and is therefore not discussed further within this chapter.<sup>117, 118</sup>

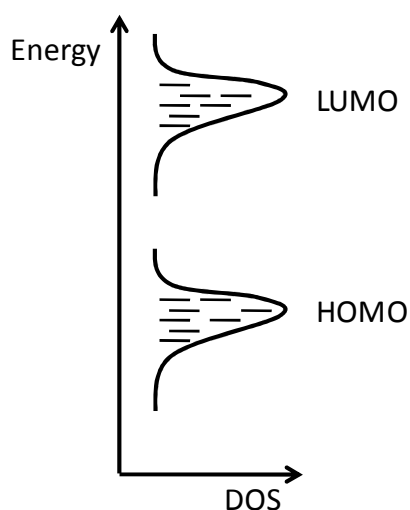


Figure 12: Energy distribution of localized states approximated by a Gaussian density of states (DOS) for the HOMO and LUMO levels.

Organic semiconductors can either preferentially transport holes or electrons. If both carrier types are transported with the same preference, the material is called ambipolar. Electron transport is considered as electron transport *via* the LUMO of a material. Hole transport refers to the transport of electrons *via* the HOMO. The ease of charge injection into either the LUMO or the HOMO decides about whether electron or hole transport is preferred.<sup>116</sup> Usually, electron deficient materials (acceptors) are good electron transport materials, whereas electron rich materials (donors) exhibit hole transporting properties.

Efficient hopping of charge carriers from molecule to molecule can be promoted not only by temperature and electric field but also by several material related factors. It is well known, that the efficiency of transport is depending on the relative positions of the interacting molecules. Electronic coupling between adjacent molecules is related to their molecular packing.<sup>116</sup> The determining factor in electronic coupling is not the degree of spatial overlap of the molecules but the degree of wavefunction overlap given by the interchain transfer integral. The interchain transfer integral is a measure of how easy charges can be transferred between two interacting molecules or polymer chains and can be influenced by the molecular packing motif.<sup>119</sup> For many conjugated polymers and small molecules,  $\pi$ - $\pi$  interaction promote self organization into various 1D or 2D structures. In general, such organized packing enhances charge transport within the stacked organic layers. Molecular size and shape have significant impact on the solid-state arrangement. For the well-known donor polymer P3HT (see Section 1.4) both increasing molecular weight and degree of regio-regularity were found to improve the charge carrier mobility by orders of magnitude by promoting a lamella structure with 2D conjugated sheets *via* interchain stacking.<sup>120</sup> Another important factor are impurities present in the semiconductor, which can act as charge-carrier trap or exciton quenching site in small molecules and polymers.<sup>121, 122</sup> Adequate understanding of trap concentration and the nature of traps are thus of great importance. Materials exhibiting very small HOMO-LUMO gaps were proposed to be suitable for achieving high mobilities of both holes and electrons as charge trapping can be avoided.<sup>123</sup>

Since the design of novel semiconductors for OPV application is a central part of this thesis, it is essential to know about the charge transport characteristics of the materials, so that device characteristics can be understood and efficiencies of solar cells can be improved. In an

OPV device, after successful photoinduced charge separation, the free charges (holes and electrons) need to be transported to the respective electrodes, either by carrier diffusion or electric field induced drift. For details of the function principle of organic bulk heterojunction solar cells please refer to Section 1.3. High quantum efficiencies and hence higher PCE can be reached, when the charge carrier transit time  $t_{tr}$  is much smaller than the charge carrier lifetime  $\tau$  ( $t_{tr} \ll \tau$ ). The transit time depends on thickness of the active layer  $L$ , charge carrier mobility and electric field.<sup>124</sup>

$$t_{tr} = \frac{L}{\mu \cdot E}$$

For drift controlled charge carrier transport, the drift distance  $l_{drift}$  is determined by

$$l_{drift} = \mu \cdot \tau \cdot E$$

and for diffusion controlled transport the diffusion distance  $l_{diffusion}$  is

$$l_{diffusion} = \sqrt{\mu \cdot \tau \cdot kT/e}$$

with the Boltzmann constant  $k$ , electron charge  $e$  and temperature  $T$ .

In both drift and diffusion cases, the mobility-lifetime product  $\mu\tau$  determines the average distance that charge carriers can travel before they recombine. In turn,  $\mu\tau$  determines whether PCE is limited by charge transport and recombination (or not). The ideal charge carrier mobility required for optimum device performance is still under debate. Values between  $10^{-2}$  and  $1 \text{ cm}^2\text{V}^{-1}\text{s}^{-1}$  have been proposed.<sup>125</sup> Materials with lower charge carrier mobility in OPV cells often suffer from bimolecular (nongeminate) recombination losses, caused by poor transport of free charges to the electrodes yielding low photocurrent and FF and  $V_{OC}$ .<sup>126, 127</sup> Furthermore, the chances of bound electron-hole pairs to dissociate into free carriers in the first instance are also reduced for low mobility semiconductors, because they are Coulombically bound, which promotes monomolecular (geminate) recombination from the CT state into the ground state. On the other hand, it was shown that too high mobilities can have a negative impact on  $V_{OC}$ .<sup>125</sup> According to Mandoc and co-workers, a lack of charge

carriers in the device, caused by efficient charge extraction as a result of high mobilities, will lead to reduced difference of quasi-Fermi levels of holes and electrons, which is equivalent to a decreased  $V_{OC}$ . It is important to mention though, that the charge carrier mobilities of the current organic semiconductors in use do generally not exceed  $1 \text{ cm}^2\text{V}^{-1}\text{s}^{-1}$ , thus performance is most likely limited by low mobility rather than by high mobility. In addition to that, devices with strongly unbalanced hole and electron mobility of donor and acceptor can result in significantly reduced FF.<sup>128</sup>

There are several methods to determine the charge carrier mobility of organic semiconductors. A brief summary of the most common ones is given as follows.

#### *Time-of-Flight (TOF)*

For TOF measurements, a thick layer (up to several  $\mu\text{m}$ ) of the semiconductor is sandwiched between two non-injecting electrodes. A bias is applied to obtain an electric field in the range of  $10^4$ - $10^6 \text{ Vcm}^{-1}$  and the material is irradiated by a laser pulse close to one of the electrodes, which generates charge carriers. The experimental setup is shown in Figure 13a. Depending on the polarity of the applied bias, the photogenerated holes or electrons migrate through the material towards the opposite electrode. The photocurrent at that electrode is recorded as a function of time. In this configuration, the bulk mobility can be described by:<sup>116</sup>

$$\mu = \frac{v}{E} = \frac{L}{E \cdot t} = \frac{L^2}{V \cdot t}$$

where  $L$  is the distance between the electrodes,  $E$  is the electric field,  $t$  is the averaged transit time and  $V$  is the applied voltage. In a well ordered, pure system, a sharp current signal is obtained in the measurement, whereas disordered materials show a broad signal because the transit times are widely distributed (dispersive). Figure 13b exemplarily shows the photocurrent transient of the organic semiconductor NBP (a triphenyldiamin derivative), from which the  $t$  can be determined. This technique was first used for organic materials by Leblanc<sup>129</sup> and Kepler<sup>130</sup> in 1960. Several requirements have to be met for this technique,

among those are:<sup>131</sup> a minimum sample thickness of several  $\mu\text{m}$  is usually required, so that the spatial spread of generated charges is small compared to the sample thickness; also, the excitation laser pulse has to be short compared to the transit time; furthermore, the following assumptions are made: a low charge concentration is present in the device, so that charges do not interact; no deep trapping is considered and the mobility is assumed to be time independent. More details are given in e.g. reference <sup>131</sup>.

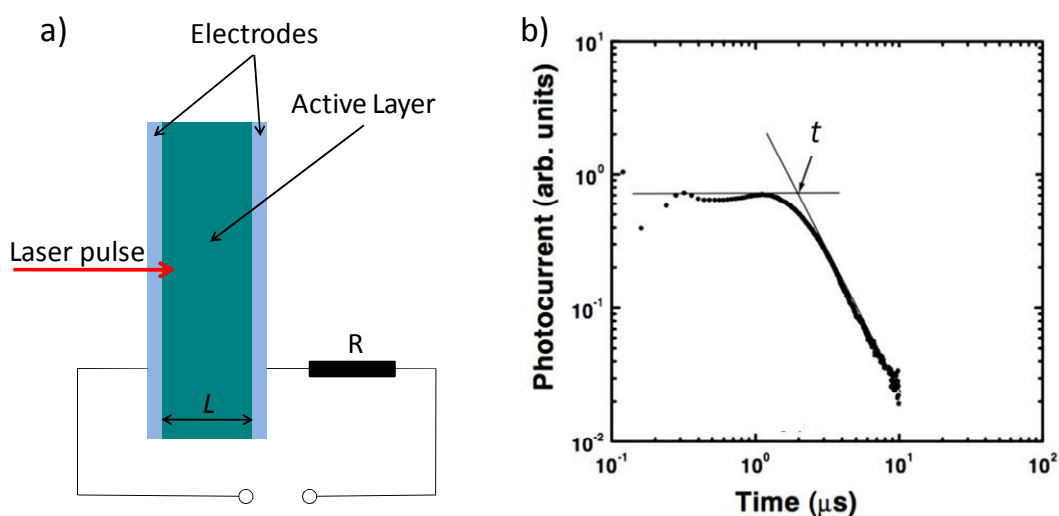


Figure 13: a) Schematic of TOF setup and b) photocurrent transient of the organic semiconductor NBP (reprinted from reference<sup>132</sup>).

#### Charge Extraction by Linearly Increasing Voltage (CELIV) and Photo-CELIV

CELIV is a technique with a similar sample geometry as TOF, however, CELIV is also suitable for thin organic films with film thicknesses in the range of a few hundreds of nanometers.<sup>133</sup> Linearly increased voltage (ramp) pulses are applied to the sample and the current is measured, which is illustrated in Figure 14. The capacitance of the sample accounts for the initial step increase in the current ( $j(0)$ ). The time  $t_{max}$ , at which the current is maximum, is used for determining the charge carrier mobility of the bulk:

$$\mu = \frac{2L^2}{3At_{max}^2} \left(1 + 0.36 \frac{\Delta j}{j(0)}\right)^{-1}$$

where  $L$  is the film thickness,  $A$  is the rate of increase of the applied voltage,  $\Delta j$  is the difference between the maximum current and  $j(0)$ .<sup>131</sup>

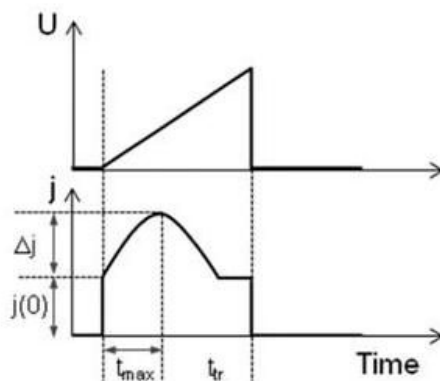


Figure 14: Schematic of an ideal current transient obtained in CELIV for the applied voltage ramp (reprinted from Kokil et al.<sup>134</sup>)

This method is also suitable for photogenerated charge carriers (Photo-CELIV).<sup>135</sup> In general, the differentiation between hole and electron mobility is not possible, which might be a drawback for ambipolar semiconductors or donor-acceptor blend systems.

### Organic Field-Effect Transistor (OFET)

The device architecture of a typical bottom gate top contact OFET is shown in Figure 15a and consists of three terminals, namely gate, source and drain. The two latter ideally form an ohmic contact with the conducting channel, the organic semiconductor. When a voltage is applied at the gate and between source and drain, current flow between source and drain is possible. The gate electrode controls the current flow in the organic semiconductor layer by capacitive coupling of the thin dielectric layer.<sup>134</sup> Depending on whether a positive or a negative gate voltage is applied, electrons or holes are the majority charge carriers. Plotting drain-source current  $I_{DS}$  versus gate voltage  $V_G$  in the transfer characteristics at a constant source-drain voltage  $V_{SD}$  gives the charge carrier mobility using the following equation for the linear regime ( $V_{DS} < (V_G - V_T)$ ):

$$I_{DS} = \frac{W}{L} \cdot \mu \cdot C \cdot (V_G - V_T) \cdot V_{DS}$$

with  $W$  and  $L$  the width and length of the conduction channel, respectively,  $C$  the capacitance of the dielectric layer and  $V_T$  the threshold voltage, at which the current starts to rise. In the saturation regime ( $V_{DS} > (V_G - V_T)$ ) the mobility can be calculated according to

$$I_{DS} = \frac{W}{2L} \cdot \mu \cdot C \cdot (V_G - V_T)^2$$

In OFETs, the charges migrate within a very narrow sheet of a few nanometers at the interface between dielectric and organic semiconductor.<sup>136</sup> Hence, the mobility measured does not necessarily describe the bulk mobility of the semiconductor. Further, structural defects within this channel, polarity of the dielectric, the presence of traps at the interface and contact resistance at the source and drain metal/organic interface are crucial factors influencing charge transport in OFET.<sup>116</sup> Due to usually higher electric fields present in the device, the charge carrier mobility values obtained from OFET experiments are usually higher compared to other methods.

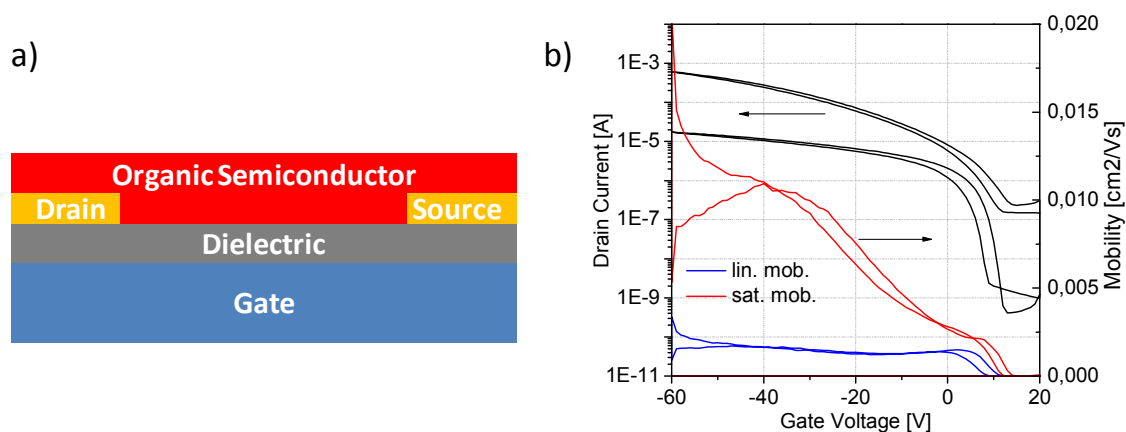


Figure 15: a) Schematic of an organic field effect transistor (OFET) in "bottom gate" architecture and b) FET transfer characteristics of a P3HT bottom gate transistor showing drain current  $I_{DS}$  vs. gate voltage  $V_G$  at constant drain-source voltages  $V_{DS}$  of 5 V giving the linear mobility (blue curve) and 55 V giving saturation mobility (red curve).

*Space-Charge Limited Currents (SCLC)*

Another method for obtaining the charge carrier mobility of organic semiconductors is measuring the current density - voltage ( $J$ - $V$ ) characteristics of a diode like device setup. The organic semiconductor is sandwiched between two electrodes and the  $J$ - $V$  curve is recorded in the dark. Two main factors determine the  $J$ - $V$  characteristics in a metal-organic-metal device, which are charge injection and charge transport in the organic bulk.<sup>112</sup> The choice of electrodes is crucial and depends on what carrier type (holes or electrons) shall be investigated. The injecting electrode has to form an Ohmic contact to either the LUMO or the HOMO of the semiconductor in order to inject electrons or holes, respectively. In general, for Ohmic injection, the difference in work function of injecting electrode and the respective energy level of the semiconductor should be smaller than 0.3 eV.<sup>137, 138</sup> The opposite electrode must be designed so that it does not hinder the respective charge carrier to leave the device and that there is a barrier for charge injection of opposite charge carriers. This way, exclusively electron (electron-only device) or hole (hole-only device) transport can be investigated. A schematic of an electron- and a hole-only device is shown in Figure 16a and b, respectively. In the case of the electron-only device, the low work function metal calcium forms an Ohmic contact with the semiconductor's LUMO for electron injection. The zinc oxide covered ITO electrode can collect electrons and provides a sufficient injection barrier for holes at the same time. For hole-only devices, PEDOT:PSS acts as hole-injecting electrode, whilst there is an injection barrier for electrons at the high work function gold electrode. Under these circumstances, the transport of charges is not contact limited or limited by charge injection, but only limited by the charge carrier mobility of the semiconductor. When charges are injected from one electrode into the active layer, the number of injected charges will reach a maximum when their electrostatic potential prevents injection of additional charges.<sup>139</sup> The point where this maximum is reached, depends on the ability of the semiconductor to transport charges to the other electrode and thus on its charge carrier mobility. The term "space-charge" herein stems from the fact that upon injection of charge carriers from one electrode, the charge density is not uniform across the thickness of the film and as a result, a space-charge region forms.

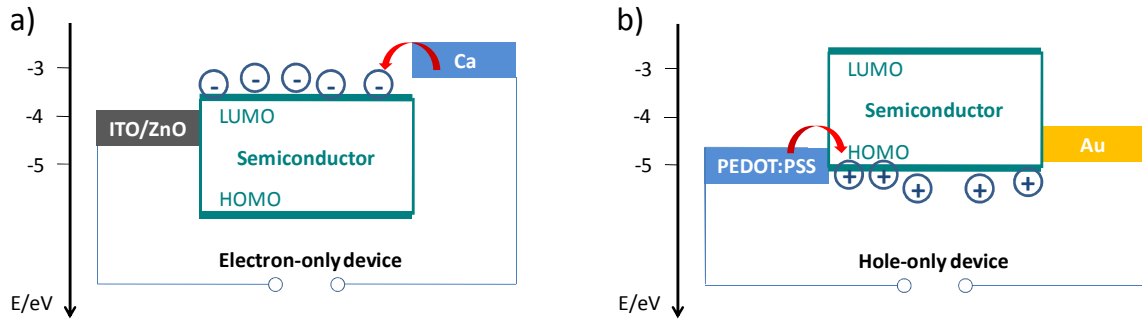


Figure 16: a) Schematic of an electron-only device with calcium electrode and a hole blocking ITO/ZnO contact; b) schematic of a hole-only device with PEDOT:PSS electrode and electron blocking gold contact.

Assuming that the concentration of deep traps is small compared to the free carrier concentration, the mobility is described by Mott-Gurney equation (which is also known as Child's law):<sup>131, 140</sup>

$$J = \frac{9}{8} \varepsilon_0 \varepsilon_r \mu \frac{V^2}{L^3}$$

where  $J$  is the current density,  $\varepsilon_0$  is the vacuum permittivity,  $\varepsilon_r$  denotes to the dielectric constant of the semiconductor,  $V$  is the voltage applied and  $L$  the active layer thickness.  $\mu$  and  $\varepsilon_r$  are assumed to be constant throughout the film. Such a quadratic scaling of the current with applied bias is typical for a space-charge limited current. In cases, where the mobility is depending on the electric field and higher currents are found as predicted by Mott-Gurney equation, especially at higher voltages, the  $J$ - $V$  curve can often be better described by the following expression:<sup>141</sup>

$$J = \frac{9}{8} \varepsilon_0 \varepsilon_r \mu_0 \exp \left( 0.89 \gamma \sqrt{\frac{V}{L}} \right) \frac{V^2}{L^3}$$

where the  $\mu_0$  is the mobility at zero electric field, and  $\gamma$  is the field activation parameter. It is important to mention, that with higher electric field, usually also the charge carrier density increases. The influences of electric field and charge carrier density are hard to distinguish with the standard experimental setup. Temperature dependent measurements and theoretical calculations described by Pasveer *et al.*,<sup>142</sup> credited higher importance to the charge carrier

density dependence of the charge carrier mobility at room temperature for several PPV based p-type materials. At low temperatures, the mobility was found to be field dependent. Furthermore, if traps are present, a deviation from the ideal square dependence of current with voltage can also be observed. Due to the filling of traps, lower currents at low voltages are expected. When all traps are filled the current often scales with  $V^m$  ( $m > 2$ ).<sup>143</sup>

Depending on the experiment, it might be necessary to modify the device architecture from the one depicted in Figure 16. For certain semiconductors, the injection barrier for electrons from a gold contact might not be sufficient and the gold contact can be replaced with another PEDOT:PSS contact (capped with e.g. silver; see Chapter 6) Moreover, if materials under investigation are predominantly electron conductors, an ITO/PEDOT:PSS bottom contact can be used instead of ITO/ZnO.<sup>144</sup> Better film formation is often observed for films coated on PEDOT:PSS, compared to ITO or ITO/ZnO, which might be due to the interactions of the semiconductor and the substrate during film drying and due to the fact, that PEDOT:PSS usually acts as a smoothing layer for the comparatively rough ITO. Therefore, the preparation of the active layer and active layer morphology are directly comparable to a common OPV device setup.

The connection between the metallic contact and the organic layer is crucial. Not only work function difference and energy levels of the semiconductor can influence the injection barrier, but also atmosphere of sample fabrication, interface dipoles, band bending and fermi level pinning caused by chemical reactions at the metal-organic interface.<sup>145-147</sup>

For an accurate evaluation of the  $J$ - $V$  curves, one should correct the applied Voltage ( $V_{ap}$ ) for the built-in potential ( $V_{bi}$ ) present in the device.  $V_{bi}$  stems from the difference in work function of the two electrode materials used.

$$V = V_{ap} - V_{bi}$$

The  $J$ - $V$  characteristics of the p-type semiconductor polymer P3HT are exemplarily shown in Figure 17. In the double logarithmic  $J$ - $V$  plot (Figure 17a), at low voltages the current scales approximately linear with the voltage, which can be seen from the slope values being 1.2-1.5. In this “ohmic” regime, the current is limited by injection from the metal contacts. At higher

voltages the quadratic dependence of the current with voltage can be seen, as the slope is approximately 2. To confirm, that the current is space-charge limited, different devices with varying active layer thickness should be prepared.

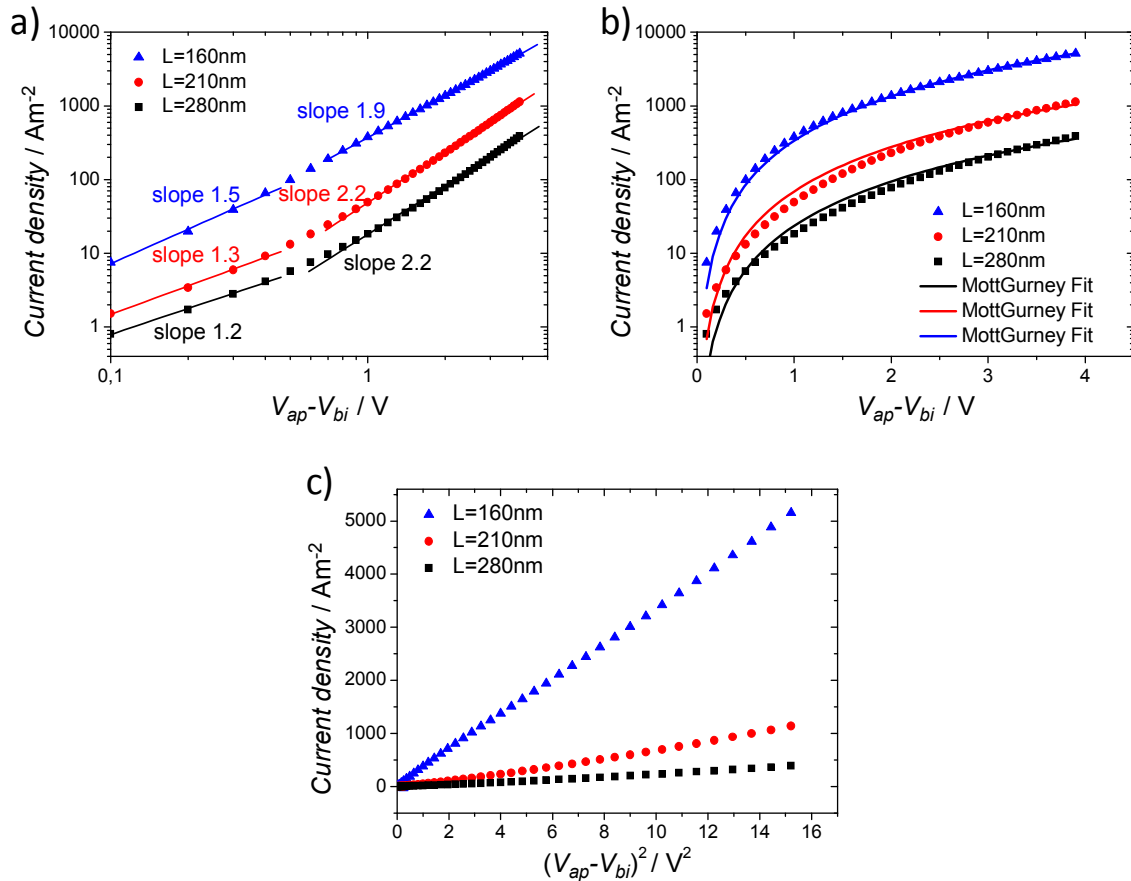


Figure 17: a)  $J$ - $V$  characteristics of hole-only devices with the structure ITO/PEDOT:PSS/P3HT/Au for varied P3HT layer thicknesses  $L$  in a double logarithmic plot, b) with data fitted according to Mott-Gurney equation and c) a  $J$  vs.  $V^2$  plot.

For thinner films, a higher current should be measured and *vice versa*. Also, the thinner the active layer is, the more significant the impact of the injecting contacts gets, which can explain the fact that the 160 nm device in Figure 17a only has a slope of 1.9. Hence, ideally, the active layer thickness of SCLC devices needs to be sufficient high to obtain reliable results. The charge carrier mobility can be calculated from the fit parameters obtained when fitting the data according to Mott-Gurney equation (Figure 17b) or from the slope of the straight line of the  $J$  vs.  $V^2$  plot at higher voltages and Mott-Gurney equation (Figure 17c).

Since the equation accounts for the film thickness  $L$ , the same mobility values within the experimental error for each  $L$  should be obtained. Since the film thickness scales with  $L^3$ , an accurate determination of the film thickness is crucial to avoid large deviations.

The SCLC method to evaluate the charge carrier mobility of organic materials was found to be a useful method for characterizing organic light emitting diodes.<sup>148, 149</sup> During recent years, also the charge transport properties of materials tailored for OPV applications are more and more investigated using the SCLC approach. The estimation of the hole mobility in p-type polymers has become a routine method.<sup>150-153</sup> N-type polymers were investigated by Steyrleuthner *et al.*, where different low workfunction metal electrodes were tested.<sup>154</sup> Ayzner and co-workers probed the effect of thermal annealing on charge transport of PCBM and found lower mobility of PCBM after annealing.<sup>155</sup> Electron- and hole-only devices were also fabricated for OPV blend systems. Charge recombination of the prominent P3HT:PCBM blend were investigated by Greenham *et al.* who found an electric field dependency of geminate recombination and increased significance of bimolecular recombination close to  $V_{OC}$  at low temperatures.<sup>156</sup> Brabec group blended the low band gap polymer Si-PCPDTBT with PCBM and bis-PCBM and a lower mobility-lifetime product was found for the bis-PCBM blend resulting in higher recombination and lower PCE. The cause of this behavior was possibly an unfavorable blend morphology.<sup>157</sup>

In general, the device setup and the active layer thicknesses within these single carrier devices are very similar to those of OPV cells. Further, the bulk transport perpendicular to the substrate plane is monitored, which is of special relevance in OPV. Because of these reasons, a realistic impression of the charge transport in an OPV device can be obtained by SCLC measurements. In this thesis, SCLC measurements are the method of choice for determining the charge carrier mobility of both p- and n-type materials and blends thereof.

## 1.6 Objective of this Thesis

The aim of this thesis is to investigate and optimize optical and electronic properties of novel electron transport materials for OPV applications and establish structure-property relations. Common bulk heterojunction solar cells comprise a blend of an electron donating (p-type) polymer and an electron accepting (n-type) fullerene small molecule, e.g. PCBM, as active layer. Currently, the vast majority of research effort is put on developing and optimizing donor polymers, while alternative acceptor materials have received less attention to date. Weak visible light absorption and comparatively high production cost of PCBM however make the quest for novel n-type materials inevitable in order to obtain high efficiency and low cost solar cells. In the first part of this thesis, novel perylene imide small molecules and polymers shall be investigated. A fundamental question of how substituents at the perylene core of perylene bisimide (PBI) small molecules influence the packing behavior, structural order and morphology shall be addressed. Therefore, a variety of techniques including UV/vis spectroscopy, polarized optical microscopy (POM), atomic force microscopy (AFM) and X-ray diffraction (XRD) shall be employed. The impact of side chain alteration on bulk electron mobility of PBI small molecules shall be investigated by the space-charge limited current (SCLC) approach. Another aim of this thesis is to improve optical properties of perylene based semiconductors by modifying the  $\pi$ -electron system of the perylene core. Suitable routes for the synthesis of monomers with extended visible light absorption and the polymerization *via* nitroxide mediated radical polymerization (NMRP) shall be addressed. Polymer characterization by means of differential scanning calorimetry (DSC), UV/vis spectroscopy, XRD, cyclic voltammetry and SCLC shall be carried out. Furthermore, a comparative study of a series of side-chain polymers with pendant perylene units, synthesized by a “click” chemistry approach, shall be carried out. The impact of the different perylene units on electronic properties shall be investigated.

In the second part of this thesis, novel fullerene acceptor materials shall be investigated. It is well known that altering the side groups attached to the fullerene core allows for tuning the HOMO and LUMO energy levels, which can be beneficial for high  $V_{OC}$ . In many cases however, an improvement of the solar cell efficiency can not be observed. An interpretation

of these findings is usually difficult because of the complex interplay of the microstructure of the donor acceptor blend, charge transport within the blend and material related properties, such as light harvesting. One aim is to investigate the effect of the substituents on the charge transport properties and morphology for a series of fullerene derivatives when blended with an electron donating polymer. Therefore, solar cells shall be prepared and characterized by recording  $J-V$  curves and measuring external quantum efficiency (EQE) and the respective blend mobilities should be determined by SCLC. Additionally, an intrinsic problem of fullerene small molecules shall be addressed by novel fullerene-grafted polymers. Diffusion and crystallization of fullerene small molecules are often disadvantageous in donor acceptor blend systems because the morphology is not stable and hence degradation of device performance is usually observed. Fullerene polymers can potentially circumvent this problem. In order to compare electronic properties of fullerene-grafted polymers with fullerene small molecules, electron mobilities shall be determined by SCLC and thin film morphology shall be studied by AFM.

## References

- (1) Troshin, P. A.; Sariciftci, N. S., *Supramolecular Chemistry for Organic Photovoltaics*. In John Wiley & Sons, Ltd: 2012.
- (2) Mishra, A.; Bäuerle, P., *Angewandte Chemie International Edition* **2012**, *51*, (9), 2020-2067.
- (3) Becquerel, A.-E., *Comptes Rendus* **1839**, *9*, 561-567.
- (4) [http://www.nrel.gov/ncpv/images/efficiency\\_chart.jpg](http://www.nrel.gov/ncpv/images/efficiency_chart.jpg) (08.August 2012),
- (5) Espinosa, N.; Hosel, M.; Angmo, D.; Krebs, F. C., *Energy & Environmental Science* **2012**, *5*, (1), 5117-5132.
- (6) Uy, R. L.; Price, S. C.; You, W., *Macromolecular Rapid Communications* **2012**, *33*, (14), 1162-1177.
- (7) [http://www.merck-performance-materials.de/en/solar\\_and\\_energy/photovoltaics/photovoltaics.html](http://www.merck-performance-materials.de/en/solar_and_energy/photovoltaics/photovoltaics.html) (04.November 2012),

- 
- (8) Hoppe, H.; Sariciftci, N. S., *Journal of Materials Research* **2004**, *19*, 1924-1945.
  - (9) Gregg, B. A.; Hanna, M. C., *Journal of Applied Physics* **2003**, *93*, (6), 3605-3614.
  - (10) Forrest, S. R., *Nature* **2004**, *428*, (6986), 911-918.
  - (11) Zhu, X. Y.; Yang, Q.; Muntwiler, M., *Accounts of Chemical Research* **2009**, *42*, (11), 1779-1787.
  - (12) Halls, J. J. M.; Pichler, K.; Friend, R. H.; Moratti, S. C.; Holmes, A. B., *Applied Physics Letters* **1996**, *68*, (22), 3120-3122.
  - (13) Markov, D. E.; Tanase, C.; Blom, P. W. M.; Wildeman, J., *Physical Review B* **2005**, *72*, (4), 045217.
  - (14) Markov, D. E.; Amsterdam, E.; Blom, P. W. M.; Sieval, A. B.; Hummelen, J. C., *The Journal of Physical Chemistry A* **2005**, *109*, (24), 5266-5274.
  - (15) Clarke, T. M.; Durrant, J. R., *Chemical Reviews* **2010**, *110*, (11), 6736-6767.
  - (16) Li, G.; Zhu, R.; Yang, Y., *Nature Photonics* **2012**, *6*, (3), 153-161.
  - (17) Kumar, P.; Chand, S., *Progress in Photovoltaics: Research and Applications* **2012**, *20*, (4), 377-415.
  - (18) Spanggaard, H.; Krebs, F. C., *Solar Energy Materials and Solar Cells* **2004**, *83*, 125-146.
  - (19) Wöhrle, D.; Meissner, D., *Advanced Materials* **1991**, *3*, (3), 129-138.
  - (20) Morel, D. L.; Ghosh, A. K.; Feng, T.; Stogryn, E. L.; Purwin, P. E.; Shaw, R. F.; Fishman, C., *Applied Physics Letters* **1978**, *32*, (8), 495-497.
  - (21) McGehee, M. D.; Topinka, M. A., *Nature Materials* **2006**, *5*, (9), 675-676.
  - (22) Tang, C. W., *Applied Physics Letters* **1986**, *48*, (2), 183-185.
  - (23) Bittner, E. R.; Ramon, J. G. S.; Karabunarliev, S., *The Journal of Chemical Physics* **2005**, *122*, (21), 214719-9.
  - (24) Peumans, P.; Yakimov, A.; Forrest, S. R., *Journal of Applied Physics* **2003**, *93*, (7), 3693-3723.
  - (25) Peumans, P.; Forrest, S. R., *Applied Physics Letters* **2001**, *79*, (1), 126-128.

- (26) [http://www.heliatek.com/newscenter/latest\\_news/heliatek-und-iapp-erreichen-produktionsrelevanten-effizienzrekord-fur-organische-solarzellen-heliatek-und-iapp-erreichen-produktionsrelevanten-effizienzrekord-fur-organische-solarzellen/](http://www.heliatek.com/newscenter/latest_news/heliatek-und-iapp-erreichen-produktionsrelevanten-effizienzrekord-fur-organische-solarzellen-heliatek-und-iapp-erreichen-produktionsrelevanten-effizienzrekord-fur-organische-solarzellen/) (31.January 2013),
- (27) Yu, G.; Gao, J.; Hummelen, J. C.; Wudl, F.; Heeger, A. J., *Science* **1995**, *270*, (5243), 1789-1791.
- (28) Halls, J. J. M.; Walsh, C. A.; Greenham, N. C.; Marseglia, E. A.; Friend, R. H.; Moratti, S. C.; Holmes, A. B., *Nature* **1995**, *376*, 498-500.
- (29) Holcombe, T. W.; Norton, J. E.; Rivnay, J.; Woo, C. H.; Goris, L.; Piliago, C.; Griffini, G.; Sellinger, A.; Brédas, J.-L.; Salleo, A.; Frechet, J. M. J., *Journal of the American Chemical Society* **2011**, *133*, (31), 12106-12114.
- (30) Li, G.; Shrotriya, V.; Huang, J.; Yao, Y.; Moriarty, T.; Emery, K.; Yang, Y., *Nature Materials* **2005**, *4*, (11), 864-868.
- (31) Ma, W.; Yang, C.; Gong, X.; Lee, K.; Heeger, A. J., *Advanced Functional Materials* **2005**, *15*, (10), 1617-1622.
- (32) Cai, W.; Gong, X.; Cao, Y., *Solar Energy Materials and Solar Cells* **2010**, *94*, (2), 114-127.
- (33) Larsen-Olsen, T. T.; Machui, F.; Lechene, B.; Berny, S.; Angmo, D.; Søndergaard, R.; Blouin, N.; Mitchell, W.; Tierney, S.; Cull, T.; Tiwana, P.; Meyer, F.; Carrasco-Orozco, M.; Scheel, A.; Lövenich, W.; de Bettignies, R.; Brabec, C. J.; Krebs, F. C., *Advanced Energy Materials* **2012**, *2*, (9), 1091-1094.
- (34) Hoppe, H.; Niggemann, M.; Winder, C.; Kraut, J.; Hiesgen, R.; Hinsch, A.; Meissner, D.; Sariciftci, N. S., *Advanced Functional Materials* **2004**, *14*, (10), 1005-1011.
- (35) Chochos, C. L.; Choulis, S. A., *Progress in Polymer Science* **2011**, *36*, (10), 1326-1414.
- (36) Kamm, V.; Battagliarin, G.; Howard, I. A.; Pisula, W.; Mavrinskiy, A.; Li, C.; Müllen, K.; Laquai, F., *Advanced Energy Materials* **2011**, *1*, (2), 297-302.
- (37) Miller, N. C.; Cho, E.; Gysel, R.; Risko, C.; Coropceanu, V.; Miller, C. E.; Sweetnam, S.; Sellinger, A.; Heeney, M.; McCulloch, I.; Brédas, J.-L.; Toney, M. F.; McGehee, M. D., *Advanced Energy Materials* **2012**, *2*, (10), 1208-1217.
- (38) Yang, X.; Loos, J.; Veenstra, S. C.; Verhees, W. J. H.; Wienk, M. M.; Kroon, J. M.; Michels, M. A. J.; Janssen, R. A. J., *Nano Letters* **2005**, *5*, (4), 579-583.

- 
- (39) Campoy-Quiles, M.; Ferenczi, T.; Agostinelli, T.; Etchegoin, P. G.; Kim, Y.; Anthopoulos, T. D.; Stavrinou, P. N.; Bradley, D. D. C.; Nelson, J., *Nature Materials* **2008**, *7*, (2), 158-164.
- (40) Kim, Y.; Choulis, S. A.; Nelson, J.; Bradley, D. D. C.; Cook, S.; Durrant, J. R., *Applied Physics Letters* **2005**, *86*, (6), 063502-3.
- (41) Nguyen, L. H.; Hoppe, H.; Erb, T.; Günes, S.; Gobsch, G.; Sariciftci, N. S., *Advanced Functional Materials* **2007**, *17*, (7), 1071-1078.
- (42) Li, G.; Yao, Y.; Yang, H.; Shrotriya, V.; Yang, G.; Yang, Y., *Advanced Functional Materials* **2007**, *17*, (10), 1636-1644.
- (43) Padinger, F.; Rittberger, R. S.; Sariciftci, N. S., *Advanced Functional Materials* **2003**, *13*, (1), 85-88.
- (44) Peet, J.; Kim, J. Y.; Coates, N. E.; Ma, W. L.; Moses, D.; Heeger, A. J.; Bazan, G. C., *Nature Materials* **2007**, *6*, (7), 497-500.
- (45) Yao, Y.; Hou, J.; Xu, Z.; Li, G.; Yang, Y., *Advanced Functional Materials* **2008**, *18*, (12), 1783-1789.
- (46) Hoven, C. V.; Dang, X.-D.; Coffin, R. C.; Peet, J.; Nguyen, T.-Q.; Bazan, G. C., *Advanced Materials* **2010**, *22*, (8), E63-E66.
- (47) Sun, Y.; Welch, G. C.; Leong, W. L.; Takacs, C. J.; Bazan, G. C.; Heeger, A. J., *Nature Materials* **2012**, *11*, (1), 44-48.
- (48) Hüttner, S.; Sommer, M.; Chiche, A.; Krausch, G.; Steiner, U.; Thelakkat, M., *Soft Matter* **2009**, *5*, (21), 4206-4211.
- (49) Vogelsang, J.; Lupton, J. M., *The Journal of Physical Chemistry Letters* **2012**, *3*, (11), 1503-1513.
- (50) Miller, S.; Fanchini, G.; Lin, Y.-Y.; Li, C.; Chen, C.-W.; Su, W.-F.; Chhowalla, M., *Journal of Materials Chemistry* **2008**, *18*, (3), 306-312.
- (51) Hoppe, H.; Glatzel, T.; Niggemann, M.; Hinsch, A.; Lux-Steiner, M. C.; Sariciftci, N. S., *Nano Letters* **2005**, *5*, (2), 269-274.
- (52) Xu, Z.; Chen, L.-M.; Yang, G.; Huang, C.-H.; Hou, J.; Wu, Y.; Li, G.; Hsu, C.-S.; Yang, Y., *Advanced Functional Materials* **2009**, *19*, (8), 1227-1234.
- (53) Erb, T.; Zhokhavets, U.; Gobsch, G.; Raleva, S.; Stühn, B.; Schilinsky, P.; Waldauf, C.; Brabec, C. J., *Advanced Functional Materials* **2005**, *15*, (7), 1193-1196.

- (54) Clark, J.; Chang, J.-F.; Spano, F. C.; Friend, R. H.; Silva, C., *Applied Physics Letters* **2009**, *94*, (16), 163306-3.
- (55) Kistler, K. A.; Pochas, C. M.; Yamagata, H.; Matsika, S.; Spano, F. C., *The Journal of Physical Chemistry B* **2012**, *116*, (1), 77-86.
- (56) Dyer-Smith, C.; Reynolds, L. X.; Bruno, A.; Bradley, D. D. C.; Haque, S. A.; Nelson, J., *Advanced Functional Materials* **2010**, *20*, (16), 2701-2708.
- (57) Shoaee, S.; An, Z.; Zhang, X.; Barlow, S.; Marder, S. R.; Duffy, W.; Heeney, M.; McCulloch, I.; Durrant, J. R., *Chemical Communications* **2009**, (36), 5445-5447.
- (58) Faist, M. A.; Keivanidis, P. E.; Foster, S.; Wöbkenberg, P. H.; Anthopoulos, T. D.; Bradley, D. D. C.; Durrant, J. R.; Nelson, J., *Journal of Polymer Science Part B: Polymer Physics* **2011**, *49*, (1), 45-51.
- (59) He, X.; Gao, F.; Tu, G.; Hasko, D.; Hüttner, S.; Steiner, U.; Greenham, N. C.; Friend, R. H.; Huck, W. T. S., *Nano Letters* **2010**, *10*, (4), 1302-1307.
- (60) Son, H. J.; He, F.; Carsten, B.; Yu, L., *Journal of Materials Chemistry* **2011**, *21*, (47), 18934-18945.
- (61) Zhou, H.; Yang, L.; You, W., *Macromolecules* **2012**, *45*, (2), 607-632.
- (62) Helgesen, M.; Sondergaard, R.; Krebs, F. C., *Journal of Materials Chemistry* **2010**, *20*, (1), 36-60.
- (63) Shaheen, S. E.; Brabec, C. J.; Sariciftci, N. S.; Padinger, F.; Fromherz, T.; Hummelen, J. C., *Applied Physics Letters* **2001**, *78*, (6), 841-843.
- (64) Brabec, C. J.; Shaheen, S. E.; Winder, C.; Sariciftci, N. S.; Denk, P., *Applied Physics Letters* **2002**, *80*, (7), 1288-1290.
- (65) Kim, Y.; Cook, S.; Tuladhar, S. M.; Choulis, S. A.; Nelson, J.; Durrant, J. R.; Bradley, D. D. C.; Giles, M.; McCulloch, I.; Ha, C.-S.; Ree, M., *Nature Materials* **2006**, *5*, (3), 197-203.
- (66) Cheng, Y.-J.; Yang, S.-H.; Hsu, C.-S., *Chemical Reviews* **2009**, *109*, (11), 5868-5923.
- (67) Kleinhenz, N.; Yang, L.; Zhou, H.; Price, S. C.; You, W., *Macromolecules* **2011**, *44*, (4), 872-877.
- (68) Roncali, J., *Macromolecular Rapid Communications* **2007**, *28*, (17), 1761-1775.
- (69) Havinga, E. E.; Hoeve, W. t.; Wynberg, H., *Polymer Bulletin* **1992**, *29*, 119-126.

- 
- (70) Zhu, Y.; Champion, R. D.; Jenekhe, S. A., *Macromolecules* **2006**, *39*, (25), 8712-8719.
- (71) Park, S. H.; Roy, A.; Beaupre, S.; Cho, S.; Coates, N.; Moon, J. S.; Moses, D.; Leclerc, M.; Lee, K.; Heeger, A. J., *Nature Photonics* **2009**, *3*, (5), 297-302.
- (72) Scharber, M. C.; Mühlbacher, D.; Koppe, M.; Denk, P.; Waldauf, C.; Heeger, A. J.; Brabec, C. J., *Advanced Materials* **2006**, *18*, (6), 789-794.
- (73) Brédas, J.-L.; Norton, J. E.; Cornil, J.; Coropceanu, V., *Accounts of Chemical Research* **2009**, *42*, (11), 1691-1699.
- (74) Stille, J. K., *Angewandte Chemie International Edition in English* **1986**, *25*, (6), 508-524.
- (75) Miyaura, N.; Suzuki, A., *Chemical Reviews* **1995**, *95*, (7), 2457-2483.
- (76) Anthony, J. E.; Facchetti, A.; Heeney, M.; Marder, S. R.; Zhan, X., *Advanced Materials* **2010**, *22*, (34), 3876-3892.
- (77) Kroto, H. W.; Heath, J. R.; O'Brien, S. C.; Curl, R. F.; Smalley, R. E., *Nature* **1985**, *318*, (6042), 162-163.
- (78) Haddock, J. N.; Zhang, X.; Domercq, B.; Kippelen, B., *Organic Electronics* **2005**, *6*, (4), 182-187.
- (79) Hummelen, J. C.; Knight, B. W.; LePeq, F.; Wudl, F.; Yao, J.; Wilkins, C. L., *The Journal of Organic Chemistry* **1995**, *60*, (3), 532-538.
- (80) Wienk, M. M.; Kroon, J. M.; Verhees, W. J. H.; Knol, J.; Hummelen, J. C.; van Hal, P. A.; Janssen, R. A. J., *Angewandte Chemie International Edition* **2003**, *42*, (29), 3371-3375.
- (81) He, Z.; Zhong, C.; Huang, X.; Wong, W.-Y.; Wu, H.; Chen, L.; Su, S.; Cao, Y., *Advanced Materials* **2011**, *23*, (40), 4636-4643.
- (82) Zhao, G.; He, Y.; Li, Y., *Advanced Materials* **2010**, *22*, (39), 4355-4358.
- (83) He, Y.; Chen, H.-Y.; Hou, J.; Li, Y., *Journal of the American Chemical Society* **2010**, *132*, (4), 1377-1382.
- (84) Voroshazi, E.; Vasseur, K.; Aernouts, T.; Heremans, P.; Baumann, A.; Deibel, C.; Xue, X.; Herring, A. J.; Athans, A. J.; Lada, T. A.; Richter, H.; Rand, B. P., *Journal of Materials Chemistry* **2011**, *21*, (43), 17345-17352.

- (85) Miller, N. C.; Sweetnam, S.; Hoke, E. T.; Gysel, R.; Miller, C. E.; Bartelt, J. A.; Xie, X.; Toney, M. F.; McGehee, M. D., *Nano Letters* **2012**, *12*, (3), 1566-1570.
- (86) Chang, L.; Lademann, H. W. A.; Bonekamp, J.-B.; Meerholz, K.; Moulé, A. J., *Advanced Functional Materials* **2011**, *21*, (10), 1779-1787.
- (87) Greene, M., Perylene Pigments. In *High Performance Pigments*, Wiley-VCH Verlag GmbH & Co. KGaA: 2009; pp 261-274.
- (88) Li, C.; Wonneberger, H., *Advanced Materials* **2012**, *24*, (5), 613-636.
- (89) Law, K. Y., *Chemical Reviews* **1993**, *93*, (1), 449-486.
- (90) Lüttich, F.; Lehmann, D.; Friedrich, M.; Chen, Z.; Facchetti, A.; Borzyskowski, C. v.; Zahn, D. R. T.; Graaf, H., *physica status solidi (a)* **2012**, *209*, (3), 585-593.
- (91) Schmidt-Mende, L.; Fechtenkotter, A.; Mullen, K.; Moons, E.; Friend, R. H.; MacKenzie, J. D., *Science* **2001**, *293*, (5532), 1119-1122.
- (92) Singh, C. R.; Sommer, M.; Himmerlich, M.; Wicklein, A.; Krischok, S.; Thelakkat, M.; Hoppe, H., *physica status solidi (RRL) – Rapid Research Letters* **2011**, *5*, (7), 247-249.
- (93) Langhals, H., *Helvetica Chimica Acta* **2005**, *88*, (6), 1309-1343.
- (94) Langhals, H.; Demmig, S.; Huber, H., *Spectrochimica Acta Part A: Molecular Spectroscopy* **1988**, *44*, (11), 1189-1193.
- (95) Wicklein, A.; Ghosh, S.; Sommer, M.; Würthner, F.; Thelakkat, M., *ACS Nano* **2009**, *3*, (5), 1107-1114.
- (96) Balakrishnan, K.; Datar, A.; Naddo, T.; Huang, J.; Oitker, R.; Yen, M.; Zhao, J.; Zang, L., *Journal of the American Chemical Society* **2006**, *128*, (22), 7390-7398.
- (97) Howard, I. A.; Laquai, F. d. r.; Keivanidis, P. E.; Friend, R. H.; Greenham, N. C., *The Journal of Physical Chemistry C* **2009**, *113*, (50), 21225-21232.
- (98) Adam, D.; Schuhmacher, P.; Simmerer, J.; Haussling, L.; Siemensmeyer, K.; Etzbachi, K. H.; Ringsdorf, H.; Haarer, D., *Nature* **1994**, *371*, (6493), 141-143.
- (99) Wicklein, A.; Lang, A.; Muth, M.; Thelakkat, M., *Journal of the American Chemical Society* **2009**, *131*, (40), 14442-14453.
- (100) Haverkate, L. A.; Zbiri, M.; Johnson, M. R.; Deme, B.; Mulder, F. M.; Kearley, G. J., *The Journal of Physical Chemistry B* **2011**, *115*, (47), 13809-13816.

- 
- (101) Wicklein, A.; Muth, M.-A.; Thelakkat, M., *Journal of Materials Chemistry* **2010**.
- (102) Mikroyannidis, J. A.; Suresh, P.; Sharma, G. D., *Synthetic Metals* **2010**, *160*, 932-938.
- (103) Molinari, A. S.; Alves, H.; Chen, Z.; Facchetti, A.; Morpurgo, A. F., *Journal of the American Chemical Society* **2009**, *131*, (7), 2462-2463.
- (104) Rajaram, S.; Shivanna, R.; Kandappa, S. K.; Narayan, K. S., *The Journal of Physical Chemistry Letters* **2012**, *3*, (17), 2405-2408.
- (105) Bu, L.; Guo, X.; Yu, B.; Fu, Y.; Qu, Y.; Xie, Z.; Yan, D.; Geng, Y.; Wang, F., *Polymer* **2011**, *52*, (19), 4253-4260.
- (106) Sommer, M.; Lindner, S.; Thelakkat, M., *Advanced Functional Materials* **2007**, *17*, (9), 1493-1500.
- (107) Hüttner, S.; Sommer, M.; Thelakkat, M., *Applied Physics Letters* **2008**, *92*, (9), 093302-3.
- (108) Segalman, R. A.; McCulloch, B.; Kirmayer, S.; Urban, J. J., *Macromolecules* **2009**, *42*, (23), 9205-9216.
- (109) Tseng, Y.-C.; Darling, S. B., *Polymers* **2010**, *2*, 470-489.
- (110) Lindner, S. M.; Hüttner, S.; Chiche, A.; Thelakkat, M.; Krausch, G., *Angewandte Chemie International Edition* **2006**, *45*, (20), 3364-3368.
- (111) Brédas, J.-L.; Cornil, J.; Heeger, A. J., *Advanced Materials* **1996**, *8*, (5), 447-452.
- (112) López Varo, P.; Jiménez Tejada, J. A.; López Villanueva, J. A.; Carceller, J. E.; Deen, M. J., *Organic Electronics* **2012**, *13*, (9), 1700-1709.
- (113) Bäessler, H., *Physica status solidi (b)* **1993**, *175*, 15-56.
- (114) Gartstein, Y. N.; Conwell, E. M., *Chemical Physics Letters* **1995**, *245*, 351-358.
- (115) Dunlap, D. H.; Parris, P. E.; Kenkre, V. M., *Physical Review Letters* **1996**, *77*, (3), 542-545.
- (116) Coropceanu, V.; Cornil, J.; da Silva Filho, D. A.; Olivier, Y.; Silbey, R.; Brédas, J.-L., *Chemical Reviews* **2007**, *107*, (4), 926-952.
- (117) Monroe, D., *Physical Review Letters* **1985**, *54*, (2), 146-149.
- (118) Vissenberg, M. C. J. M.; Matters, M., *Physical Review B* **1998**, *57*, (20), 12964-12967.

- (119) Brédas, J. L.; Calbert, J. P.; da Silva Filho, D. A.; Cornil, J., *Proceedings of the National Academy of Sciences* **2002**, *99*, (9), 5804-5809.
- (120) Sirringhaus, H.; Brown, P. J.; Friend, R. H.; Nielsen, M. M.; Bechgaard, K.; Langeveld-Voss, B. M. W.; Spiering, A. J. H.; Janssen, R. A. J.; Meijer, E. W.; Herwig, P.; de Leeuw, D. M., *Nature* **1999**, *401*, (6754), 685-688.
- (121) Leong, W. L.; Welch, G. C.; Kaake, L. G.; Takacs, C. J.; Sun, Y.; Bazan, G. C.; Heeger, A. J., *Chemical Science* **2012**, *3*, (6), 2103-2109.
- (122) Nielsen, K. T.; Bechgaard, K.; Krebs, F. C., *Macromolecules* **2005**, *38*, (3), 658-659.
- (123) Köhler, A., *Nature Materials* **2012**, *11*, 836-837.
- (124) Pivrikas, A.; Sariciftci, N. S.; Juška, G.; Österbacka, R., *Progress in Photovoltaics: Research and Applications* **2007**, *15*, (8), 677-696.
- (125) Mandoc, M. M.; Koster, L. J. A.; Blom, P. W. M., *Applied Physics Letters* **2007**, *90*, (13), 133504-3.
- (126) Mauer, R.; Howard, I. A.; Laquai, F. d. r., *The Journal of Physical Chemistry Letters* **2010**, *1*, (24), 3500-3505.
- (127) Maurano, A.; Hamilton, R.; Shuttle, C. G.; Ballantyne, A. M.; Nelson, J.; O'Regan, B.; Zhang, W.; McCulloch, I.; Azimi, H.; Morana, M.; Brabec, C. J.; Durrant, J. R., *Advanced Materials* **2010**, *22*, (44), 4987-4992.
- (128) Tress, W.; Petrich, A.; Hummert, M.; Hein, M.; Leo, K.; Riede, M., *Applied Physics Letters* **2011**, *98*, (6), 063301-3.
- (129) LeBlanc, J. O. H., *The Journal of Chemical Physics* **1960**, *33*, (2), 626-626.
- (130) Kepler, R. G., *Physical Review* **1960**, *119*, (4), 1226-1229.
- (131) Hertel, D.; Bäessler, H., *ChemPhysChem* **2008**, *9*, (5), 666-688.
- (132) Chen, B.; Lee, C.-s.; Lee, S.-t.; Webb, P.; Chan, Y.-c.; Gambling, W.; Tian, H.; Zhu, W., *Japanese Journal of Applied Physics* **2000**, *39*, 1190-1192.
- (133) Juska, G.; Arlauskas, K.; Viliunas, M.; Genevicius, K.; Österbacka, R.; Stubb, H., *Physical Review B* **2000**, *62*, (24), R16235-R16238.
- (134) Kokil, A.; Yang, K.; Kumar, J., *Journal of Polymer Science Part B: Polymer Physics* **2012**, *50*, (15), 1130-1144.
- (135) Bange, S.; Schubert, M.; Neher, D., *Physical Review B* **2010**, *81*, (3), 035209.

- 
- (136) Dodabalapur, A.; Torsi, L.; Katz, H. E., *Science* **1995**, *268*, (5208), 270-271.
- (137) Malliaras, G. G.; Scott, J. C., *Journal of Applied Physics* **1999**, *85*, (10), 7426-7432.
- (138) Liu, C.-Y.; Chen, S.-A., *Macromolecular Rapid Communications* **2007**, *28*, (17), 1743-1760.
- (139) Blom, P. W. M.; de Jong, M. J. M.; Vleggaar, J. J. M., *Applied Physics Letters* **1996**, *68*, (23), 3308-3310.
- (140) Bozano, L.; Carter, S. A.; Scott, J. C.; Malliaras, G. G.; Brock, P. J., *Applied Physics Letters* **1999**, *74*, (8), 1132-1134.
- (141) Murgatroyd, P. N., *Journal of Physics D: Applied Physics* **1970**, *3*, 151.
- (142) Pasveer, W. F.; Cottaar, J.; Tanase, C.; Coehoorn, R.; Bobbert, P. A.; Blom, P. W. M.; de Leeuw, D. M.; Michels, M. A. J., *Physical Review Letters* **2005**, *94*, (20), 206601.
- (143) Jain, S. C.; Geens, W.; Mehra, A.; Kumar, V.; Aernouts, T.; Poortmans, J.; Mertens, R.; Willander, M., *Journal of Applied Physics* **2001**, *89*, (7), 3804-3810.
- (144) Muth, M.-A.; Carrasco-Orozco, M.; Thelakkat, M., *Advanced Functional Materials* **2011**, *21*, (23), 4510-4518.
- (145) Narioka, S.; Ishii, H.; Yoshimura, D.; Sei, M.; Ouchi, Y.; Seki, K.; Hasegawa, S.; Miyazaki, T.; Harima, Y.; Yamashita, K., *Applied Physics Letters* **1995**, *67*, (13), 1899-1901.
- (146) Shimada, T.; Hamaguchi, K.; Koma, A.; Ohuchi, F. S., *Applied Physics Letters* **1998**, *72*, (15), 1869-1871.
- (147) Bharathan, J. M.; Yang, Y., *Journal of Applied Physics* **1998**, *84*, (6), 3207-3211.
- (148) Friend, R. H.; Gymer, R. W.; Holmes, A. B.; Burroughes, J. H.; Marks, R. N.; Taliani, C.; Bradley, D. D. C.; Dos Santos, D. A.; Brédas, J. L.; Logdlund, M.; Salaneck, W. R., *Nature* **1999**, *397*, 121-128.
- (149) Buckley, A. R., *Synthetic Metals* **2010**, *160*, 540-543.
- (150) Liang, Y.; Feng, D.; Wu, Y.; Tsai, S.-T.; Li, G.; Ray, C.; Yu, L., *Journal of the American Chemical Society* **2009**, *131*, (22), 7792-7799.
- (151) Huang, Y.; Wang, Y.; Sang, G.; Zhou, E.; Huo, L.; Liu, Y.; Li, Y., *The Journal of Physical Chemistry B* **2008**, *112*, (43), 13476-13482.

- (152) Goh, C.; Kline, R. J.; McGehee, M. D.; Kadnikova, E. N.; Frechet, J. M. J., *Applied Physics Letters* **2005**, *86*, (12), 122110-3.
- (153) Chan, S.-H.; Hsiao, Y.-S.; Hung, L.-I.; Hwang, G.-W.; Chen, H.-L.; Ting, C.; Chen, C.-P., *Macromolecules* **2010**, *43*, (7), 3399-3405.
- (154) Steyrlleuthner, R.; Schubert, M.; Jaiser, F.; Blakesley, J. C.; Chen, Z.; Facchetti, A.; Neher, D., *Advanced Materials* **2010**, *22*, (25), 2799-2803.
- (155) Ayzner, A. L.; Wanger, D. D.; Tassone, C. J.; Tolbert, S. H.; Schwartz, B. J., *The Journal of Physical Chemistry C* **2008**, *112*, (48), 18711-18716.
- (156) Gao, F.; Wang, J.; Blakesley, J. C.; Hwang, I.; Li, Z.; Greenham, N. C., *Advanced Energy Materials* **2012**, *2*, (8), 956-961.
- (157) Azimi, H.; Senes, A.; Scharber, M. C.; Hingerl, K.; Brabec, C. J., *Advanced Energy Materials* **2011**, *1*, (6), 1162-1168.

## 2. Overview of the Thesis

A profound understanding of structure-property relations in organic semiconductors is crucial for designing new materials for opto-electronic applications. The focus of this thesis is on organic electron transport (n-type) semiconductors for photovoltaic applications. Within the scope of this work, novel n-type semiconductors were synthesized and characterized. The influence of chemical structure on optical and electronic properties was investigated. Special attention was paid to the correlation of charge transport and morphology in electronic devices. Bulk Heterojunction (BHJ) solar cells of selected electron acceptors in combination with an electron donating polymer were fabricated and characterized. One of the aims of this thesis was to explore electron acceptors based on perylene bisimides that can be an alternative to the current state-of-the-art material PCBM. Modifications at the chemical structure of various perylene and fullerene based acceptors could improve crucial properties like light harvesting, charge carrier mobility, morphology and order in thin films, as well as HOMO and LUMO energy levels. The most important factors for the development of organic semiconductors, as well as the chemical structures of the n-type materials under investigation are depicted in Figure 1.

This dissertation contains six manuscripts, each of which forms one individual chapter. In each chapter an approach of improving one or several of the above mentioned factors is presented. Based on the chemical structure, the thesis can be divided into two parts: studies on perylene semiconductors, which are discussed in Chapters 3-5 and Chapter 8 (Annex), and fullerene compounds, which are discussed in Chapters 6 and 7. For both material classes, polymeric compounds as well as small molecules are considered and the different material and device properties are discussed and compared. A central aspect in each chapter is the evaluation of the charge transport properties of the semiconductors under investigation and their correlation with structural aspects. A suitable method for measuring charge carrier mobility was chosen and established in our group within this thesis. The method is based on single carrier devices, where the charge carrier mobility can be determined by recording

current density – voltage ( $J$ - $V$ ) characteristics and using Mott-Gurney's equation, when the current measured is space-charge limited only (SCLC, see Chapter 1.3 for more details).

The first part of the thesis including Chapters 3-5 and Chapter 8 as Annex deals with perylene imide and diester based compounds, which represent an important class of n-type semiconductors. The strong  $\pi$ - $\pi$  interaction of these molecules is generally leading to uncontrolled crystallization and large macroscopic crystals, which has been identified as a limiting factor for device efficiency in BHJ solar cells.<sup>1</sup> We envisioned to tune crystallization whilst maintaining close  $\pi$ - $\pi$  stacking by implementing an unsymmetrical substitution pattern, which is subject of Chapter 3. Three different unsymmetrical perylene bisimides (PBI) were evaluated in terms of their charge transport properties, morphology and crystalline order in thin films by means of SCLC, atomic force microscopy (AFM) and XRD measurements, as well as UV/vis and photoluminescence (PL) spectroscopy. The blend morphology and device performance of BHJ solar cells of these materials in combination with a donor polymer are studied in Chapter 8 (Annex). The nature of the side groups were found to have a strong influence on crystalline structure and orientation in thin films and thus a major impact on blend morphology, electron mobility and device performance. While side groups attached to the imide position of the perylene core only have limited effect on the optical properties of these dyes, light harvesting can be improved by modifications directly at the perylene core, which is subject of Chapter 4. Two novel classes of semiconductor polymers (PPDB and PPDI) were synthesized and the characterization of optical, electronic and structural properties was carried out. In addition to enhanced visible light absorption in the case of PPDB, altering the heterocyclic  $\pi$ -system also permits access to materials with different electronic character (n-type and p-type). Despite PPDB being superior to common perylene bisimide based polymers regarding light harvesting, a direct comparison of the electron transport properties was missing. This question, among others, is addressed in Chapter 5. Therein, a fundamental question of how molecular packing and the  $\pi$ -electron system of a semiconductor polymer influences charge transport was investigated. In this comparative study, the polymers feature pendant perylene side groups similar to the ones discussed in Chapter 4, and PBI moieties in analogy to the small molecules from Chapter 3.

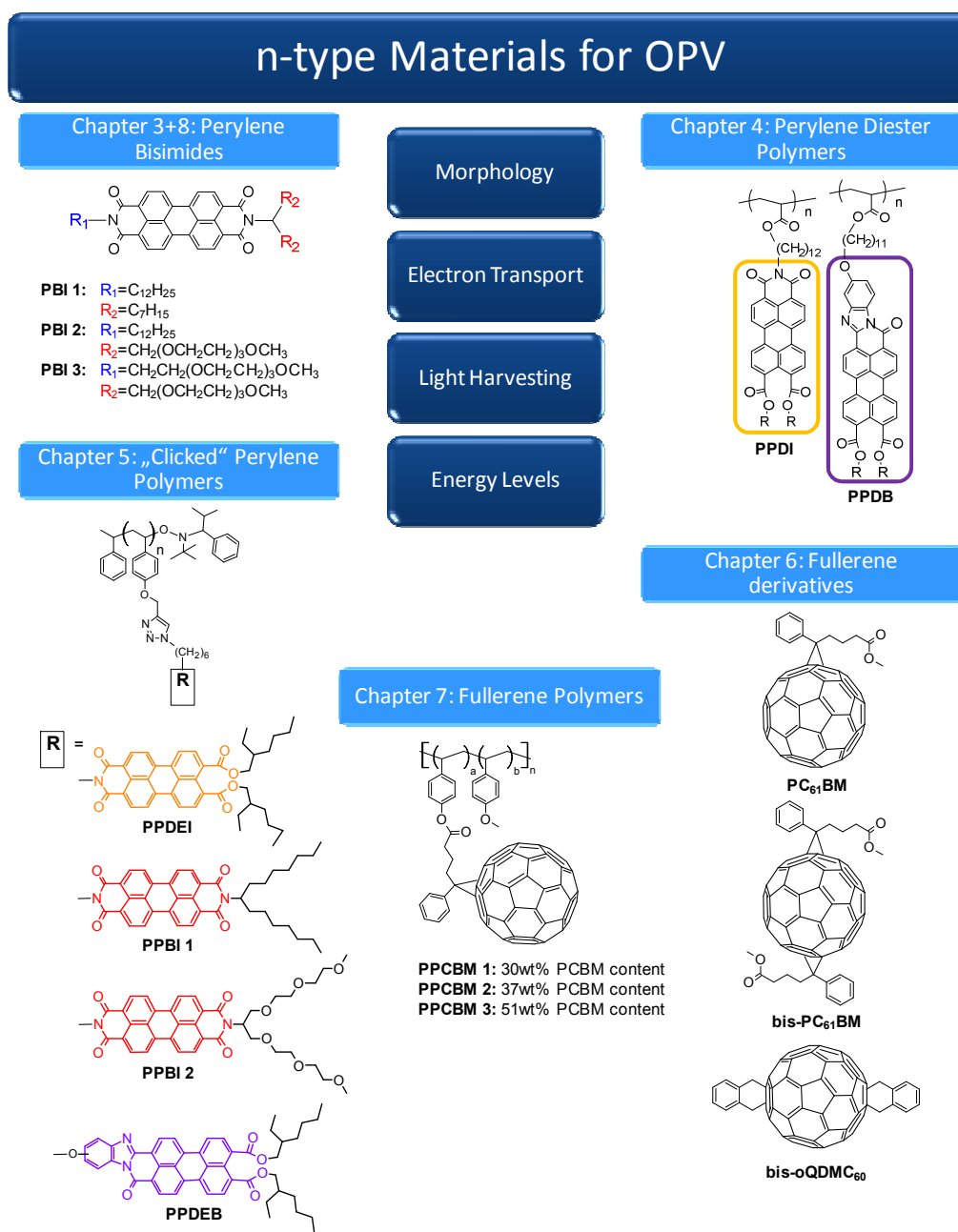


Figure 1: Important parameters of organic semiconductors for application in solar cells which can be controlled by modifying the chemical structure of the materials are presented in the middle. The interplay of crystalline structure, morphology and electron transport for perylene bisimide (PBI) small molecules is addressed in Chapter 3. Solar cell performance and blend morphology of these materials with a donor polymer is investigated in Chapter 8 (Annex). Changes at the chemical structure of perylene based polymers (PPDI, PPDB, PPDEI, PPDEB, PPBI 1 and PPBI 2) and the impact on light harvesting and charge transport is subject of Chapters 4 and 5. Device performance of Polymer:Fullerene solar cells is correlated with energy levels, charge transport and morphology of a series of fullerene derivatives (PCBM, bis-PCBM and bis-oQDMC) in Chapter 6. Fullerene-grafted polymers (PPCBM) are evaluated in terms of their electron transporting properties and thin film morphology in Chapter 7.

Since all polymers exhibit the same polymer backbone, changes in charge transport or packing behavior could directly be related to the chemical structure of the pendant perylenes.

In the first part of the thesis we demonstrated various ways how to tune and improve optical and electronic properties and morphology of perylene based semiconductors. The best power conversion efficiency (PCE) obtained for solar cells using blends of n-type PBI 2 and a p-type polymer however, was only 0.6 %, which illustrates that fundamental issues, leading to low short circuit current densities ( $J_{SC}$ ), of these blends still exist. Comparable blend devices with PCBM as acceptor instead of PBI can have a significantly higher  $J_{SC}$  and hence PCEs of around 4 % were achieved. Nevertheless, even higher PCEs on the one hand and better stability on the other hand are required for commercialization of this technology. In the second part we show attempts how to tackle these issues based on fullerene acceptor systems.

Chapter 6 describes two bis-adduct fullerene derivatives with higher LUMO energy levels compared to PCBM. Even though in photovoltaic devices, the open circuit voltage ( $V_{OC}$ ) could be improved, the short circuit current density ( $J_{SC}$ ) was lower compared to solar cells containing PCBM. The aim was to explore possible explanations for this behavior and find solutions to overcome these issues. The electron- and hole mobilities of the blends were determined. Blend systems where the performance was limited by low electron mobility in one case and by unfavorable blend morphology in another case could be identified. In Chapter 7, the problem of fullerene diffusion and crystallization, which is one limiting factor for morphological stability in OPV blends, is addressed. Electron mobilities and thin film morphology of novel fullerene side chain polymers were compared to standard PCBM small molecules dispersed in a comparable polymer matrix. Results demonstrated that good electronic properties can be achieved while disadvantageous crystallite formation could be avoided simultaneously.

In the following, a summary of each manuscript with the key results is given. All details can be found in the respective Chapters 3-8.

## Unsymmetrical Perylene bisimides: Influence of Substituents on Crystal Structure and Electron Transport

Herein, three solution processable PBI small molecules were evaluated in terms of their charge transport properties, crystalline structure and morphology in thin films. The series of PBIs comprise an unsymmetrical substitution pattern at the imide positions with linear chains at one side and branched chains at the other side of the perylene core, which reduces aggregation in thin films significantly, compared to a symmetrical analogue. The nature of the substituents was varied from hydrophobic alkyl chains to hydrophilic oligoethylenglycol (OEG) chains to allow for tuning self-assembly properties of the compounds. Figure 2a shows the chemical structures of the three PBIs and the electron mobility values.

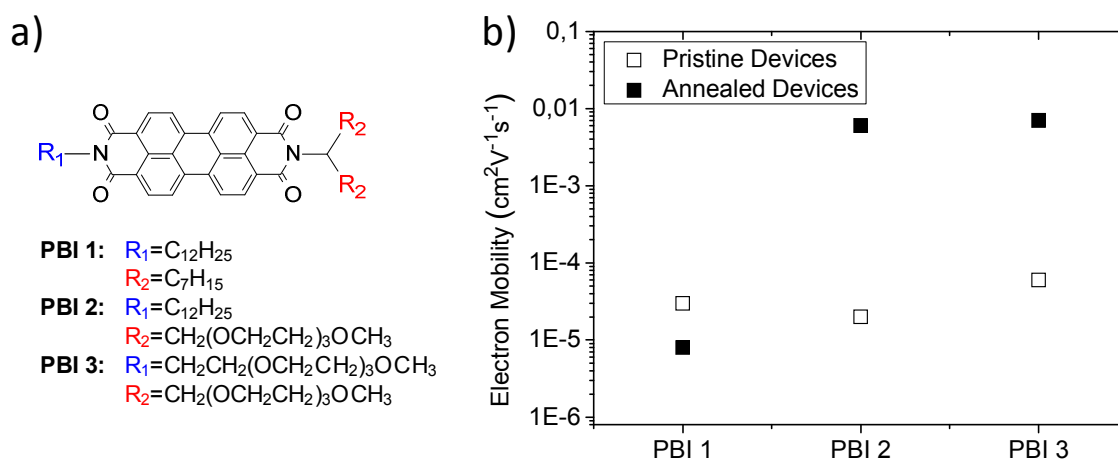


Figure 2: a) Chemical structure of perylene bisimides (PBI) with respective side groups for PBI 1, PBI 2 and PBI 3 and b) electron mobilities, determined from SCLC measurements of pristine and annealed single carrier devices.

The electron transporting properties in single carrier devices using the SCLC approach were evaluated. Measurements were recorded before and after a thermal annealing step at temperatures just below the material's melting point, to allow for better packing and orientation of the perylene molecules in thin films. When OEG side groups are attached to the perylene core (PBI 2 and PBI 3), electron mobilities of the compounds after thermal annealing were more than two orders of magnitude higher compared to the corresponding

PBI 1 with only alkyl chains (Figure 2b). Electron mobilities as high as  $7 \cdot 10^{-3} \text{ cm}^2 \text{V}^{-1} \text{s}^{-1}$  were measured. To understand these results, I studied aggregation and crystallinity of PBI thin films by polarized optical microscopy (POM), UV/vis and PL spectroscopy and AFM. The measurements showed that aggregation and crystallinity of the perylene molecules after annealing is increased.

Furthermore X-ray diffraction (XRD) experiments were carried out in collaboration with Prof. Thurn-Albrecht group from Halle University. Temperature dependant theta-2-theta scans of the bulk materials revealed that all three materials exhibit a 3D crystalline structure. While the diffractogram of PBI 2 could be indexed as a hexagonal lattice (see Figure 3a) with lattice parameters  $a = b = 3.47 \text{ nm}$  and  $\gamma = 60^\circ$ , a lamellar packing was found for PBI 1 and PBI 3 with lattice parameters  $a = 2.86 \text{ nm}$ ,  $b = 1.11 \text{ nm}$ ,  $\gamma = 86^\circ$  and  $a = 2.77 \text{ nm}$ ,  $b = 1.21 \text{ nm}$  and  $\gamma = 81^\circ$ , respectively. Lattice parameter  $c$ , which represents the  $\pi$ - $\pi$  stacking distance of the perylene molecules within one column was found to decrease gradually from PBI 1 (0.360 nm) to PBI 2 (0.350 nm) and PBI 3 (0.346 nm). Hence, OEG side chains promote a closer packing of the molecules, which is beneficial for charge transport, as better electron mobilities were measured for PBI 2 and PBI 3. An illustration of the columnar hexagonal and lamello-columnar packing of PBI 2 and PBI 3 is exemplarily shown in Figure 3d and e, respectively. The crystalline structure and orientation of pristine and annealed PBIs in thin films was examined by theta-2-theta scans. After annealing, sharper reflections with increased intensities and higher order reflections were observed for all three PBIs indicating an increase in crystallinity. Especially the OEG substituted PBI 2 and PBI 3 showed up to fourth order reflections implying that order and crystallinity is very high, compared to PBI 1, where only the second order reflection was observed. We attribute this to the higher flexibility of the OEG chains, which allows the molecules for a better orientation upon thermal annealing. Exemplarily, the theta-2-theta scan of pristine and annealed PBI 2 is depicted in Figure 3b. The texture measurement of PBI 2 is shown in Figure 3c. The relative degree of crystallinity is proportional to the integrated peak intensity, which proves that crystallinity is increasing upon thermal annealing. The increase of crystallinity is found to be significantly stronger for PBI 2 especially PBI 3, compared to PBI 1. Hence, also the thin film XRD measurements illustrate, that good packing and high crystallinity of the perylene

molecules is beneficial for charge transport. Further, photoluminescence spectroscopy showed that photons absorbed by the alkyl substituted PBI film tend to recombine radiatively, in contrast to the PBIs with OEG chains. In addition to the findings from XRD, these experimental evidences also explain the better charge transport properties of PBI 2 and PBI 3.

It was demonstrated, that the solubilizing side chains in PBI derivatives have a major impact on the bulk charge carrier mobility, which correlates with crystalline structure and order in thin films. Electron mobilities of up to  $7 \cdot 10^{-3} \text{ cm}^2 \text{ V}^{-1} \text{ s}^{-1}$  were measured where hydrophilic OEG substituents allow for well ordered packing and high crystallinity in thin films.

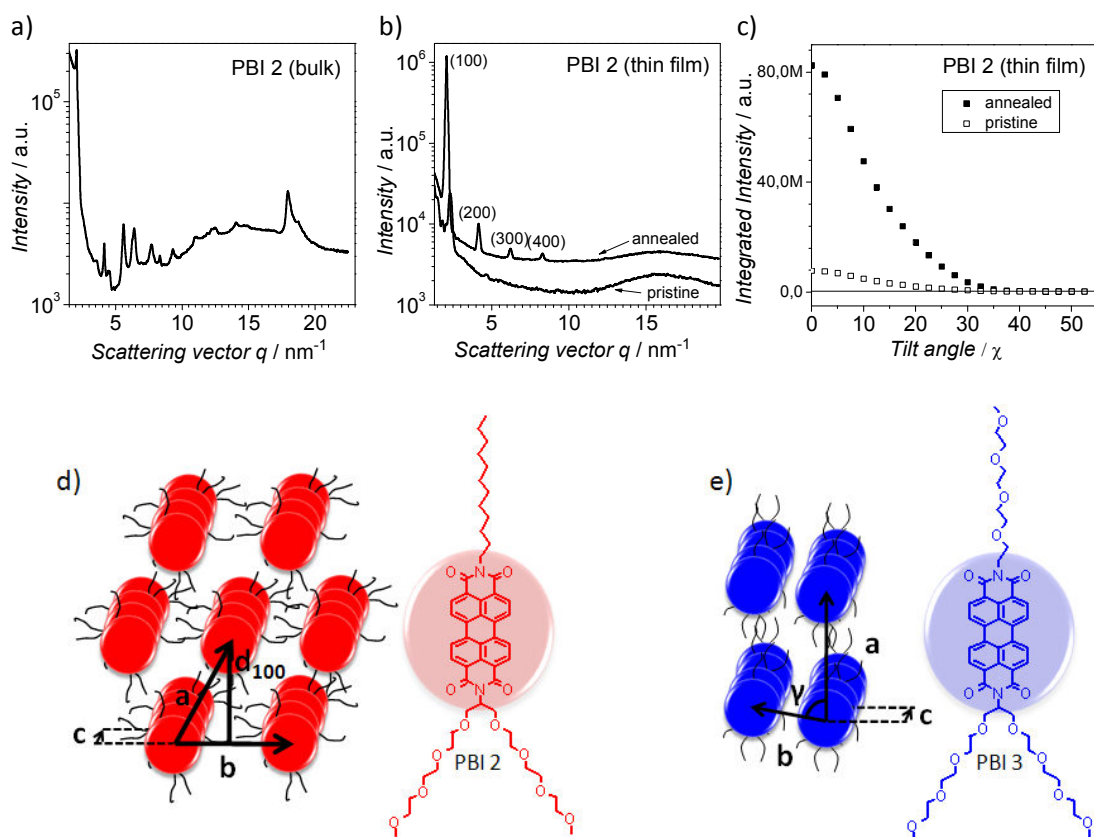


Figure 3: a) XRD theta-2-theta scan of melt crystallized PBI 2 in bulk, which can be indexed as a hexagonal lattice with lattice parameters  $a=b=3.47\text{nm}$  and  $\gamma=60^\circ$  and  $c=0.35\text{nm}$  corresponding to the  $\pi$ - $\pi$  stacking distance of the perylene cores; b) XRD theta-2-theta scan of pristine and annealed thin films and c) corresponding texture measurements, where the integrated area of the intensity curve is a proportional measure for crystallinity in thin films; d) illustration of columnar hexagonal packing of PBI 2 molecules and e) lamello-columnar packing of PBI 3 for comparison.

## Liquid Crystalline Perylene Diester Polymers with Tunable Charge Carrier Mobility

Apart from good electronic properties and a suitable morphology, light absorption is a crucial parameter for materials used in OPV. The aim of this study was to find semiconductor polymers with strong visible light absorption over a long wavelength range and high solubility in organic solvents. We envisioned improving absorption properties of well known side-chain homopolymers consisting of pendant perylene bisimides (PPBI) by modifications at the  $\pi$ -conjugation system of the perylene units. A benzimidazole unit attached to the perylene core in the case of PPDB increases the  $\pi$ -electron delocalization and is expected to result in a bathochromic shift in the absorption spectrum.

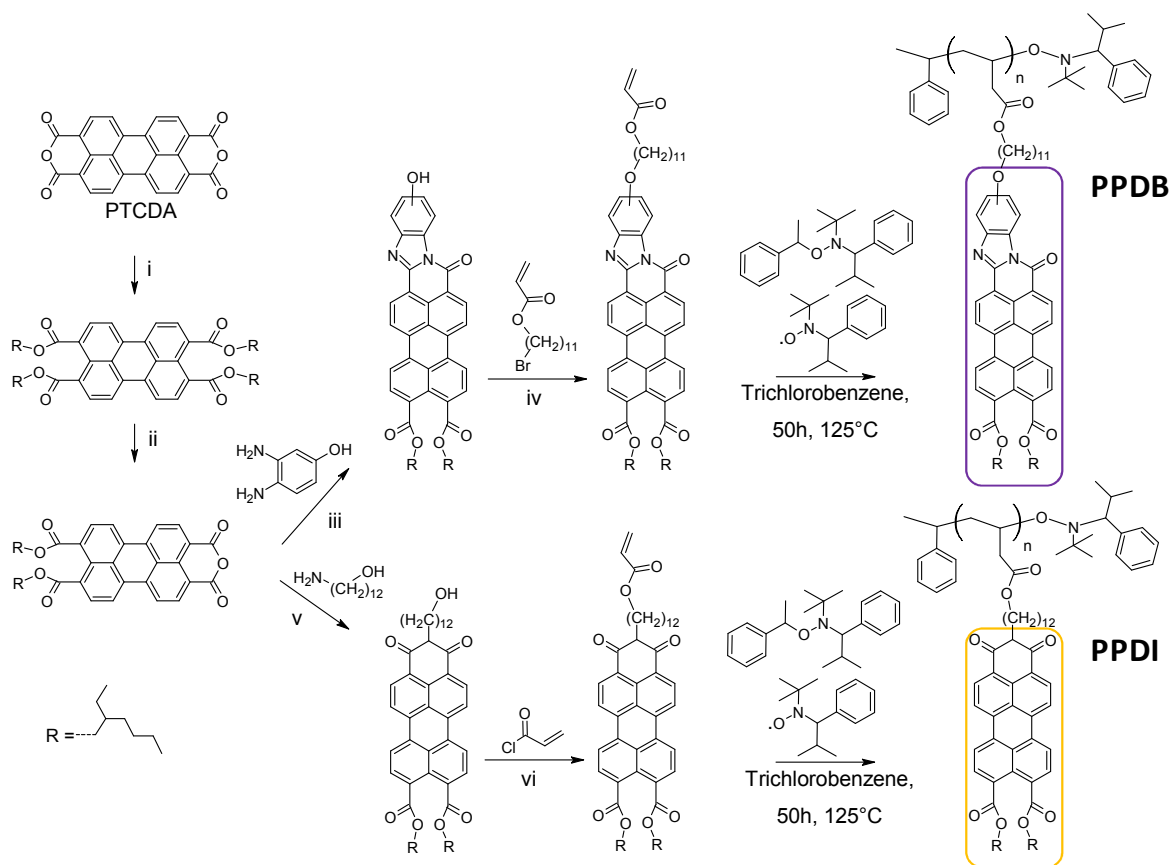


Figure 4: Synthesis route for Poly(peryene diester benzimidazole) (PPDB) and Poly(peryene diester imide) (PPDI). i) 1.  $\text{KOH}/\text{H}_2\text{O}$ , 0.5h,  $70^\circ\text{C}$ ; 2. Aliquat 336, KI, 10min, RT; 3. Br-R, 16h,  $100^\circ\text{C}$ . ii)  $p$ -toluenesulfonic acid monohydrate, toluene/ $n$ -dodecane, 5h,  $95^\circ\text{C}$ . iii)  $\text{Zn}(\text{OAc})_2/\text{DMAc}$ , 25min,  $160^\circ\text{C}$ , 300W (microwave). iv)  $\text{K}_2\text{CO}_3$ , KI, DMAc, 17h,  $85^\circ\text{C}$ . v) Imidazole,  $\text{Zn}(\text{OAc})_2$ , 4h,  $160^\circ\text{C}$ . vi)  $\text{Et}_3\text{N}/\text{DCM}$ , 24h,  $0^\circ\text{C}$ .

Two novel classes of semiconductor polymers (PPDB and PPDI) were synthesized according to the route shown in Figure 4. The starting material was perylenetetracarboxylic acid dianhydride (PTCDA), from which the perylene diester monoanhydrid was obtained in two steps (i and ii). To obtain high solubility, branched alkyl chains were used as solubilizing groups and connected *via* the two ester groups to the perylene core. The desired perylene diester benzimidazole (PDB) was obtained in a microwave reaction (iii). For comparison, perylene diester imide (PDI) was synthesized as well (v). Acrylate units as polymerizable groups were introduced (iv and vi), so that polymerization of the acrylate monomers *via* nitroxide mediated radical polymerization (NMRP) gave side chain homopolymers PPDI and PPDB. The polymers were characterized by Size Exclusion Chromatography (SEC), UV/vis spectroscopy, XRD, cyclic voltammetry (CV), differential scanning calorimetry (DSC), POM and SCLC single carrier devices.

The main conclusions are that the absorption of PPDB in the visible range is notably broadened up to 670 nm compared to PPDI (580 nm) (Figure 5a), which is due to the above mentioned extended  $\pi$ -conjugation system of PPDB. Charge transport measurements were carried out by fabricating single carrier devices to determine hole and electron mobilities. By using the SCLC approach, we discovered that not only absorption, but also the electronic character of the two polymers has changed. PPDB is a good electron transport material with an electron mobility of  $3 \cdot 10^{-4} \text{ cm}^2 \text{V}^{-1} \text{s}^{-1}$ , the hole mobility was found to be  $1 \cdot 10^{-6} \text{ cm}^2 \text{V}^{-1} \text{s}^{-1}$ . PPDI, however, shows better hole mobility with  $2 \cdot 10^{-4} \text{ cm}^2 \text{V}^{-1} \text{s}^{-1}$ , and a low electron mobility of  $2 \cdot 10^{-5} \text{ cm}^2 \text{V}^{-1} \text{s}^{-1}$ . This result implies that perylene based semiconductors can be tuned from n-type to p-type by altering the heterocyclic  $\pi$ -electron system of the pendant perylene cores (as illustrated in Figure 5c). We also found that both materials exhibit liquid-crystalline (LC) mesophases over a broad temperature range, which was shown by XRD (see Figure 5b), DSC and POM. LC semiconductors are of particular interest, because they can potentially combine order and easy alignment, which is important to obtain a suitable morphology and good charge transport in electronic devices. The impact of structural order of side-chain polymers on charge transport should therefore be further investigated, which is the subject of the following chapter.

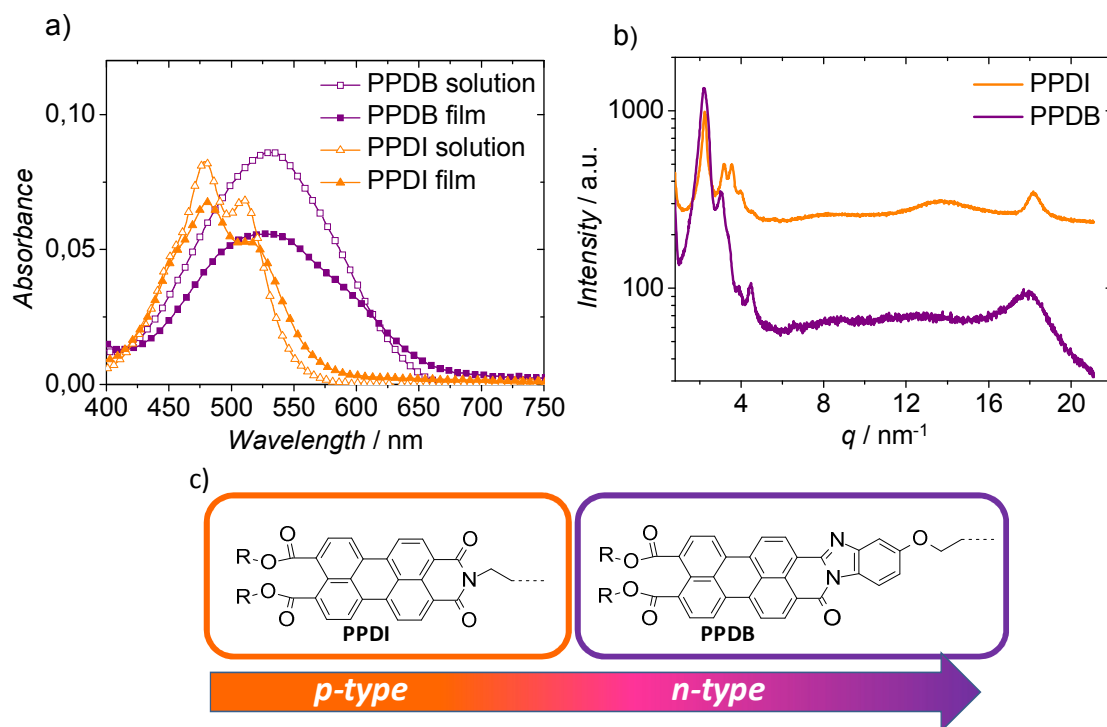


Figure 5: a) UV/vis absorption spectra of PPDI and PPDB in *o*DCB solution ( $c=10^{-5} \text{ mol}\cdot\text{L}^{-1}$ ) and of thin films; b) X-ray diffraction pattern of Poly(perylene diester imide) (PPDI) and Poly(perylene diester benzimidazole) (PPDB) and c) illustration of how modifications at the perylene core can influence the electronic character.

## Pendant Perylene Polymers with High Electron Mobility

Encouraged by the results of Chapter 3 and 4 we investigated polymers consisting of PDI and PDB units (Chapter 4) in a comparative study with polymers bearing PBI units with hydrophilic and hydrophobic groups (in analogy to Chapter 3). Four different side-chain homopolymers with pendant perylene moieties were synthesized by a combination of NMRP of propargyloxystyrol and Cu-catalyzed azide-alkyne “click” chemistry of the respective peryleneazides. The perylene units were individually attached to the same polymer backbone in a “click” reaction. Thus, the nature of the solubilizing side chains and the chromophoric  $\pi$ -conjugation system of the pendant perylene moieties were systematically varied. In the case of PPBI 1 branched alkyl and for PPBI 2 branched oligoethylenglycol (OEG) groups were used as substituents at the imide position. The structure formula of PPDEI and PPDEB are

similar to the polymers PPDI and PPDB of the previous chapter, however, an additional triazole unit due to the click reaction is present in each perylene moiety. The “click” reaction and the four “clicked” polymers are shown in Figure 6a. Since the same scaffold polymer was used for each compound, all four homopolymers possess the same chain length and polydispersity. Therefore, the aim of this chapter was to directly relate changes in charge transport, packing behavior and optical properties to the chemical structure of the pendant group.

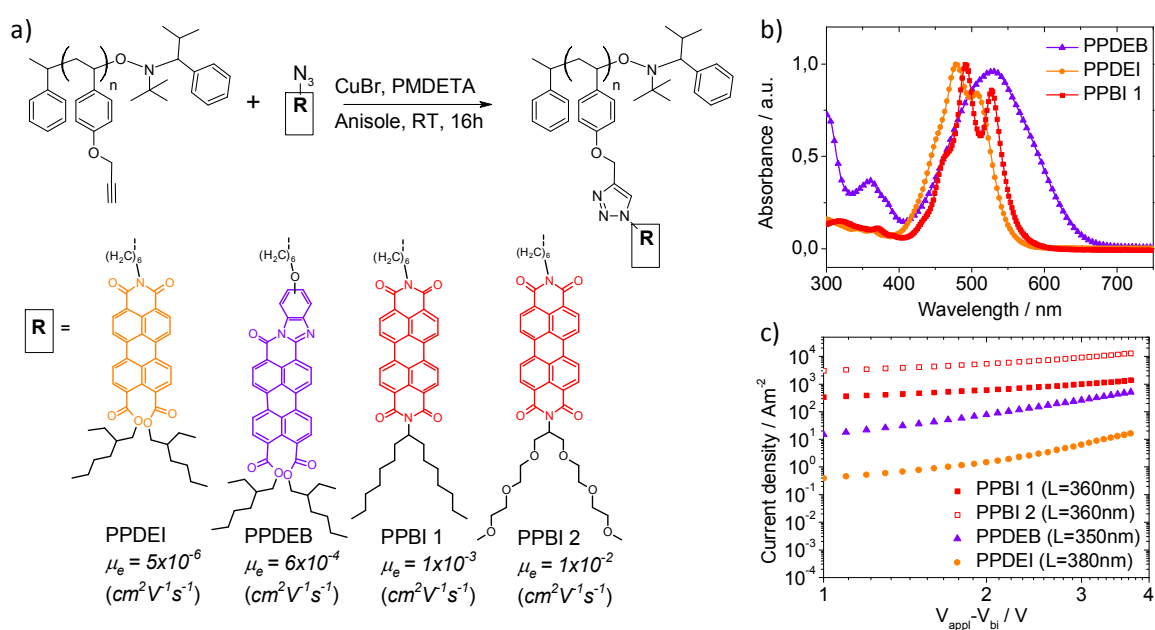


Figure 6: a) “Click” reaction of poly(propargyloxystyrene) with perylene azides giving poly(peryene diester imide) (PPDEI), poly(peryene diester benzimidazole) (PPDEB), poly(peryene bisimide) 1 (PPBI 1) and poly(peryene bisimide) 2 (PPBI 2); b) UV/vis absorption spectra of PPDEB, PPDEI and PPBI 1 in CHCl<sub>3</sub> solution ( $c=10^{-5} \text{ mol} \cdot \text{L}^{-1}$ ) and c) J-V characteristics of electron-only devices of PPBI 1, PPBI 2, PPDEB and PPDEI with active layer thickness  $L$ .

The impact of these modifications on charge transport properties by SCLC measurements in electron- and hole-only devices was investigated. Cyclic voltammetry was used to estimate HOMO and LUMO levels and optical properties were investigated using UV/vis spectroscopy. Furthermore, thermal behavior was studied by DSC, POM and XRD. PPDEI, PPDEB and PPBI 1 are liquid crystalline materials, whereas PPBI 2 is amorphous. A comparison of the electron mobility, obtained from SCLC measurements in Figure 6c shows

that PPBI 1 with  $1 \cdot 10^{-3} \text{ cm}^2 \text{ V}^{-1} \text{ s}^{-1}$  is superior to PPDB with  $6 \cdot 10^{-4} \text{ cm}^2 \text{ V}^{-1} \text{ s}^{-1}$ . Hence, even though light absorption of PPDB could be improved compared to PPBI (see Figure 6b), charge transport is negatively affected. Another striking result was the effect of the solubilizing substituent at the imide positions of PPBI 1 and PPBI 2. Branched alkyl chains lead to a liquid crystalline state in the case of PPBI 1, PPDEB and PPDEI, whereas PPBI 2 with more flexible OEG groups is an amorphous material. Surprisingly the less ordered PPBI 2 exhibits an electron mobility one order of magnitude higher than that of PPBI 1, even though it is commonly believed that increased order yields better charge transport.  $1 \cdot 10^{-2} \text{ cm}^2 \text{ V}^{-1} \text{ s}^{-1}$  were measured in single carrier devices, which is one of the highest electron mobilities reported for n-type homopolymers by SCLC. To explain these findings, we assume that energetic disorder might be reduced due to the amorphous nature caused by highly flexible OEG chains. Furthermore charge carriers trapped within grain boundaries might account for a lower mobility for PPBI 1 with LC order compared to the amorphous PPBI 2. SCLC measurements demonstrated that both the aromatic perylene core and the nature of solubilizing groups (alkyl or oligoethylenglycol (OEG)) have a major impact on the charge carrier mobilities in perylene side chain polymers.

The following chapters deal with PCBM based electron acceptors, which are another important class of n-type semiconductors for OPV application.

### **Correlation of Charge Carrier Mobilities and Solar Cell Parameters in Polymer:Fullerene Blend Devices**

Chapter 6 describes two bis-adduct fullerene derivatives, bis-PCBM and bis-oQDMC, with higher LUMO energy levels with respect to PCBM (see Figure 7 for chemical structure and energy levels). BHJ solar cells of these fullerenes in combination with a low band gap p-type polymer were prepared. Higher open circuit voltages ( $V_{OC}$ ) could be achieved, compared to the standard PCBM blend, but short circuit current density ( $J_{SC}$ ) was below the reference cells. The aim of this chapter was to explore possible explanations for this behavior and find solutions to overcome these issues. Electron- and hole mobilities of the blends in single carrier devices were measured, the results are summarized in Figure 7c.

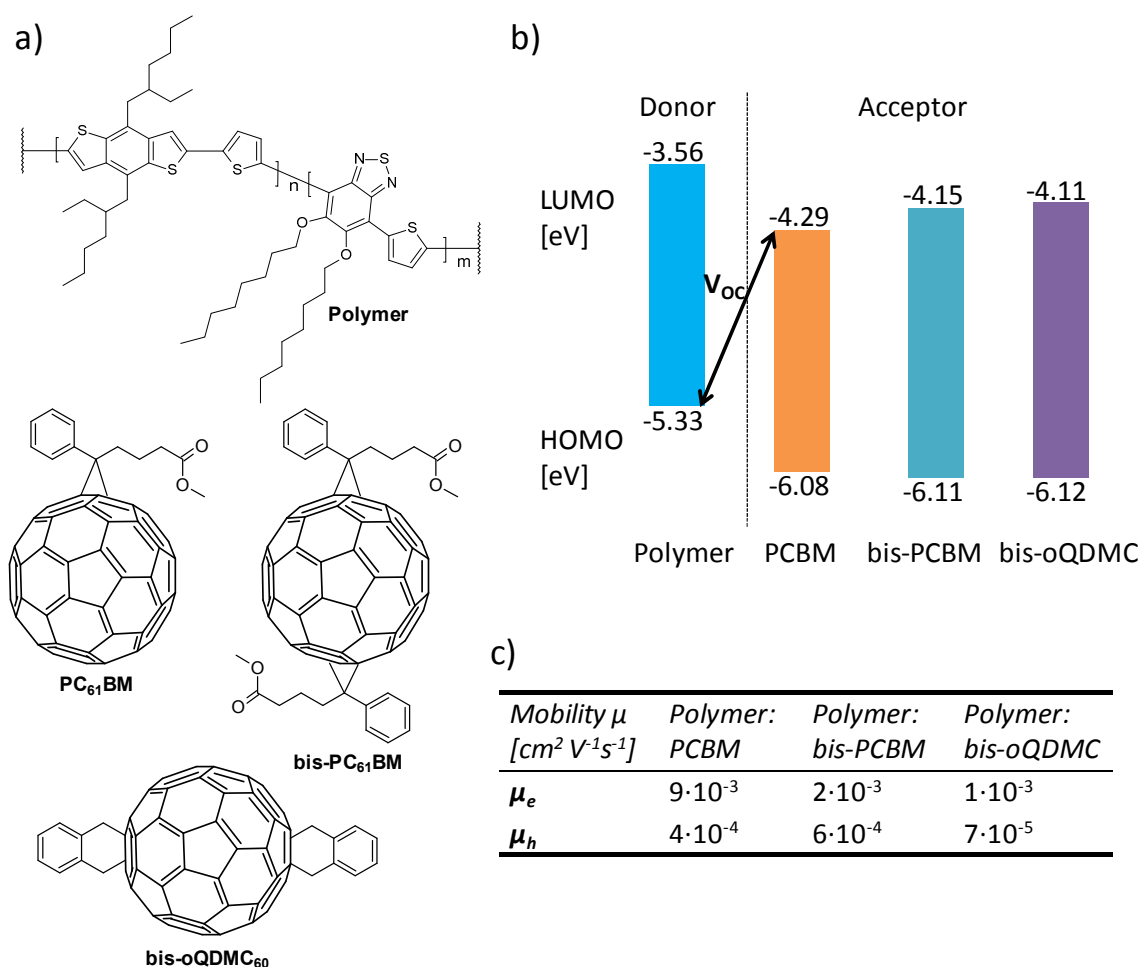


Figure 7: a) Chemical structure of the donor polymer and the acceptor fullerenes and b) energy level diagram of the materials illustrating the linear relation of  $V_{OC}$  and the difference of donor HOMO and acceptor LUMO; c) electron- and hole mobilities ( $\mu_e$  and  $\mu_h$ ) of the Polymer:Fullerene blends measured by SCLC single carrier devices.

For the Polymer:bis-PCBM blend the electron mobility was lower, but hole mobility was comparable with respect to the Polymer:PCBM reference.  $J_{SC}$  and PCE could therefore be improved by reducing the active layer thickness for the Polymer:bis-PCBM blend. In the case of Polymer:bis-oQDMC blend devices, a decrease in both electron and hole mobility was found. Since the hole transporting material was kept the same for all three blend systems, a lower hole mobility can only be explained by a change in the blend morphology with worse percolation paths for holes in this blend, which is supported by AFM images. Here, reducing the active layer thickness did not lead to improved device efficiencies. We showed that using

the SCLC approach in single carrier devices is a practical tool to help understanding and improving solar cell characteristics of Polymer:Fullerene blends.

### **Fullerene-grafted Copolymers exhibiting High Electron Mobility without Nanocrystal Formation**

Even though we demonstrated that optimization of Polymer:Fullerene solar cells, based on mobility and morphology studies, can improve the PCE, the fundamental problem of morphological stability of Polymer:Small molecule blends remains. Often, diffusion and aggregation of PCBM within the blend, which is accelerated by thermal annealing, leads to changes in the blend morphology and hence decreased lifetime of the device. Therefore, morphological stability is highly desired. One possible way of realizing more stable blends is to replace the acceptor small molecules with a polymer, or as the ultimate goal, replacing donor and acceptor blends by fully functionalized donor-acceptor blockcopolymers. In the first instance, a suitable acceptor polymer with similar properties of PCBM needs to be found, which is the subject of this chapter. Herein, the synthesis of well-soluble fullerene-grafted copolymers with varied contents of pendant phenyl-C<sub>61</sub>-butyric acid methyl ester (PCBM) is reported. The chemical structure of PPCBM is shown in Figure 8a. The grafting density of PCBM side chains was changed from 30 wt% (PPCBM-1) to 37 wt% (PPCBM-2) and 51 wt% (PPCBM-3) by using different precursor polymers (PS-OH) with changed monomer ratio. The polymers were synthesized and provided by Martin Hufnagel.

The essential question, whether the optical, electrochemical and charge transport properties of the novel polymers could be maintained with respect to blends of PCBM small molecules, was investigated by means of UV/vis spectroscopy, cyclic voltammetry and SCLC measurements. In addition to that, the morphology of the polymers was investigated by AFM and XRD. No significant changes of PPCBM in comparison with PCBM in absorption profile or HOMO and LUMO energy levels could be detected. I measured the charge carrier mobility of the novel polymers in electron-only devices, using the SCLC approach. The aim was to find out the effect of increasing fullerene content on bulk electron mobility.

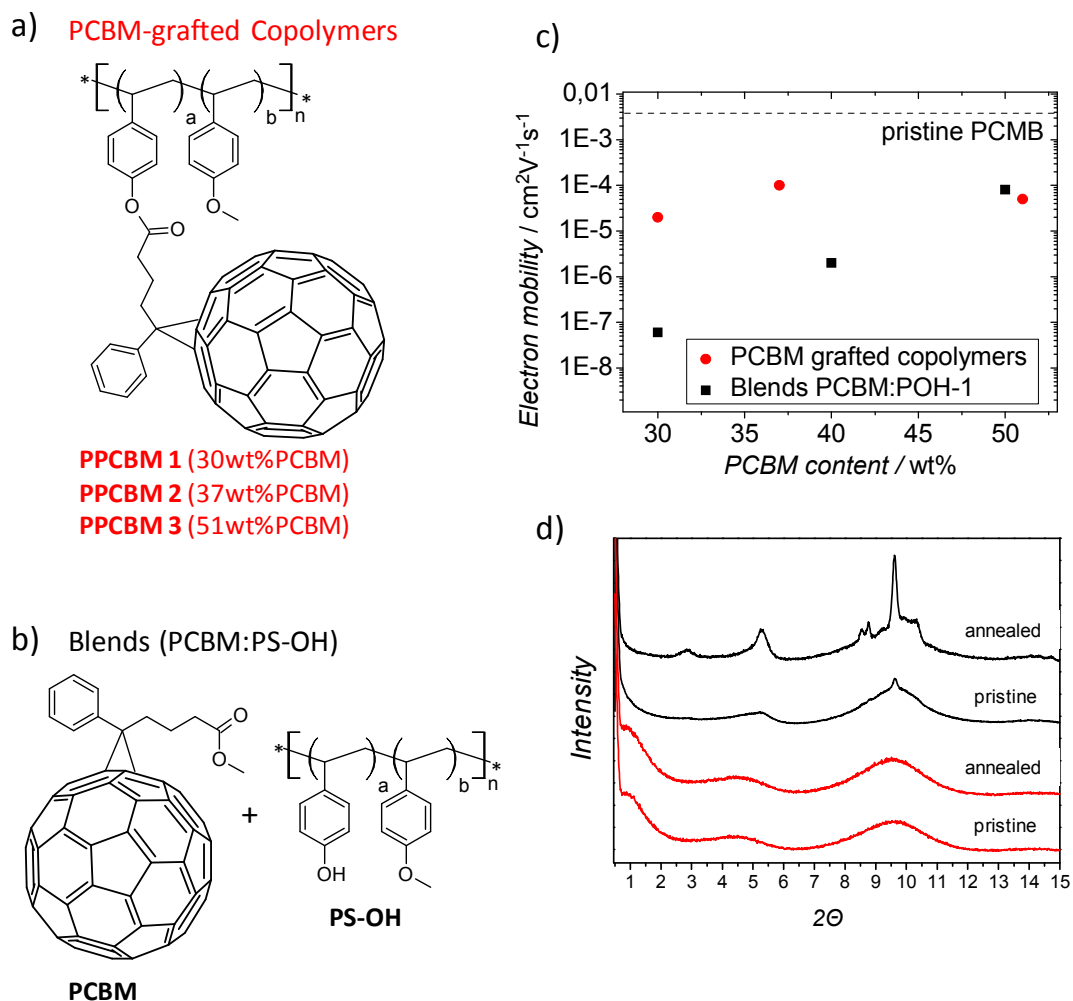


Figure 8: a) Chemical structure of the PCBM-grafted Copolymers PPCBM 1-3 with varied PCBM grafting density and b) of PCBM and the precursor polymer PS-OH; c) electron mobility values obtained from SCLC single carrier devices of the PPCBM 1-3 and the respective PCBM:POH-1 blends, the dashed line represents the electron mobility of pure PCBM; d) powder XRD of PPCBM-2 and the respective blend of PCBM:PS-OH with 50 wt% PCBM; the applied annealing procedure was 3 h at 140 °C.

PPCBM 1-3 were directly compared to blends consisting of PCBM in PS-OH (both shown in Figure 8b). The blends had approximately the same fullerene content as the respective grafted copolymers. The electron mobilities are summarized in Figure 8c. We observed strong differences in electron mobilities of the PCBM-grafted copolymers PPCBM-1, PPCBM-2 and PPCBM-3 compared to the blends. The electron mobility also varies with respect to the PCBM content. In the Polymer:PCBM blends, an exponential increase in electron mobility with increasing PCBM content was observed. At 50 wt% PCBM, the blend

exhibits an electron mobility of  $8 \cdot 10^{-5} \text{ cm}^2 \text{V}^{-1} \text{s}^{-1}$ , which however is almost two orders of magnitude below the mobility of pristine PCBM ( $4 \cdot 10^{-3} \text{ cm}^2 \text{V}^{-1} \text{s}^{-1}$ ). This clearly shows that charge transport is inhibited by the presence of an electronically inactive polymer such as PS-OH. The PCBM-grafted copolymers on the other hand exhibit a different trend of the mobility with increasing fullerene content. Electron mobility is increasing from PPCBM-1 to PPCBM-2 from  $2 \cdot 10^{-5} \text{ cm}^2 \text{V}^{-1} \text{s}^{-1}$  to  $1 \cdot 10^{-4} \text{ cm}^2 \text{V}^{-1} \text{s}^{-1}$  and is slightly lower for PPCBM-3 with  $5 \cdot 10^{-5} \text{ cm}^2 \text{V}^{-1} \text{s}^{-1}$ . Hence, below PCBM contents of 50 % wt, the grafted fullerene polymer features a significantly higher electron mobility than the respective PCBM:PS-OH blend. To understand these findings, I studied the morphology of the films by AFM.

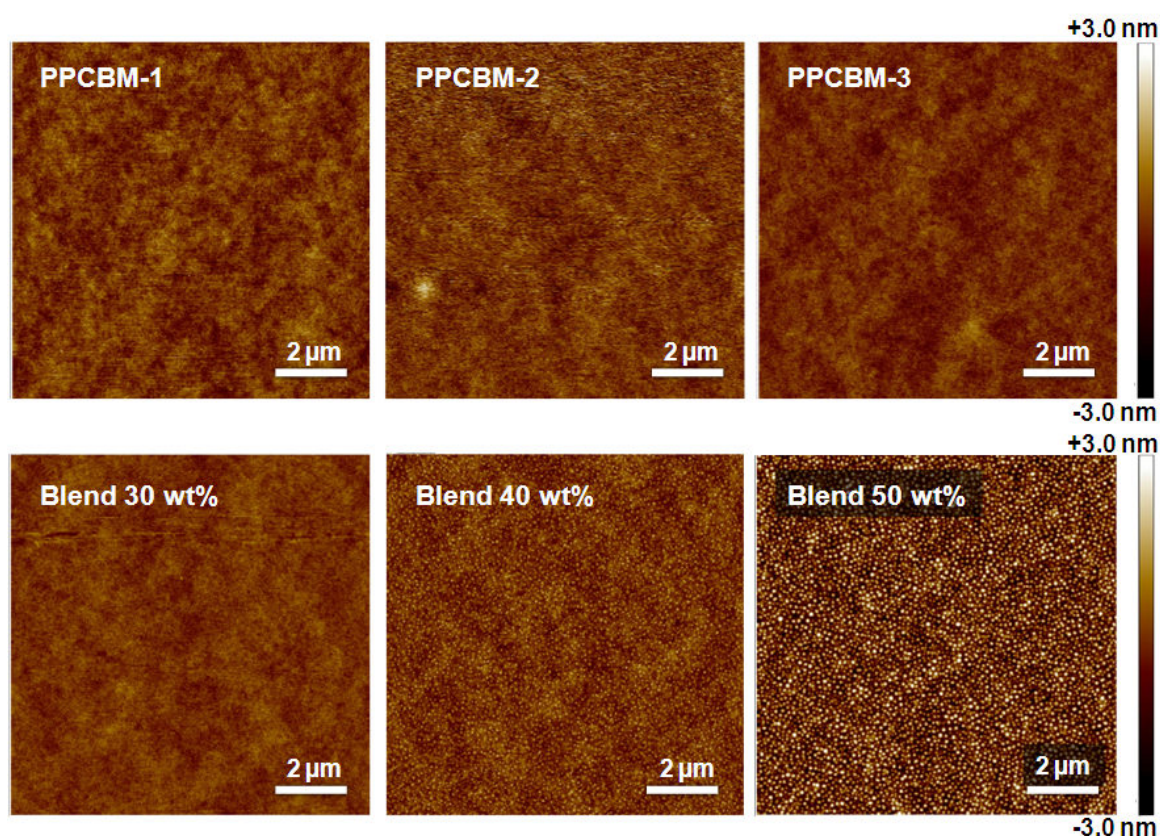


Figure 9: AFM topography images obtained in Tapping Mode for fullerene-grafted polymers PPCBM-1, PPCBM-2, PPCBM-3 and the respective PCBM:PS-OH blends.

AFM topography images, shown in Figure 9 illustrate that the morphology of the Polymer:PCBM blends is mainly dominated by crystallite and aggregate formation of PCBM. Increasing the weight fraction of PCBM leads to growth of both number and size of

the aggregates. On the other hand, all grafted PPCBM films show a smooth and featureless topography, indicating that the incorporation of PCBM in the polymer side chain does effectively suppress the tendency of PCBM to aggregate. This is further supported by XRD measurements (see Figure 8d) where pristine and thermally annealed PPCBM-2 and the Polymer:PCBM 50:50 blend were compared. The Polymer:PCBM blend shows reflections typical for fullerene crystallites within the polymer matrix. Upon annealing the intensity of the reflections increases, which indicates that further PCBM aggregation is promoted by thermal treatment and the initial blend was not in a thermodynamical stable state. On the other hand, the XRD samples of PPCBM-2 do not exhibit any crystalline reflections, the material is therefore considered as amorphous. Thermal annealing above  $T_g$  did not show any influence, which is in line with AFM images and the assumption that the covalent attachment of PCBM to the polymer suppresses the aggregation and crystallization of fullerenes. To the best of our knowledge, these PCBM-grafted copolymers are one of the first examples of fullerene-based polymers with high electron mobility in bulk, which do not show disadvantageous crystallite formation.

### **Annex: Perylene bisimide Blend Solar Cells: Influence of Substituents on Blend Morphology and Device Performance**

This chapter is following up Chapter 3 where perylene bisimide (PBI) small molecules were investigated in terms of their charge transport properties and crystalline structure in thin films. A strong influence of the different side groups attached to the PBI on these properties was found, which encouraged us to study their effect on the blend morphology of BHJ solar cells and device performance. Photovoltaic devices consisting of blends of a low band gap donor copolymer and PBI 1, PBI 2 and PBI 3, respectively, were prepared and characterized. The chemical structures of the PBI acceptors and the donor polymer are depicted in Figure 10a, the  $J-V$  characteristics of the three blends are given in Figure 10b. The blend morphology was investigated by AFM. The nature of the side chains is found to have a major impact on blend morphology (see AFM topography images in Figure 10c-e) and device performance. The topography of the Polymer:PBI 1 blend was smooth and featureless (Figure 10c).

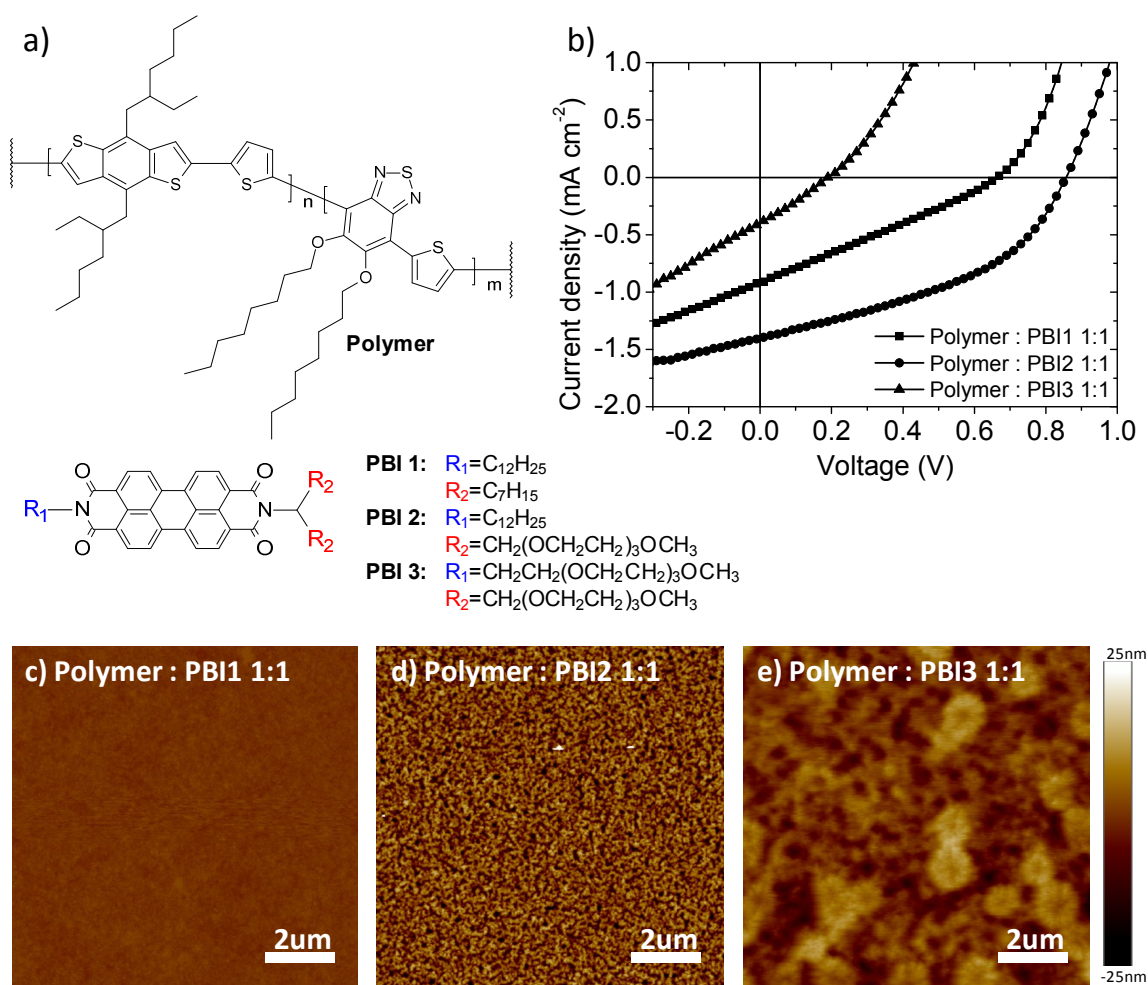


Figure 10: a) Chemical structure of the donor polymer and the three perylene bisimides (PBI); b) J-V characteristics of representative solar cells devices made of the three blends illuminated under AM1.5 (1sun); AFM Topography images recorded in Tapping Mode of a Polymer:PBI 1 blend (c), Polymer:PBI 2 blend (d) and Polymer:PBI 3 blend (e).

Both PBI 1 and the polymer possess alkyl chains as solubilizing groups, which resulted in a high miscibility of the two compounds and a highly intermixed blend system after drying of the film. The power conversion efficiency (PCE) was 0.19 %. On the other hand, for PBI 3 featuring exclusively OEG blend, a rough topography was observed (Figure 10e). Interactions of hydrophilic OEG and hydrophobic alkyl chain caused strongly phase separated domains of PBI and Polymer. PCE in this blend system was only 0.02 %. Hence, recombination losses, caused by the macroscopic phase separated morphology are limiting the device performance. PBI 2 with both alkyl and OEG groups gives a moderate phase

separated blend morphology (Figure 10d) and clearly outperforms the other PBI derivatives in solar cell devices with a PCE of 0.51 %.

An optimization of the Polymer:PBI 2 blend ratio was carried out. A PCE of 0.60 % was achieved for the Polymer:PBI2 1:1.5 blend ratio. AFM images show that the morphology of these blends is dominated by PBI 2 aggregation because surface roughness increased with increasing PBI content. We demonstrated a successful approach for tuning the morphology of OPV blends via hydrophobic-hydrophilic interactions of donor and acceptor parts by altering *N*-substituents of PBIs. Even though optical and charge transport properties of the PBIs are similar, device performance is crucially determined by blend morphology in OPV.

Based on these results, future research is directed towards determining the dominant loss mechanism in these devices by means of time resolved spectroscopy.

### Individual contributions to joint publications

The individual contributions of the authors to each manuscript are specified below.

### Chapter 3

This manuscript is prepared for submission with the title:

“Unsymmetrical Perylene Bisimides: Influence of Substituents on Crystal Structure and Electron Transport”

by **Mathis-Andreas Muth**, Gaurav Kumar Gupta, André Wicklein, Helga Wietasch, Thomas Thurn-Albrecht, Miguel Carrasco-Orozco and Mukundan Thelakkat.

I carried out the SCLC charge transport measurements, performed the characterization of the thin films by means of atomic force microscopy, UV/vis spectroscopy, photoluminescence spectroscopy and polarized optical microscopy and wrote the manuscript.

Gaurav Kumar Gupta performed the structural characterization of the materials and thin films by X-ray diffraction experiments and differential scanning calorimetry, was involved in the scientific discussion and wrote the X-ray diffraction paragraph.

André Wicklein and Helga Wietasch synthesized compounds PBI 1, PBI 2 and PBI 3 and the symmetrical PBI.

Mukundan Thelakkat, Miguel Carrasco-Orozco and Thomas Thurn-Albrecht supervised the project, were involved in the scientific discussion and corrected the manuscript.

## Chapter 4

This work is published in *Advanced Functional Materials* (2011, 21, 4510-4518) with the title:

“Liquid-Crystalline Perylene Diester Polymers with Tunable Charge-Carrier Mobility”

by **Mathis-Andreas Muth**, Miguel Carrasco-Orozco and Mukundan Thelakkat

I synthesized and characterized the polymers, did the SCLC charge transport measurements, thermal and optical characterization and wrote the manuscript.

Miguel Carrasco-Orozco and Mukundan Thelakkat supervised the project, were involved in the scientific discussion and corrected the manuscript.

## Chapter 5

This manuscript is published in *Journal of Polymer Science: Polymer Physics* (DOI: 10.1002/polb.23357) with the title:

“Pendant Perylene Polymers with High Electron Mobility”

by Andreas S. Lang, **Mathis-Andreas Muth**, Miguel Carrasco-Orozco and Mukundan Thelakkat

I performed the SCLC charge transport measurements, characterized the polymers by means of cyclic voltammetry, polarized optical microscopy, photoluminescence spectroscopy, wrote the manuscript.

Andreas S. Lang synthesized and characterized the polymers by means of SEC, DSC, TGA, XRD and UV/vis spectroscopy and was involved in the scientific discussion.

Miguel Carrasco-Orozco and Mukundan Thelakkat supervised the project, were involved in the scientific discussion and corrected the manuscript.

## Chapter 6

This manuscript is accepted in *Nanotechnology* with the title:

“Correlation of Charge Carrier Mobilities and Solar Cell Parameters in Polymer:Fullerene Blend Devices”

by **Mathis-Andreas Muth**, William Mitchell, Steven Tierney, Miguel Carrasco-Orozco and Mukundan Thelakkat

I carried out the SCLC charge transport measurements, characterized the blend films by means of UV/vis spectroscopy and AFM, prepared and characterized the solar cell devices and wrote the manuscript.

William Mitchell and Steven Tierney synthesized the polymer.

Mukundan Thelakkat and Miguel Carrasco-Orozco supervised the project, were involved in the scientific discussion and corrected the manuscript.

## Chapter 7

This manuscript is prepared for submission with the title:

“Fullerene-grafted Copolymers exhibiting High Electron Mobility without Nanocrystal Formation”

by Martin Hufnagel, **Mathis-Andreas Muth**, Johannes C. Brendel and Mukundan Thelakkat

I performed the SCLC charge transport measurements, characterized the thin films by AFM, carried out the SEC measurements and was involved in the scientific discussions.

Martin Hufnagel synthesized and characterized the polymers, performed DSC, TGA, UV/vis spectroscopy, X-ray diffraction experiments, cyclic voltammetry and wrote the manuscript.

Johannes C. Brendel was involved in the scientific discussion.

Mukundan Thelakkat supervised the project, was involved in the scientific discussion and corrected the manuscript.

## Chaper 8: Annex

This manuscript is prepared as a basis for further investigations with the title:

“Perylene bisimide Blend Solar Cells: Influence of Substituents on Blend Morphology and Device Performance”

by **Mathis-Andreas Muth**, André Wicklein, Helga Wietasch, William Mitchell, Steven Tierney, Miguel Carrasco-Orozco and Mukundan Thelakkat

I carried out the SCLC charge transport measurements, characterized the blend films by means of UV/vis spectroscopy and AFM, prepared and characterized the solar cell devices and wrote the manuscript.

André Wicklein and Helga Wietasch synthesized compounds PBI 1, PBI 2 and PBI 3 and the symmetrical PBI.

William Mitchell and Steven Tierney synthesized the polymer.

Mukundan Thelakkat and Miguel Carrasco-Orozco supervised the project, were involved in the scientific discussion and corrected the manuscript.

## References:

- (1) Howard, I. A.; Laquai, F. d. r.; Keivanidis, P. E.; Friend, R. H.; Greenham, N. C. *The Journal of Physical Chemistry C*, 2009, **113**, 21225.



### **3. Unsymmetrical Perylene bisimides: Influence of Substituents on Crystal Structure and Electron Transport**

*Mathis-Andreas Muth<sup>a,c</sup>, Gaurav Kumar Gupta<sup>b</sup>, André Wicklein<sup>a</sup>, Helga Wietasch<sup>a</sup>, Thomas Thurn-Albrecht<sup>b</sup>, Miguel Carrasco-Orozco<sup>c</sup> and Mukundan Thelakkat<sup>a\*</sup>*

[a] Prof. Dr. Mukundan Thelakkat, Applied Functional Polymers, Department of Macromolecular Chemistry I, University of Bayreuth, Universitaetsstr.30, 95440 Bayreuth (Germany)

[b] Prof. Dr. Thomas Thurn-Albrecht, Experimental Polymer Physics, Department of Physics, Martin-Luther University Halle-Wittenberg, Von-Danckelmann-Platz 3, 06120 Halle (Germany)

[c] Dr. Miguel Carrasco-Orozco, Merck Chemicals Ltd., Chilworth Technical Centre, University Parkway, Southampton SO16 7QD (UK)

\*corresponding author: [mukundan.thelakkat@uni-bayreuth.de](mailto:mukundan.thelakkat@uni-bayreuth.de)

This manuscript is prepared for submission.

## Abstract

Three solution processable n-type semiconducting Perylene bisimides PBI 1, PBI 2 and PBI 3 are evaluated in terms of their charge transport properties, morphology and crystal structure. All compounds have an unsymmetrical substitution pattern at the imide positions, which influences the aggregation in thin films significantly. The nature of the substituents is varied from hydrophobic alkyl chains to hydrophilic oligoethylenglycol (OEG) chains to control intermolecular interactions and to tune self-assembly properties of the compounds. In this paper, structure formation, crystallinity and morphology of PBI thin films are studied by polarized optical microscopy, UV/vis and photoluminescence spectroscopy, X-ray diffraction (XRD) and atomic force microscopy (AFM). A correlation of structure and morphology with charge transport properties obtained from space-charge limited current (SCLC) measurements is attempted. Bulk XRD data are indicative for a lamella-columnar packing motif in the case of PBI 1 and PBI 3 and a columnar hexagonal packing for PBI 2. Further, OEG chains help reducing the  $\pi$ - $\pi$  stacking distance of the perylene cores, which correlates with higher charge carrier mobilities of these PBI derivatives. XRD data on thin films give evidence for a highly ordered packing of the molecules after an annealing step with the dominant orientation axis  $a$  perpendicular and the  $\pi$ - $\pi$  stacking direction parallel to the substrate (“edge-on”). An increase in crystallinity of the annealed films compared to the pristine films was found for all PBIs, especially for compounds featuring OEG substituents (PBI 2 and PBI 3). Electron mobilities of as high as  $6 \cdot 10^{-3} \text{ cm}^2 \text{ V}^{-1} \text{ s}^{-1}$  and  $7 \cdot 10^{-3} \text{ cm}^2 \text{ V}^{-1} \text{ s}^{-1}$  were measured for PBI 2 and PBI 3 featuring OEG side chains, which is more than two orders of magnitude higher than for PBI 1.

## Introduction

Over the last decades, the use of Perylene tetracarboxylic acid bisimide, abbreviated as Perylene bisimide or PBI in the following, in optoelectronic devices has become a subject of extensive research. Applications involve xerographic devices,<sup>1</sup> organic field effect transistors (OFETs),<sup>2-4</sup> and organic photovoltaic cells (OPV).<sup>5-7</sup> The relatively high electron affinity and strong visible light absorption, combined with good photochemical and thermal stability

make PBI related derivatives an important class of n-type semiconductors.<sup>8</sup> Especially solution processable PBIs are of great interest because of their potential for large area film casting or printing of blends.<sup>9</sup> PBIs can be modified by attaching solubilizing groups either at the bay or ortho positions of the perylene or at the imide nitrogen atoms. An overview about differently substituted perylene derivatives is given by Li *et al.*<sup>10</sup> Substituents at the bay and ortho positions can alter not only the solubility, but also electronic properties and absorption spectra of the perylenes.<sup>11</sup> In contrast, *N*-substitution generally results in PBI derivatives with similar optical properties and energy levels. By introducing long or branched alkyl groups at the imide positions, PBIs with excellent solubility in common organic solvents like chloroform, THF, acetone, etc. can be obtained. The nature of these substituents has been found to play a crucial role for the self-assembly properties of PBIs.<sup>12</sup> In general, the driving force for self-assembly, aggregation and crystallization of PBI molecules is the strong  $\pi$ - $\pi$  interaction of the aromatic perylene cores. Bulky or small side groups attached to the perylene can either hinder or promote  $\pi$ - $\pi$  stacking. Thus, substituents have both an effect on the intermolecular interaction and the solvent-molecule interaction and are therefore are a powerful tool to tune aggregation of PBIs. Using this approach, the self-assembly of symmetrically substituted PBIs with linear and branched alkyl chains could be controlled to achieve various one- and two dimensional morphologies.<sup>13</sup> Furthermore, the formation of nanobelt and nanosphere morphologies for similar PBIs carrying linear and branched alkyl chains respectively, was reported.<sup>12</sup> When replacing alkyl substituents with ethylenglycol groups, stacking angle as well as phase behavior of the PBI molecules can be modified.<sup>14</sup> This is attributed to the increased motion of PBI cores due to the highly flexible ethylenglycol side chains. We reported recently a series of *N*-substituted PBIs carrying branched “swallow-tail” oligoethylenglycol (OEG) and alkyl chains.<sup>15</sup> Therein, a systematic study on the influence of side chains on thermotropic behavior was presented. By combining specific branched OEG and alkyl substituents, we were able to obtain liquid crystalline (LC) PBIs and control the thermal properties of these columnar hexagonal mesophases. In other words, the inherent tendency of PBI molecules to strongly crystallize could be suppressed by substituting alkyl with certain OEG substituents. In optoelectronic applications like organic photovoltaic cells, the high crystallinity of perylene compounds usually results in unfavorable blend morphologies of large domains sizes and poor device efficiencies.

Therefore, the use of perylene in OPV is still limited even though the fundamental steps of charge transfer in combination with various polymers is excellent.<sup>16, 17</sup> On the other hand, crystallinity and long range structural order are generally believed to enhance fundamental properties of organic semiconductors like exciton diffusion length and charge carrier mobility.<sup>18</sup>

Here, we investigate structure-property relations of a series of unsymmetrical *N*-substituted PBI compounds with linear side chains at one imide *N*-atom, and a “swallow-tail” substituent at the other imide nitrogen. The nature of the side groups is systematically changed from hydrophobic alkyl to hydrophilic OEG chains. By avoiding any bay substitution at the perylene core, changes in optical and electronic properties can exclusively be attributed to aggregation effects caused by the side chains. Electron mobilities of these materials are correlated with molecular arrangement and structural features in thin films.

## Results and Discussion

We studied the structural and electronic properties of three unsymmetrical *N*-substituted Perylene bisimides PBI 1, PBI 2 and PBI 3, where the nature of the solubilizing side chains is varied from hydrophobic alkyl to hydrophilic oligoethylenglycol (OEG). The molecular structures are depicted in Figure 1. All compounds possess one linear side chain and one branched “swallow-tail” substituent. This unsymmetrical substitution pattern can help reducing excessive crystallization in thin films, compared to a symmetrical analogue (see Supporting Information Figure S1 for more details). PBI 1 comprises a C-12 alkyl and a C-15 “swallow-tail” alkyl chain attached to the perylene core. For PBI 2, the branched substituent consists of a hydrophilic C-17 “swallow-tail” OEG chain. PBI 3 possesses both linear and branched OEG substituents. We described the synthesis and thermal characterization of PBI 2 in detail earlier.<sup>15</sup> PBI 1 and PBI 3 were synthesized analogously, the DSC data can be found as Supporting Information in Figure S2 and Table S1. DSC measurements indicate that all three compounds are crystalline. A more detailed investigation is given in the XRD section of this paper. The melting temperatures of PBI 1, PBI 2 and PBI 3 are 181 °C, 140 °C and 165 °C, respectively.

Thin films of the PBI compounds were deposited with a doctor blading technique from chloroform solutions. Due to the fast evaporation rate of this low boiling point solvent, the thin film morphology is possibly not in a thermodynamical equilibrium state. To allow for better packing and orientation whilst keeping the quality of the films intact, all films were thermally annealed for 5 min below  $T_m$  (PBI 1 at 176 °C, PBI 2 at 135 °C and PBI 3 at 160 °C). The following measurements were carried out before and after the annealing step.

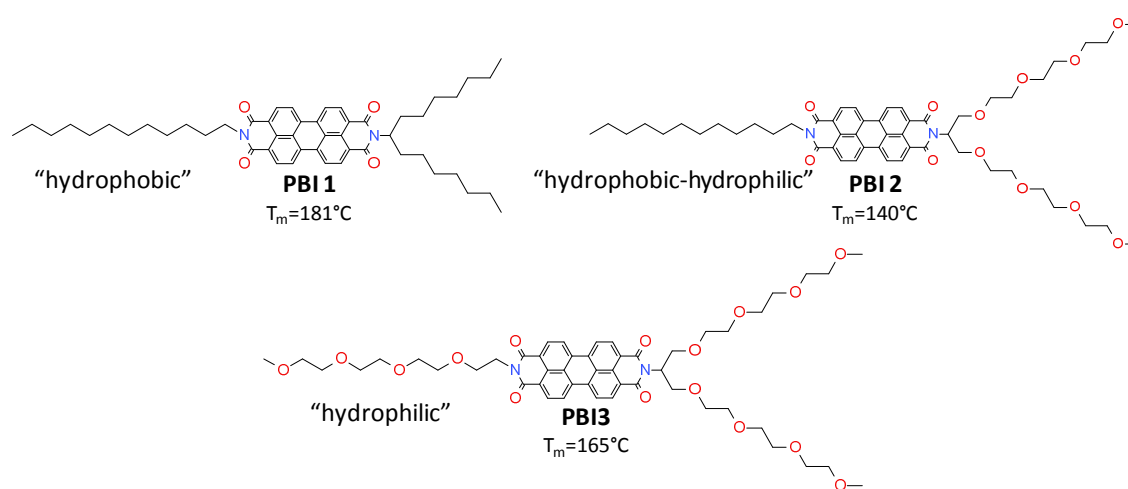


Figure 1: Structure formula and melting temperatures (obtained from DSC measurements) of PBI 1, PBI 2 and PBI 3.

### Charge transport of PBI thin films

An important figure of merit for semiconductors is the charge carrier mobility. The electron mobility of PBI 1, PBI 2 and PBI 3 was studied by using the space-charge limited current (SCLC) method. According to a procedure published recently,<sup>19</sup> the following device structure was used to estimate the bulk electron mobility of the compounds. The semiconducting PBIs were sandwiched between an electron injecting calcium electrode and an ITO/PEDOT:PSS bottom contact. The current density – voltage ( $J$ - $V$ ) characteristics were recorded under inert gas atmosphere in the dark. At high voltages ohmic injecting contacts and trap free transport can be assumed and the current measured is space-charge limited only. The charge carrier mobility can be estimated by using Mott-Gurney's equation:<sup>20</sup>

$$J = \frac{9}{8} \varepsilon_r \varepsilon_0 \mu \frac{V^2}{L^3}$$

where  $J$  is the current density,  $\varepsilon_r$  is the dielectric constant of the organic semiconductor (assumed to be 3 in our calculations<sup>21</sup>),  $\varepsilon_0$  is the permittivity of free space,  $\mu$  is the charge carrier mobility,  $L$  is the thickness of the active layer and  $V$  is the voltage drop across the device. It is well known, that PBIs are good n-type materials.<sup>4</sup> Thus, electrons transported via the LUMO are assumed to be the majority charge carriers in these devices and the resulting mobility values are electron mobilities ( $\mu_e$ ).  $J$ - $V$  characteristics of pristine and annealed films of PBI 1, PBI 2 and PBI 3 with an active layer thickness of ca. 300 nm are shown in Figure 2. As discussed above, the annealing step was performed for 5 min at temperatures 5 °C below the compounds' melting temperature in inert gas atmosphere. To check the thickness scaling of the space-charge limited currents,  $J$ - $V$  curves across various active layer thicknesses were recorded, which are given as supporting information in Figure S3. The electron mobilities of the pristine and thermally annealed films of the three PBIs are summarized in Table 1. All pristine devices exhibit electron mobilities  $\mu_e$  in the range of  $10^{-5} \text{ cm}^2 \text{V}^{-1} \text{s}^{-1}$ , with  $\mu_e$  (PBI 3) =  $6 \cdot 10^{-5} \text{ cm}^2 \text{V}^{-1} \text{s}^{-1}$  being the highest. After annealing however, drastic changes in  $\mu_e$  can be observed for the three compounds under investigation. A fourfold drop in  $\mu_e$  to  $8 \cdot 10^{-6} \text{ cm}^2 \text{V}^{-1} \text{s}^{-1}$  of PBI 1 with two alkyl chain substituents was measured. On the other hand,  $\mu_e$  of PBI 2 and PBI 3 bearing OEG side groups were improved by over two orders of magnitude to  $6 \cdot 10^{-3} \text{ cm}^2 \text{V}^{-1} \text{s}^{-1}$  and  $7 \cdot 10^{-3} \text{ cm}^2 \text{V}^{-1} \text{s}^{-1}$ , respectively.

Table 1: Electron mobilities  $\mu_e$  of pristine and annealed films of PBI 1, PBI 2 and PBI 3, determined by the SCLC method; the values reported represent an average over varied active layer thicknesses  $L$ .

<i>Compound</i>	<i>Pristine Films</i> <i>Electron mobility <math>\mu_e</math></i>	<i>Annealed Films</i> <i>Electron mobility <math>\mu_e</math></i>
<b>PBI 1</b>	$3 \cdot 10^{-5} \text{ cm}^2 \text{V}^{-1} \text{s}^{-1}$	$8 \cdot 10^{-6} \text{ cm}^2 \text{V}^{-1} \text{s}^{-1}$
<b>PBI 2</b>	$2 \cdot 10^{-5} \text{ cm}^2 \text{V}^{-1} \text{s}^{-1}$	$6 \cdot 10^{-3} \text{ cm}^2 \text{V}^{-1} \text{s}^{-1}$
<b>PBI 3</b>	$6 \cdot 10^{-5} \text{ cm}^2 \text{V}^{-1} \text{s}^{-1}$	$7 \cdot 10^{-3} \text{ cm}^2 \text{V}^{-1} \text{s}^{-1}$

These findings indicate that upon annealing, a reorientation of the molecules in the film might take place, which is beneficial for charge transport only in the case of PBI 2 and PBI 3 with OEG substituents. Differences in bulk electron mobility can be expected depending on the orientation and morphology of the molecules. In the following, structural features of the PBIs in thin films shall be investigated in order to understand the charge transport properties.

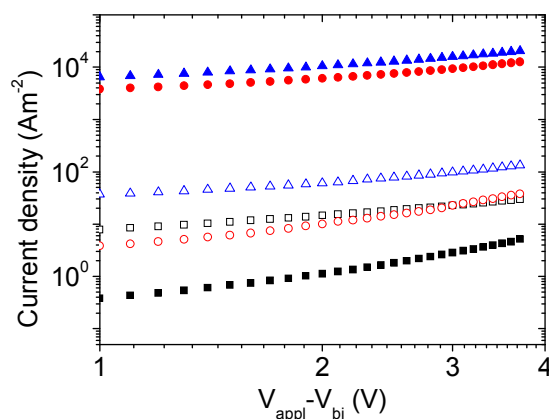


Figure 2: Current density-voltage ( $J$ - $V$ ) characteristics of electron-only devices before (empty symbols) and after annealing (filled symbols) of PBI 1 (black squares), PBI 2 (red circles) and PBI 3 (blue triangles); the active layer thickness  $L$  is ca. 300 nm; annealing was carried out for 5 min at 176 °C (PBI 1), 135 °C (PBI 2) and 160 °C (PBI 3), which is 5 °C below the materials' respective melting temperature; the voltage applied ( $V_{\text{appl}}$ ) was corrected for a built in potential ( $V_{\text{bi}}$ ) of 2.2 eV resulting from the differences in work function of calcium and ITO/PEDOT:PSS.

### Optical properties of PBI thin films

UV/vis and photoluminescence (PL) spectroscopy of PBI 1, PBI 2 and PBI 3 were carried out to probe the influence of thermal annealing on molecular stacking and aggregation in thin films. Thin films (100 nm) on quartz glass substrates were prepared similarly to the SCLC devices. A comparison of thin film and solution absorption spectra of all three compounds is shown in Figure 3a. It is evident that in diluted chloroform solution ( $c=10^{-5} \text{ mol}\cdot\text{L}^{-1}$ ), where the intermolecular interactions are considered to be low, the absorption pattern is very similar to characteristic non aggregated PBI species.

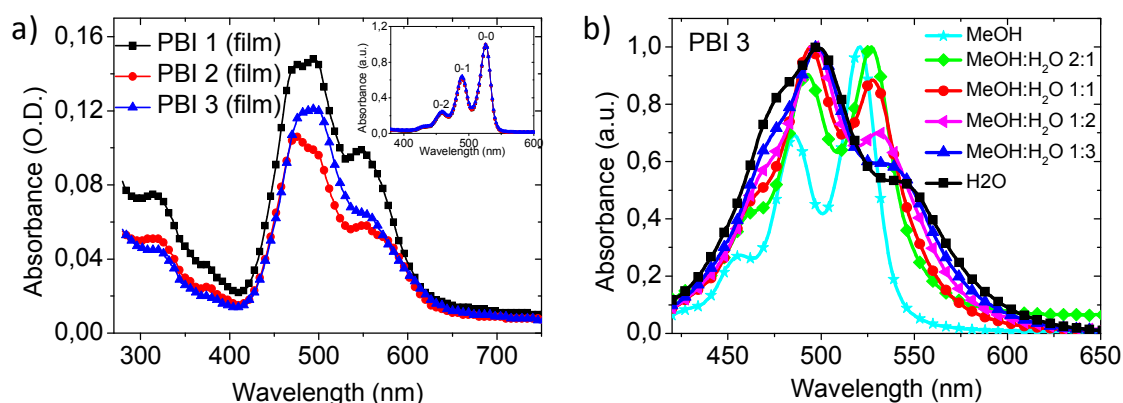


Figure 3: a) UV/vis spectra of thin films of PBI 1 (black squares), 2 (red circles) and 3 (blue triangles) coated on quartz glass from 10 mg/mL chloroform solutions; the inset shows the normalized absorption spectra of the three compounds in chloroform solution ( $c=10^{-5} \text{ mol L}^{-1}$ ); b) UV/vis spectra of PBI 3 in different methanol:water (MeOH:H<sub>2</sub>O) ratios demonstrating that the vibronic bands are redshifted with increasing water content due to the increasing presence of aggregated species; while the intensity of the (0-0) band decreases, both intensities of (0-1) and (0-2) band increase.

Hence, the different *N*-substituents have no influence on the optical properties. Three prominent absorption peaks arising from the  $S_0 \rightarrow S_1$  electronic transitions and its vibronic overtones,<sup>22, 23</sup> are observed. The peaks are labeled as the (0-0), (0-1) and (0-2) transitions at 526 nm, 490 nm and 460 nm, (see inset Figure 3a) respectively. The absorption spectra of all three compounds in thin films are clearly different to the molecular absorption in solution. A broadening of the spectra and a loss of fine structure can be observed. To assign the absorption bands in the thin films, Figure 3b is taken into account, where the absorption pattern of the water soluble PBI 3 is shown in varied methanol:water (MeOH:H<sub>2</sub>O) mixtures ( $c=10^{-5} \text{ mol L}^{-1}$ ). With increasing water content, the aggregation of PBI 3 molecules increases. As a result, the (0-0) band is red shifted and loses intensity. At the same time, both (0-1) and (0-2) band are also red shifted, but feature increasing intensity. At a water content of 100%, PBI 3 molecules are highly aggregated and the absorption spectrum resembles the thin film spectrum in Figure 3a. Similar aggregation effects are assumed for PBI 1 and PBI 2. Thus we assign the peaks of the PBI 1 thin film in Figure 3a to the (0-0) band at 550 nm, the (0-1) band at 496 nm and the (0-2) band at 476 nm. For PBI 2 and PBI 3 the peaks are located similar at 552 nm (0-0), 495 nm (0-1), 470 nm and 480 nm (0-2), respectively. These findings indicate strong molecular packing and  $\pi$ - $\pi$  interaction of the

perylene moieties.<sup>24</sup> The evolution of the absorption pattern of these films upon thermal annealing is depicted in Figure 4a-c. For all PBI derivatives, annealing leads to an increase of the intensity of the (0-2) transitions, compared to the (0-1) transition, which can be explained by an increase in aggregate-to-monomer ratio.<sup>25</sup> The absorption peaks of the films after annealing are located at 468 nm (PBI 1), 472 nm (PBI 2) and 478 nm (PBI 3). UV/vis spectra of the PBI films reveal notable changes in intermolecular interactions for each compound before and after annealing, compared to the solution spectra.

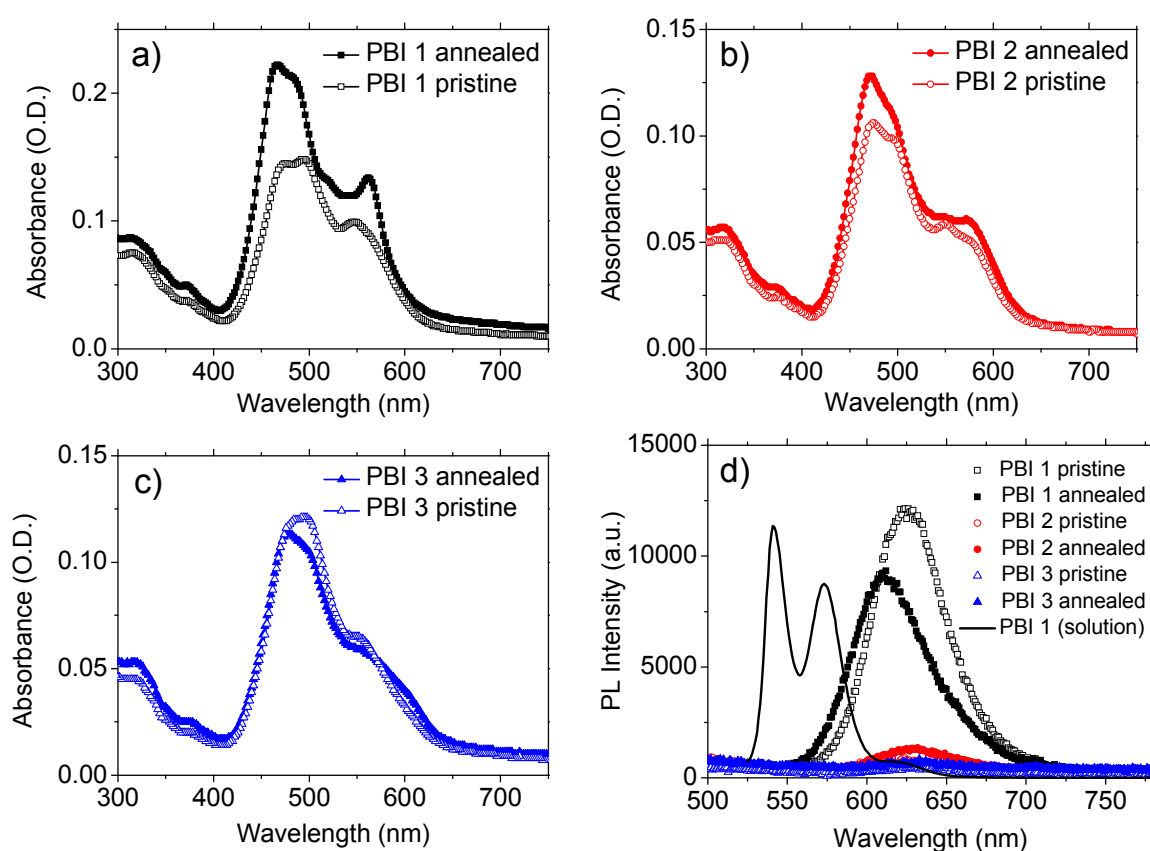


Figure 4: a-c) UV/vis and d) photoluminescence (PL) spectra ( $\lambda_{ex}=525$  nm) of pristine and annealed films of PBI 1, PBI 2 and PBI 3; annealing was carried out for 5 min at 176 °C (PBI 1), 135 °C (PBI 2) and 160 °C (PBI 3), which is 5 °C below the materials' respective melting temperature.

Steady state photoluminescence (PL) spectra of the pristine and annealed films of PBI 1, PBI 2 and PBI 3 are shown in Figure 4d, with an excitation wavelength of  $\lambda_{ex}=525$  nm. For comparison, the solid line in Figure 4d represents the solution PL spectrum of PBI 1 (since

all PBIs exhibit very similar PL spectra in solution, the PBI 1 spectrum in chloroform is shown as a typical example). Here, only films of PBI 1 show notable PL intensity with broad and structureless spectra, which can be attributed to charge transfer (CT) or excimer emission as per literature.<sup>26, 27</sup> The emission peak of the pristine film is at 625 nm, whereas in the annealed film it is blue shifted with a lower intensity compared to the pristine film and peaks at 611 nm, which is an indication of H-aggregates. Since almost no PL was detected for PBI 2 and PBI 3, non-radiative losses seem to be preferred in these films. These findings demonstrate that the packing behavior of the three PBIs under investigation are different. The almost complete PL quenching of PBI 2 and PBI 3 films suggest better packing of the perylene cores in thin films, which can lead to a more efficient electron transport process.<sup>11</sup> Good packing due to  $\pi$ - $\pi$  interaction is believed to be beneficial for charge transport, which is in agreement with the considerably higher electron mobilities found for PBI 2 and PBI 3, compared to PBI 1. The morphology of these films is investigated in the following sections.

### **Morphology of PBI thin films**

#### *Polarized Optical Microscopy*

Polarized optical microscopy (POM) images of the perylene films (with crossed polarizers) are shown in Figure 5a-f. The pristine films of PBI 1 and PBI 2 in Figure 5a and b do not show birefringent textures, indicating a rather amorphous state of the molecules after film formation. In contrast, the PBI 3 film in its pristine state exhibits small crystallites, as birefringence can be observed in POM (Figure 5c). After annealing, a strong increase in crystallites as indicated by birefringence in POM can be observed for all three compounds, which is illustrated in Figure 5d-f. Polycrystalline textures with grain sizes in the range of 10  $\mu\text{m}$  are visible for PBI 2 and PBI 3, whereas the crystallites of the PBI 1 film appear slightly smaller and less uniform.

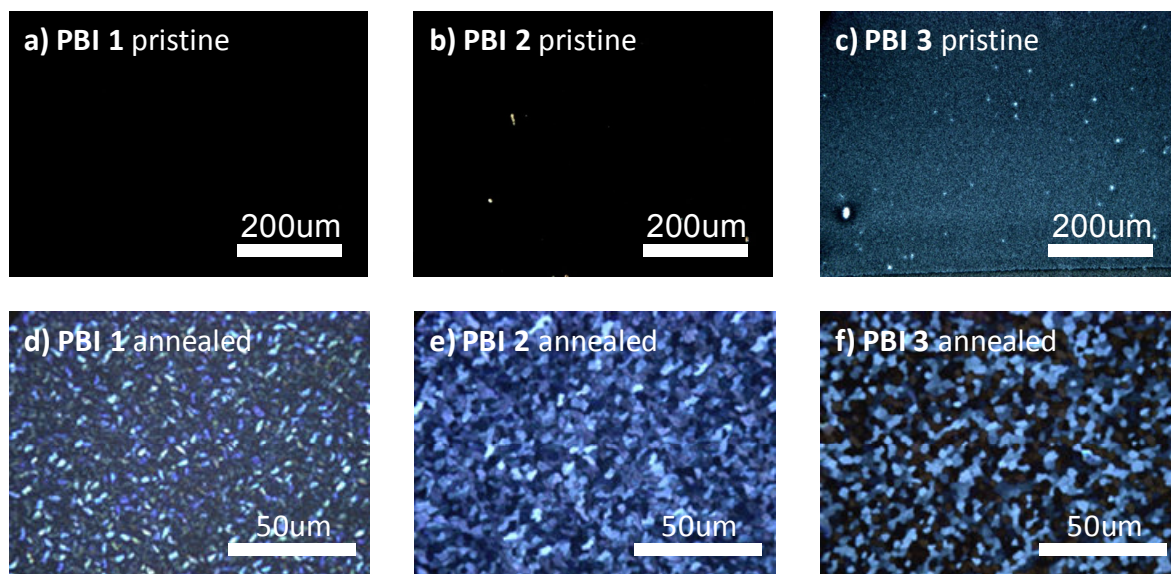


Figure 5: Polarized optical microscopy images (polarizers crossed) of the pristine PBI thin films (a-c) and after annealing for 5 min at 176 °C (d), 135 °C (e) and 160 °C (f).

#### Atomic Force Microscopy (AFM)

To investigate the nanoscale morphology, atomic force microscopy (AFM) on pristine and annealed PBI films was performed in Tapping Mode. Topography images are shown in Figure 6. The pristine films have a RMS roughness of 2.5 nm (PBI 1, Figure 6a), 3.9 nm (PBI 2, Figure 6b) and 1.6 nm (PBI 3, Figure 6c) and show a rather featureless surface. Upon thermal annealing, morphology of all three films changes considerably. The formation of crystallites composed of flat terraces is observed. Especially for PBI 2 (Figure 6e), the terraces are remarkably large, smooth and exhibit abrupt steps with a well defined depth of ca. 3 nm (see Figure S4 in Supporting Information for a cross section). This is an indication of highly ordered molecular packing within the film.<sup>13</sup> Further interpretation and a proposed packing motif for the PBIs, supported by detailed XRD measurements are presented in the next section of this paper. The RMS roughness of the annealed PBI 2 film is 1.1 nm, which is over three times smoother compared to the pristine film. Again, this demonstrates that a short thermal annealing step of 5 min below the melting temperature can induce a severe reorientation of the molecules towards uniform crystal growth. For PBI 3, the RMS

roughness increases to 3.1 nm after the annealing step (Figure 6f). This can also be explained by crystal growth, however in comparison to PBI 2, the crystals growth is more anisotropic, and therefore the initially smooth pristine film becomes rougher. Also, for PBI 1, the AFM image in Figure 6d indicates an increased crystallinity after annealing. The RMS roughness measured here is 2.4 nm and does not change significantly. AFM measurements of these thin films give valuable information about ordered domains and morphology on the surface. For a better understanding of the bulk morphology, XRD experiments were carried out, which is described in the next section.

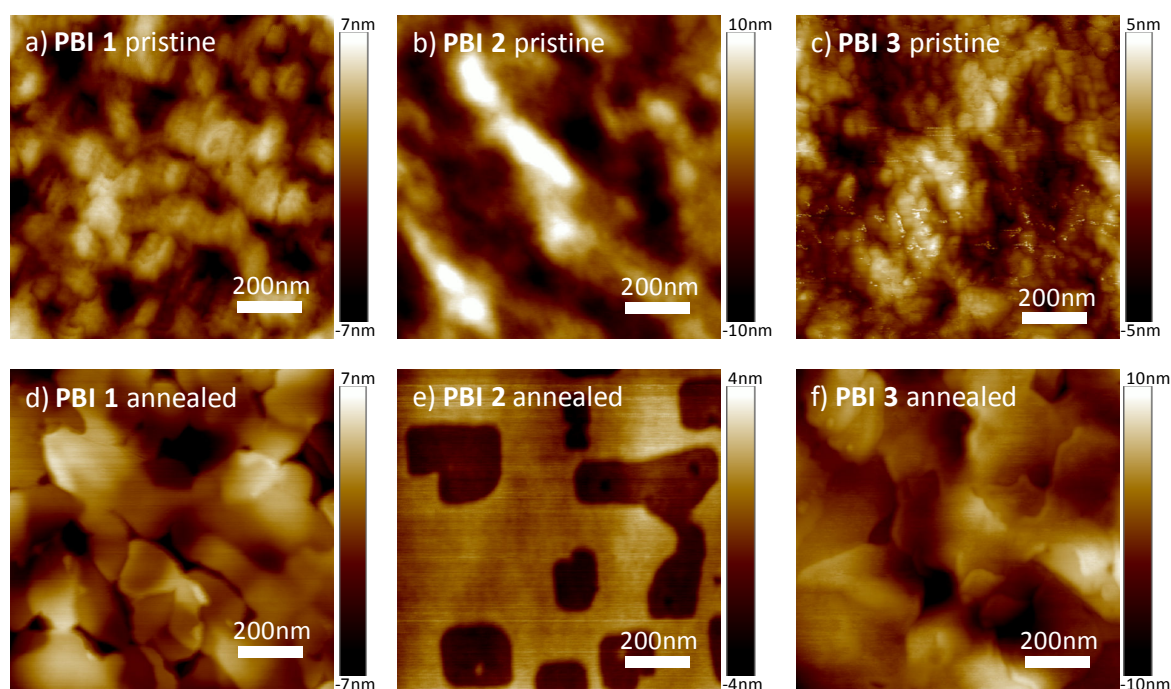


Figure 6: AFM Topography images obtained in Tapping Mode of the pristine PBI thin films (a-c) and after annealing for 5 min at 176 °C (d), 135 °C (e) and 160 °C (f).

### Structure properties (XRD)

The complete structural investigation of PBI 1 in bulk has been published recently.<sup>28</sup> To investigate the structure of the compounds PBI 2 and PBI 3, temperature dependent X-ray scattering measurements in bulk were performed. Both PBI 2 and PBI 3 were heated up to

their respective melting temperature and scattering data were recorded during the stepwise cooling run. The complete temperature dependent scans of PBI 2 and PBI 3 can be found in the Supporting Information (Figure S5). Both PBI 2 and PBI 3 reveal a single transition from the melt state to the crystalline state below which no changes in the scattering pattern are observed. This is in agreement with the DSC scans (see Supporting Information Figure S2) which also show a single transition from the melt to the crystalline phase.

The scattering pattern of PBI 2 recorded at  $T=30\text{ }^{\circ}\text{C}$  at intermediate and large  $q$  range is shown in Figure 7a and b. All reflections can be assigned to the respective  $hkl$  indices and can be indexed by a 2D hexagonal unit cell with lattice constants  $a=b=3.47\text{ nm}$  and  $\gamma=60^{\circ}$  according to Figure 7a. The WAXS pattern of PBI 2 (Figure 7b) reveals a large number of reflections in the  $q$  range  $7\text{-}15\text{ nm}^{-1}$  which is consistent with a well ordered crystalline structure. The peak observed at  $q=17.95\text{ nm}^{-1}$  is assigned to the packing of PBI molecules within the stacks, and corresponds to a  $\pi$ - $\pi$  stacking distance  $c=0.350\text{ nm}$ . Based on these lattice parameters, a unit cell containing 2 molecules give a reasonable crystallographic density of  $0.84\text{ g/cc}$  according to the following equation

$$\rho = 2 \cdot \frac{M}{V \cdot N_A}$$

with  $\rho$  being the crystallographic density (in grams per cubic centimeter),  $M$  the molecular weight of the molecule,  $V$  the volume of the unit cell and  $N_A$  the Avogadro constant.

A further peak is observed at  $q=18.74\text{ nm}^{-1}$  (indicated by an arrow in Figure 7b). Such reflections are indicative for a 3D lattice as they correspond to mixed ( $hkl$ ) reflections with  $h$  and/or  $k$  and additionally  $l$  non zero. The occurrence of such reflections is observed generally in crystalline or in plastic phases<sup>29, 30</sup>. An illustration of PBI columns forming a hexagonal packing is shown in Figure 7c. The observed reflections in the scattering pattern of PBI 3 shown in Figure 7d can be indexed by a 2D oblique unit cell having lattice parameters  $a=2.77\text{ nm}$ ,  $b=1.21\text{ nm}$  and  $\gamma=81^{\circ}$ , which is shown in Figure 7f. All reflections can be assigned accordingly. The WAXS pattern of PBI 3 is similar to that of PBI 2 exhibiting many reflections in the  $q$  range  $7\text{-}15\text{ nm}^{-1}$  as shown in Figure 7e. The reflection observed at  $q=18.12\text{ nm}^{-1}$  can be assigned to the packing of PBI molecules within the stacks, and

corresponds to a  $\pi$ - $\pi$  stacking distance  $c=0.346$  nm. The crystallographic density calculation based on the calculated lattice parameters give a density of 1.3 g/cc for a unit cell containing 1 PBI 3 molecule. Again, a peak observed at  $q=18.9$  nm<sup>-1</sup> (indicated by an arrow in the inset of Figure 7e) corresponds to mixed  $(hkl)$  reflections with  $h$  and/or  $k$  and additionally  $l$  non zero.

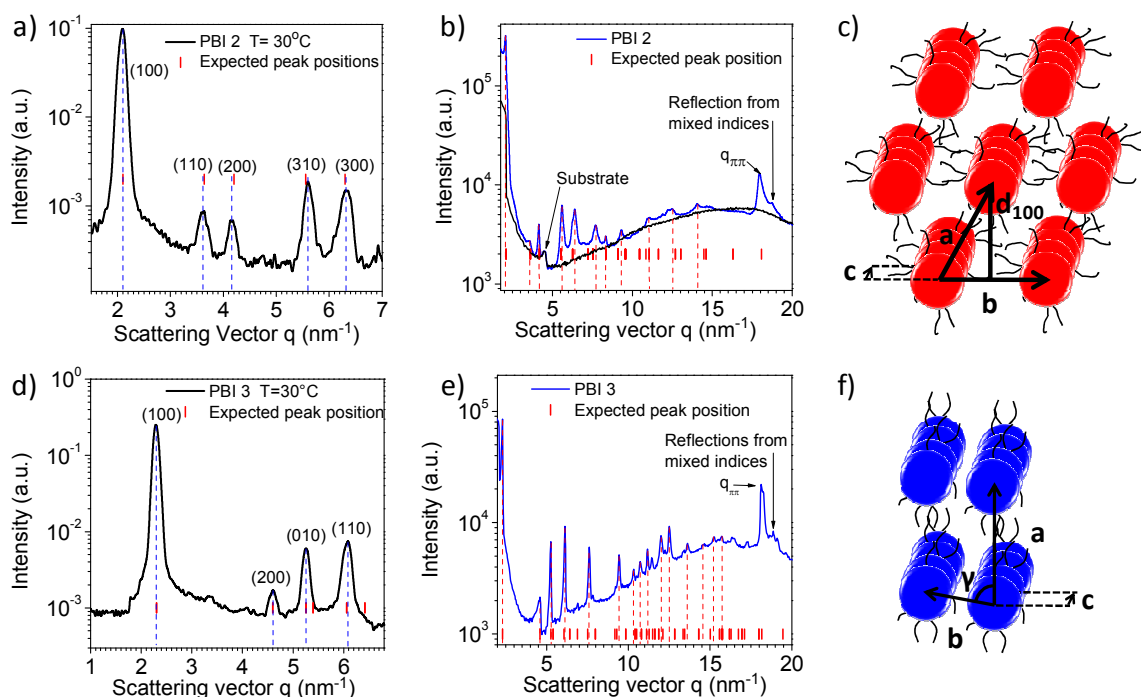


Figure 7: Bulk X-ray scattering measurements for PBI 2 at  $T=300^{\circ}\text{C}$  at (a) intermediate and (b) wide angle range; the observed Bragg reflections in (a) can be indexed for a hexagonal lattice; red bars denote the expected peak positions for a hexagonal unit cell with lattice parameters  $a=b=3.47\text{nm}$  and  $\gamma=60^{\circ}$ ; c) illustration of columnar hexagonal packing based on PBI stacks; bulk X-ray scattering measurements for PBI 3 at  $T=300^{\circ}\text{C}$  at (d) intermediate (e) wide angle range; the observed Bragg reflections in (d) can be indexed for a 2D lamello-columnar unit cell; red bars denote the expected peak positions for the unit cell with lattice parameters  $a=2.77\text{nm}$ ;  $b=1.21\text{nm}$  and  $\gamma=81^{\circ}$ ; f) illustration of lamello-columnar packing of PBI 3.

Hence from bulk measurements we conclude that both PBI 2 and PBI 3 form a 3D crystalline structure. A striking result of these bulk measurements is that the  $\pi$ - $\pi$  stacking distance is found to decrease from the alkyl substituted hydrophobic PBI 1 ( $c=0.360$  nm) to OEG substituted hydrophilic PBI 2 ( $c=0.350$  nm) and PBI 3 ( $c=0.346$  nm). These findings, along with the observations from PL studies, support the better packing in PBI 2 and PBI 3 and the

increased charge carrier mobilities. A summary of lattice parameters of PBI 1, PBI 2 and PBI 3 is given in Table 2.

Table 2: Summary of results from XRD measurements in bulk, thin films and texture scans; interplanar spacing  $d_{100}$  as calculated from theta-2-theta scans of PBI thin films; crystal size along (100) direction  $t_{100}$  calculated using Scherrer equation; relative degree of crystallinity obtained from the ratios of the integrated area under the intensity curve of Figure 8d-f.

		<b>PBI 1</b>	<b>PBI 2</b>	<b>PBI 3</b>
<b>Bulk</b>	<i>Lattice parameters</i>	a=2.86nm b=1.11nm $\gamma=86^\circ$	a=b=3.47nm $\gamma=60^\circ$	a=2.77nm b=1.21nm $\gamma=81^\circ$
	<i><math>\pi</math>-<math>\pi</math> stacking distance (c)</i>	0.360nm	0.350nm	0.346nm
	<i>Packing motif</i>	Lamello-columnar 3D crystalline	Columnar hexagonal 3D crystalline	Lamello-columnar 3D crystalline
<b>Pristine Films</b>	$q_{100}$	2.20nm <sup>-1</sup>	2.32nm <sup>-1</sup>	2.29nm <sup>-1</sup>
	$d_{100}$	2.86nm	2.73nm	2.72nm
	$t_{100}$	24.8nm	22.1nm	23.4nm
<b>Annealed Films</b>	$q_{100}$	2.40nm <sup>-1</sup>	2.08nm <sup>-1</sup>	2.30nm <sup>-1</sup>
	$d_{100}$	2.62nm	3.03nm	2.72nm
	$t_{100}$	40.9nm	52.9nm	61.1nm
<b>Texture Scans: Relative degree of crystallinity</b>		2.5	10.0	38.3

It is known that thermal treatment can have a drastic effect on the packing and crystalline structure of thin films which in turn affects the overall charge transport properties<sup>3, 28</sup>. Hence it is important to understand the crystalline structure and orientation of the molecules in thin film. For this purpose, both theta-2-theta scans and texture measurements (see Supporting Information Figure S7 for experimental setup of texture measurements) were performed on thin films. In a theta-2-theta scan only the lattice planes having their normal vector parallel to the substrate normal can contribute to the signal. Thus, texture measurements are required, which provide quantitative information on the orientation distribution of the films along a single Bragg reflection direction.

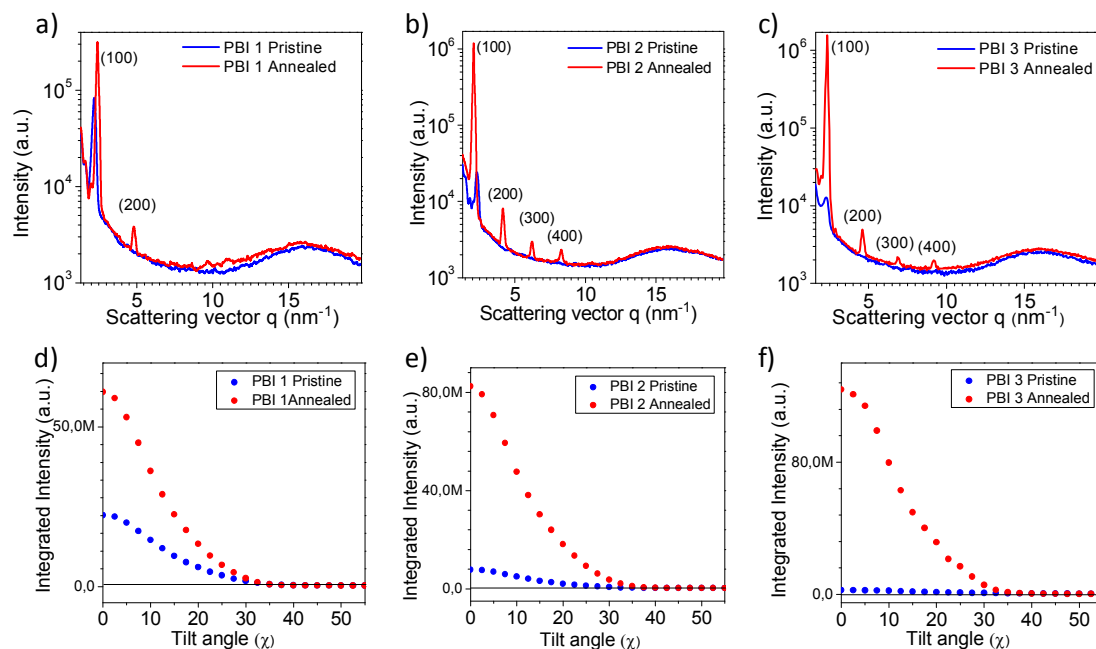


Figure 8: Theta-2-theta scans of thin films of (a) PBI 1 (b) PBI 2 and (c) PBI 3; higher orders for annealed films indicate stronger ordering of molecules; no (001) reflection corresponding to the  $\pi$ - $\pi$  stacking was observed; intensity variation with the tilt angle  $\chi$  of texture scans for (d) PBI 1, (e) PBI 2 and (f) PBI 3 in pristine and annealed films; the integrated area of the intensity curve is a proportional measure for bulk crystallinity in thin films.

Figure 8a-c show the theta-2-theta scans performed on pristine and annealed films of PBI 1, PBI 2 and PBI 3. The scattering pattern of the pristine films of all the materials shows a single reflection at  $q_{100} \sim 2 \text{ nm}^{-1}$ . The interplanar spacing correlates with PBI core-core distance  $a$  as obtained from the bulk measurements. No higher orders of reflections corresponding to the (100) family of planes were observed. This gives a first indication that there is a considerably weak ordering of the molecules in pristine films. A broad halo originating from the amorphous glass at around  $q=16 \text{ nm}^{-1}$  was also observed. However, thermal annealing of the pristine films lead to a significant increase in the scattering intensity of the (100) reflection with a reduced width. No reflection corresponding to (001) lattice planes corresponding to the  $\pi$ - $\pi$  stacking could be observed in pristine or annealed films. The reduced width of the (100) reflection indicates an increased crystal size ( $t_{hkl}$ ) in direction perpendicular to the substrate (see Figure 9), which can be evaluated quantitatively using the Scherrer equation. The increase in intensity can either be caused by an increased crystallinity,

or by a narrower orientation distribution with a prevalent orientation of the (100) lattice planes parallel to the substrate, or by both. Higher order reflections from (*l*00) family of planes were observed for all annealed films. While PBI 1 exhibits reflections up to the second order of the (*l*00) family of planes, PBI 2 and PBI 3 show reflections up to the fourth order as well. The appearance of higher orders in PBI 2 and PBI 3 implies a stronger ordering of PBI molecules with OEG substituted side chains compared to the alkyl substituted PBI 1. The interplanar spacings  $d_{100}$  calculated from the  $q$  value of the first Bragg reflection for PBI 1, PBI 2 and PBI 3, as well as the respective crystallite sizes along the (100) direction  $t_{100}$  (Figure 9) are tabulated in Table 2.

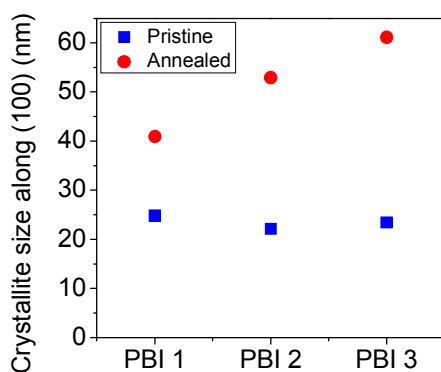


Figure 9: Crystal size along (100) direction  $t_{100}$  for pristine and annealed films calculated using Scherrer equation; the increase in the crystal size was found to be most pronounced for PBI 3 (by a factor of 3) after annealing.

Figure 8d-f show exemplary intensity data  $I(\chi)$  obtained from texture measurements for pristine and annealed films of PBI 1, PBI 2 and PBI 3 using the procedure described in the Supporting Information. The reduction in full width half maximum (FWHM) of the intensity curve for the annealed films in comparison to the pristine films demonstrates a narrower orientation distribution of the (100) lattice planes. Supporting Figure S6 gives the FWHM values obtained for the different PBI films from such a measurement. The most significant decrease in the orientation distribution was observed for PBI 3. An increase in the integrated intensity  $I_{int}$  (see Equation 2 in Supporting Information) was observed for all PBI films after annealing indicating an increased crystallinity. Thus both effects, an increase in intensity as well as a narrowing of the orientation distribution were observed. In Table 2, the ratio of the integrated peak intensity  $I_{int}$  for the annealed films against their respective pristine films is

given. Since the chemical structure of PBIs are different and hence the corresponding films have a different microstructure,  $I_{int}$  can only be compared for a given sample before and after thermal treatment. These results indicate an increase in the relative degree of crystallinity upon annealing for all the PBIs. However the increase in the relative crystallinity measured by the ratio  $I_{int}$  is significantly higher for OEG substituted PBIs (especially for PBI 3) than the alkyl substituted PBI molecules. Based on the structural investigations in thin films, we find that OEG substituted PBIs show stronger ordering of PBI molecules as compared to the alkyl substituted PBIs. Further, the crystallite size along (100)  $t_{100}$  direction increases upon annealing. Given the packing motif of the PBIs found in the bulk measurements and the absence of (00 $l$ ) reflections in thin film measurements, we assume the  $\pi$ - $\pi$  stacking direction  $c$  in the substrate plane. The columns of PBI stacks (Figure 7c and f) are therefore lying flat on the substrate, which is equivalent to an edge-on orientation of the molecules. This assumption is further confirmed by the AFM image in Figure 6e in the case of PBI 2, where the depth of the steps observed corresponds well with the interplanar spacing of  $d_{100}=3.03\text{ nm}$  (for more details see also Figure S4). This finding demonstrates that one single layer of PBI columns are partially missing on the surface of the film. Even though the  $\pi$ - $\pi$  stacking direction is assumed to be parallel to the substrate, high mobilities are obtained in direction perpendicular to the substrate, as demonstrated by the SCLC measurements. It is well known that charge transport in organic semiconductors is highly dependent on the overlap between  $\pi$ -orbitals of adjacent molecules. The overlap, in turn, is determined by the microscopic structure and the density of structural defects in the organic film. It has been proposed for similar polycrystalline perylene derivatives, that sufficient  $\pi$ -orbital overlap does not only exist along the  $\pi$ - $\pi$  stacking direction, but also normal to it, if the molecules pack close enough.<sup>31</sup> For both OEG substituted PBIs, we observed very high vertical ordering in the film after annealing, which relates to good electron mobilities in SCLC devices.

## Conclusion

In conclusion, we correlated charge transport, morphology and crystallinity of three unsymmetrical *N*-substituted Perylene bisimide (PBI) derivatives with the substituents varying from hydrophobic alkyl to hydrophilic oligoethylenglycol (OEG). When OEG side groups are attached to the perylene core, electron mobilities of the compounds after thermal annealing are more than two orders of magnitude higher compared to the corresponding PBI with only alkyl chains. Using the SCLC approach, electron mobilities as high as  $7 \cdot 10^{-3} \text{ cm}^2 \text{V}^{-1} \text{s}^{-1}$  were measured. Aggregation and crystallinity of PBI thin films were investigated. Polarized optical microscopy, AFM and UV/vis spectroscopy give evidence for increased order in the thin films after thermal annealing. Furthermore, only the PBI derivative with alkyl chains shows photoluminescence (PL) in the film, while PL is quenched for PBIs carrying OEG substituents. Crystallinity of the films was studied by XRD. The thermal annealing step leads to high crystallinity for all three PBIs. Especially, both OEG substituted PBIs show higher order and increased crystallite size along (100) direction compared to the PBI with only alkyl chains after annealing in films. We propose a lamella-columnar structure for PBI1 and PBI3 and a columnar hexagonal packing structure for PBI2. The columns formed by PBI stacks exhibit an edge-on orientation with respect to the substrate. In addition, bulk XRD measurements show that the  $\pi$ - $\pi$  stacking distance is gradually reduced when replacing alkyl chains with OEG chains. Findings from XRD experiments are in line with the electron mobility measured. We demonstrated that charge transport, crystalline structure and morphology of PBI thin films are highly affected by the nature of the substituents. High electron mobilities can be obtained where hydrophilic OEG substituents allow for well ordered packing and high crystallinity in thin films.

## Experimental Section

*Chemicals:* The synthesis route to obtain unsymmetrical *N*-substituted PBIs is described elsewhere.<sup>15</sup> Chloroform (anhydrous with crown cap, 99%) was purchased from Sigma-Aldrich. PEDOT:PSS (Clevios P VP Al 4083) was purchased from Heraeus.

*Instrumentation:* UV/vis spectra of solutions in chloroform with a concentration of  $10^{-5}$  molL<sup>-1</sup> and thin films coated on quartz glass were recorded on a Hitachi 3000 spectrophotometer. Photoluminescence spectra of thin films coated on quartz glass were acquired on a Shimadzu RF 5301 PC spectrofluorophotometer upon excitation at 525 nm. Film thicknesses were determined on an Alphastep 500 surface profilometer. Differential scanning calorimetry experiments were conducted at heating rates of 10 K·min<sup>-1</sup> or 40 K·min<sup>-1</sup> under N<sub>2</sub> atmosphere with a Perkin Elmer Diamond DSC, calibrated with indium. The endothermic maximum was taken as T<sub>m</sub>. Atomic force microscopy was performed on a Veeco Dimension Icon with Nanoscope V controller, in Tapping Mode. The used cantilevers were NSC15/AIBS from Mikromasch. Thermal annealing was done on a Stuart SD162 hotplate under N<sub>2</sub> atmosphere. X-ray scattering experiments on bulk samples at intermediate angles were performed in transmission geometry with a laboratory setup consisting of a Rigaku rotating anode, a focusing X-ray optics device (Osmic confocal max flux), and a Bruker 2D-detector (HighStar). The optics also served as monochromator for Cu K $\alpha$  radiation ( $\lambda=0.154$  nm). Aluminum discs with a central hole of 0.8 mm diameter were used as sample holders. The largest scattering vector  $q$  accessible in these experiments was about  $q\approx 6.5$  nm<sup>-1</sup>. The samples were mounted on a Linkam hotstage for temperature control. Heat conducting paste was used to ensure good thermal contact. Wide angle X-ray scattering measurements were performed on an Empyrean diffractometer from PANalytical operating in Bragg-Brentano geometry using a programmable divergence slit to keep the illuminated area constant and a PIXEL detector. Here also Cu K $\alpha$  radiation ( $\lambda=0.154$  nm) was used. Measurements on thin film samples were also performed on the Empyrean diffractometer in parallel beam geometry using a double crystal Ge hybrid monochromator and parallel plate collimator coupled with an open detector. Quantitative determination of crystallinity in pristine and annealed films was done by performing texture measurements (also referred as pole figure measurements) utilising Schulz geometry.<sup>32</sup> Details can be found in the Supporting Information.

*Device preparation:* SCLC electron-only devices were fabricated using the following structure: glass/ ITO/ PEDOT:PSS/ Active Layer/ Ca/Al. Commercial ITO coated glass substrates with a sheet resistance of 13 Ohms per sq (Lumtec) were cleaned using following

sequence in an ultrasonic bath: detergent, water, acetone and 2-propanol. After ozone treatment of the substrates for 5 min, PEDOT:PSS was spin-coated on the ITO surface and dried at 130 °C for 30 min. All following steps were carried out under nitrogen atmosphere with water and oxygen levels  $\leq 0.1$  ppm. After cooling the substrate, the active layer was blade coated from chloroform solutions. The substrates were then put in a thermal evaporation chamber to evaporate the top electrodes (30 nm Ca/ 100 nm Al) under high vacuum ( $1 \cdot 10^{-6}$  mbar) through a shadow mask (active area 4 mm<sup>2</sup>). The current-voltage characteristics of the devices were measured using a Keithley 2420 (*I-V*) Digital SourceMeter at 25 °C. Thin films for UV/vis, XRD and photoluminescence measurements were blade coated from chloroform solutions on quartz glass substrates. The films were annealed at a temperature below the melting point of each compound in an inert atmosphere of nitrogen.

## References

- (1) Law, K. Y., *Chemical Reviews* **1993**, *93*, (1), 449-486.
- (2) Lüttich, F.; Lehmann, D.; Friedrich, M.; Chen, Z.; Facchetti, A.; Borczykowski, C. v.; Zahn, D. R. T.; Graaf, H., *physica status solidi (a)* **2012**, *209*, (3), 585-593.
- (3) Hüttner, S.; Sommer, M.; Thelakkat, M., *Applied Physics Letters* **2008**, *92*, (9), 093302-3.
- (4) Huang, C.; Barlow, S.; Marder, S. R., *The Journal of Organic Chemistry* **2011**, *76*, (8), 2386-2407.
- (5) Kamm, V.; Battagliarin, G.; Howard, I. A.; Pisula, W.; Mavrinskiy, A.; Li, C.; Müllen, K.; Laquai, F., *Advanced Energy Materials* **2011**, *1*, (2), 297-302.
- (6) Sommer, M.; Lindner, S.; Thelakkat, M., *Advanced Functional Materials* **2007**, *17*, (9), 1493-1500.
- (7) Holcombe, T. W.; Norton, J. E.; Rivnay, J.; Woo, C. H.; Goris, L.; Piliago, C.; Griffini, G.; Sellinger, A.; Brédas, J.-L.; Salleo, A.; Frechet, J. M. J., *Journal of the American Chemical Society* **2011**, *133*, (31), 12106-12114.
- (8) Zhan, X.; Facchetti, A.; Barlow, S.; Marks, T. J.; Ratner, M. A.; Wasielewski, M. R.; Marder, S. R., *Advanced Materials* **2011**, *23*, (2), 268-284.
- (9) Zaumseil, J.; Sirringhaus, H., *Chemical Reviews* **2007**, *107*, (4), 1296-1323.
- (10) Li, C.; Wonneberger, H., *Advanced Materials* **2012**, *24*, (5), 613-636.

- (11) Würthner, F., *Chemical Communications* **2004**, (14), 1564-1579.
- (12) Balakrishnan, K.; Datar, A.; Naddo, T.; Huang, J.; Oitker, R.; Yen, M.; Zhao, J.; Zang, L., *Journal of the American Chemical Society* **2006**, *128*, (22), 7390-7398.
- (13) Usowicz, M. T.; Kelley, M. J.; Singer, K. D.; Duzhko, V. V., *The Journal of Physical Chemistry B* **2011**, *115*, (32), 9703-9709.
- (14) Hansen, M. R.; Schnitzler, T.; Pisula, W.; Graf, R.; Müllen, K.; Spiess, H. W., *Angewandte Chemie International Edition* **2009**, *48*, (25), 4621-4624.
- (15) Wicklein, A.; Lang, A.; Muth, M.; Thelakkat, M., *Journal of the American Chemical Society* **2009**, *131*, (40), 14442-14453.
- (16) Howard, I. A.; Laquai, F. d. r.; Keivanidis, P. E.; Friend, R. H.; Greenham, N. C., *The Journal of Physical Chemistry C* **2009**, *113*, (50), 21225-21232.
- (17) Shoaee, S.; An, Z.; Zhang, X.; Barlow, S.; Marder, S. R.; Duffy, W.; Heeney, M.; McCulloch, I.; Durrant, J. R., *Chemical Communications* **2009**, (36), 5445-5447.
- (18) Lunt, R. R.; Benziger, J. B.; Forrest, S. R., *Advanced Materials* **2010**, *22*, (11), 1233-1236.
- (19) Muth, M.-A.; Carrasco-Orozco, M.; Thelakkat, M., *Advanced Functional Materials* **2011**, *21*, (23), 4510-4518.
- (20) Bozano, L.; Carter, S. A.; Scott, J. C.; Malliaras, G. G.; Brock, P. J., *Applied Physics Letters* **1999**, *74*, (8), 1132-1134.
- (21) Goh, C.; Kline, R. J.; McGehee, M. D.; Kadnikova, E. N.; Frechet, J. M. J., *Applied Physics Letters* **2005**, *86*, (12), 122110-3.
- (22) Langhals, H.; Karolin, J.; B-A. Johansson, L., *Journal of the Chemical Society, Faraday Transactions* **1998**, *94*, (19), 2919-2922.
- (23) Kistler, K. A.; Pochas, C. M.; Yamagata, H.; Matsika, S.; Spano, F. C., *The Journal of Physical Chemistry B* **2012**, *116*, (1), 77-86.
- (24) Chen, Z.; Baumeister, U.; Tschierske, C.; Würthner, F., *Chemistry – A European Journal* **2007**, *13*, (2), 450-465.
- (25) Gallaher, J. K.; Aitken, E. J.; Keyzers, R. A.; Hodgkiss, J. M., *Chemical Communications* **2012**, *48*, (64), 7961-7963.
- (26) Bulovic, V.; Burrows, P. E.; Forrest, S. R.; Cronin, J. A.; Thompson, M. E., *Chemical Physics* **1996**, *210*, 1-12.
- (27) Giaimo, J. M.; Lockard, J. V.; Sinks, L. E.; Scott, A. M.; Wilson, T. M.; Wasielewski, M. R., *The Journal of Physical Chemistry A* **2008**, *112*, (11), 2322-2330.

- (28) Kohn, P.; Ghazaryan, L.; Gupta, G.; Sommer, M.; Wicklein, A. e.; Thelakkat, M.; Thurn-Albrecht, T., *Macromolecules* **2012**, *45*, (14), 5676-5683.
- (29) Gluesen, B.; Heitz, W.; Kettner, A.; Wendorff, J. H., *Liquid Crystals* **1996**, *20*, (5), 627-633.
- (30) Wicklein, A.; Kohn, P.; Ghazaryan, L.; Thurn-Albrecht, T.; Thelakkat, M., *Chemical Communications* **2010**, *46*, (13), 2328-2330.
- (31) Krauss, T. N.; Barrena, E.; de Oteyza, D. G.; Zhang, X. N.; Major, J.; Dehm, V.; Würthner, F.; Dosch, H., *The Journal of Physical Chemistry C* **2009**, *113*, (11), 4502-4506.
- (32) Schulz, L. G., *Journal of Applied Physics* **1949**, *20*, 1030-1032.

### Supporting Information

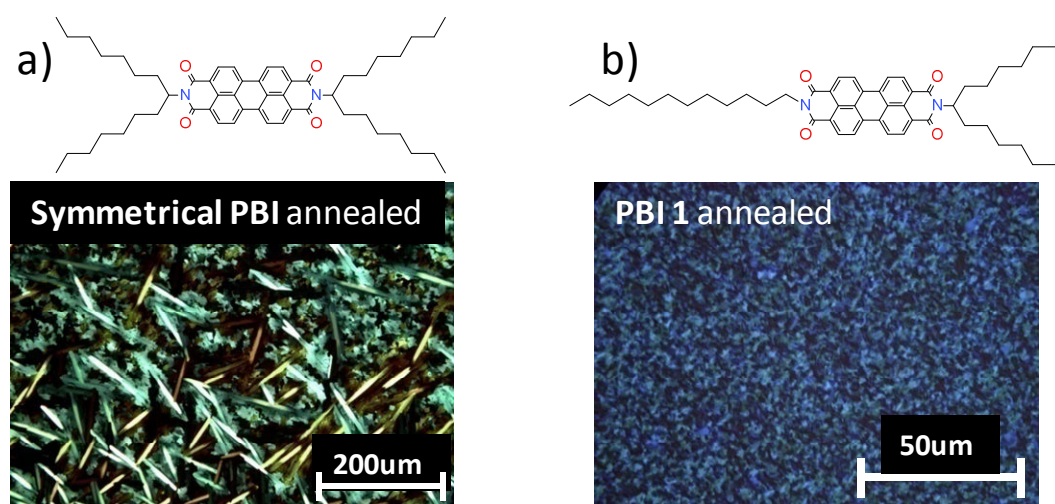


Figure S 1: Chemical structure and polarized optical microscopy image of annealed thin films of a symmetrical *N*-substituted PBI (a) and the unsymmetrical *N*-substituted PBI 1 (b); the annealing procedure was 5 min at a temperature of 128°C for symmetrical PBI and 176°C for PBI 1, which is 5 °C below the  $T_m$  of each compound. It is clear that the symmetrical PBI has a stronger tendency to crystallize compared to the unsymmetrical PBI.

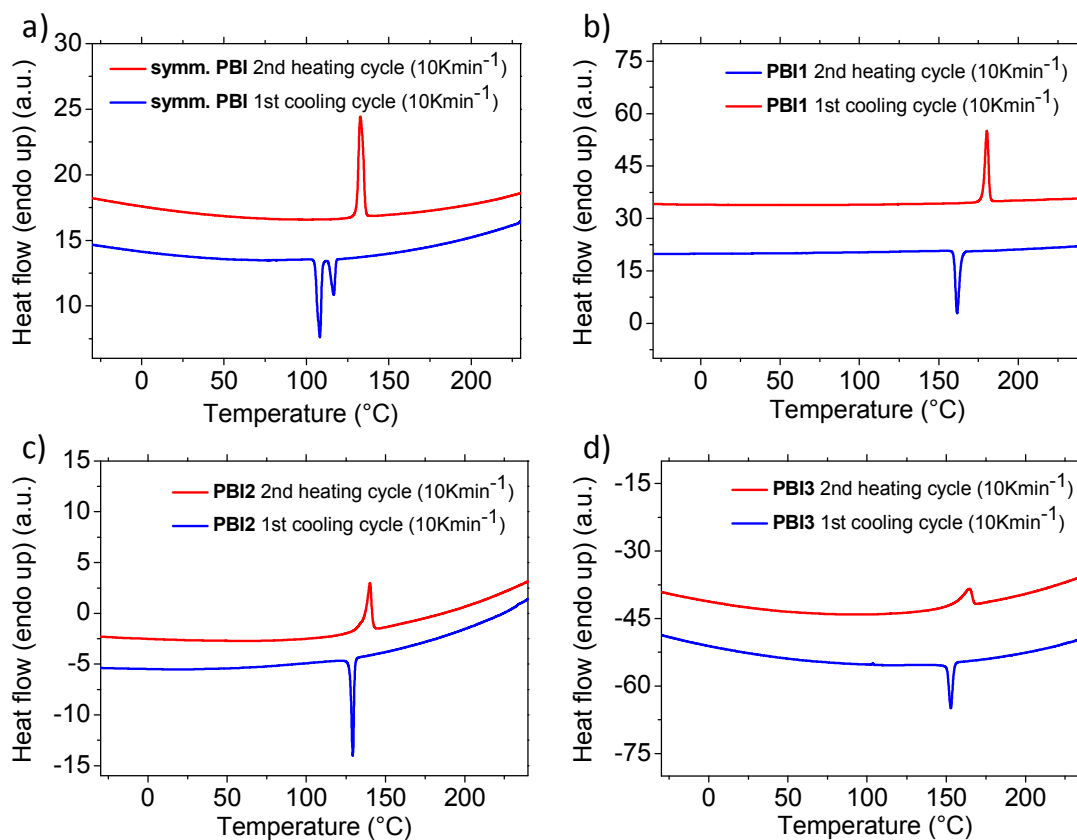


Figure S 2: Differential scanning calorimetry (DSC) thermograms of the symmetrical *N*-substituted PBI (a), PBI 1 (b), PBI 2 (c) and PBI 3 (d) showing the second heating cycle and the first cooling cycle at a rate of 10 Kmin<sup>-1</sup>.

Table S 1: Summary of DSC results of the second heating cycle and the first cooling cycle at a rate of 10 Kmin<sup>-1</sup>.

Compound	Phase transitions and corresponding enthalpies $\Delta H$ (in paranthesis) [°C (kJ mol <sup>-1</sup> )]	
	2nd heating cycle	1st cooling cycle
<b>Symmetrical PBI</b>	Cr 133.2 (19.5) → I	I 118.3 (-5.0) → Col <sub>h</sub> → 110.7 (-11.6) → Cr
<b>PBI 1</b>	Cr 180.6 (21.2) → I	I 161.6 (-19.2) → Cr
<b>PBI 2</b>	Cr 140.1 (10.6) → I	I 129.3 (-10.6) → Cr
<b>PBI 3</b>	Cr 164.5 (10.4) → I	I 152.9 (-16.3) → Cr

Cr=crystal phase; I=isotropic; Col<sub>h</sub>=columnar hexagonal mesophase.

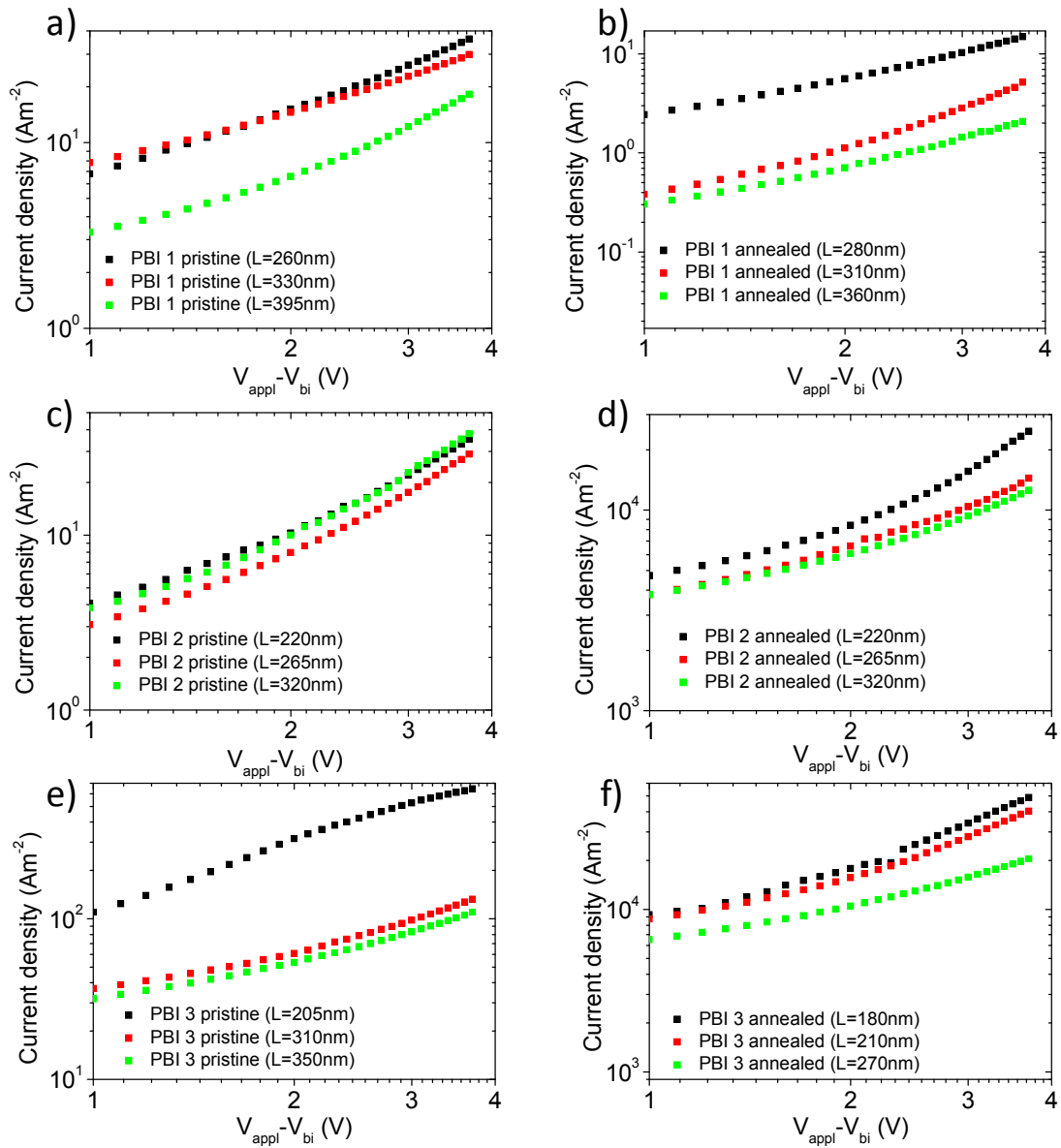
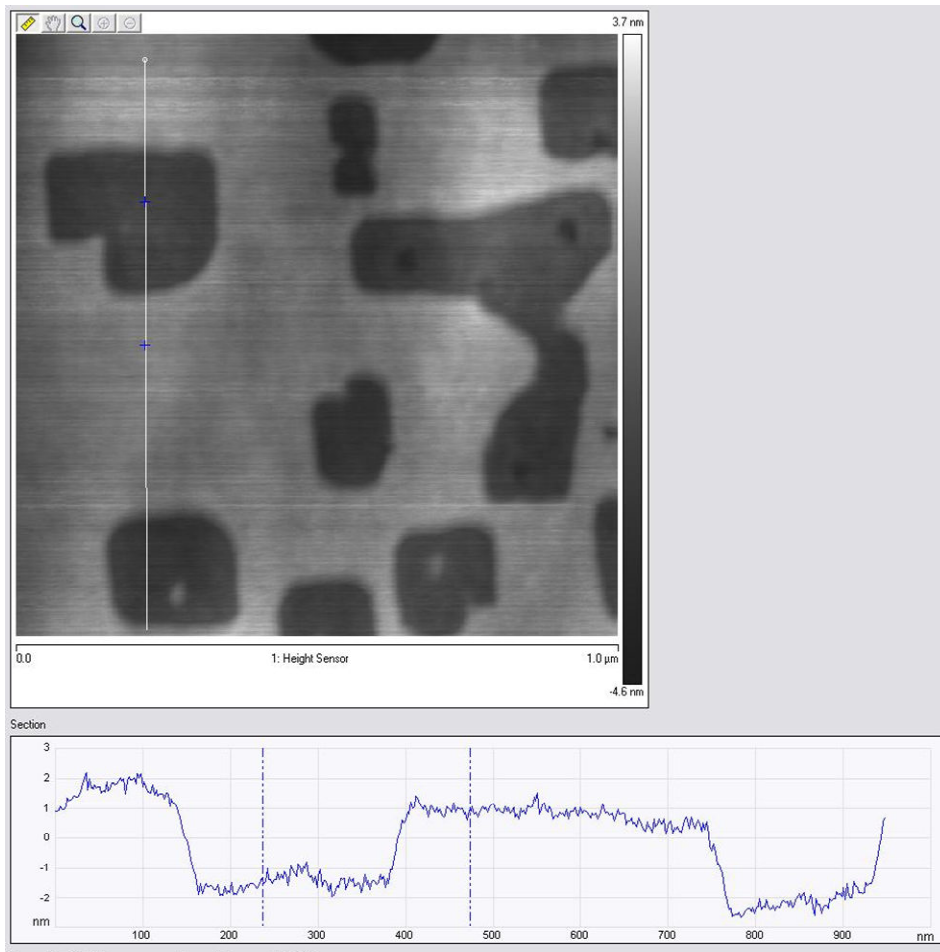


Figure S 1: Current density – Voltage characteristics of pristine and annealed electron-only devices with varied active layer thickness  $L$  of PBI 1 (a and b), PBI 2 (c and d) and PBI 3 (e and f); the voltage applied was corrected for a built in potential of 2.2 eV resulting from the differences in work function of calcium and ITO/PEDOT:PSS.



*Figure S 4: AFM topography image and cross section thereof, obtained in Tapping Mode of the annealed film of PBI 2 with a scan size of 1 μm; the depth of the steps found on the film surface are around 3 nm.*

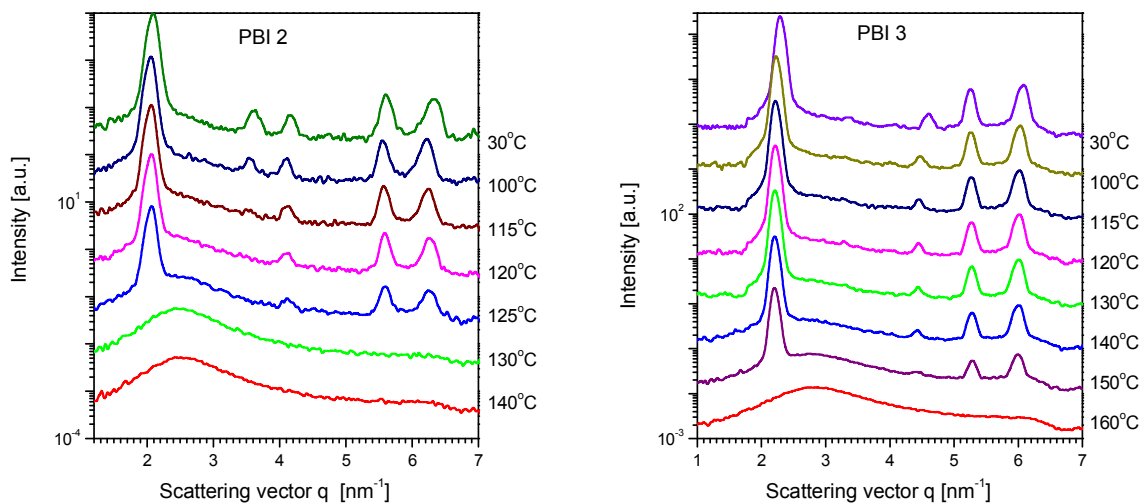


Figure S 5: Temperature dependent XRD cooling scan for PBI2 and PBI3.

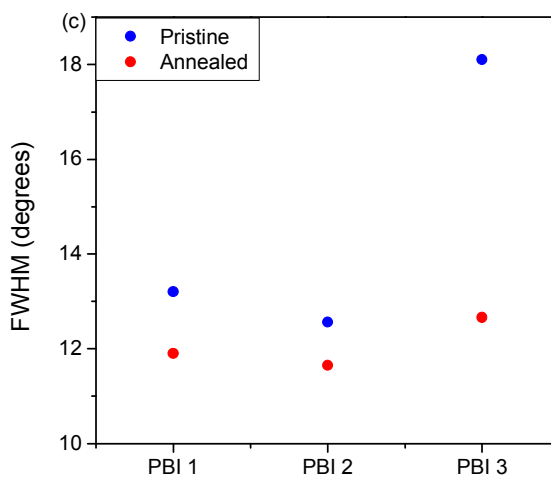


Figure S 6: Full-width-half-maximum (FWHM) of the orientation distribution of the (100) crystallographic lattice planes for different PBIs films obtained from pole figure measurements.

*Texture measurements*

Texture measurements were made at a fixed angle of incidence, corresponding to the (100)-reflection of PBI cores as obtained from  $\theta$ - $2\theta$  scan, while the polar angle  $\chi$ , was varied from  $0^\circ$  to  $55^\circ$ . For each  $\chi$ , the azimuthal angle  $\phi$  was scanned over  $360^\circ$ . While generally in a texture measurement, the intensity of a given Bragg reflection can depend on the angles  $\chi$  and  $\phi$ , the microstructure of our thin film samples is isotropic in the plane of the substrate. In order to eliminate any  $\phi$  dependence, for the analysis only azimuthally averaged intensity  $I(\chi)$  was considered.

$$I(\chi) = \int_{\chi=const} I(\chi, \phi) d\phi \quad \text{Equation 1}$$

A schematic of such a texture measurement is shown in Figure S7. The intensity  $I(\chi)$  is directly proportional to the orientation distribution of the crystals. We used the FWHM of the peaks around  $\chi=0$  as a quantitative measure. The integrated intensity  $I_{int}$  after background correction as defined in equation 2 is proportional to the crystallinity of the sample.

$$I_{int} = \int_0^{55} \{I(\chi) \sin(\chi) - I_{bkg}\} d\chi \quad \text{Equation 2}$$

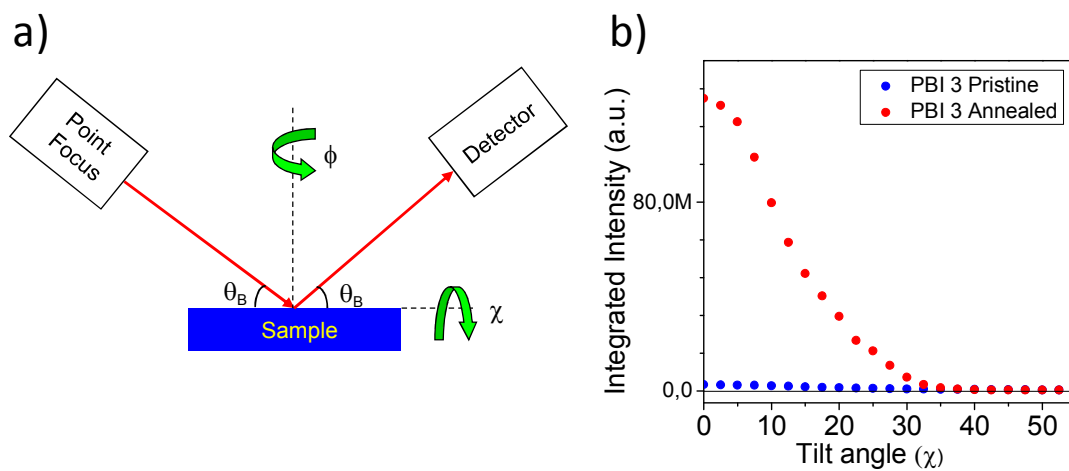


Figure S 7: a) Schematic of the pole figure measurement performed at the fixed angle of incidence of the (100) reflection of P3HT and b) example of a pole figure plot for PBI 3.



## 4. Liquid Crystalline Perylene Diester Polymers with Tunable Charge Carrier Mobility

*Mathis-Andreas Muth<sup>a,b</sup>, Miguel Carrasco-Orozco<sup>b</sup> and Mukundan Thelakkat<sup>a,\*</sup>*

[a] Prof. Dr. Mukundan Thelakkat, Applied Functional Polymers, Department of Macromolecular Chemistry I, University of Bayreuth, Universitaetsstr.30, 95440 Bayreuth (Germany)

[b] Dr. Miguel Carrasco-Orozco, Merck Chemicals Ltd., Chilworth Technical Centre, University Parkway, Southampton SO16 7QD (UK)

\*corresponding author: mukundan.thelakkat@uni-bayreuth.de

This manuscript is published in *Advanced Functional Materials* **2011**, *21*, 4510-4518.

## Abstract

Here we report new classes of liquid crystalline semiconductor polymers based on perylene diester benzimidazole and perylene diester imide mesogens. Two highly soluble side-chain polymers, poly(perylenediester benzimidazole acrylate) (PPDB) and poly(perylenediester imide acrylate) (PPDI) are synthesized by nitroxide mediated radical polymerization (NMRP). PPDB shows n-type semiconductor performance with electron mobilities of  $3.2 \cdot 10^{-4} \text{ cm}^2 \text{ V}^{-1} \text{ s}^{-1}$  obtained in a diode configuration by fitting the space-charge limited currents (SCLC) according to Mott-Gurney equation. Interestingly, PPDI performs preferentially as a p-type material with a hole mobility of  $1.5 \cdot 10^{-4} \text{ cm}^2 \text{ V}^{-1} \text{ s}^{-1}$ , which we attribute to the less electron deficient perylene core of PPDI compared to PPDB. Optical properties are investigated by UV/vis and fluorescence spectroscopy. The extended  $\pi$ -conjugation system due to the benzimidazole unit of PPDB leads to a considerably broader absorption in the visible region compared to PPDI. HOMO and LUMO levels of the polymers are also determined by cyclic voltammetry; the resulting energy band gaps are 1.86 eV for PPDB and 2.16 eV for PPDI. Thermal behavior and liquid crystallinity are studied by differential scanning calorimetry (DSC), polarized optical microscopy (POM) and X-ray diffraction measurements (XRD). The results indicate liquid crystalline order of the polymers over a broad temperature range. These thermal, electrical and optical properties make the perylene side chain polymers attractive materials for organic photovoltaics.

## Introduction

The development of polymeric n-type semiconductors for electronic devices such as organic photovoltaic cells or organic field effect transistors is still challenging and less extensively investigated, compared to the remarkable work done on p-type polymers recently<sup>1-3</sup>. Poor processability, insufficient electron mobilities or lack of air stability are present obstacles that have to be overcome in designing novel n-type polymer materials<sup>4</sup>. The successful integration of a naphthalenedicarboximide based n-channel polymer in thin film transistors, leading to high electron mobilities under ambient conditions, was demonstrated recently<sup>5</sup>. In comparison, in donor acceptor bulk heterojunction solar cells, polymeric n-type materials

used as electron acceptor show significantly lower performances than acceptors based on small molecules such as PCBM.<sup>6, 7</sup> Polymers however, usually show better film forming properties compared to low molecular weight compounds<sup>8</sup>. This property is essential for solution processability, illustrating the need for n-type polymers. Perylene bisimides (PBI) are a relevant class of n-type semiconductors due to their relatively high electron affinity and strong visible light absorption, combined with good photochemical and thermal stability<sup>9, 10</sup>. Due to strong  $\pi$ - $\pi$  interaction of the perylene cores, electron mobilities of 0.1-1  $\text{cm}^2\text{V}^{-1}\text{s}^{-1}$  for low molecular weight PBIs and  $1.2 \cdot 10^{-3} \text{ cm}^2\text{V}^{-1}\text{s}^{-1}$  for a solution processable PBI side chain homopolymer in organic field effect transistors were reported<sup>11, 12</sup>. It has been shown, that in terms of photoinduced charge generation, PBIs can be more effective electron acceptors than PCBM<sup>13</sup>. Due to comparatively poor device performance, this class of material has received limited attention in bulk heterojunction solar cells to date. The main issue is assumed to be an unfavorable blend morphology due to the tendency of PBI to form large crystals<sup>14</sup>. We reported recently on a series of highly soluble, small molecular weight discotic liquid crystalline (LC) PBI<sup>15</sup> and perylene diester benzimidazole (PDB) molecules<sup>16</sup>. The latter exhibit mesophases even at room temperature, combined with extended visible light absorption compared to PBIs. The self-organization of discotic LC materials can be exploited in optoelectronic applications in such a way that optimized morphology<sup>17, 18</sup> and good charge carrier transport properties along the  $\pi$ - $\pi$  stacking axis<sup>19</sup> can be combined. The concept of utilizing LC semiconducting polymers in organic photovoltaic cells<sup>20</sup>, as well as in organic light emitting diodes (OLED)<sup>21</sup> and organic field effect transistors (OFET)<sup>22</sup> has been demonstrated successfully. In this context, to the best of our knowledge, the polymerization of LC perylene benzimidazole moieties has not yet been reported.

Herein, we describe the synthesis of novel perylene side chain homopolymers, based on LC perylene diester benzimidazole and perylene diester imide mesogens. Nitroxide mediated radical polymerization (NMRP) was found to be a suitable method for the controlled synthesis of homopolymers and block copolymers based on acrylate monomers with pendant perylene moieties<sup>23-25</sup>. This radical polymerization method allows for a metal free polymerization of acrylate monomers giving narrow molecular weight distributions.

Additionally, a thorough characterization of LC phases by DSC, POM and XRD and bulk electron transport properties by the space-charge limited current (SCLC) method are given.

## Results and Discussion

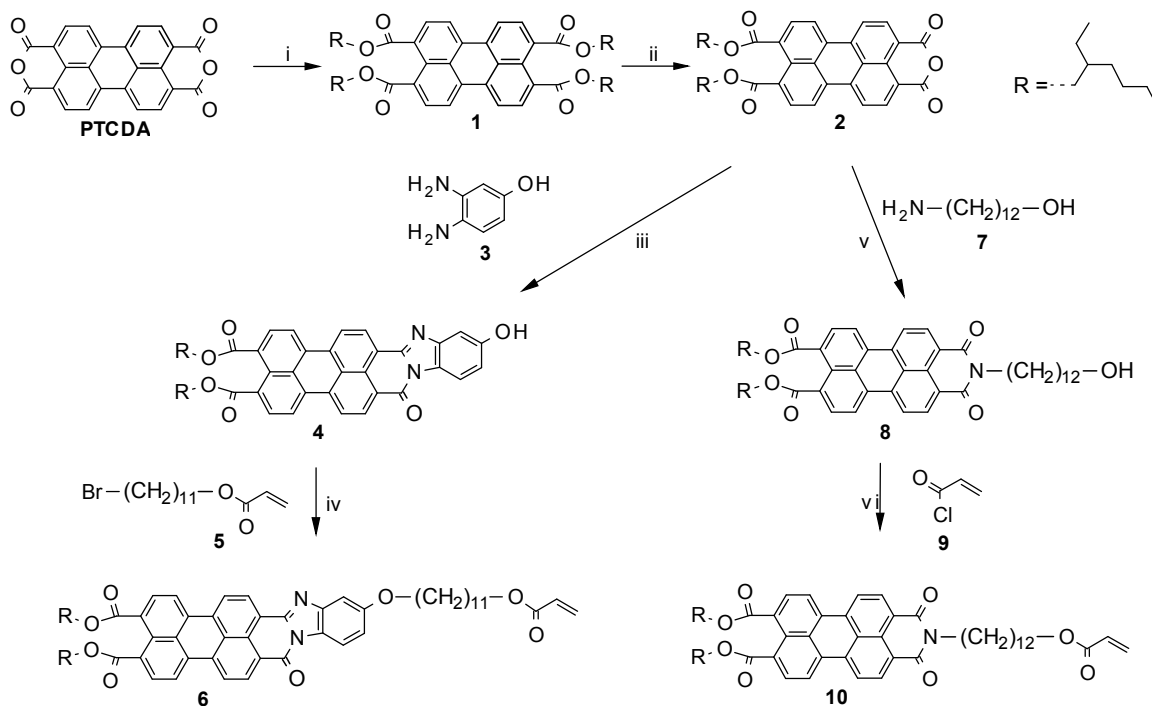
### Synthesis

In this chapter, the synthesis of perylene acrylate monomers **6** and **10**, and their polymerization to the corresponding polymers PPDB and PPDI *via* NMRP are described. The synthetic route for perylene acrylate monomers **6** and **10** is shown in Scheme 1. Perylene diester monoanhydride **2** was obtained from perylene-3,4,9,10-tetracarboxylic dianhydride PTCDA as the starting material according to a procedure described recently<sup>16</sup>. The branched aliphatic ethyl hexyl substituents linked to the ester groups give excellent solubility in various organic solvents. A benzimidazole unit was introduced to the perylene core by condensation reaction of **2** with 3,4-diaminophenol (**3**) giving perylene benzimidazole **4** carrying an OH-group. This zinc acetate catalyzed reaction was carried out under microwave irradiation to get adequate yield (54 %). Finally, to obtain monomer **6**, 11-bromoundecyl acrylate (**5**), bearing an acrylate moiety with alkyl spacer, was attached to **4** in a nucleophilic substitution under alkaline conditions. The acrylate unit of **5** serves as the polymerizable group and the alkyl chain provides sufficient flexibility to facilitate the polymerization in the presence of sterically hindering pendant perylene cores. The monomer **6** was obtained in 75 % yield, the reaction conditions were similar to the perylene bisimide acrylate monomer synthesis described by Lindner *et al.*<sup>23</sup>.

A second perylene diester acrylate monomer **10**, consisting of an imide group instead of a benzimidazole unit was synthesized in order to study the effect of the size of the conjugated  $\pi$ -system on optical, electronic and thermal properties. Monoanhydride diester **2** and the primary amine **7** were reacted to give hydroxy functionalized perylene diester imide **8**. The reaction was carried out in molten imidazole with an excess of **7** to give **8** in a high yield of 90 %. The OH-group attached at the alkyl spacer served as functional group for esterification with acryloyl chloride (**9**). Finally, perylene diester imide acrylate **10** was obtained under

basic conditions in a good yield of 68 %. A detailed description of the synthesis and purification of monomers, polymers and reactants **3**, **5** and **7**, is given in the experimental section. All compounds were characterized by  $^1\text{H-NMR}$  and IR spectroscopy.

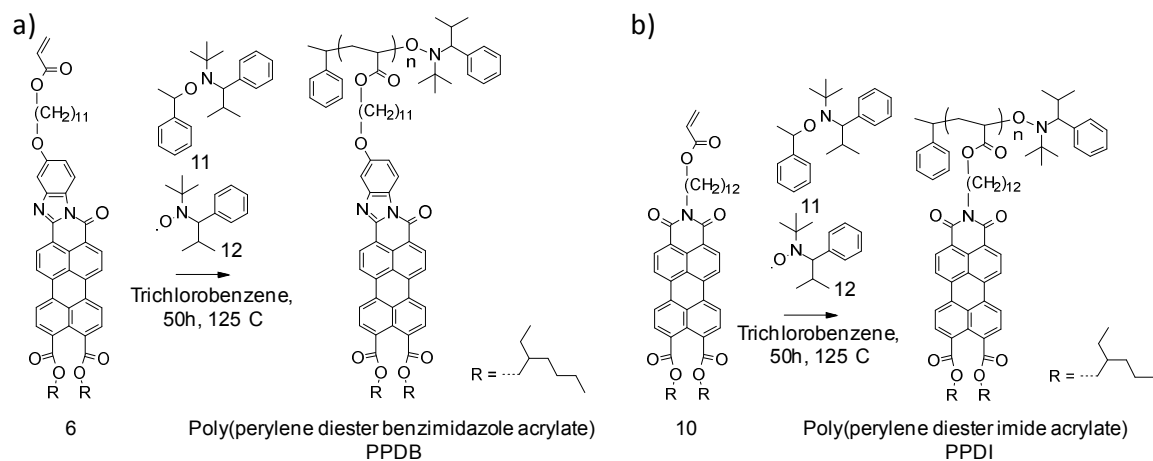
*Scheme 1. Synthesis of perylene acrylate monomers 6 and 10; i) 1. KOH/H<sub>2</sub>O, 0.5h, 70°C; 2. Aliquat 336, KI, 10min, RT; 3. Br-R, 16h, 100°C. ii) p-toluenesulfonic acid monohydrate, toluene/n-dodecane, 5h, 95°C. iii) Zn(OAc)<sub>2</sub>/DMAc, 25min, 160°C, 300W (microwave). iv) K<sub>2</sub>CO<sub>3</sub>, KI, DMAc, 17h, 85°C. v) Imidazole, Zn(OAc)<sub>2</sub>, 4h, 160°C. vi) Et<sub>3</sub>N/DCM, 24h, 0°C.*



NMRP was utilized to homopolymerize monomers **6** and **10**. The reactants and the resultant perylene homopolymers PPDB and PPDI are depicted in Scheme 2. The ratio of monomer to 2,2,5-trimethyl-3-(1-phenylethoxy)-4-phenyl-3-azahexan (**11**), serving as unimolecular initiator, was  $[\text{M}]:[\text{I}] = 100:1$ . To shift the reaction equilibrium towards the dormant species, 0.1 equivalents of *N-tert-butyl- $\alpha$ -isopropyl- $\alpha$ -phenylnitroxid* (**12**) were added to the reaction mixture. This slowed the reaction rate and decreased the concentration of growing polymer radicals leading to better control over the polymerization. The initiator **11** and free nitroxide **12** were synthesized according to a procedure described by Hawker *et al.*<sup>26</sup>. Only small

amounts of solvent were used to prevent dilution of acrylate groups, so that the polymerization rate is not further decreased.

Scheme 2. Polymerization of (a) 6 and (b) 10 via nitroxide mediated radical polymerization (NMRP).



The reactions were quenched at conversion of 35 %, determined by  $^1\text{H-NMR}$ , in order to prevent transfer reactions leading to increasing molecular weight distributions<sup>27</sup>. Molecular weights of the polymers were identified by size exclusion chromatography (SEC) in chlorobenzene, which was calibrated with polystyrene standards. The refractive index detector signal of the SEC traces of PPDB and PPDI are shown in Figure 1.

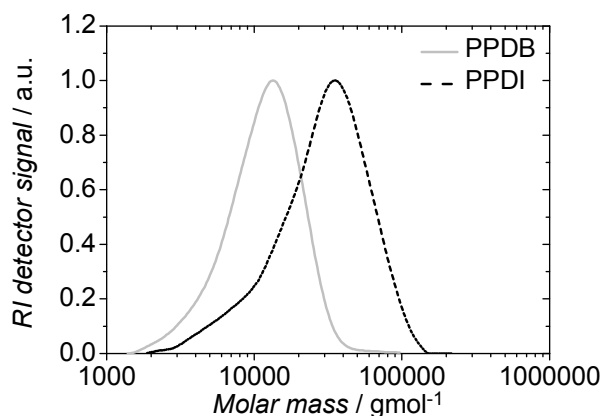


Figure 1: SEC traces (refractive index detection) of PPDB and PPDI.

$M_n$  and  $M_w$  of PPDB was found to be 9400 g·mol<sup>-1</sup> and 13300 g·mol<sup>-1</sup> respectively with a polydispersity index (PDI) of 1.4. PPDI has a higher molecular weight of  $M_n = 20400$  g·mol<sup>-1</sup> and  $M_w = 35300$  g·mol<sup>-1</sup>, with a PDI of 1.7. Considering that a controlled radical polymerization method was used, the molecular weight distributions are rather broad. This suggests that termination reactions took place, especially after long reaction times of 50 h. The higher molecular weights obtained for PPDI compared to PPDB are attributed to the better solubility of PPDI in 1,2,4-trichlorobenzene. The high molecular weight PPDI is still soluble, whereas PPDB becomes insoluble after having reached an average molecular weight ( $M_n$ ) above 10000 g mol<sup>-1</sup>, which decreases the further polymerization rate significantly. SEC data are summarized in Table 2.

## Polymer characterization

### *Thermotropic properties*

The thermotropic behavior of the two polymers was studied by differential scanning calorimetry (DSC), polarized optical microscopy (POM) and X-ray diffraction measurements (XRD). The DSC traces shown in Figure 2a and b were recorded with a scanning rate of 10 Kmin<sup>-1</sup>. Phase transition temperatures and the corresponding enthalpies  $\Delta H$  are summarized in Table 1. The first heating cycles were ignored to rule out influences of the thermal history of the samples. For PPDB a glass transition ( $T_g$ ) at 151 °C and a reversible phase transition to isotropic state at 312 °C was found. The comparatively small enthalpy of 3.8 Jg<sup>-1</sup> suggests a phase transition from a liquid crystalline (LC) mesophase to the isotropic melt. The corresponding crystallization peak upon cooling was detected at 279 °C. The existence of a LC phase was confirmed by POM, which was equipped with a temperature-controlled hot stage. Upon cooling from the isotropic state with a cooling rate of 3 Kmin<sup>-1</sup>, birefringent textures under crossed polarizers for PPDB were observed, which are shown in Figure 2c. The image was obtained at a temperature of 300 °C. The sample was viscous liquid, which indicates a LC rather than a crystalline phase. The temperature difference observed for the phase transition between POM (300 °C) and DSC (279 °C) is due to the

supercooling effect caused by a faster cooling rate in the DSC measurement. Similar observations were made for PPDI, where the melting point was identified at 132 °C by DSC and POM. In the same way, the small transition enthalpy ( $2.8 \text{ Jg}^{-1}$ ) in DSC and birefringent textures under crossed polarizers in POM (Figure 2d) indicates that PPDI also exhibits a LC mesophase. Figure 2d was obtained after annealing PPDI at 110 °C for 5 h. The absence of other phase transitions in the DSC traces implies that PPDI is still in the liquid crystalline state at room temperature, however the viscosity of the compounds increases with decreasing temperature and crystallization of the materials might be thus kinetically hindered.

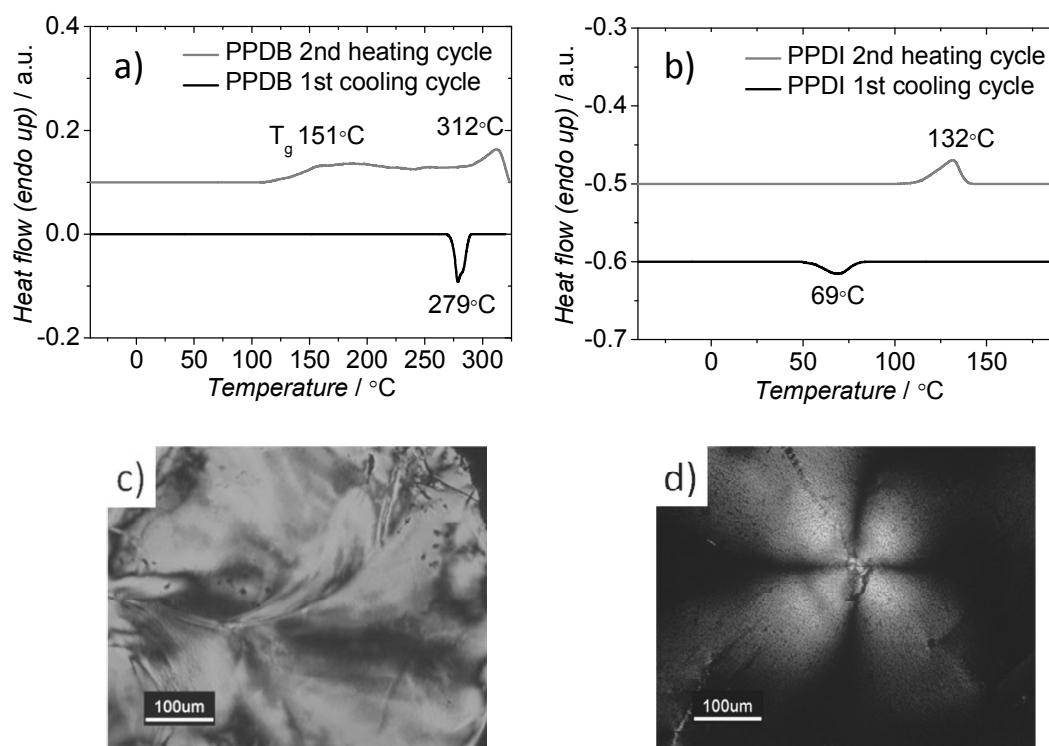


Figure 2: DSC thermogram (scan rate  $10 \text{ Kmin}^{-1}$ ) for PPDB (a) and PPDI (b) showing the second heating and the first cooling cycle. Peak values for the phase transitions are given. Optical microscopy images (polarizers crossed) of the LC mesophases of PPDB at 300 °C (c) and PPDI at 110 °C (d). The textures were obtained upon cooling the sample from the isotropic melt and annealing at the respective temperature.

Table 1: Phase behavior of PPDB and PPDI obtained from DSC measurements.

	<b>Phase transitions and corresponding enthalpies <math>\Delta H</math></b>	
	<b>2<sup>nd</sup> heating cycle</b> ( $T / ^\circ\text{C}; \Delta H / \text{Jg}^{-1}$ )	<b>1<sup>st</sup> cooling cycle</b> ( $T / ^\circ\text{C}; \Delta H / \text{Jg}^{-1}$ )
<b>PPDB</b>	g (151) $\rightarrow$ LC (312; 3.8) $\rightarrow$ I	I (279; 3.7) $\rightarrow$ LC
<b>PPDI</b>	LC (132; 2.8) $\rightarrow$ I	I (69; 1.6) $\rightarrow$ LC

g: glassy, LC: liquid crystalline, I: isotropic.

To further verify the thermotropic liquid crystalline character of both polymers, X-ray scattering experiments were carried out. The instrument was equipped with a Guinier camera and a hot stage. The X-ray diffraction (XRD) patterns of PPDB and PPDI are shown in Figure 3. As reported recently<sup>16</sup>, for liquid crystalline perylene derivatives a columnar hexagonal ordering of the disc like mesogens is often observed. According to the X-ray diffractogram (Figure 3), the packing behavior of the perylene side chain polymers PPDB and PPDI could not be identified as columnar hexagonal. Here, the Bragg reflections in the low  $q$  regime are indicative for a 2D columnar rectangular or columnar oblique ordering<sup>28</sup>. For clarification of the particular structure of the mesophases additional temperature dependent small angle X-ray scattering (SAXS) experiments will be carried out at ESRF Grenoble. In the wide angle regime of the PPDB diffractogram a comparatively broad reflection at a  $q$  value of  $17.89 \text{ nm}^{-1}$  corresponds to a short range repeat distance of  $3.51 \text{ \AA}$ . This can be attributed to the  $\pi$ - $\pi$  stacking distance of perylene cores of adjacent polymer side chains. For PPDI a clearly sharper reflection at  $q=18.21 \text{ nm}^{-1}$  depicts a  $\pi$ - $\pi$  stacking distance of  $3.45 \text{ \AA}$ . The more defined and sharper reflection and the closer packing distance of PPDI compared to PPDB demonstrate a slightly better organization and more regular packing of the perylene cores. It is important to mention, that PPDB, in contrast to PPDI, was not heated above the melting temperature before measurement due to temperature limitation of our X-ray instrument. Therefore the preconditions for self organization were not similar for the two polymers. More detailed temperature dependent wide angle X-ray scattering (WAXS) experiments are currently under investigation. An amorphous halo and the absence of further

reflections at high  $q$  values verify the liquid like character of the alkyl chains. In conclusion, PPDB and PPDI are liquid crystalline, the latter even at room temperature.

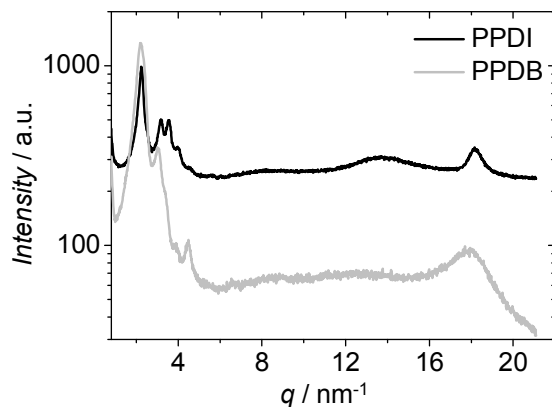


Figure 3: X-ray diffraction pattern of PPDI recorded at room temperature after annealing at 140 °C and PPDB recorded at 250 °C.

#### *Optical and electronic properties*

In this section, the two homopolymers PPDB and PPDI are investigated in terms of their absorption behavior in solution and in solid state, their HOMO and LUMO levels and their charge carrier mobilities. The UV/vis absorption spectra of PPDB and PPDI in chlorobenzene solution and in thin films are shown in Figure 4a. The characteristic vibronic bands for perylene diester imide PPDI, similar to those of PBI based homopolymers<sup>29</sup> are found. The three vibronic transitions in solution at 510 nm, 479 nm and 450 nm are hypsochromic shifted by 20 nm compared to PBI homopolymer. The fluorescence maximum of PPDI measured in film with an excitation wavelength of 525 nm is at 573 nm (Figure 4b). The presence of a benzimidazole unit in PPDB extends the absorption considerably, up to 670 nm in solution and 680 nm in film, with an absorption maximum at 530 nm. Thus the absorption edge of PPDB is almost 100 nm red shifted compared to PPDI. Neither vibronic fine structure in the absorption spectra nor fluorescence could be observed for PPDB. A spectral broadening for both polymers in thin films, compared to the solution spectra is observed, indicating a change in aggregation in the solid state.

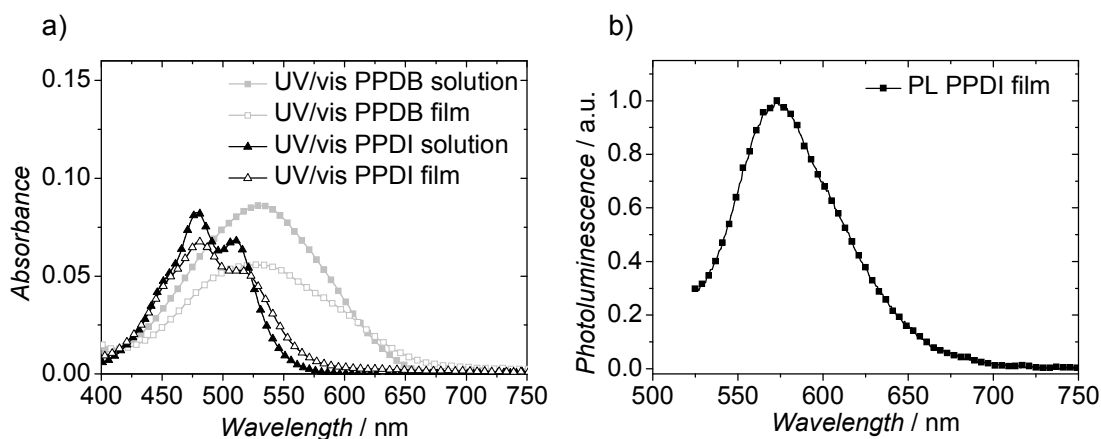


Figure 4: (a) UV/vis absorption spectra of PPDB and PPDI measured in chlorobenzene solution and in thin films and (b) photoluminescence spectra of PPDI thin film ( $\lambda_{ex} = 525$  nm).

Cyclic voltammetry was carried out to estimate HOMO/LUMO levels and study electrochemical stability of the compounds. To determine LUMO energy values, each measurement was calibrated with ferrocene-ferrocenium couple  $Fc/Fc^+$  taking 4.8 eV as ferrocene HOMO level<sup>30</sup>. The cyclic voltammograms (Figure 5) show two reversible reduction peaks for both polymers, characteristic for the perylene unit. The first reduction peaks occurring at -1.27 V for PPDB and -1.28 V for PPDI result in almost identical LUMO energy levels of -3.53 eV and -3.52 eV respectively. Up to five cycles were recorded and no changes in the redox peaks were observed indicating electrochemical stability and reversibility. HOMO values were estimated from the optical band gap and the LUMO levels. The optical band gap, obtained from the absorption edges of absorption spectra in chlorobenzene solution (see Figure 4a) was found to be 1.86 eV for PPDB and 2.16 eV for PPDI. The resulting HOMO and LUMO energy levels and the band gaps are summarized in Table 3. UV/vis absorption measurements and cyclic voltammetry both demonstrate the effect of the benzimidazole unit in PPDB on optical and electronic properties. The  $\pi$ -conjugation system of the perylene core is enlarged due to the fused benzimidazole moiety in PPDB compared to PPDI, leading to an increase of delocalized  $\pi$ -electrons. Therefore, less energy is needed to excite an electron from the HOMO to the LUMO, which explains the bathochromic shift in absorption spectra and the lowered band gap of PPDB. Strong light harvesting in the visible range and favorable energy levels are important prerequisites for the

use in organic electronic devices such as photovoltaic cells. In addition, the charge carrier mobility is a crucial feature.

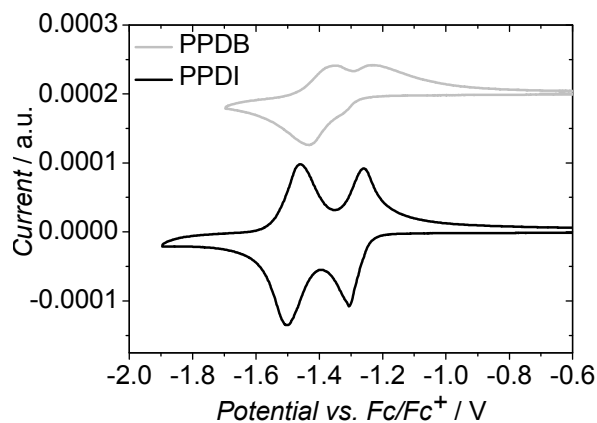


Figure 5: Cyclic voltammograms of PPDB and PPDI showing the first and second reduction peaks. The measurements were conducted in acetonitrile with respect to a ferrocene-ferrocenium couple ( $Fc/Fc^+$ ) at a scan rate of  $50 \text{ mVs}^{-1}$ .

Table 2: Number average molecular weight ( $M_n$ ), weight average molecular weight ( $M_w$ ), polydispersity indices (PDI), HOMO and LUMO energy values and calculated band gap ( $E_g$ ) of PPDB and PPDI.

	$M_n$	$M_w$	PDI	HOMO	LUMO	$E_g$
	[g/mol]	[g/mol]		[eV]	[eV]	[eV]
<b>PPDB</b>	9400	13300	1.4	-5.39	-3.53	1.86
<b>PPDI</b>	20400	35300	1.7	-5.68	-3.52	2.16

To determine the bulk charge carrier mobilities of both polymers, current-voltage  $I$ - $V$  characteristics of each material sandwiched between two electrodes were measured and the space-charge limited currents (SCLC) were fitted according to Mott-Gurney equation<sup>31</sup>,

$$J = \frac{9}{8} \varepsilon_0 \varepsilon_r \mu_0 \exp\left(0.89\gamma\sqrt{\frac{V}{L}}\right) \frac{V^2}{L^3} \quad (1)$$

where  $J$  is the current density,  $\epsilon_r$  is the dielectric constant of the polymer (assumed to be 3 in our calculations<sup>32</sup>),  $\epsilon_0$  is the permittivity of free space,  $\mu_0$  is the zero-field charge carrier mobility,  $\gamma$  is the field activation parameter,  $E$  is the electric field,  $L$  is the thickness of the polymer layer and  $V$  is the voltage drop across the device.

This method estimates the material's charge carrier mobility in bulk. In comparison, organic field effect transistor (OFET) measurements only measure the charge transport within a very narrow sheet at the interface with the gate insulator<sup>32-34</sup>. Charge carrier densities in OFET devices are orders of magnitudes higher than in organic solar cells or organic light emitting diodes. Since charge carrier mobilities depend on charge carrier densities, the mobility values obtained from OFETs do not necessarily describe the bulk carrier transport at low carrier densities like in OPV devices. Furthermore, initial testing of the two polymers under investigation in OFET devices show poor performance, which we attribute to potential unfavorable alignment of the active material in the channel of the transistor. This does not seem problematic for SCLC devices, since architecture and underlying layers are different from those of OFET devices. Two different types of SCLC devices were fabricated in order to determine both electron and hole mobilities of the perylene polymers. Electron-only devices based on PPDB and PPDI comprise a poly(3,4-ethylenedioxythiophene):poly(styrenesulfonate) (PEDOT:PSS) covered indium tin oxide (ITO) bottom contact and a calcium top electrode capped with aluminum. The device architecture is depicted in Figure 6a. Calcium has a work function of 2.9 eV and serves as an Ohmic contact for electron injection into the LUMO of PPDB and PPDI (~3.5 eV). Concurrently, the bottom contact does not hinder electrons from leaving the device. Hole-only devices (Figure 6b) were fabricated correspondingly with an ITO/PEDOT:PSS bottom contact, but with a gold top electrode instead of calcium. The low work function of gold (5.1 eV) provides a large mismatch with the LUMO of PPDB and PPDI, which prevents electron injection and therefore holes injected from the bottom electrode are the dominant charge carriers in these devices. The polymer layer thicknesses of those single carrier devices were varied from 300 nm to 650 nm.  $I$ - $V$  characteristics of the devices were recorded at up to 6 V at room temperature in inert gas atmosphere. The experimental data and the corresponding fits according to Equation 1 are shown in Figure 6c-f. For calculation, voltages were corrected

for a built-in potential of 2.2 eV from the difference in work function of calcium ( $\sim 2.9$  eV) and ITO/PEDOT:PSS ( $\sim 5.1$  eV) for electron-only devices<sup>35</sup>. At high voltages the current is space-charge limited only, assuming ohmic contacts to the injecting electrode. In this regime, the current density approximately scales with  $J \sim V^2$ , so the charge carrier mobility at zero-field  $\mu_0$  and the field activation parameter  $\gamma$  can be determined by fitting the curve according to Equation 1. The values obtained for  $\mu_0$  and  $\gamma$  for the best fits are summarized in Table 3. Inserting these values into Equation 2<sup>34</sup>

$$\mu = \mu_0 \cdot e^{\gamma \cdot \sqrt{E}} \quad (2)$$

yields the charge carrier mobilities  $\mu$  depending on the electric field within the device.

Table 3: SCLC charge carrier mobilities and associated field activation parameters for PPDB and PPDI.

	<b>Electron mobility</b>		<b>Hole mobility</b>			
	$\mu_{0e}$ [cm <sup>2</sup> V <sup>-1</sup> s <sup>-1</sup> ]	$\gamma$ [m <sup>0.5</sup> V <sup>0.5</sup> ]	$\mu_e$ [cm <sup>2</sup> V <sup>-1</sup> s <sup>-1</sup> ]	$\mu_{0h}$ [cm <sup>2</sup> V <sup>-1</sup> s <sup>-1</sup> ]	$\gamma$ [m <sup>0.5</sup> V <sup>0.5</sup> ]	$\mu_h$ [cm <sup>2</sup> V <sup>-1</sup> s <sup>-1</sup> ]
<b>PPDB</b>	$2.2 \cdot 10^{-7}$	$2.6 \cdot 10^{-3}$	<b><math>3.2 \cdot 10^{-4}</math></b>	$6.0 \cdot 10^{-8}$	$8.2 \cdot 10^{-4}$	<b><math>1.0 \cdot 10^{-6}</math></b>
<b>PPDI</b>	$2.3 \cdot 10^{-6}$	$6.8 \cdot 10^{-4}$	<b><math>1.9 \cdot 10^{-5}</math></b>	$1.6 \cdot 10^{-6}$	$1.5 \cdot 10^{-3}$	<b><math>1.5 \cdot 10^{-4}</math></b>

$\mu_0$  and  $\gamma$  values were obtained by fitting the  $J$ - $V$  curves of the single carrier devices according to equation 1.  $\mu$  was determined from equation 2 and the maximum electric field in the device.

Table 3 shows the charge carrier mobilities calculated for the maximum electric field. Using this method, the electron mobility  $\mu_e$  was found to be  $3.2 \cdot 10^{-4}$  cm<sup>2</sup>V<sup>-1</sup>s<sup>-1</sup> for PPDB and the hole mobility  $\mu_h$  was determined to be  $1.0 \cdot 10^{-6}$  cm<sup>2</sup>V<sup>-1</sup>s<sup>-1</sup>. The hole mobility is two orders of magnitude smaller than the electron mobility, thus this polymer can be considered an n-type semiconductor. PPDI shows an electron mobility of  $1.9 \cdot 10^{-5}$  cm<sup>2</sup>V<sup>-1</sup>s<sup>-1</sup> and a hole mobility of  $1.5 \cdot 10^{-4}$  cm<sup>2</sup>V<sup>-1</sup>s<sup>-1</sup>. The results from the SCLC measurements are summarized in Table 3. Interestingly, the hole mobility of PPDI is nearly one order of magnitude higher than its electron mobility. As a result, we assign PPDI to a new class of p-type materials. In contrast to perylene bisimides, which are well known electron acceptors because of their two electron withdrawing imide groups<sup>36</sup>, the perylene core of PPDI only contains one imide group. This

results in a less electron deficient character and therefore a more donor-type behavior. In comparison, the benzimidazole unit of PPDB provides enough electron deficiency in the heterocyclic aromatic system to enhance the electron-accepting properties of this material. We therefore demonstrate here, that the electronic character of perylene side chain polymers can be tuned by modifying the aromatic perylene core.

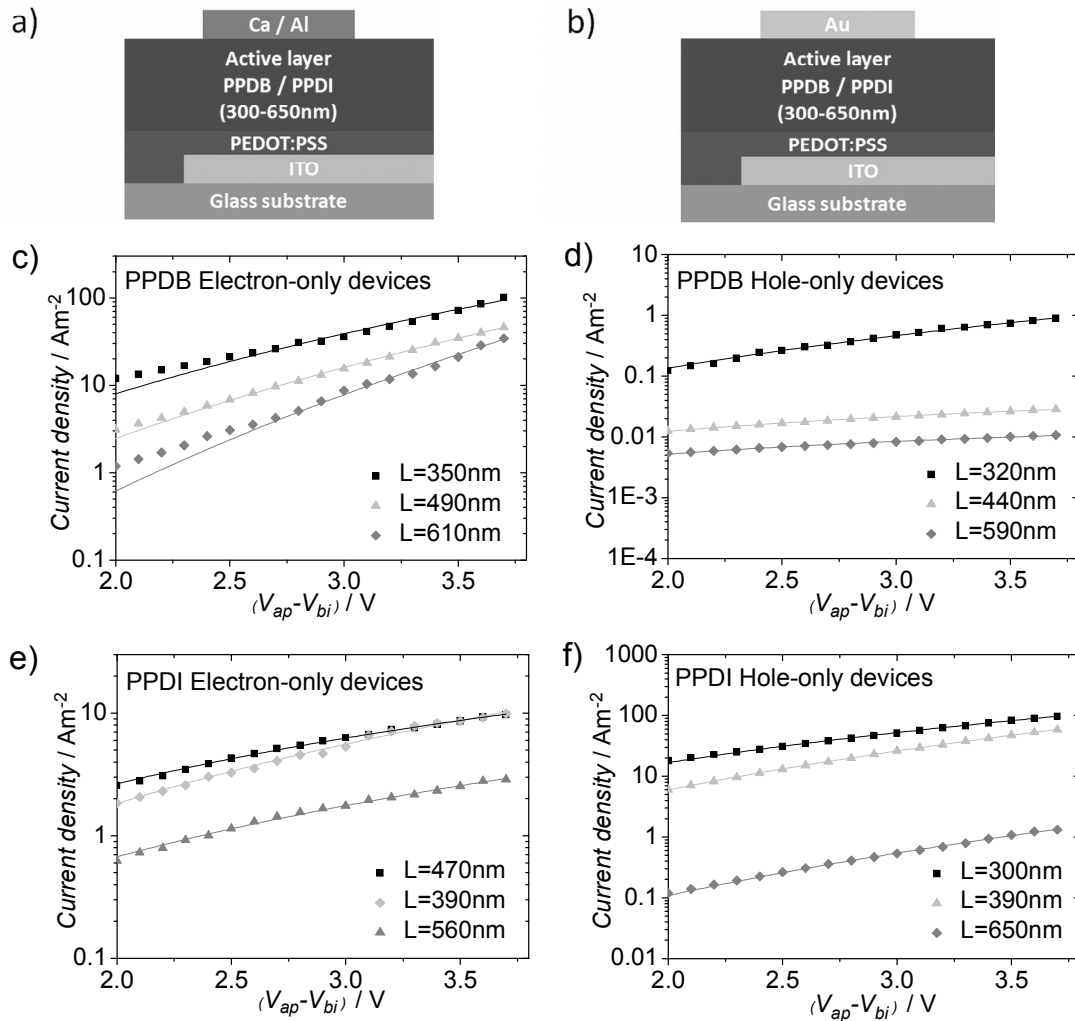


Figure 6: Scheme of an electron-only device with a calcium top electrode, capped with aluminum (a) and a hole-only device with gold top electrode (b); Current density  $J$  vs. voltage  $V$  plots (data points) and fits according to Equation 1 (straight lines) at room temperature for PPDB electron-only devices (c), PPDB hole-only devices (d), PPDI electron-only devices (e) and PPDI hole-only devices (f) with varied layer thicknesses  $L$ . The voltage applied ( $V_{ap}$ ) was corrected for a built in potential ( $V_{bi}$ ) of 2.2eV for electron-only devices resulting from the differences in work function of calcium and ITO/PEDOT:PSS.  $V_{bi}$  in hole-only devices was estimated to be 0eV.

## Conclusion

In summary, two novel liquid crystalline perylene diester side chain homopolymers were synthesized via nitroxide mediated radical polymerization (NMRP). We have demonstrated that changing the heterocyclic  $\pi$ -system permits access to materials with different electronic character. PPDB has n-type semiconducting properties with an electron mobility of  $3.2 \cdot 10^{-4} \text{ cm}^2 \text{ V}^{-1} \text{ s}^{-1}$ , whereas PPDI shows p-type behavior with the hole mobility being  $1.5 \cdot 10^{-4} \text{ cm}^2 \text{ V}^{-1} \text{ s}^{-1}$  as determined from SCLC measurements. Altering the aromatic system of the perylene core does not only affect the electrical properties of the investigated polymers. The absorption of PPDB in the visible range is notably broadened up to 670 nm compared to PPDI (580 nm), which is due to extension of  $\pi$ -conjugation of the perylene core by the benzimidazole unit of PPDB. The optical band gaps as determined by the absorption edge of UV/vis measurements and cyclic voltammetry were 1.86 eV for PPDB and 2.16 eV for PPDI with similar LUMO energy levels of -3.53 eV and -3.52 eV respectively. Furthermore, the ethyl hexyl substituents attached to the ester groups of the perylene core give excellent solubility in common organic solvents. These findings qualify the two polymers as potential materials for applications in optoelectronic devices, which will be the subject of future investigations. Thermotropic behavior of PPDB and PPDI were studied by polarized optical microscopy, differential scanning calorimetry and X-ray diffraction. Both polymers exhibit liquid crystalline mesophases over a broad temperature range.

## Experimental section

*Instrumentation:*  $^1\text{H-NMR}$  spectra were recorded using a Bruker AC 300 spectrometer (300 MHz) at 25 °C with deuterated chloroform as solvent and tetramethylsilane as an internal standard. Chemical shifts are reported in ppm, abbreviations used for splitting patterns are  $s$  = singlet,  $d$  = doublet,  $t$  = triplet,  $q$  = quartet,  $m$  = multiplet. FTIR data were recorded with a Perkin Elmer Spectrum 100 (FTIR) in the range of 400-4000  $\text{cm}^{-1}$ . Molecular weight determinations were carried out in chlorobenzene solution at 60 °C on an Agilent 1100 series GPC using two Polymer Laboratories mixed B columns in series. The system was calibrated against narrow weight PL polystyrene calibration standards. DSC

measurements were performed on a TA Q1000 under nitrogen with a heating and cooling rate of  $10 \text{ Kmin}^{-1}$ . Phase transitions were also examined by a polarized optical microscope (POM) Nikon Diaphot 300 with a Mettler FP 90 temperature controlled hot stage. X-ray diffraction measurements were performed on a Huber Guinier Diffraktometer 6000 equipped with a Huber quartz monochromator 611 with  $\text{Cu K}_{\alpha 1}$ :  $1.54051 \text{ \AA}$ . UV/vis spectra of solutions in chlorobenzene with a concentration of  $10^{-5} \text{ molL}^{-1}$  and thin films spin cast on quartz glass were recorded on a Hitachi 3000 spectrophotometer. Photoluminescence spectra were acquired on a Shimadzu RF 5301 PC spectrofluorophotometer upon excitation at 525 nm. Cyclic voltammetry (CV) was recorded on a Princeton Applied Research VersaSTAT 4 Potentiostat/Galvanostat using platinum electrodes at a scan rate of  $50 \text{ mVs}^{-1}$  and a  $\text{Ag/Ag}^+$  (0.10 M of  $\text{AgNO}_3$  in acetonitrile) reference electrode at  $25 \text{ }^\circ\text{C}$  in an anhydrous and nitrogen saturated solution of 0.1 M of tetrabutylammonium tetrafluoroborate ( $\text{Bu}_4\text{NBF}_4$ ) in acetonitrile. In these conditions, the oxidation potential of ferrocene was 0.10 V versus  $\text{Ag/Ag}^+$ , whereas the oxidation potential of ferrocene was 0.41 V versus saturated calomel electrode (SCE). The LUMO energy levels were determined from the reduction peak taking into account the SCE level at -4.7 eV. Film thicknesses were determined on an Alphastep 500 surface profilometer.

*Chemicals:* The starting materials, perylenetetracarboxylic acid dianhydride (PTCDA), 3 (bromomethyl)heptane, Aliquat 336, *p*-toluenesulfonic acid monohydrate, zinc acetate, 11-bromoundecanol, sodium cyanide, Raney-Ni, acryloyl chloride and solvents were purchased from Aldrich, Fluka or Acros and used without any further purification. Solvents used for precipitation and column chromatography were distilled prior to use. DMAc (anhydrous with crown cap, 99.5%), DMSO (anhydrous with crown cap, 99.5 %) and 1,2,4 trichlorobenzene (anhydrous with crown cap, 99.0%) were purchased from Aldrich. PEDOT:PSS (Clevios P VP Al 4083) was purchased from H.C. Starck.

The preparation of *tetra(2-ethylhexyl)-perylene-3,4,9,10-tetracarboxylate* (**1**) and *bis(2-ethylhexyl)-perylene-3,4,9,10-tetracarboxyl-monoanhydride* (**2**) was described recently by Wicklein *et al.*<sup>16</sup>. *11-bromoundecyl acrylate* (**5**) was prepared according to Lang *et al.*<sup>27</sup>. The initiator 2,2,5-trimethyl-3-(1-phenylethoxy)-4-phenyl-3-azahexan (**11**) and the free nitroxide

*N-tert-butyl- $\alpha$ -isopropyl- $\alpha$ -phenylnitroxid (12)* were synthesized according to published procedures<sup>26</sup>.

*Synthesis of 3,4 Diaminophenol (3):* 4-amino-3-nitrophenol (6.5 mmol, 1.00 g) and palladium on charcoal (0.10 g, 10 %) were added to methanol (55 mL) under inert gas atmosphere. The reaction flask was flushed with hydrogen twice before stirring the reaction mixture for 3.5 h at room temperature under hydrogen atmosphere. The solution was filtered through Celite under argon atmosphere. After the solvent was evaporated under reduced pressure, the product was obtained in quantitative yield as a brownish white solid, which was unstable in air and used immediately upon preparation.

*Synthesis of bis(2-ethylhexyl)-perylene-3,4-(4-hydroxy-1,2-benzimidazole)-9,10-dicarboxylate (4):* **2** (2.4 mmol, 1.50 g), zinc acetate (3.5 mmol, 0.65 g) and **3** (4.7 mmol, 0.59 g) were dissolved in dry DMAc (50 mL) in a microwave pressure tube. The condensation reaction was carried out under microwave irradiation conditions for 30 min at 150 °C and 100 W. The violet crude product was precipitated in methanol (300 mL) and filtered. The residue was washed with water (2x 30 mL) and methanol (3x 30 mL) and dried over night at 60 °C in vacuo. The crude product was purified by column chromatography (silica flashgel, eluent chloroform:methanol 9:1 v/v). Yield: 0.90 g (53 %) as a violet solid. <sup>1</sup>H NMR (300 MHz, CDCl<sub>3</sub>, 298 K,  $\delta$ ): 8.45-8.38 (m, 1H, H<sub>Ar</sub>), 8.32-8.09 (m, 5H, H<sub>Ar</sub>), 8.03-7.91 (m, 2H, H<sub>Ar</sub>), 7.64-7.57 (m, 1H, H<sub>Ar</sub>), 6.62-6.59 (m, 1H, OH), 6.42-6.28 (m, 2H, H<sub>Ar</sub>), 4.44-4.26 (m, 4H, OCH<sub>2</sub>), 1.96-1.80 (m, 2H, OCH<sub>2</sub>CH), 1.72-1.17 (m, 16H, CH<sub>2</sub>), 1.14-0.94 (m, 12H, CH<sub>3</sub>); IR (ATR):  $\nu$  = 3360 (b), 2960 (m), 2930 (m), 2860 (m), 1691 (s), 1593 (s), 1445 (m), 1362 (s), 1260 (s), 1171 (s), 804 (s), 745 (s) cm<sup>-1</sup>.

*Synthesis of bis(2-ethylhexyl)-perylene-3,4-(4-undecyloxyacrylic acid-1,2-benzimidazole)-9,10-dicarboxylate (6):* **4** (0.7 mmol, 0.51 g), **5** (1.4 mmol, 0.43 g), potassium carbonate (1.4 mmol, 0.19 g) and potassium iodide (0.14 mmol, 0.02 g) were dissolved in dry DMAc (20 mL) and stirred for 24 h at 85 °C under argon atmosphere. The crude product was precipitated in a mixture of methanol and water (MeOH:H<sub>2</sub>O 3:1 v/v, 150 mL), filtered and washed (2x MeOH:H<sub>2</sub>O 3:1 v/v, 30 mL). The residue was dried over night at 60 °C in vacuo. The crude product was purified by column chromatography (silica flashgel, eluent

chloroform:acetone 95:5 v/v). Yield: 0.59 g (88 %) as a violet solid.  $^1\text{H}$  NMR (300 MHz,  $\text{CDCl}_3$ , 298 K,  $\delta$ ): 8.74-8.62 (m, 2H,  $\text{H}_{\text{Ar}}$ ), 8.48-8.31 (m, 5H,  $\text{H}_{\text{Ar}}$ ), 8.10-8.01 (m, 2H,  $\text{H}_{\text{Ar}}$ ), 7.30 (m, 1H,  $\text{H}_{\text{Ar}}$ ), 7.07-7.00 (m, 1H,  $\text{H}_{\text{Ar}}$ ), 6.42 (dd,  $^2J = 17.3$  Hz,  $^3J = 1.6$  Hz, 1H, acryl- $\text{CH}_2$ ), 6.14 (dd,  $^2J = 17.3$  Hz,  $^3J = 10.4$  Hz, 1H, acryl-CH), 5.83 (dd,  $^2J = 10.4$  Hz,  $^3J = 1.5$  Hz, 1H, acryl- $\text{CH}_2$ ), 4.37-4.25 (m, 4H,  $\text{OCH}_2$ ), 4.18 (t,  $J = 6.8$  Hz, 2H, acryl- $\text{OCH}_2$ ), 4.07 (m, 2H, benzimidazole- $\text{OCH}_2$ ), 1.94-1.77 (m, 4H,  $\text{OCH}_2\text{CH}$ , benzimidazole- $\text{OCH}_2\text{CH}_2$ ), 1.75-1.63 (m, 2H, acryl- $\text{OCH}_2\text{CH}_2$ ), 1.60-1.24 (m, 30H,  $\text{CH}_2$ ), 1.06-0.88 (m, 12H,  $\text{CH}_3$ ); IR (ATR):  $\nu = 2926$  (s), 2856 (m), 1712 (s), 1688 (s), 1592 (m), 1466 (m), 1268 (s), 1171 (s), 1062 (m), 804 (s), 742 (m)  $\text{cm}^{-1}$ .

*Synthesis of 12-hydroxydodecanenitrile*: the synthesis was adapted from the work of Jaeger *et al.*<sup>37</sup>. A mixture of 11-bromoundecanol (20.0 mmol, 5.00 g), sodium cyanide (38.9 mmol, 1.91 g) and DMSO (75 mL) was stirred for 24 h at 90 °C. Then the reaction mixture was added to water (150 mL) and extracted four times with DCM (4x 100 mL). The combined extracts were washed six times with water, dried over sodium sulfate and the solvent was removed on the rotary evaporator to give 3.85 g (98 %) of the product.  $^1\text{H}$  NMR (300 MHz,  $\text{CDCl}_3$ , 298 K,  $\delta$ ): 3.65 (q,  $J = 6.3$  Hz, 2H,  $\text{CH}_2\text{O}$ ), 2.35 (t,  $J = 7.1$  Hz, 2H,  $\text{CH}_2\text{CN}$ ), 1.74-1.52 (m, 5H,  $\text{CH}_2\text{CH}_2\text{CN}$ , OH), 1.51-1.40 (m, 2H,  $\text{CH}_2\text{CH}_2\text{O}$ ), 1.38-1.24 (br s, 12H,  $(\text{CH}_2)_6$ ); IR (ATR):  $\nu = 3383$  (m), 2919 (s), 2851 (s), 2248 (m), 1470 (s), 1335 (m), 1053 (s), 1013 (m), 722 (s)  $\text{cm}^{-1}$ .

*Synthesis of 12-aminododecan-1-ol (7)*: the synthesis was adapted from the work of Jaeger *et al.*<sup>37</sup>. A mixture of 12-hydroxydodecanenitrile (19.3 mmol, 3.80 g), Raney-Ni (38.9 mmol, 5.00 g), ethanol (80 mL, 95 %) and concentrated ammonium hydroxide (50 mL, 25 %) was stirred under hydrogen atmosphere for 20 h at room temperature. Then the reaction mixture was filtered through a pad of Celite, which was washed with ethanol (50 mL, 95 %). The combined filtrates were concentrated on the rotary evaporator to give 3.6 g (95 %) of 7.  $^1\text{H}$  NMR (300 MHz,  $\text{CDCl}_3$ , 298 K,  $\delta$ ): 3.65 (t,  $J = 6.5$  Hz, 2H,  $\text{CH}_2\text{O}$ ), 2.71 (br s, 2H,  $\text{NH}_2$ ), 1.64-1.52 (m, 2H,  $\text{CH}_2\text{CH}_2\text{NH}_2$ ), 1.51-1.41 (m, 2H,  $\text{CH}_2\text{CH}_2\text{O}$ ), 1.29 (br s, 19H, OH,  $(\text{CH}_2)_9$ ); IR (ATR):  $\nu = 3329$  (m), 3286 (m), 2917 (s), 2849 (s), 1614 (m), 1470 (s), 1372 (m), 1065 (s), 1044 (m), 999 (m), 855 (w), 828 (w), 719 (s)  $\text{cm}^{-1}$ .

*Synthesis of N-(dodecyl-1-ol)-bis(2-ethylhexyl)-perylene-3,4,9,10-tetracarboxyl-monoimide (8)*: A mixture of **2** (6.0 mmol, 3.86 g), imidazole (350 mmol, 24 g) and **7** (9.1 mmol, 1.84 g) was stirred for 2 h at 130 °C. After cooling to room temperature the mixture was dissolved in THF (1 mL), precipitated in water (200 mL) and filtered. The residue was washed with water (2x 30 mL) and dried over night at 60 °C in vacuo. The crude product was purified by column chromatography (silica flashgel, eluent chloroform:acetone 20:1 v/v). Yield: 4.47 g (90 %) as a orange-red solid. <sup>1</sup>H NMR (300 MHz, CDCl<sub>3</sub>, 298 K, δ): 8.63 (d, *J* = 8.0 Hz, 2H, H<sub>Ar</sub>), 8.47 (dd, <sup>2</sup>*J* = 8.2 Hz, <sup>3</sup>*J* = 4.6 Hz, 4H, H<sub>Ar</sub>), 8.10 (d, *J* = 7.9 Hz, 2H, H<sub>Ar</sub>), 4.38-4.27 (m, 4H, OCH<sub>2</sub>), 4.25-4.16 (m, 2H, OCH<sub>2</sub>), 3.70-3.62 (m, 2H, NCH<sub>2</sub>), 1.87-1.72 (m, 4H, OCH<sub>2</sub>CH, OCH<sub>2</sub>), 1.61-1.22 (m, 35H, CH<sub>2</sub>, OH), 1.04-0.88 (m, 12H, CH<sub>3</sub>); IR (ATR):  $\nu$  = 3505 (w), 2924 (s), 2854 (m), 1695 (s), 1652 (s), 1593 (s), 1511 (m), 1356 (m), 1294 (s), 1261 (s), 1171 (s), 1076 (s), 956 (m), 846 (m), 806 (m), 745 (s) cm<sup>-1</sup>.

*Synthesis of N-(dodecylacrylic acid)-bis(2-ethylhexyl)-perylene-3,4,9,10-tetracarboxyl-monoimide (10)*: **8** (4.3 mmol, 3.5 g) was dissolved in dry THF (120 mL) under argon atmosphere and potassium carbonate (8.6 mmol, 1.18 g) were added. Acyloyl chloride (19.3 mmol, 1.74 g) was added dropwise at 0 °C and the reaction mixture was stirred for 20 h at 60 °C. The mixture was poured into water (100 mL) and the crude product was extracted with chloroform (3x 100 mL). The combined extracts were washed with water (3x 100 mL), dried over sodium sulfate and the solvent was removed on the rotary evaporator. The crude product was purified by column chromatography (silica flashgel, eluent chloroform:acetone 20:1 v/v). Yield: 2.50 g (67 %) as a orange-red solid. <sup>1</sup>H NMR (300 MHz, CDCl<sub>3</sub>, 298 K, δ): 8.62 (d, *J* = 8.0 Hz, 2H, H<sub>Ar</sub>), 8.45 (dd, <sup>2</sup>*J* = 8.2 Hz, <sup>3</sup>*J* = 3.3 Hz, 4H, H<sub>Ar</sub>), 8.09 (d, *J* = 7.9 Hz, 2H, H<sub>Ar</sub>), 6.41 (dd, <sup>2</sup>*J* = 17.3 Hz, <sup>3</sup>*J* = 1.6 Hz, 1H, acryl-CH<sub>2</sub>), 6.13 (dd, <sup>2</sup>*J* = 17.3 Hz, <sup>3</sup>*J* = 10.4 Hz, 1H, acryl-CH), 5.82 (dd, <sup>2</sup>*J* = 10.4 Hz, <sup>3</sup>*J* = 1.5 Hz, 1H, acryl-CH<sub>2</sub>), 4.38-4.26 (m, 4H, OCH<sub>2</sub>), 4.25-4.10 (m, 4H, acryl-OCH<sub>2</sub>, NCH<sub>2</sub>), 1.89-1.74 (m, 4H, OCH<sub>2</sub>CH, acryl-OCH<sub>2</sub>CH<sub>2</sub>), 1.74-1.60 (m, 2H, NCH<sub>2</sub>CH<sub>2</sub>), 1.58-1.21 (m, 32H, CH<sub>2</sub>), 1.05-0.86 (m, 12H, CH<sub>3</sub>); IR (ATR):  $\nu$  = 2957 (m), 2925 (s), 2855 (s), 1723 (s), 1695 (s), 1652 (s), 1593 (s), 1511 (m), 1356 (s), 1294 (s), 1260 (s), 1171 (s), 1076 (s), 984 (m), 961 (m), 847 (m), 806 (s), 745 (s) cm<sup>-1</sup>.

*Synthesis of Poly(perylene diester benzimidazole acrylate) (PPDB):* A mixture of **6** (1.0 mmol, 740 mg), **11** (0.01 mmol, 3.2 mg), **12** (0.001 mmol, 0.22 mg) and 1,2,4-Trichlorobenzene (1250  $\mu$ L) was degassed by three freeze/thaw cycles, sealed under argon and heated for 50 h at 125 °C. The reaction mixture was cooled, dissolved in chloroform (4 mL), precipitated in acetone (250 mL) and filtered. The residue was dried and further purified by Soxhlet extraction with methyl ethyl ketone. Yield: 0.26 g (35 %) as a violet powder. GPC:  $M_n = 9400 \text{ g}\cdot\text{mol}^{-1}$ ,  $M_w = 13300 \text{ g}\cdot\text{mol}^{-1}$ , PDI = 1.4.

*Synthesis of Poly(perylene diester imide acrylate) (PPDI):* A mixture of **10** (1.7 mmol, 1500 mg), **11** (0.017 mmol, 5.3 mg), **12** (0.0017 mmol, 0.37 mg) and 1,2,4-Trichlorobenzene (915  $\mu$ L) were degassed by three freeze/thaw cycles, sealed under argon and heated for 50 h at 125 °C. The reaction mixture was cooled, dissolved in chloroform (3 mL), precipitated in methanol (250 mL) and filtered. The residue was dried and further purified by Soxhlet extraction with acetone. Yield: 0.48 g (32 %) as a orange powder. GPC:  $M_n = 20400 \text{ g}\cdot\text{mol}^{-1}$ ,  $M_w = 35300 \text{ g}\cdot\text{mol}^{-1}$ , PDI = 1.7.

*SCLC devices:* SCLC electron-only devices were fabricated using the following structure: glass/ ITO/ PEDOT:PSS/ polymer/ Ca/Al. SCLC hole-only devices were fabricated using the following structure: glass/ ITO/ PEDOT:PSS/ polymer/ Au. Commercial ITO coated glass substrates with a sheet resistance of 13 Ohms per sq (Lumtec) were cleaned using following sequence in an ultrasonic bath: water, acetone and 2-propanol. Each ITO substrate was patterned using photolithography techniques. After ozone treatment of the substrates for 5 min, PEDOT:PSS was spin-coated on the ITO surface and dried at 130 C for 30 min. All following steps were carried out under nitrogen atmosphere with water and oxygen levels  $\leq 0.1$  ppm. After cooling the substrate, the polymer layer was blade coated from chloroform solutions. The substrates were then put in a thermal evaporation chamber to evaporate the top electrode (30 nm Ca/ 100 nm Al for electron-only devices, 80 nm Au for hole-only devices) under high vacuum ( $1\cdot 10^{-6}$  mbar) through a shadow mask (active area 4 mm<sup>2</sup>). The current-voltage characteristics of the devices were measured using a Keithley 2420 (I-V) Digital SourceMeter at 25 °C.

## Acknowledgment

Financial support from Merck Chemicals Ltd. and EU-India project “largecells” is kindly acknowledged.

## References

- (1) Chua, L.-L.; Zaumseil, J.; Chang, J.-F.; Ou, E. C. W.; Ho, P. K. H.; Siringhaus, H.; Friend, R. H., *Nature* **2005**, *434*, (7030), 194-199.
- (2) Coakley, K. M.; McGehee, M. D., *Chemistry of Materials* **2004**, *16*, (23), 4533-4542.
- (3) Liang, Y.; Xu, Z.; Xia, J.; Tsai, S. T.; Wu, Y.; Li, G.; Ray, C.; Yu, L., *Advanced Materials* **22**, (20), E135-E138.
- (4) Chen, Z.; Zheng, Y.; Yan, H.; Facchetti, A., *Journal of the American Chemical Society* **2008**, *131*, (1), 8-9.
- (5) Yan, H.; Chen, Z.; Zheng, Y.; Newman, C.; Quinn, J. R.; Dotz, F.; Kastler, M.; Facchetti, A., *Nature* **2009**, *457*, (7230), 679-686.
- (6) Zhan, X.; Tan, Z. a.; Domercq, B.; An, Z.; Zhang, X.; Barlow, S.; Li, Y.; Zhu, D.; Kippelen, B.; Marder, S. R., *Journal of the American Chemical Society* **2007**, *129*, (23), 7246-7247.
- (7) Koppe, M.; Egelhaaf, H. J.; Dennler, G.; Scharber, M. C.; Brabec, C. J.; Schilinsky, P.; Hoth, C. N., *Advanced Functional Materials* **20**, (2), 338-346.
- (8) Kang, J.; Shin, N.; Jang, D. Y.; Prabhu, V. M.; Yoon, D. Y., *Journal of the American Chemical Society* **2008**, *130*, (37), 12273-12275.
- (9) Jancy, B.; Asha, S. K., *The Journal of Physical Chemistry B* **2006**, *110*, (42), 20937-20947.
- (10) Avlasevich, Y.; Li, C.; Mullen, K., *Journal of Materials Chemistry* **2010**, *20*, (19), 3814-3826.
- (11) Jones, B. A.; Facchetti, A.; Wasielewski, M. R.; Marks, T. J., *Journal of the American Chemical Society* **2007**, *129*, (49), 15259-15278.
- (12) Hüttner, S.; Sommer, M.; Thelakkat, M., *Applied Physics Letters* **2008**, *92*, (9), 093302-3.
- (13) Shoaee, S.; An, Z.; Zhang, X.; Barlow, S.; Marder, S. R.; Duffy, W.; Heeney, M.; McCulloch, I.; Durrant, J. R., *Chemical Communications* **2009**, (36), 5445-5447.

- (14) Dittmer, J. J.; Marseglia, E. A.; Friend, R. H., *Advanced Materials* **2000**, *12*, (17), 1270-1274.
- (15) Wicklein, A.; Lang, A.; Muth, M.; Thelakkat, M., *Journal of the American Chemical Society* **2009**, *131*, (40), 14442-14453.
- (16) Wicklein, A.; Muth, M.-A.; Thelakkat, M., *Journal of Materials Chemistry* **2010**.
- (17) Schmidt-Mende, L.; Fechtenkötter, A.; Mullen, K.; Moons, E.; Friend, R. H.; MacKenzie, J. D., *Science* **2001**, *293*, (5532), 1119-1122.
- (18) Li, J. L.; Kastler, M.; Pisula, W.; Robertson, J. W. F.; Wasserfallen, D.; Grimsdale, A. C.; Wu, J. S.; Müllen, K., *Advanced Functional Materials* **2007**, *17*, (14), 2528-2533.
- (19) Sergeev, S.; Pisula, W.; Geerts, Y. H., *Chemical Society Reviews* **2007**, *36*, (12), 1902-1929.
- (20) Carrasco-Orozco, M.; Tsoi, W. C.; O'Neill, M.; Aldred, M. P.; Vlachos, P.; Kelly, S. M., *Advanced Materials* **2006**, *18*, (13), 1754-1758.
- (21) Levermore, P. A.; Jin, R.; Wang, X.; de Mello, J. C.; Bradley, D. D. C., *Advanced Functional Materials* **2009**, *19*, (6), 950-957.
- (22) McCulloch, I.; Heeney, M.; Bailey, C.; Genevicius, K.; MacDonald, I.; Shkunov, M.; Sparrowe, D.; Tierney, S.; Wagner, R.; Zhang, W.; Chabinyc, M. L.; Kline, R. J.; McGehee, M. D.; Toney, M. F., *Nature Materials* **2006**, *5*, (4), 328-333.
- (23) Lindner, S. M.; Thelakkat, M., *Macromolecules* **2004**, *37*, (24), 8832-8835.
- (24) Lang, A. S.; Kogler, F. R.; Sommer, M.; Wiesner, U.; Thelakkat, M., *Macromolecular Rapid Communications* **2009**, *30*, (14), 1243-1248.
- (25) Zhang, Q.; Cirpan, A.; Russell, T. P.; Emrick, T., *Macromolecules* **2009**, *42*, (4), 1079-1082.
- (26) Benoit, D.; Chaplinski, V.; Braslau, R.; Hawker, C. J., *Journal of the American Chemical Society* **1999**, *121*, (16), 3904-3920.
- (27) Lang, A. S.; Neubig, A.; Sommer, M.; Thelakkat, M., *Macromolecules* **2010**, *43*, (17), 7001-7010.
- (28) Laschat, S.; Baro, A.; Steinke, N.; Giesselmann, F.; Hägele, C.; Scalia, G.; Judele, R.; Kapatsina, E.; Sauer, S.; Schreivogel, A.; Tosoni, M., *Angewandte Chemie International Edition* **2007**, *46*, (26), 4832-4887.
- (29) Sommer, M.; Hüttner, S.; Wunder, S.; Thelakkat, M., *Advanced Materials* **2008**, *20*, (13), 2523-2527.

- (30) Pommerehne, J.; Vestweber, H.; Guss, W.; Mahrt, R. F.; Bäessler, H.; Porsch, M.; Daub, J., *Advanced Materials* **1995**, 7, (6), 551-554.
- (31) Blom, P. W. M.; Tanase, C.; Leeuw, D. M. d.; Coehoorn, R., Thickness scaling of the space-charge-limited current in poly(*p*-phenylene vinylene). In AIP: 2005; Vol. 86, p 092105.
- (32) Goh, C.; Kline, R. J.; McGehee, M. D.; Kadnikova, E. N.; Frechet, J. M. J., *Applied Physics Letters* **2005**, 86, (12), 122110-3.
- (33) Steyrlleuthner, R.; Schubert, M.; Jaiser, F.; Blakesley, J. C.; Chen, Z.; Facchetti, A.; Neher, D., *Advanced Materials* **2010**, 22, (25), 2799-2803.
- (34) An, Z.; Yu, J.; Domercq, B.; Jones, S. C.; Barlow, S.; Kippelen, B.; Marder, S. R., *Journal of Materials Chemistry* **2009**, 19, (37), 6688-6698.
- (35) Mihailetschi, V. D.; van Duren, J. K. J.; Blom, P. W. M.; Hummelen, J. C.; Janssen, R. A. J.; Kroon, J. M.; Rispens, M. T.; Verhees, W. J. H.; Wienk, M. M., *Advanced Functional Materials* **2003**, 13, (1), 43-46.
- (36) Alibert-Fouet, S.; Seguy, I.; Bobo, J.-F.; Destruel, P.; Bock, H., *Chemistry – A European Journal* **2007**, 13, (6), 1746-1753.
- (37) Jaeger, D. A.; Jose, R.; Mendoza, A.; Apkarian, R. P., *Colloids and Surfaces A: Physicochemical and Engineering Aspects* **2007**, 302, (1-3), 186-196.

## 5. Pendant Perylene Polymers with High Electron Mobility

*Andreas S. Lang<sup>a</sup>, Mathis-Andreas Muth<sup>a,b</sup>, Miguel Carrasco-Orozco<sup>b</sup> and Mukundan Thelakkat<sup>a\*</sup>*

[a] Prof. Dr. Mukundan Thelakkat, Applied Functional Polymers, Department of Macromolecular Chemistry I, University of Bayreuth, Universitaetsstr.30, 95440 Bayreuth (Germany)

[b] Dr. Miguel Carrasco-Orozco, Merck Chemicals Ltd., Chilworth Technical Centre, University Parkway, Southampton SO16 7QD (UK)

\*corresponding author: mukundan.thelakkat@uni-bayreuth.de

This manuscript is published in *Journal of Polymer Science: Polymer Physics*.

(DOI: 10.1002/polb.23357)

## Abstract

Four different perylene side chain semiconductor polymers, synthesized by a combination of “click” chemistry and nitroxide mediated radical polymerization (NMRP), are presented. The nature of the solubilizing side chains and the chromophoric  $\pi$ -conjugation system of the pendant perylene moieties are systematically changed. We investigate the impact of these modifications on optical and charge transport properties by UV/vis spectroscopy and space-charge-limited current (SCLC) measurements, respectively. Furthermore, thermal behavior is studied by differential scanning calorimetry (DSC), polarized optical microscopy (POM) and X-ray diffraction measurements (XRD). Cyclic voltammetry is used to estimate HOMO and LUMO levels. For the synthesis, the same parent scaffold polymer, poly(propargyloxystyrene) is “clicked” with the four different perylene chromophores. We compare here two poly(peryene bisimide)s with hydrophobic (PPBI 1) and hydrophilic substituents (PPBI 2) with newly synthesized poly(peryene diester benzimidazole), PPDEB and poly(peryene diester imide), PPDEI. The new polymers exhibit narrow molecular weight distributions of 1.09 and molecular weights around  $M_{n,SEC} = 15000 \text{ g}\cdot\text{mol}^{-1}$  and  $26000 \text{ g}\cdot\text{mol}^{-1}$  in SEC. The extended  $\pi$ -conjugation system of PPDEB leads to a broader absorption in the visible region compared to PPDEI and PPBIs. While absorption properties of PPDEB could be considerably improved by varying the perylene core, the charge carrier mobility could be drastically improved by tuning the substituents. Very high electron mobilities of  $1 \times 10^{-2} \text{ cm}^2\text{V}^{-1}\text{s}^{-1}$  were achieved for PPBI 2 carrying oligoethylenglycol substituents. The differences in charge transport properties are due to different packing and order in solid state, as studied by DSC and XRD. PPDEB and PPDEI exhibit a liquid crystalline (LC) mesophase at room temperature. For PPBI 1, the results are indicative for a LC SmC bilayer structure, whereas PPBI 2 is an amorphous polymer.

## Introduction

Solution processable organic materials for semiconductor applications such as organic light emitting diodes<sup>1</sup>, organic field effect transistors<sup>2</sup> and organic photovoltaic devices<sup>3</sup> is a field of intensive research. The majority of the semiconductor materials available are good hole

transporting materials (p-type), while the number of suitable electron transporting materials (n-type) is still limited<sup>4-6</sup>. For solar cell applications, the most efficient devices are currently based on polymer/fullerene blends, where fullerene small molecules (such as PCBM) serve as the n-type semiconductor<sup>7</sup>. Generally, materials used in organic photovoltaic devices require high charge carrier mobility and good light harvesting properties in the visible range, in combination with adequate solubility and film forming properties. The visible light absorption of PCBM however is relatively poor and small molecules in general can reveal problematic thin film formation<sup>8</sup>, which illustrates the need for alternative n-type polymers. In this context perylene bisimides (PBI) and related molecules such as perylene diester benzimidazole (PDEB) and perylene diester imide (PDEI) with their favorable absorption properties in the visible wavelength regime are a promising class of semiconductor dyes. Besides PBI, PDEI and PDEB have already been incorporated in side chain polymers.<sup>9,10</sup> While PDEB shows an enhanced absorption up to 700 nm,<sup>11, 12</sup> PDEI absorption is blue shifted compared to PBI. Although polymers carrying diverse perylene chromophores as pendant group can be synthesized by direct nitroxide mediated radical polymerization from their acrylate monomers,<sup>9, 10, 13, 14</sup> these polymerizations have some drawbacks. They have to be conducted in highly concentrated solutions at high temperatures. Furthermore, they are difficult to control and usually show broad PDIs, even under controlled radical polymerization conditions. We found out, that this is due to transfer reactions occurring in the polymerization as observed in the polymerization of PBI acrylates.<sup>15</sup> The polymer analogous functionalization of alkyne bearing polymers by “click” chemistry allows the easy and fast synthesis of quite complex polymer architectures.<sup>16</sup> We have already shown that differently substituted poly(peryene bisimide)s can be synthesized by such methods.<sup>15, 17</sup>

In this article, we use the “click” chemistry approach to synthesize two new homopolymers poly(peryene diester benzimidazole) (PPDEB) and poly(peryene diester imide) (PPDEI), where the pendant perylene groups are varied to tune the optical properties. The synthesis is described in the first part of this publication. The new materials are compared to recently published PPBI 1 with hydrophobic alkyl swallow-tail and PPBI 2 with hydrophilic oligoethylenglycol (OEG) swallow-tail substituents<sup>17</sup>, respectively. We demonstrated lately, that OEG swallow-tail groups attached to the imide position of PBI small molecules can

change the thermotropic properties drastically<sup>18</sup>. Due to the higher flexibility of OEG substituents compared to alkyl groups, strong crystallization due to  $\pi$ - $\pi$  interaction of the perylene cores could be suppressed and the formation of liquid crystalline phases was supported. Herein, this concept is transferred from PBI small molecules to polymers bearing pendant PBI groups. The chemical structures of these two “clicked” PBI polymers PPBI 1 and PPBI 2 along with the novel polymers with modified perylene units PPDEB and PPDEI are shown in Figure 1. Since the same parent scaffold polymer was used for “clicking” the different perylene derivatives, the identical polymer backbones and hence polydispersities of all four compounds under investigation allow for a comparative study of their optical and charge transport properties. This is the focus of the second part of this article. Furthermore, energy levels of these polymers are determined by cyclic voltammetry and thermotropic behavior is studied by DSC, polarized optical microscopy and X-ray diffraction measurements.

## Experimental section

### General

The perylene diester benzimidazole (PDEB-OH) and the perylene diester anhydride were synthesized according to a literature procedure.<sup>10</sup> 6-azido-1-hexanol was synthesized according to a reference.<sup>17</sup> Dimethylformamide (99.8%) was purchased from Sigma-Aldrich. PMDETA ( $\geq 98\%$ ) was purchased from Fluka. CuBr (98%) was purchased from Acros. All reagents were used without further purification unless otherwise noted.

### Synthesis

*Perylene diester NH-imide:* Perylene diester anhydride (1800 mg, 2.84 mmol) and ammonium decanoate (1.73 g, 8.5 mmol) were added to molten imidazole (16 g) at 120 °C. The reaction was stirred for 1 h. Subsequently, the reaction was cooled to 90 °C and 150 mL of H<sub>2</sub>O were added to dissolve the imidazole. The perylene diester NH-imide was filtered off and dried. The product was obtained as a orange solid and weighed 1.57 g (87%). <sup>1</sup>H NMR

(300 MHz, CHCl<sub>3</sub>):  $\delta$  (ppm) 8.98 (s, 1H, NH), 8.37 (d, 2H,  $J = 7.3$  Hz, ArH), 8.15 (dd, 4H,  $J = 11.8$  Hz,  $J = 8.5$  Hz, ArH), 7.95 (d, 2H,  $J = 7.4$  Hz, ArH), 4.38-4.24 (m, 4 H, COOCH<sub>2</sub>), 1.94-1.18 (m, CH<sub>2</sub>), 1.11-0.76 (m, 12H, CH<sub>3</sub>).

*Perylene diester imide azide PDEI-N<sub>3</sub>*: Perylene diester NH-imide (500 mg, 0.79 mmol), 1-bromo-6-azido hexane (230 mg, 1.10 mmol) and K<sub>2</sub>CO<sub>3</sub> (196 mg, 1.42 mmol) were added in 8 mL of DMF. The reaction was heated to 100 °C for 2 d, precipitated in MeOH/H<sub>2</sub>O and purified by column chromatography over silica with cyclohexane : ethyl acetate 2:1 v/v. The product was obtained as a orange waxy solid and weighed 340 mg (56 %). <sup>1</sup>H NMR (300 MHz, CHCl<sub>3</sub>):  $\delta$  (ppm) 8.20 (d, 2H,  $J = 7.3$  Hz, ArH), 7.96 (d, 2H,  $J = 7.7$  Hz, ArH), 7.87 (dd, 4H,  $J = 11.8$ ,  $J = 8.11$  Hz, ArH), 4.38-4.24 (m, 2H, N-CH<sub>2,perylene</sub>), 4.17-4.07 (m, 4 H, COOCH<sub>2</sub>), 3.30 (t, 2H,  $J = 7.0$  Hz, m, 2H, N-CH<sub>2,azide</sub>), 1.91-1.31 (m, CH<sub>2</sub>), 1.07-0.90 (m, 12H, CH<sub>3</sub>).

*Perylene diester benzimidazole azide PDEB-N<sub>3</sub>*: PDEB-OH (1000 mg, 1.38 mmol), 1-bromo-6-azido hexane (569 mg, 2.76 mmol) and K<sub>2</sub>CO<sub>3</sub> (343 mg, 2.48 mmol) were dissolved in 35 mL of DMF. The reaction was heated to 85 °C for 2 d, precipitated in H<sub>2</sub>O and filtered. The pure purple product weighed 1123 mg (96%). <sup>1</sup>H NMR (300 MHz, CHCl<sub>3</sub>):  $\delta$  (ppm) 8.92-6.91 (m, 8H, ArH), 4.31-4.20 (m, 4 H, COOCH<sub>2</sub>), 4.19-4.04 (m, 2H, OCH<sub>2</sub>) 3.38-3.28 (m, 2H, CH<sub>2</sub>N<sub>3</sub>), 1.98-1.27 (m, 26H, CH<sub>2</sub>), 1.07-0.85 (m, 12H, CH<sub>3</sub>).

### General procedure for the preparation of “click” polymers

*Poly(perylene diester benzimidazole) (PPDEB)*: PDEB-N<sub>3</sub> (65 mg, 0.076 mmol) and poly(propargyloxystyrene) (10 mg, 0.063 mmol) were dissolved in 4 mL of anisole. The mixture was degassed by purging with nitrogen for 10 min. Subsequently, one drop of a degassed stock solution of anisole/PMDETA/CuBr was added. The reaction was stirred over night. The substance was precipitated in MeOH, filtered and cleaned from residual azide by soxhlet extraction with methyl ethyl ketone. The pure product was obtained as a purple powder. <sup>1</sup>H NMR (300 MHz, CHCl<sub>3</sub>):  $\delta$  (ppm) 8.11-7.23 (br s, 9H, ArH<sub>perylene</sub>, ArH<sub>triazole</sub>), 6.96-6.26 (br s, 4H, ArH<sub>styrene</sub>), 5.15 (br s, 2H, O<sub>Sty</sub>CH<sub>2</sub>), 4.43 (br s, 2H, N<sub>triazole</sub>CH<sub>2</sub>), 4.27 (br

s, 4H, 2COOCH<sub>2</sub>), 4.00 (br s, 2H, N<sub>perylene</sub>CH<sub>2</sub>), 2.03-1.10 (m, 29H, 14CH<sub>2</sub>, CH<sub>backbone</sub>), 1.12-0.84 (m, 12H, CH<sub>3</sub>).

*Poly(perylene diester imide) (PPDEI)*: PDEI-N<sub>3</sub> (58 mg, 0.076 mmol) and poly(propargyloxystyrene) (10 mg, 0.063 mmol) were dissolved in 4 mL of anisole. The mixture was degassed by purging with nitrogen for 10 min. Subsequently, one drop of a degassed stock solution of anisole/PMDETA/CuBr was added. The reaction was stirred overnight. The substance was precipitated in MeOH, filtered and cleaned from residual azide by soxhlet extraction with methyl ethyl ketone. The pure product was obtained as an orange powder. <sup>1</sup>H NMR (300 MHz, CHCl<sub>3</sub>): δ (ppm) 8.16-6.31 (m, 12H, ArH<sub>perylene</sub>, ArH<sub>triazole</sub>, ArH<sub>benzimidazole</sub>), 5.24 (br s, 2H, O<sub>styrene</sub>CH<sub>2</sub>), 4.47 (br s, 2H, N<sub>triazole</sub>CH<sub>2</sub>), 4.13 (br s, 4H, COOCH<sub>2</sub>), 3.70 (br s, 2H, O<sub>benzimidazol</sub>CH<sub>2</sub>), 2.20-1.10 (m, 29H, 14CH<sub>2</sub>, CH<sub>backbone</sub>), 1.10-0.78 (m, 12H, CH<sub>3</sub>).

### Characterization

<sup>1</sup>H NMR (300 MHz) spectra were recorded on a Bruker AC 300 spectrometer in CDCl<sub>3</sub> and calibrated to CHCl<sub>3</sub> signal (7.26 ppm for <sup>1</sup>H). UV/vis spectra of solutions in CHCl<sub>3</sub> with a concentration of 10<sup>-5</sup> mol·L<sup>-1</sup> were recorded on a Hitachi 3000 spectrophotometer. SEC measurements were carried out in THF with 0.25% tetrabutylammoniumbromide with two Varian MIXED-C columns (300x7.5 mm) at room temperature and at a flow rate of 0.5 mL·min<sup>-1</sup> using UV (Waters model 486) with 254 nm detector wavelength and refractive index (Waters model 410) detectors. Polystyrene in combination with *o*DCB as an internal standard was used for calibration. Differential scanning calorimetry experiments were conducted at heating rates of 10 K·min<sup>-1</sup> or 40 K·min<sup>-1</sup> under N<sub>2</sub> atmosphere with a Perkin Elmer Diamond DSC, calibrated with indium. The endothermic maximum was taken as T<sub>m</sub>. X-ray diffraction experiments were performed on a Huber Guinier Diffractometer 6000 equipped with a Huber quartz monochromator 611 with Cu-K<sub>α1</sub>: 1.54051 Å. Cyclic voltammetry (CV) was recorded on a Princeton Applied Research VersaSTAT 4 Potentiostat/Galvanostat using platinum electrodes at a scan rate of 50 mVs<sup>-1</sup> and a Ag/Ag<sup>+</sup> (0.10 M of AgNO<sub>3</sub> in acetonitrile) reference electrode at 25 °C in an anhydrous and nitrogen saturated solution of 0.1 M of tetrabutylammonium tetrafluoroborate (Bu<sub>4</sub>NBF<sub>4</sub>) in

acetonitrile. Each measurement was calibrated with the ferrocene-ferrocenium couple (Fc/Fc<sup>+</sup>) considering 4.8 eV as ferrocene's HOMO level. SCLC electron-only devices were fabricated using the following structure: glass/ ITO/ PEDOT:PSS/ polymer/ Ca/Al. SCLC hole-only devices were fabricated using the following structure: glass/ ITO/ PEDOT:PSS/ polymer/ Au. Commercial ITO coated glass substrates with a sheet resistance of 13 Ohms per sq (Lumtec) were cleaned using following sequence in an ultrasonic bath: detergent, water, acetone and 2-propanol. After ozone treatment of the substrates for 5 min, PEDOT:PSS was spin-coated on the ITO surface and dried at 130 C for 30 min. All following steps were carried out under nitrogen atmosphere with water and oxygen levels  $\leq 0.1$  ppm. After cooling the substrate, the polymer layer was blade coated from chloroform solutions. The substrates were then put in a thermal evaporation chamber to evaporate the top electrode (30 nm Ca/ 100 nm Al for electron-only devices, 80 nm Au for hole-only devices) under high vacuum ( $1 \cdot 10^{-6}$  mbar) through a shadow mask (active area 4 mm<sup>2</sup>). The current-voltage characteristics of the devices were measured using a Keithley 2420 (I-V) Digital SourceMeter at 25 °C.

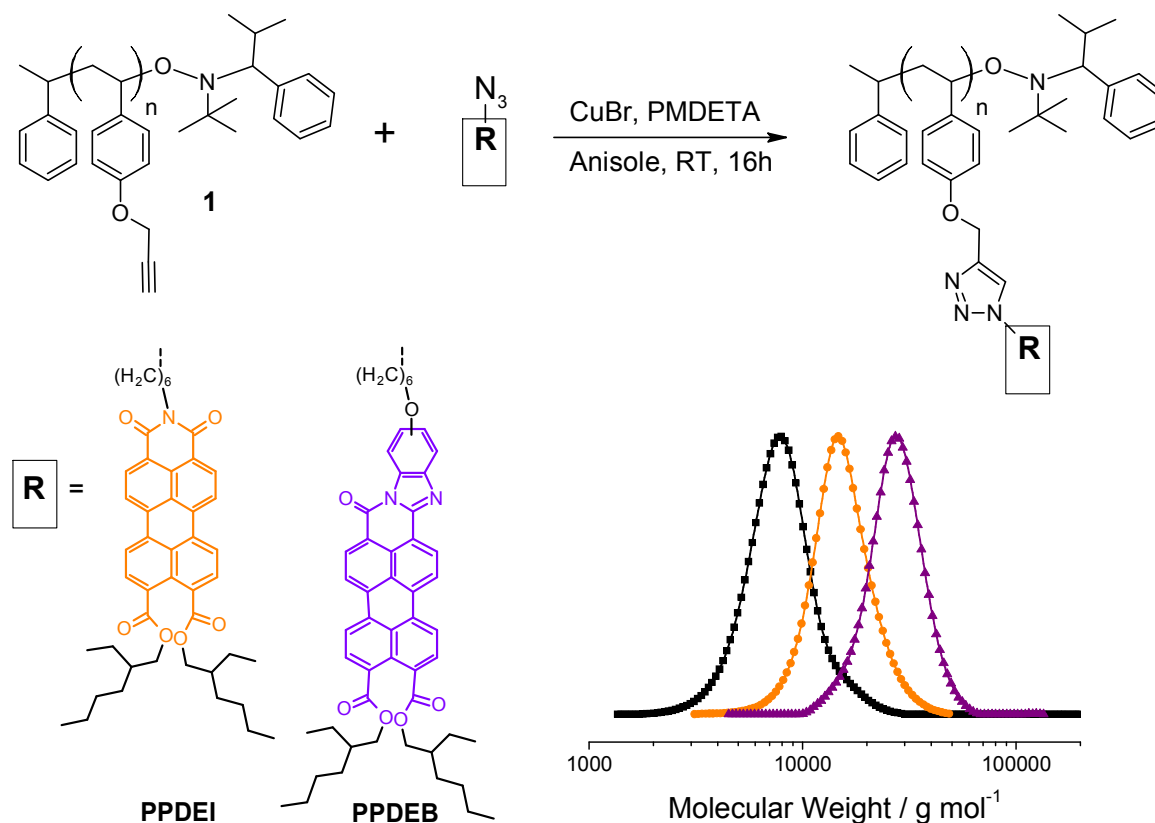
## Results and discussion

### Synthesis

For the synthesis of the poly(perylene diester benzimidazole) PPDEB and poly(perylene diester imide) PPDEI using “click” reaction, poly(propargyloxystyrene) with  $M_n(\text{SEC}) = 7400$  g/mol and a PDI of 1.11 was synthesized as scaffold polymer. Poly(propargyloxystyrene) was chosen as an alkyne carrying scaffold polymer because it is easy to synthesize and polymers with narrow PDIs are accessible.<sup>19, 20</sup> The synthesis of the azide carrying perylene derivatives PDEB-N<sub>3</sub> and PDEI-N<sub>3</sub> is shown in Scheme 1. The azides were obtained by the reaction of 1-bromo-6-azido-hexane with perylene diester benzimidazole alcohol or perylene diester imide, respectively. The “click” reaction of the azides (1.2 eq) with poly(propargyloxystyrene) was conducted in anisole at RT, using PMDETA/CuBr as catalyst, which was added to the reaction from a stock solution (Scheme 2). The approach of using a stock solution, which can be stored under inert gas atmosphere for long time, is more exact and convenient than adding ligand and copper species separately.



Scheme 2: Synthetic scheme of the „click” reaction of poly(propargyloxystyrene) **1** with perylene azides and SEC traces of **1** (black line), poly(peryene diester imide) PPDEI (orange line) and poly(peryene diester benzimidazole) PPDEB (purple line). The curves of the “clicked” polymers are clearly shifted to higher molecular weights compared to the scaffold polymer. It is evident that the shape and molecular weight distribution of the “clicked” polymers is preserved.



It is evident that the molecular weights of PPDEB and PPDEI determined by SEC are underestimated compared to the theoretical molecular weights, whereas PPBI 1 and PPBI 2 show higher values in SEC. This can be attributed by the ester groups in PPDEB and PPDEI, which seem to interact with the SEC column differently compared to the PPBI polymers. Moreover, the polymers show different degrees of aggregation. PPDEI and PPDEB were analyzed by <sup>1</sup>H NMR to estimate the conversion in “click” reaction. After the “click” reaction, the signals of the prominent alkyne proton at 2.5 ppm, as well as that of the OCH<sub>2</sub> group at 4.6 ppm of **1** disappear completely. Further, in PPDEI and PPDEB the OCH<sub>2</sub> signals are shifted to 5.24 and 5.15 ppm, respectively. The signal of the newly formed triazole proton, usually occurring around 7.6 ppm, cannot be seen in the spectra because it is

superimposed by the broad signals of the aromatic protons of perylene, but can be determined by integration between 8.4 and 7.4 ppm. The  $\text{CH}_2\text{N}_3$  protons of the perylene azides around 3.3 ppm cannot be observed any more in the “clicked” polymers, proving the absence of unreacted PDEI- $\text{N}_3$  and PDEB- $\text{N}_3$ . The corresponding  $\text{CH}_2$ -protons in the “clicked” polymers are now located adjacent to the newly-built triazole unit and occur around 4.45 ppm. The fact that a) no acetylene protons are present and b) all  $\text{OCH}_2(\text{C}\equiv\text{C})$  protons are converted to  $\text{OCH}_2(\text{triazole})$  indicates a quantitative conversion within the margins of the experimental error in  $^1\text{H}$  NMR. The direct nitroxide mediated radical polymerization of acrylate monomers carrying similar perylene chromophores were studied and reported earlier.<sup>10</sup> In the direct synthesis we could not achieve as high molecular weights as those obtained here with the “click” chemistry route. Additionally, high PDIs over 1.4 resulted during direct polymerization.

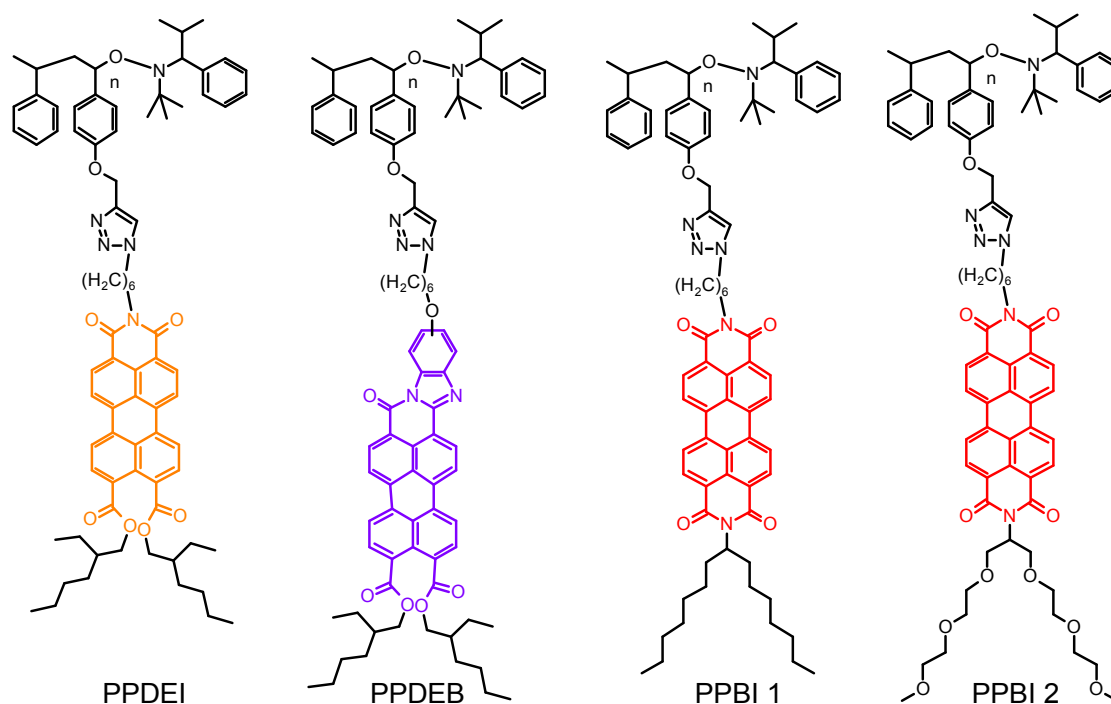


Figure 1: Chemical structures of poly(perylene diester imide) PPDEI, poly(perylene diester benzimidazole) PPDEB, and of poly(perylene bisimide) with alkyl swallow-tail PPBI 1 and with OEG swallow-tail PPBI 2.

Table 1: Molecular weight, Polydispersity index (both determined by SEC), theoretical molecular weight of the „clicked“ polymers and the scaffold polymer 1 assuming 100% conversion and thermal properties observed by DSC and TGA.

Polymer	$M_n$ [g·mol <sup>-1</sup> ] (SEC) <sup>a</sup>	$M_w/M_n$ (SEC) <sup>a</sup>	$M_n$ [g·mol <sup>-1</sup> ] (theor.) <sup>b</sup>	$T_{onset}$ [°C] <sup>c</sup>	$T_g$ [°C] <sup>d</sup>	$T_m$ [°C] <sup>d</sup>	$\Delta H$ [J/g] <sup>d</sup>	Notes
<b>1</b>	7400	1.11		386	59	n.o.		P(Propargyloxy-styrene)
<b>PPDEB</b>	26000	1.09	44000			285	8.9	P(Perylene diester benzimidazole)
<b>PPDEI</b>	15000	1.09	40000		124	192	0.3	P(Perylene diester imide)
<b>PPBI 1</b>	59700	1.09	39000	330	182	298	1.8	Hydrophobic PPBI <sup>17</sup>
<b>PPBI 2</b>	59600	1.09	42000	330	142	n.o.		Hydrophilic PPBI <sup>17</sup>

<sup>a</sup> Measured with size exclusion chromatography in tetrahydrofuran and calibrated to polystyrene standards. <sup>b</sup> Theoretical molecular weights calculated from 44 repeating units of 1 assuming 100 % conversion. <sup>c</sup> Measured by thermogravimetric analysis under N<sub>2</sub> atmosphere. <sup>d</sup> Measured by differential scanning calorimetry under N<sub>2</sub> atmosphere.

### Thermotropic properties of PPDEB and PPDEI

The DSC thermograms and XRD patterns of PPDEB and PPDEI are shown in Figure 2a) and b) respectively. PPDEB exhibits a clear melting peak with  $\Delta H = 8.87$  J/g at 285 °C into the isotropic phase. There has been no observation of a  $T_g$  in this polymer. The XRD pattern of PPDEB shows three clear reflections in the low  $q$  regime at 1.05 nm<sup>-1</sup>, 2.05 nm<sup>-1</sup> and 2.84 nm<sup>-1</sup>. No reflections at higher  $q$  values can be observed except the  $\pi$ - $\pi$  stacking distance of the perylene core at 18.13 nm<sup>-1</sup>, which corresponds to 3.5 Å. This shows that the observed phase in PPDEB is a liquid crystalline (LC) ordering. The existence of a LC phase is supported by polarized optical microscopy (POM, see Figure 2c), where birefringent textures could be observed at 280 °C when cooling the sample from the isotropic melt.

PPDEI shows a  $T_g$  at 124 °C and a very weak melting peak at 192 °C with a small melting enthalpy of  $\Delta H = 0.32$  J/g. The XRD pattern of PPDEI shows three reflections in the low  $q$  regime at  $1.31 \text{ nm}^{-1}$ ,  $2.48 \text{ nm}^{-1}$  and  $3.51 \text{ nm}^{-1}$ . No reflections at higher  $q$  values can be observed except the  $\pi$ - $\pi$  stacking distance of the perylene core at  $17.93 \text{ nm}^{-1}$  ( $\approx 3.5 \text{ \AA}$ ) which is much weaker compared to PPDEB.

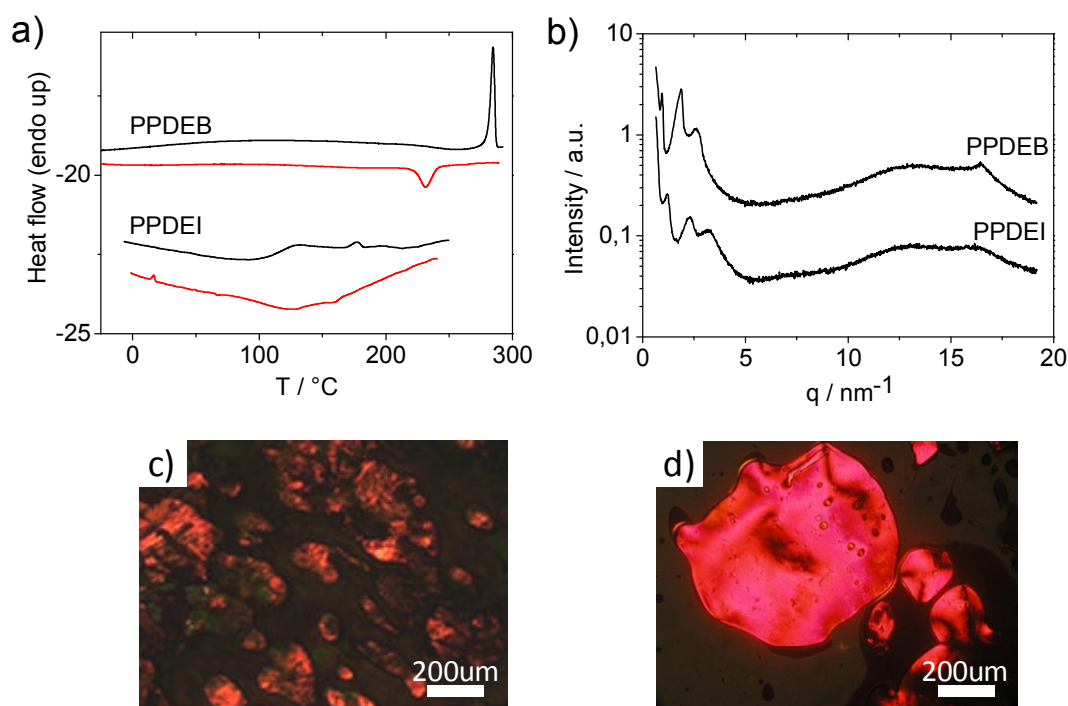


Figure 2: a) Second heating and first cooling curve from DSC measurements of poly(perylenediester benzimidazole) PPDEB and poly(perylenediester imide) PPDEI; PPDEB exhibits a clear melting peak at 285 °C while PPDEI shows a glass transition at 124 °C and a very weak melting peak at 192 °C; b) X-Ray diffractions of PPDEB and PPDEI at RT; c) Polarization Optical Microscopy images (polarizers crossed) of PPDEB at 280 °C and d) PPDEI at 190 °C showing birefringent textures of LC mesophases after cooling the samples from isotropic state and annealing at the respective temperature.

In addition, LC textures, typical for nematic phases were observed at temperatures below  $T_m$  with POM (see Figure 2d), when cooling the sample from the isotropic phase. Hence, also PPDEI is a liquid crystalline material. The textures observed with POM for PPDEB and PPDEI do not change upon further cooling to RT. Therefore, the LC state of the two polymers is “frozen in” due to the viscosity of the materials. LC compounds are of great interest for use in applications like printed electronics, because of their potential to overcome common problems of crystalline materials, often related to grain boundaries<sup>21, 22</sup>. This can

help optimizing morphology and hence device performance. Compared to directly synthesized acrylate polymers carrying similar chromophores<sup>10</sup>, the here presented polymers show a slightly different thermotropic behavior. The directly polymerized PPDEB shows a  $T_m$  at 312 °C, while the clicked counterpart exhibits  $T_m$  at 285 °C. For PPDEI, directly polymerized PPDEI shows a  $T_m$  at 132 °C and the clicked one melts at  $T_m = 191$  °C. Hence the “clicked” PPDEB shows a  $T_m$  only slightly different from the one of the directly polymerized PPDEB, whereas the PPDEI derivatives show a difference of 60 °C. The reason for these variations might be the different molecular weights of the clicked and the directly polymerized compounds. In addition, the triazole linkage present in the “clicked” polymer can potentially affect the packing and hence the thermal properties of these materials.

### Optical and electrochemical properties

The optical properties of the novel perylene polymers were investigated by UV/vis spectroscopy in  $\text{CHCl}_3$  solution ( $c = 10^{-5} \text{ mol}\cdot\text{L}^{-1}$ ) as depicted in Figure 3a. PPDEI shows a fine vibronic structure in absorption similar to the one of poly(peryene bisimides) with absorption maxima at 507 nm, 478 nm and 453 nm. Both PPBI 1 and 2 show similar spectra and therefore PPBI 1 is shown in Figure 3a as a typical example. The spectrum of PPDEI is blue shifted compared to PPBI due to the smaller aromatic system. PPDEB shows no fine structure but a featureless broad absorption up to 700 nm and with a maximum at 528 nm. This can be attributed to the expanded  $\pi$ -system. The enhanced absorption property of PPDEB could be very beneficial for the application in photovoltaic cells due to the broader light harvesting. Figure 3b shows the comparison of PL-spectra of the PPBI 1 and 2 in thin films, which have similar optical density. It is important to mention that the PL-intensity for PPBI 1 carrying alkyl substituent is about half of that of PPBI 2, which carries an OEG swallow-tail substituent. This clearly indicates that the PL-quenching in PPBI 2 is less pronounced.

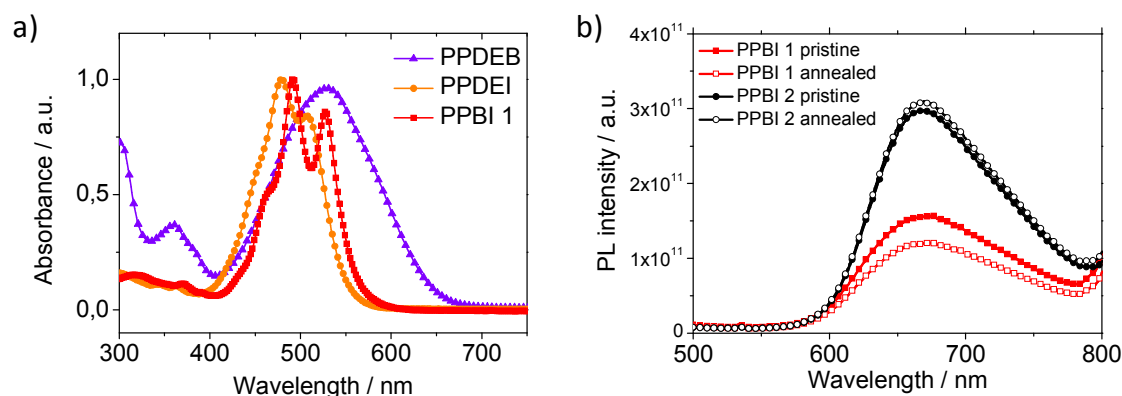


Figure 3: a) Absorption spectrum of poly(perylene diester benzimidazole) PPDEB (purple line), poly(perylene diester imide) PPDEI (orange line) and poly(perylene bisimide) PPBI 1 (red line) in  $\text{CHCl}_3$  ( $c=10^{-5} \text{ mol}\cdot\text{L}^{-1}$ ) solution. PPDEB shows a broad absorption up to 700 nm with a maximum at 528 nm. PPDEI exhibits a fine vibronic structure which is blue-shifted compared to the absorption of PPBI 1, b) PL spectra of as spun and annealed films of PPBI 1 and PPBI 2 with similar optical density. The excitation wavelength was  $\lambda_{\text{ex}}=405\text{nm}$ .

Cyclic voltammetry is a widely accepted method to estimate the position of both the HOMO and the LUMO energy levels and the band gap of the polymers under investigation. In addition, reversibility and electrochemical stability of the material can be studied. LUMO values were directly obtained from cyclic voltammetry measurements, whereas HOMO values and optical band gap were determined from the absorption edge from UV/vis absorption spectroscopy (Figure 3). The results are summarized in Table 2 and the cyclic voltammograms can be found as supporting information in Figure S1. Each polymer shows two reversible reduction peaks, which is characteristic for the perylene unit. For the two polymers containing perylene bisimides PPBI 1 and PPBI 2 LUMO values of -3.80 eV and -3.94 eV and HOMO values of -5.85 eV and -5.99 eV were obtained. The optical band gap for both materials is 2.05 eV. In comparison, PPDEB with a benzimidazole unit attached to the perylene cores has a smaller band gap of 1.82 eV, which can be explained by the extended  $\pi$ -conjugation system and thus an increase in delocalized  $\pi$ -electrons. Here, both a higher lying LUMO (-3.56 eV) and HOMO (-5.38 eV), compared to the two PPBI derivatives, were measured. Consequently, PPDEI with the smallest  $\pi$ -conjugation system among the four polymers, exhibits the highest band gap (2.12 eV) with a LUMO energy level of -3.56 eV and a HOMO energy level of -5.68 eV. These optical and electronic properties, especially those of PPDEB with extended absorption and elevated LUMO energy level compared to

PPDEI, PPBI 1 and PPBI 2, are important features for applications of these compounds in organic photovoltaic cells. In addition, efficient solar cells also require high charge carrier mobility of the semiconducting materials in use. A detailed study of the charge transport behavior is described in the next section.

*Table 2: Lowest unoccupied molecular orbital (LUMO) and Highest occupied molecular orbital (HOMO) energy values and optical band gap for PPDEB, PPDEI, PPBI 1 and PPBI 2. Each measurement was calibrated with the ferrocene-ferrocenium couple (Fc/Fc<sup>+</sup>) considering 4.8 eV as ferrocene's HOMO level.*

Polymer	LUMO [eV]	HOMO <sup>a</sup> [eV]	Optical band gap <sup>b</sup> [eV]
<b>PPDEB</b>	-3.56	-5.38	1.82
<b>PPDEI</b>	-3.56	-5.68	2.12
<b>PPBI 1</b>	-3.80	-5.85	2.05
<b>PPBI 2</b>	-3.94	-5.99	2.05

<sup>a</sup> determined from optical bandgap and LUMO value. <sup>b</sup> determined from absorption edge in Figure 3.

### Charge carrier mobility

Since all compounds under investigation were derived from the same polymer scaffold, their chain length and polydispersities are identical. This allows for studying the effect of the chemical structure of the perylene pendant groups on charge carrier mobility of side-chain polymers. Therefore, we compared the charge transport of the newly synthesized perylene polymers PPDEB and PPDEI with structural modifications at the perylene core with the two poly(peryene bisimides) PPBI 1 and PPBI 2. PPBI 1 is substituted with an alkyl swallow-tail and exhibits a liquid crystalline SmC phase between 298 °C and RT (T<sub>g</sub> at 182 °C) whereas PPBI 2 is substituted with an oligoethylenglycol swallow-tail and does not exhibit any crystallinity or liquid crystallinity but only a T<sub>g</sub> at 142 °C<sup>17</sup>. All of these polymers exhibit  $\pi$ - $\pi$  stacking signal in WAXS region. The bulk charge carrier mobilities of PPDEB, PPDEI, PPBI 1 and PPBI 2 were determined by recording current-voltage (*I-V*) characteristics of each material in single carrier devices; both electron-only devices and hole-only devices. The device structures of both single carrier devices are shown in Figure S2 as Supporting

Information. At high voltages, the current measured is space-charge limited only, and the charge carrier mobility can be extracted by fitting the  $J$ - $V$  curve according to Mott-Gurney equation<sup>23-26</sup>

$$J = \frac{9}{8} \varepsilon_0 \varepsilon_r \mu \frac{V^2}{L^3} \quad \text{Equation 1}$$

where  $J$  is the current density,  $\varepsilon_r$  is the dielectric constant of the polymer (assumed to be 3 in our calculations<sup>27</sup>),  $\varepsilon_0$  is the permittivity of free space,  $\mu$  is the charge carrier mobility,  $L$  is the thickness of the polymer layer and  $V$  is the voltage drop across the device.

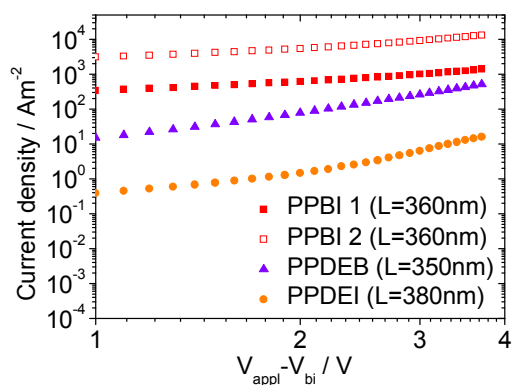


Figure 4:  $J$ - $V$  characteristics for electron-only devices of compounds PPBI 1, PPBI 2, PPDEB and PPDEI with active layer thickness  $L$ .

Table3: SCLC electron and hole mobilities for PPDEI, PPDEB, PPBI 1 and PPBI 2 obtained from single carrier devices with an active layer thickness  $L$  of ca. 350nm.

Polymer	Electron mobility $\mu_e$ [ $\text{cm}^2\text{V}^{-1}\text{s}^{-1}$ ]	Hole mobility $\mu_h$ [ $\text{cm}^2\text{V}^{-1}\text{s}^{-1}$ ]
PPDEI	$5 \cdot 10^{-6}$	$7 \cdot 10^{-6}$
PPDEB	$6 \cdot 10^{-4}$	$4 \cdot 10^{-7}$
PPBI 1	$1 \cdot 10^{-3}$	$2 \cdot 10^{-5}$
PPBI 2	$1 \cdot 10^{-2}$	$4 \cdot 10^{-5}$

Devices with different layer thicknesses  $L$  were prepared according to a procedure described recently.<sup>10</sup> For PPBI 1 and PPBI 2, the SCLC samples were thermally annealed above the material's glass transition temperatures ( $T_g$ ) and allowed to cool to room temperature before measurement, which gave significantly higher performances. No such improvement was observed for PPDEB and PPDEI devices. The individual  $J$ - $V$  characteristics of all the electron-only devices and hole-only devices of PPDEB, PPDEI, PPBI 1 and PPBI 2 for different layer thicknesses are shown as supporting information in Figure S2. The obtained mobility values for each material are constant across different layer thicknesses within the experimental error. Electron- and hole mobilities obtained from devices with an active layer thickness of ca. 350 nm are summarized in Table 3 and the  $J$ - $V$  curves of these electron-only devices are depicted in Figure 4. All the polymers except PPDEI are excellent electron transport materials. As expected for perylene imide derivatives, all of them exhibit very weak hole carrier mobility. A comparison of the hole mobilities of the compounds shows that PPDEI has a hole mobility of  $7 \times 10^{-6} \text{ cm}^2 \text{V}^{-1} \text{s}^{-1}$ , which is slightly higher than its electron mobility. Hence, a perylene core modified by a diester and an imide unit leads to a more pronounced p-type rather than n-type behavior. For compounds PPDEI, PPBI 1 and PPBI 2 the hole mobilities are at least 2 orders of magnitude below their electron mobilities. This demonstrates that electron transport through the LUMO is preferred to hole transport via the HOMO, as expected for n-type semiconductors.

As can be seen from Table 3, PPDEI has an electron mobility of  $5 \times 10^{-6} \text{ cm}^2 \text{V}^{-1} \text{s}^{-1}$  which is two orders of magnitude below the electron mobility of PPDEB ( $6 \times 10^{-4} \text{ cm}^2 \text{V}^{-1} \text{s}^{-1}$ ). This is in agreement with previous observations of charge carrier mobilities of perylene diester imide and perylene diester benzimidazole acrylate polymers.<sup>10</sup> Here, the less electron deficient perylene diester imide groups of PPDEI possesses worse electron mobility compared to PPDEB with benzimidazole functionalized perylene cores. Annealed devices of PPBI 1 however show a higher electron mobility of  $1 \times 10^{-3} \text{ cm}^2 \text{V}^{-1} \text{s}^{-1}$  compared to PPDEB devices. Although optical properties were improved through the implementation of a benzimidazole unit to the perylene core, the charge transport of PPDEB suffers compared to the perylene bisimide derivatives, PPBI 1 and PPBI 2.

A comparison between PPBI 1 and PPBI 2 shows that not only the core of the  $\pi$ -conjugation system, but also the substituent has an impact on the charge carrier transport properties of the material. Altering the solubilizing side chains of the PBI from a branched alkyl (PPBI 1) to a branched-OEG (PPBI 2) results in a major increase of one order of magnitude in electron mobility from  $1 \times 10^{-3} \text{ cm}^2 \text{ V}^{-1} \text{ s}^{-1}$  to  $1 \times 10^{-2} \text{ cm}^2 \text{ V}^{-1} \text{ s}^{-1}$ . This is one of the highest electron mobility values reported for side chain polymers. It is worth mentioning, that the electronic coupling between the PBI core and the imide substituents are negligible because of the nodes in the HOMO and LUMO at the imide nitrogen.<sup>28</sup> The drastic improvement of charge transport observed here, can therefore be attributed to the difference in packing and morphology obtained for the thin polymer films. Hydrophilic and hydrophobic side chains implemented in organic electron transport materials have been proven to be crucial for the resulting film morphologies and charge carrier mobility.<sup>29</sup> The XRD data reported earlier supports a liquid crystalline (LC) SmC bilayer structure for PPBI 1, whereas PPBI 2 is amorphous, even though both polymers exhibit a  $\pi$ - $\pi$  stacking distance of 0.35 nm in WAXS region<sup>13</sup>. In our SCLC experiment, where the charge transport within the film perpendicular to the substrate is probed, the less ordered PPBI 2 is superior in terms of mobility. In general, the charge carrier mobility in organic materials depends on hopping distances, concentration of hopping centers and energetic disorder. For organic semiconductors it was observed that ordered (polycrystalline or LC) regions, with stronger electronic coupling compared to disordered regions, often exhibit a larger amount of deep charge traps. This observation was attributed to the fact that in polycrystalline or LC materials grain boundaries can isolate charge carriers within the ordered regions.<sup>30</sup> The stronger PL quenching (Figure 3b) observed for PPBI 1 compared to PPBI 2 is an indication for deep traps present in this LC material, which is in line with the lower charge carrier mobility found. Moreover, the pendant polymers differ from conjugated main chain polymers due to the fact that the electronic moiety is independent of the backbone length in the former. Other additional factors of importance for the electron transport in PBIs are the degree of aggregation and the intermolecular rotational angle of the PBI discs to one another. Thus the high flexibility of OEG substituent of PPBI 2 favors less aggregation and probably less energetic disorder. The PL studies (Figure 3b) also support this argument. But further detailed temperature dependent mobility studies are necessary to quantify the energetic disorder.

## Conclusion

We showed the elegant and feasible synthesis of diverse poly-perylene derivatives through a “click” chemistry approach starting from poly(propargyloxystyrene) and respective perylene azides. The resulting poly(peryene diester benzimidazole) PPDEB and poly(peryene diester imide) PPDEI showed high molecular weights and narrow PDIs around 1.09. Very high conversion in the “click” reaction could be proven by  $^1\text{H}$  NMR. Both polymers are liquid crystalline as observed by a combination of XRD, POM and DSC. A comparison of optical and charge transport properties of these polymers results in two major findings: first, improved optical absorption up to 700 nm for PPDEB was found, while PPDEI showed a blue shifted absorption compared to PPBI. This is due to modifications at the chromophoric system at the perylene units. The measurement of charge transport by the SCLC method resulted in electron mobilities for PPDEB of  $6 \times 10^{-4} \text{ cm}^2\text{V}^{-1}\text{s}^{-1}$ . While light harvesting could be improved for this compound, the charge carrier mobility is lower compared to the conventional perylene bisimide based polymers PPBI 1 and PPBI 2. The second finding is related to the influence of the solubilizing side groups of PPBI 1 (branched alkyl groups) and PPBI 2 (branched oligoethylenglycol groups) on structure and charge carrier mobility. PPBI 2, which is an amorphous polymer, shows a very high electron mobility of  $1 \times 10^{-2} \text{ cm}^2\text{V}^{-1}\text{s}^{-1}$ , which is almost one order of magnitude higher than the electron mobility of the liquid crystalline PPBI 1. This demonstrates that side groups, due to their ability to alter the molecular packing behavior, can influence the charge carrier mobility of perylene bisimide derivatives strongly. In conclusion, we have demonstrated the tuning of the optical properties of semiconducting side chain polymers by modifying the pendant perylene core and the charge carrier mobility by varying the substituents on PBI. Understanding these structure-property relations is important for the design of new materials for optoelectronic applications.

## Acknowledgments

The financial support from EU (Largecells Grant No. 261936) and Merck Chemicals Ltd., Southampton for this work is gratefully acknowledged. We also thank Prof. Thomas Thurn-

Albrecht and Gaurav Gupta from Martin Luther University of Halle-Wittenberg, Germany for fruitful discussions and Prof. Anna Köhler and Markus Reichenberger, Experimental Physics II, University of Bayreuth for their help with PL measurements.

## References

- (1) Friend, R. H.; Gymer, R. W.; Holmes, A. B.; Burroughes, J. H.; Marks, R. N.; Taliani, C.; Bradley, D. D. C.; Santos, D. A. D.; Bredas, J. L.; Logdlund, M.; Salaneck, W. R., *Nature* **1999**, *397*, (6715), 121-128.
- (2) Chua, L.-L.; Zaumseil, J.; Chang, J.-F.; Ou, E. C. W.; Ho, P. K. H.; Sirringhaus, H.; Friend, R. H., *Nature* **2005**, *434*, (7030), 194-199.
- (3) Maurano, A.; Hamilton, R.; Shuttle, C. G.; Ballantyne, A. M.; Nelson, J.; O'Regan, B.; Zhang, W.; McCulloch, I.; Azimi, H.; Morana, M.; Brabec, C. J.; Durrant, J. R., *Advanced Materials* **2010**, *22*, (44), 4987-4992.
- (4) Chen, Z.; Zheng, Y.; Yan, H.; Facchetti, A., *Journal of the American Chemical Society* **2008**, *131*, (1), 8-9.
- (5) Anthony, J. E.; Facchetti, A.; Heeney, M.; Marder, S. R.; Zhan, X., *Advanced Materials* **2010**, *22*, (34), 3876-3892.
- (6) Son, H. J.; He, F.; Carsten, B.; Yu, L., *Journal of Materials Chemistry* **2011**, *21*, (47), 18934-18945.
- (7) Li, G.; Zhu, R.; Yang, Y., *Nature Photonics* **2012**, *6*, (3), 153-161.
- (8) Kang, J.; Shin, N.; Jang, D. Y.; Prabhu, V. M.; Yoon, D. Y., *Journal of the American Chemical Society* **2008**, *130*, (37), 12273-12275.
- (9) Lindner, S. M.; Thelakkat, M., *Macromolecules* **2004**, *37*, (24), 8832-8835.
- (10) Muth, M.-A.; Carrasco-Orozco, M.; Thelakkat, M., *Advanced Functional Materials* **2011**, *21*, (23), 4510-4518.
- (11) Wicklein, A.; Kohn, P.; Ghazaryan, L.; Thurn-Albrecht, T.; Thelakkat, M., *Chemical Communications* **2010**, *46*, (13), 2328-2330.
- (12) Wicklein, A.; Muth, M.-A.; Thelakkat, M., *Journal of Materials Chemistry* **2010**, *20*, (39), 8646-8652.

- 
- (13) Lindner, S. M.; Hüttner, S.; Chiche, A.; Thelakkat, M.; Krausch, G., *Angewandte Chemie International Edition* **2006**, *45*, (20), 3364-3368.
- (14) Sommer, M.; Lang, A. S.; Thelakkat, M., *Angewandte Chemie, International Edition* **2008**, *47*, (41), 7901-7904.
- (15) Lang, A. S.; Neubig, A.; Sommer, M.; Thelakkat, M., *Macromolecules* **2010**, *43*, (17), 7001-7010.
- (16) Binder, W. H.; Sachsenhofer, R., *Macromolecular Rapid Communications* **2008**, *29*, (12-13), 952-981.
- (17) Lang, A. S.; Thelakkat, M., *Polymer Chemistry* **2011**, *2*, 2213-2221.
- (18) Wicklein, A.; Lang, A.; Muth, M.; Thelakkat, M., *Journal of the American Chemical Society* **2009**, *131*, (40), 14442-14453.
- (19) Fleischmann, S.; Komber, H.; Voit, B., *Macromolecules* **2008**, *41*, (14), 5255-5264.
- (20) Fleischmann, S.; Komber, H.; Appelhans, D.; Voit, B. I., *Macromolecular Chemistry and Physics* **2007**, *208*, (10), 1050-1060.
- (21) Holcombe, T. W.; Norton, J. E.; Rivnay, J.; Woo, C. H.; Goris, L.; Piliago, C.; Griffini, G.; Sellinger, A.; Brédas, J.-L.; Salleo, A.; Frechet, J. M. J., *Journal of the American Chemical Society* **2011**, *133*, (31), 12106-12114.
- (22) Weitz, R. T.; Amsharov, K.; Zschieschang, U.; Burghard, M.; Jansen, M.; Kelsch, M.; Rhamati, B.; van Aken, P. A.; Kern, K.; Klauk, H., *Chemistry of Materials* **2009**, *21*, (20), 4949-4954.
- (23) Blom, P. W. M.; Tanase, C.; de Leeuw, D. M.; Coehoorn, R., *Applied Physics Letters* **2005**, *86*, (9), 092105.
- (24) Mihailetchi, V. D.; Wildeman, J.; Blom, P. W. M., *Physical Review Letters* **2005**, *94*, (12), 126602.
- (25) Malliaras, G. G.; Salem, J. R.; Brock, P. J.; Scott, C., *Physical Review B* **1998**, *58*, (20), R13411-R13414.
- (26) Blom, P. W. M.; Tanase, C.; Leeuw, D. M. d.; Coehoorn, R., *Applied Physics Letters* **2005**, *86*, 092105.
- (27) Goh, C.; Kline, R. J.; McGehee, M. D.; Kadnikova, E. N.; Frechet, J. M. J., *Applied Physics Letters* **2005**, *86*, (12), 122110-3.
- (28) Würthner, F., *Chemical Communications* **2004**, (14), 1564-1579.

- (29) Sakurai, T.; Shi, K.; Sato, H.; Tashiro, K.; Osuka, A.; Saeki, A.; Seki, S.; Tagawa, S.; Sasaki, S.; Masunaga, H.; Osaka, K.; Takata, M.; Aida, T., *Journal of the American Chemical Society* **2008**, *130*, (42), 13812-13813.
- (30) Kaake, L. G.; Barbara, P. F.; Zhu, X. Y., *The Journal of Physical Chemistry Letters* **2010**, *1*, (3), 628-635.

## Supporting Information

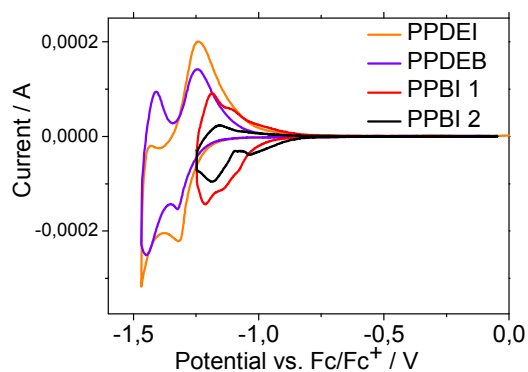


Figure S1: Cyclic voltammograms of PPDI, PPDB, PPBI 1 and PPBI 2 showing the first and second reduction peaks. The measurements were conducted in acetonitrile with respect to Fc/Fc<sup>+</sup> at a scan rate of 50 mVs<sup>-1</sup>.

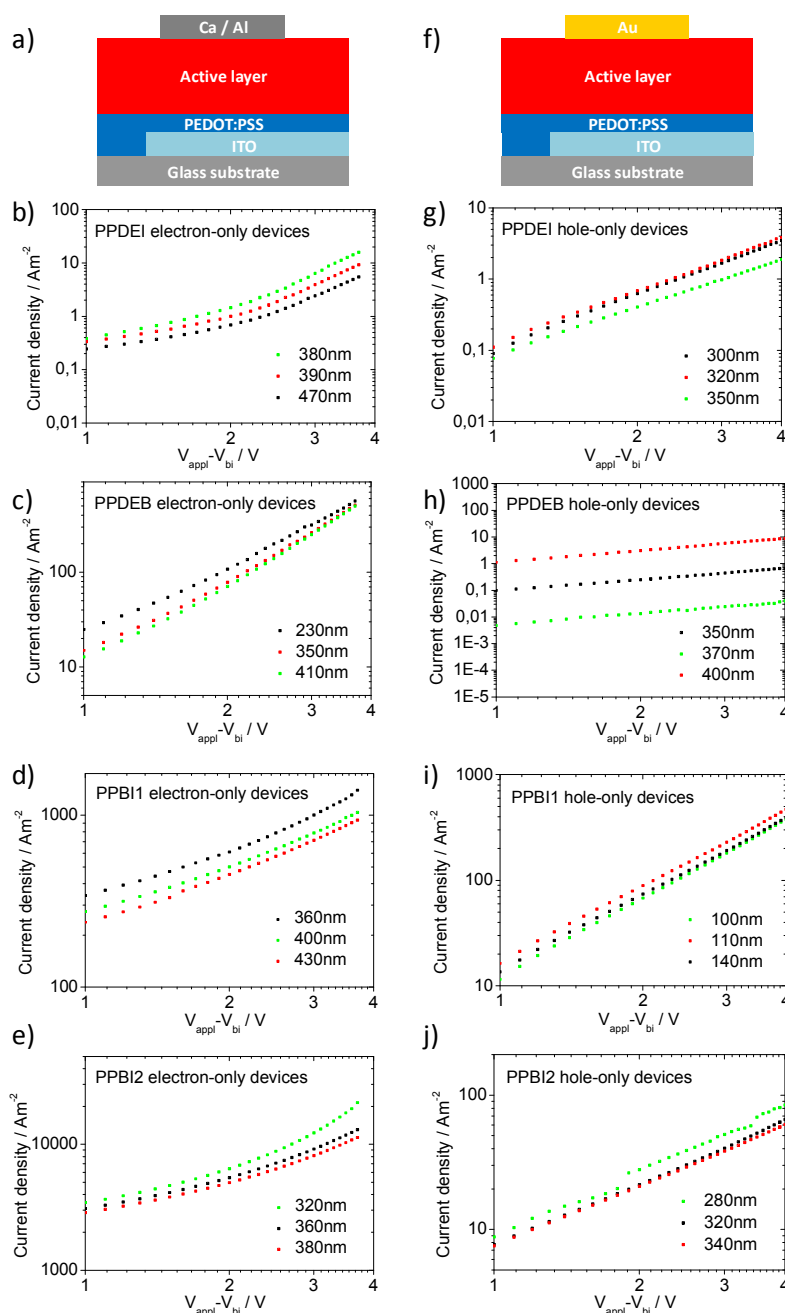


Figure S2: Scheme of an electron-only device with a calcium top electrode, capped with aluminum (a); Current density  $J$  vs. voltage  $V$  plots at room temperature for electron-only devices of PPDI, PPDB, PPBI 1 and PPBI 2 (b-e); Scheme of a hole-only device with gold top electrode (f); Current density  $J$  vs. voltage  $V$  plots at room temperature for hole-only devices of PPDI, PPDB, PPBI 1 and PPBI 2 (g-j); the voltage applied ( $V_{\text{ap}}$ ) was corrected for a built in potential ( $V_{\text{bi}}$ ) of 2.2 eV for electron-only devices resulting from the differences in work function of calcium and ITO/PEDOT:PSS.  $V_{\text{bi}}$  in hole-only devices was estimated to be 0 eV.



## 6. Correlation of Charge Carrier Mobilities and Solar Cell Parameters in Polymer:Fullerene Blend Devices

*Mathis-Andreas Muth<sup>a,b</sup>, William Mitchell<sup>b</sup>, Steven Tierney<sup>b</sup>, Miguel Carrasco-Orozco<sup>b</sup>, and Mukundan Thelakkat<sup>a\*</sup>*

[a] Prof. Dr. Mukundan Thelakkat, Applied Functional Polymers, Department of Macromolecular Chemistry I, University of Bayreuth, Universitaetsstr.30, 95440 Bayreuth (Germany)

[b] Dr. Miguel Carrasco-Orozco, Merck Chemicals Ltd., Chilworth Technical Centre, University Parkway, Southampton SO16 7QD (UK)

\*corresponding author: mukundan.thelakkat@uni-bayreuth.de

This manuscript is accepted in *Nanotechnology*.

## Abstract

Herein, we analyze fundamental material properties such as charge carrier mobility and morphology of the active layer in thin film organic solar cells and correlate them with thickness optimization in the devices. A low band gap donor-acceptor copolymer in combination with PCBM and two bis-adduct fullerenes, bis-PCBM and bis-oQDMC, are investigated. We studied charge transport of Polymer:Fullerene blends in hole- and electron-only devices using the SCLC method. Lower electron mobilities were observed in both bis-adduct fullerene blends. Hole mobility, however, was decreased only in the blend containing bis-oQDMC. Both bis-adduct fullerene blends show very high open circuit voltage in solar cell devices, but poor photocurrent compared to the standard PCBM blend for an active layer thickness of 200 nm. Therefore, a higher short circuit current was feasible for the Polymer:bis-PCBM blend by reducing the active layer thickness in order to compensate for the low electron mobility. For the Polymer:bis-oQMC blend, no such improvement was achieved, which in turn indicates an unfavorable morphology in this particular blend system. The results are supported by external quantum efficiency (EQE) measurements, atomic force microscopy (AFM) and UV/vis spectroscopy. Based on these results, the investigations presented herein give a more scientific basis for the optimization of solar cells.

## Introduction

Efficient and low-cost solutions for converting solar energy into electricity are of great interest for the future, which has drawn the attention of researchers to organic photovoltaic cells (OPV) during recent years.<sup>1-3</sup> So far, the most successful solution processable OPV devices are achieved with Polymer:Fullerene solar cells, consisting of an electron-donating (p-type) conjugated polymer and an electron-accepting (n-type) fullerene, such as Phenyl-C<sub>61</sub>-butyric acid methyl ester (PCBM). In a bulk heterojunction (BHJ) solar cell, the active layer consists of a blend of p- and n-type material. High power conversion efficiencies (PCE) of more than 8 % were reported on a laboratory scale<sup>4</sup>, but for commercial viability of this technology, even higher efficiencies are required to achieve adequate PCEs in module fabrication<sup>5</sup>. Extensive research has been done on finding better donor polymers<sup>6-8</sup>, while

alternative acceptors have received significantly less attention to date. The trend is towards engineering low band gap polymers as hole transport materials, so that light harvesting in the red and infrared region is enhanced and as much light of the solar spectrum as possible can be absorbed. Consequently, more photons absorbed can enable higher short circuit current densities ( $J_{SC}$ ) and hence better PCEs. In general this can be achieved by changing the chemical structure of the polymer to tune HOMO and LUMO energy levels, so that the band gap is lowered and the absorption is shifted to longer wavelength. However, if the HOMO energy level of the donor is shifted up, the open circuit voltage ( $V_{OC}$ ) of the solar cell is often negatively affected. This is due to the linear relation between  $V_{OC}$  of a BHJ solar cell and the difference in HOMO of donor and LUMO of acceptor.<sup>9</sup> Therefore, acceptor materials with high LUMO levels are desirable to obtain high  $V_{OC}$ . In this context, several mono- bis- and tris-fullerene adducts have been reported, in which the LUMO energy levels are higher compared to PCBM. In devices, even though higher  $V_{OC}$  were realized, the PCE was often low for various blend devices with multi-adduct fullerenes due to reduced photocurrents. In literature it has been attributed to different effects: for P3HT:bis-PCBM blend devices, Jarzab *et al.* found that the dynamics of photoexcitation is slower compared to P3HT:PCBM, which was ascribed to changes in the microstructure of the blend.<sup>10</sup> Nelson and co-workers reported that the formation of triplet states in blends of PCBM multi-adducts with a polyfluorene polymer competes with charge separation and is responsible for losses in OPV performance. This however, was only observed when the offset between the donor HOMO and the acceptor LUMO was larger than 1.6 eV.<sup>11</sup> Mono- bis- and tris-PCBM in combination with P3HT were shown to have similar charge generation efficiency as measured by transient absorption spectroscopy. Still the overall performance was low because the crystallinity of P3HT was reduced for blends with multiple side-chain fullerenes.<sup>12</sup> Also, electron mobility of these fullerenes was found to be lower, especially for the tris-PCBM, as shown in OFET measurements of the pristine compounds. The molecular packing motif of several donor polymers and fullerene acceptors was investigated by McGehee and co-workers.<sup>13</sup> Intercalation of fullerene molecules between the side chains of conjugated donor polymers and the formation of bimolecular crystals was studied by means of X-ray diffraction. In blends, where there was intercalation, the performance of solar cells was decreased, when multi-adduct fullerenes were employed. This was explained by a change in orientation of the

fullerene within the bimolecular crystal caused by the steric hindrance of multiple side-groups. As a consequence, electron transport was presumably impeded. When there was no intercalation, improved efficiencies for multi-adduct fullerene devices could be observed. Voroshazi *et al.* reported CELIV measurements to determine the charge carrier mobility of P3HT:Fullerene blends with Mono- and Bis-o-quinodimethane C<sub>60</sub> (oQDMC), compared to PCBM and bis-PCBM.<sup>14</sup> Mobility values of the blend systems were found to be reduced for both bis-adduct fullerenes bis-PCBM and bis-oQDMC compared to PCBM and mono-oQDMC. The CELIV method however only gives an overall mobility of both hole and electron transport material. Hence no conclusion about individual charge transport of the blends could be made. These examples from literature demonstrate that mostly blend morphology and charge transport properties in the resulting blend are responsible for lower J<sub>SC</sub> and hence PCE in OPV devices. The fundamental question how the intrinsic mobility of these materials is affected or an unfavorable morphology resulting in insufficient percolation paths causes a change in charge transport properties often remains open. Thus it is important to study the hole and electron mobilities separately in blend films with thickness ranges comparable to those in solar cell devices. In addition, very little is known about novel fullerenes in combination with low band gap polymers, since most studies were done on P3HT to date. Especially a different behavior of novel donor-acceptor copolymers can be expected, since they mostly are rather amorphous materials, compared to P3HT which is highly crystalline. Herein we directly compare charge carrier mobilities of two n-type bis-adduct fullerene derivatives and PCBM within blends with a donor-acceptor copolymer serving as p-type material. By using the SCLC approach, electron and hole mobility can be measured separately by fabricating electron- and hole-only devices. The results are correlated with the performance of OPV devices. Furthermore, the blend morphology is investigated by atomic force microscopy (AFM) and UV/vis spectroscopy.

## Results and Discussion

Chemical structures of the donor-acceptor copolymer (in the following referred to as Polymer) and the three fullerene derivatives under investigation are depicted in Figure 1a,

along with the HOMO and LUMO values obtained from cyclic voltammetry (CV) (Figure 1b). The Polymer consisting of benzodithiophene, benzothiadiazole and thiophene units has a molecular weight of  $M_n=30000 \text{ gmol}^{-1}$ , a PDI of 1.8 and did not show any melting point in differential scanning calorimetry (DSC). Details about the polymer characterization and optimization of solar cell devices are reported elsewhere.<sup>15</sup> The commonly used Phenyl- $C_{61}$ -butyric acid methyl ester (PCBM) is taken as a reference material. The two bis-adduct  $C_{60}$  fullerenes, namely Bis-Phenyl- $C_{61}$ -butyric acid methyl ester (bis-PCBM) and Bis-*o*-quino-dimethane  $C_{60}$  (bis-*o*QDMC) exhibit higher LUMO energy levels with respect to PCBM. This is because more double bonds of the fullerene core become saturated, the more side chains are attached to the fullerene.<sup>16</sup> All compounds are well soluble in organic solvents, such as 1,2-dichlorobenzene (*o*DCB) or chloroform. Three different blends, consisting of Polymer:PCBM (Blend 1), Polymer:bis-PCBM (Blend 2) and Polymer:bis-*o*QDMC (Blend 3) were prepared. Polymer and fullerenes were dissolved in *o*DCB and mixed in the weight ratio 1:2. All films were investigated “as coated” without thermal or solvent annealing steps, because any annealing resulted in decreased device performance.

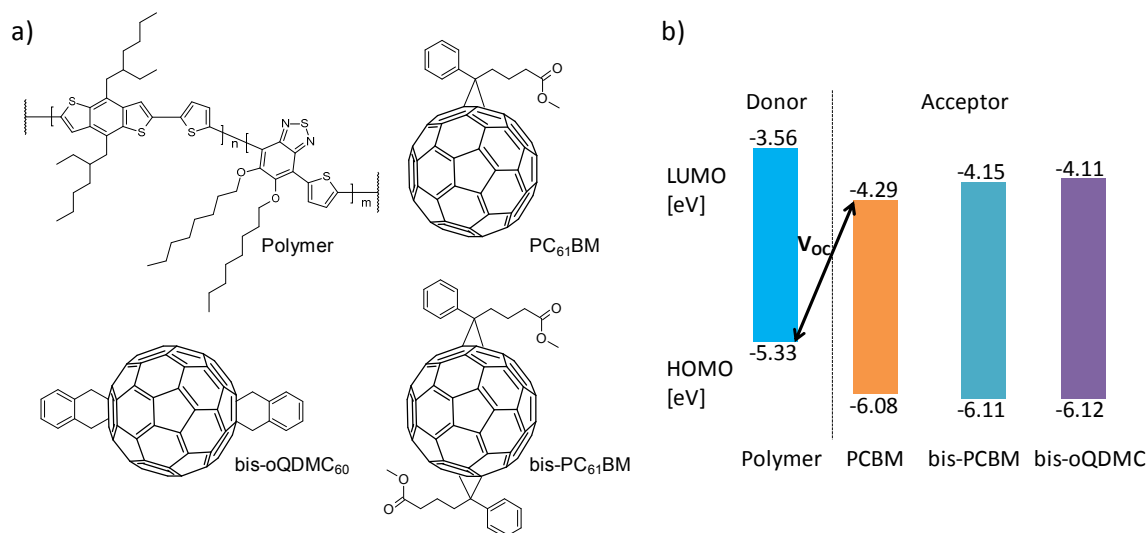


Figure 1: a) Chemical structure of the *p*-type donor-acceptor copolymer (Polymer) and the three *n*-type fullerene derivatives Phenyl- $C_{61}$ -butyric acid methyl ester (PCBM), Bis-Phenyl- $C_{61}$ -butyric acid methyl ester (bis-PCBM) and Bis-*o*-quino-dimethane  $C_{60}$  (bis-*o*QDMC); b) energy level diagram of the materials illustrating the linear relation of  $V_{oc}$  of a solar cell with difference in HOMO of donor and LUMO of acceptor.

Electron- and hole-only devices were individually fabricated in order to estimate the electron and hole mobilities within the blends. The device architecture is depicted in Figure 2a and e. Electron-only devices possess an ITO/Zinc oxide bottom contact and calcium, capped with aluminum, as top electrode. Zinc oxide and calcium electrodes provide, due to their low workfunctions, a hole injection barrier. Therefore, charges can only be injected into the LUMO of the materials and the charge transport through the bulk is determined by the electron mobility of the blend. In hole-only devices, with ITO/PEDOT:PSS bottom contact and PEDOT:PSS/silver top contact, charges are exclusively injected into the HOMO of the material, which allows for determining the hole mobility of the blend. These single carrier devices allow us to study charge transport of the blends in a geometry very similar to that of OPV devices. The active layer was deposited using a doctor blade technique. See Experimental Section for details. The current density–voltage ( $J$ - $V$ ) characteristics were recorded under inert gas atmosphere in the dark. At higher voltages, assuming Ohmic injecting contacts and trap free transport, the current measured is space-charge limited only, and the charge carrier mobility can be estimated by using Mott-Gurney's equation<sup>17</sup>:

$$J = \frac{9}{8} \varepsilon_0 \varepsilon_r \mu \frac{V^2}{L^3}$$

where  $J$  is the current density,  $\varepsilon_r$  is the dielectric constant of the organic semiconductor blend (assumed to be 3 in our calculations<sup>18</sup>),  $\varepsilon_0$  is the permittivity of free space,  $\mu$  is the charge carrier mobility,  $L$  is the thickness of the active layer and  $V$  is the voltage drop across the device. Figure 2b-d and f-h show  $J$ - $V$  characteristics of the single carrier devices for each blend and for various active layer thicknesses. The resulting charge carrier mobilities of the blends are summarized in Table 1.

Before evaluating Polymer:Fullerene blend devices, the charge carrier mobilities of the pristine materials were studied. The hole mobility of the pristine Polymer film, and the electron mobility of pristine PCBM and bis-PCBM are shown in Table 1. Hole-only devices were prepared from *o*DCB solution. Similarly, the electron transport of the three pristine acceptor materials was also investigated. Film formation from *o*DCB solution resulted in non-homogeneous films for the fullerene derivatives, so chloroform was chosen instead.

Good films were obtained for PCBM and bis-PCBM, however the film formation for bis-oQDMC still remained problematic. Hence, only for PCBM and bis-PCBM reliable electron mobilities could be obtained. A higher electron mobility of  $3 \cdot 10^{-3} \text{ cm}^2 \text{V}^{-1} \text{s}^{-1}$  was determined for PCBM, compared to  $5 \cdot 10^{-4} \text{ cm}^2 \text{V}^{-1} \text{s}^{-1}$  for bis-PCBM electron-only devices. The same trend was also observed by Faist *et al.* in OFET experiments.<sup>12</sup> The question whether the electron transport correlates with the respective blend devices (Figure 2b-d) is investigated in the following.

*Table 1: Summary of electron and hole mobilities ( $\mu_e$  and  $\mu_h$ ) for Blend 1, Blend 2, Blend 3 and pristine material films; the values were obtained from J-V curves shown in Figure 2, Figure S1 and Mott-Gurney equation and represent an average mobility over the thickness range measured. See supporting information for J-V curves of pristine materials films and mobility value for each J-V curve.*

Mobility [ $\text{cm}^2 \text{V}^{-1} \text{s}^{-1}$ ]	Polymer	PCBM*	bis-PCBM*	Blend 1	Blend 2	Blend 3
$\mu_e$	-	$3 \cdot 10^{-3}$	$5 \cdot 10^{-4}$	$9 \cdot 10^{-3}$	$2 \cdot 10^{-3}$	$1 \cdot 10^{-3}$
$\mu_h$	$4 \cdot 10^{-4}$	-	-	$4 \cdot 10^{-4}$	$6 \cdot 10^{-4}$	$7 \cdot 10^{-5}$

\* Films coated from chloroform solution; no reliable devices were obtained for bis-oQDMC due to non-homogeneous films.

In Blend 1, containing PCBM as electron transport material, an electron mobility of  $9 \cdot 10^{-3} \text{ cm}^2 \text{V}^{-1} \text{s}^{-1}$  was found. For both blends containing bis-adduct fullerenes, electron mobilities were significantly lower, with  $2 \cdot 10^{-3} \text{ cm}^2 \text{V}^{-1} \text{s}^{-1}$  for Blend 2 and  $1 \cdot 10^{-3} \text{ cm}^2 \text{V}^{-1} \text{s}^{-1}$  for Blend 3. Hence, electrons are transported less efficiently through the bulk of the bis-adduct fullerene blends. Worse electron transport of bis-PCBM is apparently also reflected in the Polymer:Fullerene blend. The fact, that both mobility values obtained in the blend are higher compared to the pristine fullerene films is potentially due to the different coating solvent used. The high boiling point solvent oDCB allows for a slower solvent evaporation rate in the case of the blend devices, which could result in better crystallization of fullerene domains and thus enhance charge transport compared to the films coated from chloroform. However, in both blend and pristine devices, the same trend of a higher electron mobility for PCBM compared to bis-PCBM was observed. The differences in electron mobility for a pristine compound and its blend depend on the changes in morphology.

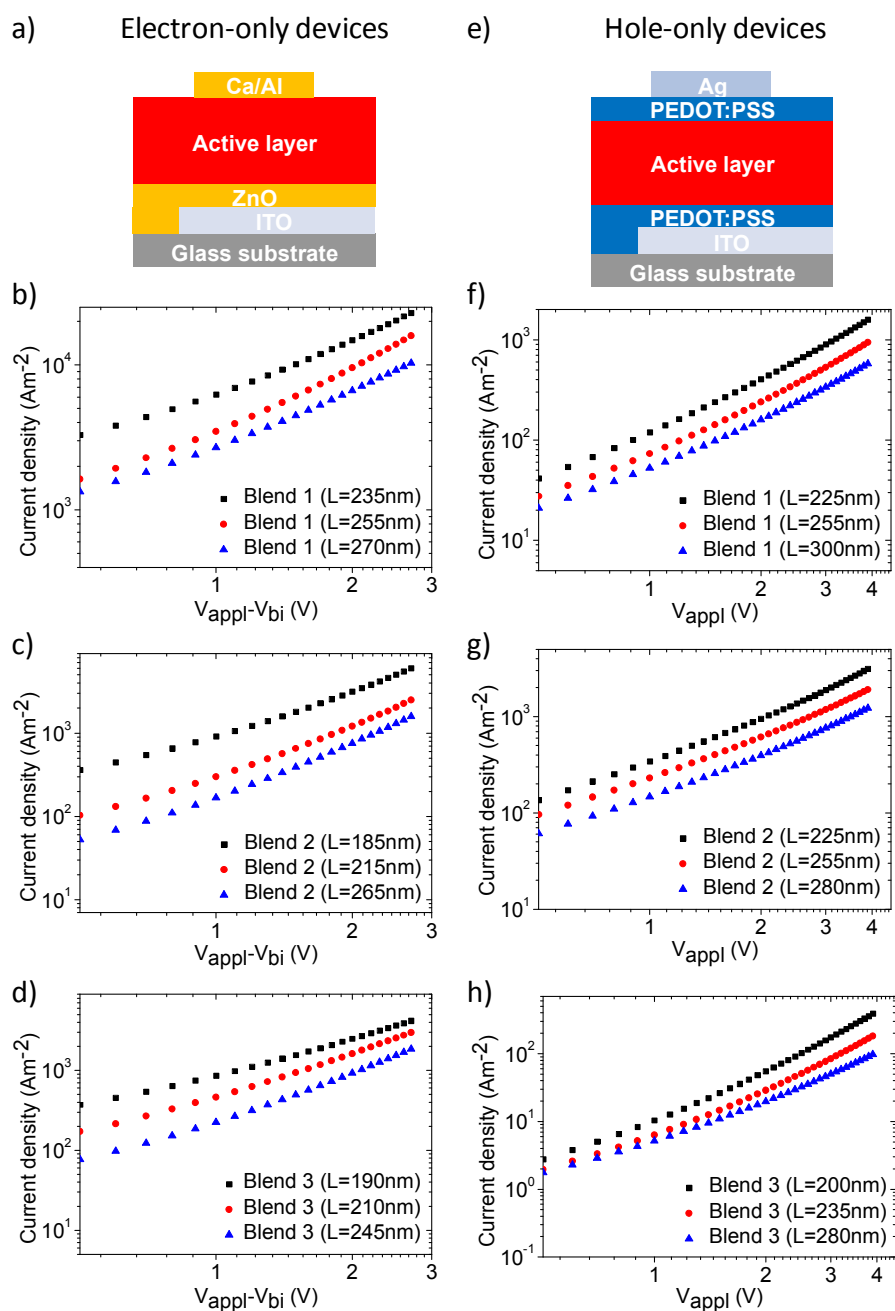


Figure 2: a) Schematic of an electron-only device and e) a hole-only device; Current density – Voltage ( $J$ - $V$ ) characteristics of electron-only (b, c, d) and hole-only (f, g, h) devices for the three different blend systems;  $J$ - $V$  curves were recorded in the dark at RT under inert gas atmosphere for various active layer thicknesses. For electron-only devices, the applied Voltage ( $V_{\text{appl}}$ ) was corrected for a built-in potential ( $V_{\text{bi}}$ ) resulting from the differences in work function for ZnO and calcium.

Different phase separation of donor and acceptor materials can affect the percolation paths of the charge carriers and result in changes in electron transport. An attempt to disentangle the effect of blend morphology and intrinsic fullerene properties on charge transport is made by comparing electron mobilities with hole mobilities (from hole-only devices) of the same blends. The  $J$ - $V$  curves of hole-only devices are shown in the bottom row of Figure 2f, g and h. Blend 1 has a hole mobility of  $4 \cdot 10^{-4} \text{ cm}^2 \text{V}^{-1} \text{s}^{-1}$ , which is slightly below the hole mobility of the Blend 2 with  $6 \cdot 10^{-4} \text{ cm}^2 \text{V}^{-1} \text{s}^{-1}$ . The fact that the hole mobility of pristine Polymer is of the same order of magnitude as in the Blends 1 and 2 ( $10^{-4} \text{ cm}^2 \text{V}^{-1} \text{s}^{-1}$ ) shows, that hole transport is not impeded by the presence of these fullerenes and that blend morphology provides sufficient percolation paths for holes. The lowest hole mobility by far was measured in the Blend 3 ( $7 \cdot 10^{-5} \text{ cm}^2 \text{V}^{-1} \text{s}^{-1}$ ). This comparison shows that hole mobility decreases in Blend 3, even though the p-type material is kept constant. Hence, we attribute this drop in hole mobility in Blend 3 to changes in the blend morphology. If donor and acceptor material interact differently, for instance due to different side groups of the acceptor, this can also affect the blend morphology upon film formation. Since hole mobility does not change drastically for the PCBM and bis-PCBM blends, the percolation paths for holes are likely to be similar. For Blend 3 however, the drop in hole mobility indicates worse percolation paths for holes and thus a problematic morphology in this blend. In our experiment, hole mobility in the blend is generally found to be smaller compared to the electron mobility measured. This might be due to the Polymer:Fullerene blend ratio being 1:2 and hence more of the electron transporting fullerene being present in the blend system.

To study absorption and aggregation effects in these blends, UV/vis spectroscopy of thin films was performed. Absorption spectra of the blend films and a pristine polymer reference coated on quartz glass are depicted in Figure 3. Films were prepared under similar conditions to give a comparable thickness of 100 nm for all samples. In the short wavelength region, where mainly fullerene absorbs, the maximum absorbance can be observed for the PCBM blend, while bis-PCBM and bis-oQDMC absorb only slightly less. This can be attributed to the increased number of side-chains, which do not contribute to the light absorption in this wavelength region and therefore weaken the overall fullerene absorption. At longer wavelength, where the polymer absorbs, no significant changes in absorption are observed.

Thus, UV/vis measurements indicate that the conformation of the polymer is not heavily affected by different fullerenes in the blend.

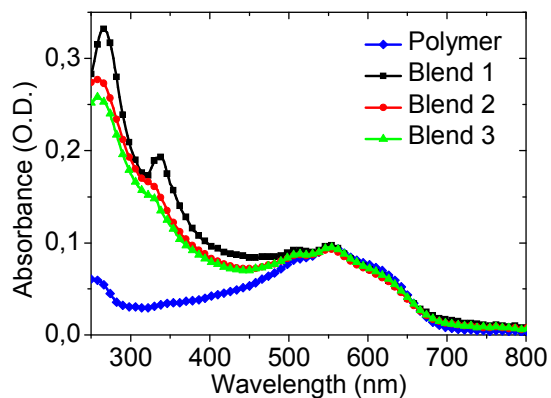


Figure 3: UV/vis absorption spectra of a pristine Polymer film and Blend 1, Blend 2 and Blend 3 with a thickness of ca. 100 nm coated from oDCB solution.

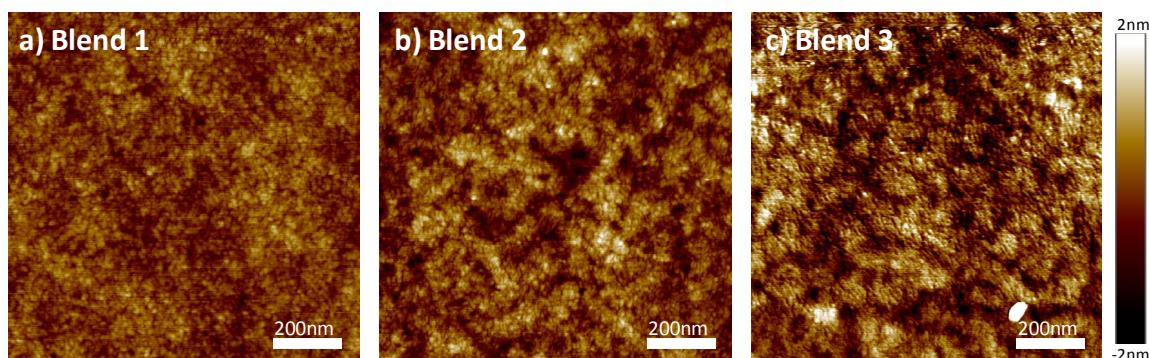


Figure 4: AFM Topography images obtained in Tapping Mode of a) Blend 1, b) Blend 2 and c) Blend 3 on 200nm thin films.

To investigate the blend morphology, atomic force microscopy (AFM) was performed on the blends in Tapping Mode. Topography images are depicted in Figure 4a-c. From surface roughness and feature sizes visible on the surface, we can, to some extent, draw conclusions about phase separation of donor and acceptor also in the bulk of the blend. Surface roughness slightly increases from Blend 1 ( $RMS=0.4nm$ ) to Blend 2 ( $RMS=0.5nm$ ) and Blend 3 ( $RMS=0.6nm$ ) blends. Slightly bigger features visible in Figure 4c, compared to the almost

featureless surface in Figure 4a indicate a coarser phase separation for the bis-oQDMC blend. This supports our assumption that both decreased electron and hole mobility in the bis-oQDMC blends might be caused by a unfavorable blend morphology for charge percolation and transport.

In the following, we compare photovoltaic devices made of the three blends under investigation with active layer thicknesses of 200 nm (Blend 1a, Blend 2a and Blend 3a) and 100 nm (Blend 1b, Blend 2b and Blend 3b), respectively. A standard device architecture with an ITO/PEDOT:PSS bottom contact and calcium/aluminum top electrodes were chosen. For the active layer preparation, conditions were similar as for the SCLC devices (see Experimental Part for details). The  $J$ - $V$  curves under AM1.5 illumination ( $1000 \text{ Wm}^{-2}$ ) and external quantum efficiency (EQE) of the solar cells are plotted in Figure 5a and b, respectively. Solar cell parameters are shown in Table 2. Regarding the  $V_{OC}$ , a clear trend can be observed. Both bis-adduct fullerene blends have higher  $V_{OC}$  than the PCBM reference. For thick films, a maximum  $V_{OC}$  of 980 mV could be reached for both bis-adduct fullerenes compared to 830 mV for the PCBM blend. For the devices with thinner active layer, the maximum  $V_{OC}$  was obtained for Blend 3b with 1050 mV, Blend 2b showed 1000 mV and Blend 1b was clearly below with 900 mV. This is in agreement with the LUMO energy levels and meets the expectations of higher acceptor LUMOs giving higher  $V_{OC}$ . A comparison of  $J_{SC}$  is more complex. For an active layer thickness of 200 nm, the highest  $J_{SC}$  was obtained for the PCBM blend ( $9.9 \text{ mAcm}^{-2}$ ), both bis-adduct fullerenes have lower  $J_{SC}$  values (Blend 2a:  $5.9 \text{ mAcm}^{-2}$ , Blend 3a:  $5.5 \text{ mAcm}^{-2}$ ). As a result, PCEs of the bis-adduct fullerenes with 2.9 % are below the PCBM blend with 3.8 %.

As shown in Figure 3, light harvesting in these devices is very similar, so the reason for lower  $J_{SC}$  must be due to less efficient charge generation, charge collection or higher recombination losses. Knowing that electron mobility in the bis-fullerene blends is lower, we can assume that recombination of free charges due to insufficient charge carrier mobility might be a critical parameter. A simple way to test this hypothesis is to compare the  $J_{SC}$  of thick films to those of thinner films. Since charges in thin films need to travel shorter distances to reach the electrode, high charge carrier mobilities are not as crucial as in thick films. In fact, the experiments with only 100 nm active layer thickness show a different trend

in  $J_{SC}$ . For the bis-PCBM blend (2b),  $J_{SC}$  increases from  $5.9 \text{ mAcm}^{-2}$  to  $7.7 \text{ mAcm}^{-2}$  for thinner films, which means that in spite of reduced light harvesting, the solar cell gives higher photocurrent. This, we attribute to less recombination processes taking place in the device. In the case of Blend 3b however,  $J_{SC}$  remains at about  $5.5 \text{ mAcm}^{-2}$ . Also, the fill factor (FF) in Blend 3b is significantly lower, compared to the other two blends, where an increase in FF could be observed for the thin devices. The EQE data shown in Figure 5b support the observed trends in  $J_{SC}$ . To better understand the origin of low FF, series and parallel or shunt resistance ( $R_S$  and  $R_{SH}$ ) of the solar cells are discussed in the following. In general, to obtain high FF, low  $R_S$  and high  $R_{SH}$  are required.

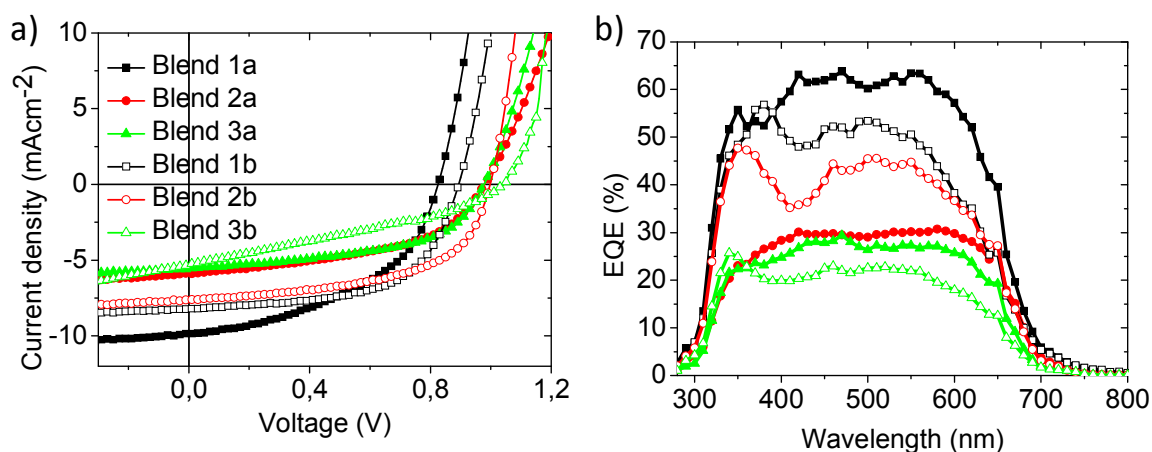


Figure 5: a)  $J$ - $V$  characteristics under AM1.5 solar irradiation ( $1000 \text{ Wm}^{-2}$ ) and b) external quantum efficiency (EQE) of photovoltaic cells of Blend 1 (squares), Blend 2 (circles) and Blend 3 (triangles) with active layer thicknesses of 200nm (filled symbols) and 100nm (empty symbols).

A straight-forward method for estimating  $R_S$  and  $R_{SH}$  in solar cells is determining the slope of the  $J$ - $V$  curve at  $V_{OC}$  and  $J_{SC}$ , respectively. The inverse of the slopes give the specific resistances in  $\Omega\text{cm}^2$ , which are tabulated in Table 2 for all cells under investigation. Due to identical device fabrication conditions we assume that series resistance accounting from the bottom and top electrode conductivity and interfacial layer resistances are constant for all solar cells under investigation. Therefore, changes in  $R_S$  are attributed to differences in active layer resistance, which can be altered by blend morphology causing differences in charge

percolation.<sup>19, 20</sup> Comparing  $R_S$  values of solar cells made of Blend 1, the active layer thickness does not seem to have a big impact, with both cells having a series resistance of  $9.1 \Omega\text{cm}^2$  (Blend 1a) and  $9.3 \Omega\text{cm}^2$  (Blend 1b). In other words, the percolation paths remain almost the same and the charge carrier mobility seems sufficient high within the range of thicknesses tested. For Blend 2 however, reducing the active layer thickness results in a threefold improvement of  $R_S$  from  $21.7 \Omega\text{cm}^2$  to  $7.2 \Omega\text{cm}^2$ . Hence, the thick film was limited by high active layer series resistance resulting in poor charge transport, which is consistent with our SCLC measurements. For both Blend 1 and Blend 2 a higher  $R_{SH}$  is achieved for the 100 nm devices, compared to devices with an active layer of 200 nm. As a consequence the FF is higher for the thin devices.  $R_S$  of Blend 3a and Blend 3b cells are  $14.5 \Omega\text{cm}^2$  and  $23.8 \Omega\text{cm}^2$ , respectively. The higher  $R_S$  even in thin active layer demonstrates that the unfavorable blend morphology is the main factor influencing series resistance and devices performance. Both high  $R_S$  and low  $R_{SH}$  in Blend 3b account for the poor FF.

Table 2: Solar cell parameters obtained from J-V curves from Figure 5a for the three different blend systems with active layer thicknesses of 200nm ("a") and 100nm ("b"), respectively.  $R_S$  and  $R_{SH}$  account for series and shunt resistance of the cells, which were estimated considering the inverse slopes of the J-V curve at  $V_{OC}$  and  $J_{SC}$  respectively.

<b>Device</b>	<b><math>V_{OC}</math> [mV]</b>	<b><math>J_{SC}</math> [mAcm<sup>-2</sup>]</b>	<b>FF [%]</b>	<b>PCE [%]</b>	<b><math>R_S</math> [<math>\Omega\text{cm}^2</math>]</b>	<b><math>R_{SH}</math> [<math>\Omega\text{cm}^2</math>]</b>
<b>200 nm</b>						
<b>Blend 1a</b>	830	-9.9	46.5	3.8	9.1	645.7
<b>Blend 2a</b>	980	-5.9	49.3	2.9	21.7	653.6
<b>Blend 3a</b>	980	-5.5	53.2	2.9	14.5	1012
<b>100 nm</b>						
<b>Blend 1b</b>	900	-8.2	59.1	4.4	9.3	1266
<b>Blend 2b</b>	1000	-7.7	55.7	4.3	7.2	909.1
<b>Blend 3b</b>	1050	-5.3	33.7	1.9	23.8	287.4

## Conclusion

We have investigated blends of a donor-acceptor copolymer as donor and three different fullerene derivatives (PCBM, bis-PCBM and bis-oQDMC) as acceptors. By fabricating single carrier devices, the hole and electron mobilities within the blends were estimated,

which helped interpreting their performance in solar cells in 200 nm and 100 nm thin films, respectively. For the Blend 1 (featuring PCBM),  $J_{SC}$  is decreased when the active layer thickness is reduced from 200 nm to 100 nm, which is due to less light harvested within the active layer. Overall device performance, however, is increased due to higher FF and  $V_{OC}$ . Higher FF and  $V_{OC}$  are also observed for 100 nm Blend 2 devices with bis-PCBM. In addition,  $J_{SC}$  is notably higher compared to the 200 nm device. The electron mobility in this blend was found to be lower compared to Blend 1. By reducing the film thickness, this issue could be overcome, which is shown by the improved solar cell parameters. In Blend 3 devices, containing bis-oQDMC, both low electron and hole mobilities were measured. Since the hole transporting material was kept the same for all three blend systems, a lower hole mobility can only be explained by a change in the nanoscale morphology with worse percolation paths for holes in this blend. As a consequence, OPV devices with reduced film thickness still have low  $J_{SC}$ , FF and PCE. In this paper we show that using the SCLC approach in single carrier devices is a practical tool to help understanding solar cell characteristics of Polymer:Fullerene blends. Photoluminescence and photoinduced absorption measurements are subject of current investigation in order to identify the major loss mechanism in this blend.

## Experimental Section

*Chemicals:* Phenyl- $C_{60}$ -butyric acid methyl ester (PCBM), Bis-Phenyl- $C_{60}$ -butyric acid methyl ester (bis-PCBM) and Bis-o-quino-dimethane  $C_{60}$  (bis-oQDMC) were purchased from Nano-C. Polymer was provided by Merck Chemicals Ltd.. DMSO and 1,2-dichlorobenzene (*o*DCB) (anhydrous with crown cap, 99%) were purchased from Sigma-Aldrich. PEDOT:PSS (Clevios P VP Al 4083) was purchased from Heraeus. Zinc-acetate dihydrate (99.0%) was purchased from Sigma-Aldrich.

*Instrumentation:* UV/vis spectra of thin films coated on quartz glass were recorded on a Hitachi 3000 spectrophotometer. Film thicknesses were determined on an Alphastep 500 surface profilometer. Atomic force microscopy was performed on a Veeco Dimension Icon with Nanoscope V controller, in Tapping Mode. The used cantilevers were NSC15/AIBS

from Mikromasch. External quantum efficiency was measured on a QE-PV-SI QE/IPCE Measurement kit from Newport. Cyclic voltammograms were recorded on a Princeton Applied Research VersaSTAT 4 Potentiostat/Galvanostat 108 using platinum electrodes at a scan rate of  $50 \text{ mVs}^{-1}$  and a  $\text{Ag/Ag}^+$  (0.10 M of  $\text{AgNO}_3$  in acetonitrile) reference electrode in a anhydrous and nitrogen-saturated solution of 0.1 M of tetrabutylammonium tetrafluoroborate in acetonitrile. Oxidation potential ( $E_{\text{ox}}^{1/2}$ ) of ferrocene is 0.08-0.11 V versus  $\text{Ag/Ag}^+$ , and 0.41 V versus SCE. The HOMO and LUMO energy levels were determined from the oxidation and reduction onset of the second scan from CV data taking into account the SCE level at -4.7 eV .

*Device preparation:* SCLC electron-only devices were fabricated using the following structure: glass/ITO/ZnO/Active Layer/Ca/Al. Commercial ITO coated glass substrates with a sheet resistance of 13 Ohms per sq (Lumtec) were cleaned using following sequence in an ultrasonic bath: detergent, water, acetone and 2-propanol. After ozone treatment of the substrates for 10 min, a solution of Zinc-acetate dihydrate in DMSO ( $160 \text{ mgmL}^{-1}$ ) was spin coated on the substrate and the substrates were subsequently heated on a hotplate at  $300 \text{ }^\circ\text{C}$  for 5 min. The substrates were rinsed with water and acetone. All following steps were carried out under nitrogen atmosphere with water and oxygen levels  $\leq 0.1 \text{ ppm}$ . After cooling the substrate, the active layer was blade coated from *o*DCB solutions on an Erichsen Coatmaster 509MC. The substrates were then put in a thermal evaporation chamber to evaporate the top electrodes (30 nm Ca/ 100 nm Al) under high vacuum ( $1 \cdot 10^{-6} \text{ mbar}$ ) through a shadow mask (active area  $4 \text{ mm}^2$ ). SCLC hole-only devices were fabricated using the following structure: glass/ITO/PEDOT:PSS/Active Layer/PEDOT:PSS/Ag. Commercial ITO coated glass substrates with a sheet resistance of 13 Ohms per sq (Lumtec) were cleaned using following sequence in an ultrasonic bath: detergent, water, acetone and 2-propanol. After ozone treatment of the substrates for 10 min, PEDOT:PSS was spin coated on the ITO surface and dried at  $130 \text{ }^\circ\text{C}$  for 30 min. After cooling the substrate, the active layer was blade coated from *o*DCB solutions on a Erichsen Coatmaster 509MC under nitrogen atmosphere with water and oxygen levels  $\leq 0.1 \text{ ppm}$ . Another PEDOT:PSS layer was spin coated on top of the active layer. The substrates were then put in a thermal evaporation chamber to evaporate the top electrode (100 nm Ag) under high vacuum ( $1 \cdot 10^{-6} \text{ mbar}$ ) through a shadow

mask (active area 4 mm<sup>2</sup>). The current-voltage characteristics of the devices were measured using a Keithley 2420 (*I-V*) Digital SourceMeter at 25 °C.

*Photovoltaic device preparation:* OPV cells were fabricated using a standard device architecture: glass/ITO/PEDOT:PSS/Active Layer/Ca/Al. Commercial ITO coated glass substrates with a sheet resistance of 13 Ohms per sq (Lumtec) were cleaned using following sequence in an ultrasonic bath: detergent, water, acetone and 2-propanol. After ozone treatment of the substrates for 10 min, PEDOT:PSS was spin coated on the ITO surface and dried at 130 C for 30 min. All following steps were carried out under nitrogen atmosphere with water and oxygen levels  $\leq 0.1$  ppm. After cooling the substrate, the active layer was blade coated from *o*DCB solution on a Erichsen Coatmaster 509MC. The substrates were then put in a thermal evaporation chamber to evaporate the top electrodes (30 nm Ca/ 100 nm Al) under high vacuum ( $1 \cdot 10^{-6}$  mbar) through a shadow mask (active area 4 mm<sup>2</sup>). The current-voltage characteristics of the devices were measured using a Keithley 2420 (*I-V*) Digital SourceMeter at 25 °C. An oriel solar simulator was used to provide an AM1.5 spectrum (1000 Wm<sup>-2</sup>). The power of the solar simulator was calibrated using a reference Silicon cell by Newport.

## Acknowledgement

We thank Amy Topley from Merck Chemicals Ltd. for cyclic voltammetry measurements. Financial support from Merck Chemicals Ltd. and EU Largecells is kindly acknowledged.

## References

- (1) Dennler, G.; Scharber, M. C.; Brabec, C. J., *Advanced Materials* **2009**, *21*, (13), 1323-1338.
- (2) Sun, Y.; Welch, G. C.; Leong, W. L.; Takacs, C. J.; Bazan, G. C.; Heeger, A. J., *Nature Materials* **2012**, *11*, (1), 44-48.

- 
- (3) Bakulin, A. A.; Rao, A.; Pavelyev, V. G.; van Loosdrecht, P. H. M.; Pshenichnikov, M. S.; Niedzialek, D.; Cornil, J. r. m.; Beljonne, D.; Friend, R. H., *Science* **2012**, *335*, (6074), 1340-1344.
  - (4) He, Z.; Zhong, C.; Huang, X.; Wong, W.-Y.; Wu, H.; Chen, L.; Su, S.; Cao, Y., *Advanced Materials* **2011**, *23*, (40), 4636-4643.
  - (5) Li, G.; Zhu, R.; Yang, Y., *Nature Photonics* **2012**, *6*, (3), 153-161.
  - (6) Son, H. J.; He, F.; Carsten, B.; Yu, L., *Journal of Materials Chemistry* **2011**, *21*, (47), 18934-18945.
  - (7) Zhou, H.; Yang, L.; You, W., *Macromolecules* **2012**, *45*, (2), 607-632.
  - (8) Chochos, C. L.; Choulis, S. A., *Progress in Polymer Science* **2011**, *36*, (10), 1326-1414.
  - (9) Scharber, M. C.; Mühlbacher, D.; Koppe, M.; Denk, P.; Waldauf, C.; Heeger, A. J.; Brabec, C. J., *Advanced Materials* **2006**, *18*, (6), 789-794.
  - (10) Jarzab, D.; Cordella, F.; Lenes, M.; Kooistra, F. B.; Blom, P. W. M.; Hummelen, J. C.; Loi, M. A., *The Journal of Physical Chemistry B* **2009**, *113*, (52), 16513-16517.
  - (11) Dyer-Smith, C.; Reynolds, L. X.; Bruno, A.; Bradley, D. D. C.; Haque, S. A.; Nelson, J., *Advanced Functional Materials* **2010**, *20*, (16), 2701-2708.
  - (12) Faist, M. A.; Keivanidis, P. E.; Foster, S.; Wöbkenberg, P. H.; Anthopoulos, T. D.; Bradley, D. D. C.; Durrant, J. R.; Nelson, J., *Journal of Polymer Science Part B: Polymer Physics* **2011**, *49*, (1), 45-51.
  - (13) Miller, N. C.; Sweetnam, S.; Hoke, E. T.; Gysel, R.; Miller, C. E.; Bartelt, J. A.; Xie, X.; Toney, M. F.; McGehee, M. D., *Nano Letters* **2012**, *12*, (3), 1566-1570.
  - (14) Voroshazi, E.; Vasseur, K.; Aernouts, T.; Heremans, P.; Baumann, A.; Deibel, C.; Xue, X.; Herring, A. J.; Athans, A. J.; Lada, T. A.; Richter, H.; Rand, B. P., *Journal of Materials Chemistry* **2011**, *21*, (43), 17345-17352.
  - (15) Hoppe, H.; Mitchell, W.; Tierney, S.; Carrasco-Orozco, M., *unpublished work*.
  - (16) Lenes, M.; Shelton, S. W.; Sieval, A. B.; Kronholm, D. F.; Hummelen, J. C.; Blom, P. W. M., *Advanced Functional Materials* **2009**, *19*, (18), 3002-3007.
  - (17) Bozano, L.; Carter, S. A.; Scott, J. C.; Malliaras, G. G.; Brock, P. J., *Applied Physics Letters* **1999**, *74*, (8), 1132-1134.

- (18) Goh, C.; Kline, R. J.; McGehee, M. D.; Kadnikova, E. N.; Frechet, J. M. J., *Applied Physics Letters* **2005**, *86*, (12), 122110-3.
- (19) Yang, F.; Shtein, M.; Forrest, S. R., *Nature Materials* **2005**, *4*, (1), 37-41.
- (20) Servaites, J. D.; Yeganeh, S.; Marks, T. J.; Ratner, M. A., *Advanced Functional Materials* **2010**, *20*, (1), 97-104.

## Supporting Information

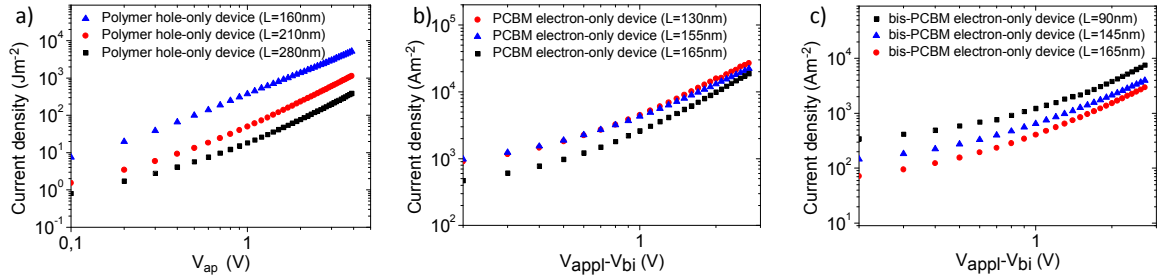


Figure S1: J-V characteristics of hole-only devices of Polymer films (a) and electron-only devices of PCBM (b) and bis-PCBM films (c). J-V curves were recorded in the dark at RT under inert gas atmosphere for various active layer thicknesses. For electron-only devices, the applied Voltage ( $V_{appl}$ ) was corrected for a built-in potential ( $V_{bi}$ ) resulting from the differences in work function for ZnO and Ca.

Table S 1: Electron and hole mobilities ( $\mu_e$  and  $\mu_h$ ) for Blend 1, Blend 2, Blend 3 and pristine material films of varied active layer thicknesses; the values were obtained from J-V curves shown in Figure 2, Figure S1 and Mott-Gurney equation.

Mobility $\mu$ [cm <sup>2</sup> V <sup>-1</sup> s <sup>-1</sup> ]	Polymer	PCBM <sup>†</sup>	bis-PCBM <sup>†</sup>	bis-o-QDMC <sup>#</sup>	Blend 1	Blend 2	Blend 3
$\mu_e$	-	$2 \cdot 10^{-3}$ L=130nm	$3 \cdot 10^{-4}$ L=90nm	-	$1 \cdot 10^{-2}$ L=235nm	$2 \cdot 10^{-3}$ L=185nm	$1 \cdot 10^{-3}$ L=190nm
	-	$3 \cdot 10^{-3}$ L=155nm	$6 \cdot 10^{-4}$ L=145nm	-	$1 \cdot 10^{-2}$ L=255nm	$1 \cdot 10^{-3}$ L=215nm	$1 \cdot 10^{-3}$ L=210nm
	-	$5 \cdot 10^{-3}$ L=165nm	$6 \cdot 10^{-4}$ L=165nm	-	$8 \cdot 10^{-3}$ L=270nm	$2 \cdot 10^{-3}$ L=265nm	$1 \cdot 10^{-3}$ L=245nm
$\mu_h$	$5 \cdot 10^{-4}$ L=160nm	-	-	-	$4 \cdot 10^{-4}$ L=225nm	$7 \cdot 10^{-4}$ L=225nm	$9 \cdot 10^{-5}$ L=200nm
	$3 \cdot 10^{-4}$ L=210nm	-	-	-	$3 \cdot 10^{-4}$ L=255nm	$6 \cdot 10^{-4}$ L=255nm	$7 \cdot 10^{-5}$ L=235nm
	$3 \cdot 10^{-4}$ L=280nm	-	-	-	$4 \cdot 10^{-4}$ L=300nm	$5 \cdot 10^{-4}$ L=280nm	$5 \cdot 10^{-5}$ L=280nm

<sup>†</sup> Films coated from chloroform solution; <sup>#</sup> no reliable devices obtained due to unhomogeneous films.



## **7. Fullerene-grafted Copolymers exhibiting High Electron Mobility without Nanocrystal Formation**

*Martin Hufnagel, Mathis-Andreas Muth, Johannes C. Brendel and Mukundan Thelakkat\**

Prof. Dr. Mukundan Thelakkat, Applied Functional Polymers, Department of Macromolecular Chemistry I, University of Bayreuth, Universitaetsstr.30, 95440 Bayreuth (Germany)

This manuscript is prepared for submission.

## Abstract

Well-soluble fullerene-grafted polymers with high contents of pendant phenyl-C<sub>61</sub>-butyric acid methyl ester (PCBM) between 30 and 64 wt% are reported. Herein, the tailor-made precursor copolymers poly(4-methoxystyrene-*stat*-4-*tert*-butoxystyrene) obtained by reversible addition fragmentation chain transfer (RAFT) polymerization are functionalized *via* an efficient polymer-analogous esterification. The synthesized acceptor copolymers retain the optical and electrochemical properties of the incorporated PCBM independent of their fullerene weight fraction. Their electron transport properties are studied by the space-charge limited current (SCLC) method. The maximum electron mobility  $\mu_e$  of  $1 \cdot 10^{-4} \text{ cm}^2 \text{ V}^{-1} \text{ s}^{-1}$  is achieved for 37 wt% of incorporated PCBM. Below 50 wt% of PCBM, the acceptor polymers exhibit exceptional high charge carrier mobility compared to the corresponding blends of molecular PCBM and precursor copolymer. We attribute this behaviour to the amorphous morphology both in thin films and in bulk, which clearly indicates the absence of PCBM nanocrystals in the PCBM-grafted copolymers. Hence, an efficient charge carrier percolation is facilitated by the homogeneous distribution of PCBM. This novel electron transport material is an attractive candidate for the application in organic photovoltaic cells.

## Introduction

Buckminster fullerene and its derivatives exhibit a unique electron-accepting/transporting capability<sup>1</sup> and their application as n-type semiconductors for organic photovoltaic (OPV) cells has been extensively studied.<sup>2</sup> Physically mixed blends of phenyl-C<sub>61</sub>-butyric acid methyl ester (PCBM) and poly(3-hexylthiophene) (P3HT) as donor material for bulk heterojunction (BHJ) solar cells have achieved power conversion efficiencies (PCEs) up to 5%.<sup>3</sup> This benchmark value was outperformed by the application of low-bandgap donor materials, yielding PCEs of more than 8%.<sup>4</sup> A crucial requirement for high solar cell performance is an efficient but balanced charge transport of electrons and holes through the active layer of organic solar cells. Regarding the morphology in blend devices based on P3HT:PCBM or poly(*p*-phenylenevinylene):PCBM, it was found that PCBM forms a crystallization-induced network of PCBM-rich domains, which consist of PCBM

nanocrystals.<sup>5,6</sup> In these blend systems the bulk electron mobility improved with an increasing fraction of crystalline PCBM. With a sufficiently large content of PCBM, roughly 60-70 wt% in the blend, a dense network of percolation pathways is opened up which enables charge carrier transport over macroscopic distances.<sup>7-9</sup> Pure PCBM is a crystalline n-type semiconductor<sup>10</sup> and forms different crystal structures depending on the crystallization solvent.<sup>11</sup>

However, new concepts to overcome the inherent problem of limited thermodynamic stability of nanostructured blends direct towards a replacement of small molecule fullerenes by polymeric electron transport materials. Studies on side chain polymers carrying pendant C<sub>60</sub> show a correlation of increasing electron mobility with increasing C<sub>60</sub> content.<sup>12,13</sup> The bulk electron mobility derived from the space-charge limited current (SCLC) method reached up to 10<sup>-5</sup> cm<sup>2</sup>V<sup>-1</sup>s<sup>-1</sup> for only 13 vol% of incorporated C<sub>60</sub>.<sup>13</sup> Further, the potential of this emerging class of electron transport materials was recently demonstrated in polymer solar cells with a promising PCE of 1.5 %.<sup>14</sup>

While the electronic properties of side chain polymers can be tuned by the type of attached fullerene derivative, the physicochemical parameters are determined by the nature of the polymer backbone. Their preparation is achieved either by polymer-analogous modification or directly by polymerization of fullerene-derivatized monomers using organometallic catalysis.<sup>14-16</sup> Polymer-analogous synthetic routes rely on functionalized polymers, which are decorated with fullerene derivatives in a further step. Various types of reactions were reported to attach C<sub>60</sub> covalently to functional polymers including atom transfer radical addition (ATRA),<sup>17</sup> [3+2]-cycloaddition with azides,<sup>18,19</sup> Friedel-Crafts type reactions,<sup>20</sup> tosylhydrazone addition,<sup>21</sup> lithiation,<sup>22</sup> Bingel reaction<sup>23</sup> and azide-alkyne Huisgen cycloaddition.<sup>24,25</sup> Since all these methods are based on the reaction with double bonds, C<sub>60</sub> acts as an inherently multifunctional reactant. In particular for high fullerene loads, this fact leads to multiple additions, polymer cross-linking and diminished solubility. Therefore, selective grafting reactions with mono-functionalized C<sub>60</sub> derivatives are highly preferred. Jo *et al.* have presented such a well-controlled method to prepare fullerene-grafted block copolymers by an efficient Steglich esterification with phenyl-C<sub>61</sub>-butyric acid (PCBA).<sup>26</sup>

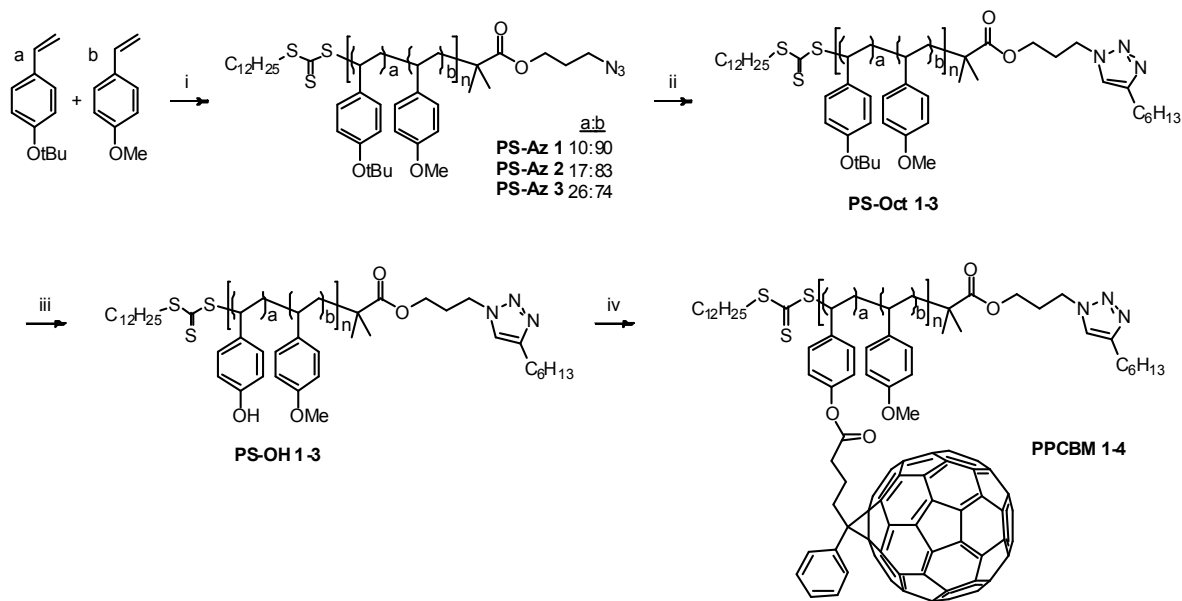
In this work we present a tailor-made synthesis for highly soluble PCBM-grafted copolymers without cross-linking. Further, the impact of covalent fullerene attachment to the polymer backbone is investigated with regard to morphology and fullerene nanocrystal formation and compared to blend systems. Here, we can demonstrate that efficient electron transport can be achieved, even if the pendant PCBM polymers do not show any indication for fullerene nanocrystals or aggregates.

## Results and Discussion

### Synthesis

The key aspect of our approach, depicted in Scheme 1, relies on the synthesis of a statistical precursor copolymer consisting of 4-methoxystyrene (MS) and 4-butoxystyrene (BS). The monomer BS can easily be deprotected to yield hydroxyl groups. In a subsequent step, the resulting 4-hydroxystyrene (HS) units were covalently linked to the C<sub>60</sub> fullerene derivative, phenyl-C<sub>61</sub>-butyric acid (PCBA). The proposed strategy provides both a precise tailoring of the overall number and density of the pendant fullerenes. Hence, there are two ways to tune the PCBM content in the copolymers: First, controlling the amount of grafted PCBM while the copolymer composition is kept the same. Second, varying the copolymer composition followed by a complete grafting with PCBM. In this work, we followed the second route.

We applied a reversible addition fragmentation chain transfer (RAFT) polymerization for the synthesis of the precursor copolymer using an azide-derivatized trithiocarbonate chain transfer agent<sup>27</sup> (CTA). Thereby, an azide mono-terminated polymer is obtained that is giving access to a wide range of synthetic opportunities via click chemistry. Here, the RAFT polymerization was carried out with varying feed ratios of the monomers MS and BS in presence of the CTA and the initiator 2,2'-azobisisobutyronitrile (AIBN) in toluene at 80 °C. Samples for <sup>1</sup>H-NMR spectroscopy were periodically taken to monitor the progress of polymerization. Thus, we could prove that the consumption of both monomer species is equally fast leading to statistical copolymers with a built-in ratio of BS:MS = 10:90, 17:83 and 26:74, respectively.



**Scheme 1:** Synthesis route towards PCBM-grafted copolymers. i) 3-azidopropyl-2-((dodecylthio)carbonothioyl)thio-2-methylpropanoate, AIBN, toluene, 80 °C; ii) 1-octyne, CuI/PMDETA, THF, room temperature, 24 h; iii) concentrated HCl, THF, 35 °C, 22h; iv) PCBA, DCC, DMAP, DMAP-HCl, DSC:CS2:AcN=3:3:1 (v:v:v), 40 °C, 72-91 h.

The polymerization was stopped at around 50 % total monomer conversion to ensure narrow molecular weight distributions. The synthesized precursor copolymers PS-Az 1, PS-Az 2 and PS-Az 3 differ both in monomer ratio and chain length (see Table 1). With increasing mole fraction of BS in the precursor copolymer, here 10 (PS-Az 1), 17 (PS-Az 2) and 26 mol% (PS-Az 3), the overall chain length was reduced from 117, 73 to 45 repeating units, respectively. Note that the number of BS units per chain is then 12 in all the copolymers according to our calculation based on the molecular weight which was determined by matrix-assisted laser desorption/ionization mass spectrometry with time of flight detection (MALDI-TOF MS). This number was selected to give appreciable amounts of fullerene in the final copolymer. The molecular weight distribution of the obtained copolymers measured by size exclusion chromatography (SEC) in THF is narrow, ranging from 1.09 to 1.11 (Table 1 and Figure 1a,b). Due to the calibration with polystyrene as standard, the number average molecular weights  $M_n$  of 12.7 (PS-Az 1), 10.0 (PS-Az 2) and 6.9 kg/mol (PS-Az 3) do not represent the theoretically expected values, which are considerably higher.

The azide end group is relevant only for clicking functional moieties or a second polymer block. We have deactivated it to avoid [3+2]-cycloaddition between the fullerenes and the azide end group<sup>18</sup>, which may lead to cross-linking of the PCBM-grafted copolymers. The Huisgen 1,3-dipolar cycloaddition (click chemistry)<sup>28</sup> is an elegant method to couple the azide end group with an alkyne reagent. Therefore, the precursor polymers PS-Az 1-3 were reacted with a ten-fold excess of 1-octyne in presence of 23 mol% CuI/PMDETA catalyst at room temperature. The success of this reaction was proved by Fourier-transform infrared (IR) spectroscopy, which is very sensitive towards azides due to its strong asymmetric vibration<sup>29</sup>. The azide vibration at 2098 cm<sup>-1</sup> disappears completely in the IR spectra of PS-Oct 1-3, indicating a quantitative end-capping of the azide end groups upon formation of a 1,2,3-triazole ring (Figure S1). The analysis by SEC in THF shows only a negligible shift of  $M_n$ , but exhibit a very weak shoulder at approximately double weight  $2M_n$  (Figure 1a). This polymer coupling is attributed to a transformation of the trithiocarbonate to a thiol end group by nucleophilic reagents, which can result in polymer-polymer disulfide formation<sup>30</sup>.

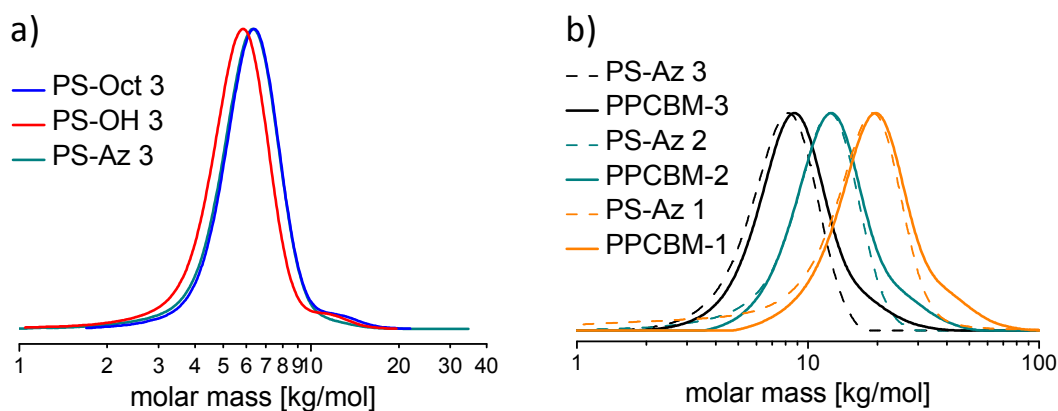


Figure 1: a) SEC traces after each step during the postpolymerization modification of precursor copolymer PS-Az 3 (UV 254 nm, eluent THF) and b) SEC traces of the PCBM-grafted copolymers PPCBM 1-3 in comparison to their respective precursor copolymers PS-Az 1-3 (RI detector, eluent chlorobenzene).

Table 1: Experimentally determined data of the synthesized copolymers.

<b>Polymer</b>	<b>Molar Ratio a:b</b>	<b><math>M_n</math> SEC<sup>[a]</sup> [kg/mol]</b>	<b><math>M_n/M_w</math> SEC<sup>[a]</sup></b>	<b><math>M_n</math> SEC<sup>[b]</sup> [kg/mol]</b>	<b><math>M_n/M_w</math> SEC<sup>[b]</sup></b>
PS-Az 1	10:90	12.3	1.11	12.7	1.37
PS-OH 1	10:90	9.3	1.29		
PPCBM 1	10:90			17.2	1.27
PS-Az 2	17:83	9.0	1.11	10.0	1.18
PS-OH 2	17:83	7.9	1.17		
PPCBM 2	17:83			11.6	1.21
PS-Az 3	26:74	5.7	1.09	6.9	1.14
PS-OH 3	26:74	5.3	1.10		
PPCBM 3	26:74			7.6	1.21
PPCBM 4	26:74				

<b>Polymer</b>	<b>Molar Ratio a:b</b>	<b><math>M_n</math> MALDI [kg/mol]</b>	<b><math>M_p</math> MALDI<sup>[c]</sup> [kg/mol]</b>	<b>Repeating units a:b<sup>[d]</sup></b>	<b>PCBM content<sup>[d]</sup> [wt%]</b>
PS-Az 1	10:90				
PS-OH 1	10:90	16.0	16.0	12:105	
PPCBM 1	10:90	35.1	22.9		30
PS-Az 2	17:83				
PS-OH 2	17:83	10.2	10.1	12:61	
PPCBM 2	17:83	25.8	16.1		37
PS-Az 3	26:74				
PS-OH 3	26:74	6.3	6.4	12:33	
PPCBM 3	26:74	19.6	13.0		51
PPCBM 4	26:74	25.2	17.8		64

[a] SEC in THF as eluent. [b] SEC in chlorobenzene as eluent. [c] Peak maximum  $M_p$  determined by MALDI-TOF mass spectrometry. [d] Determined by MALDI-TOF mass spectrometry.

The polymer-analogous cleavage of *tert*-butyl ether groups was carried out at very mild thermal conditions of 35 °C with an excess of hydrochloric acid. Quantitative conversion of *tert*-butyl ether to hydroxyl groups in PS-OH 1-3 was achieved after 22 h reaction time, which was evidenced by <sup>1</sup>H-NMR. Exemplarily shown for PS-OH 2, the full conversion of BS to 4-hydroxystyrene is indicated by the integral ratio of the hydroxyl proton signal at  $\delta = 9.23\text{--}8.88$  ppm and the phenyl protons at  $\delta = 6.85\text{--}6.15$  ppm which matches perfectly the expected content of 17 mol% of HS (Figure 2). Accordingly, the strong singlet at  $\delta = 1.29$  ppm associated with the *tert*-butyl protons, is significantly decreased. The residual signal belongs to the remaining alkyl chains and methyl groups of the CTA. The SEC trace is shifted to lower molecular weight, which is in accordance with the expected weight loss (see Table 1) and can be seen in Figure 1 for PS-OH 3. Note that also the increased polarity of the polymers PS-OH 1-3 significantly affects the elution time, which is dependent on interactions between polymer and solvent or column material.

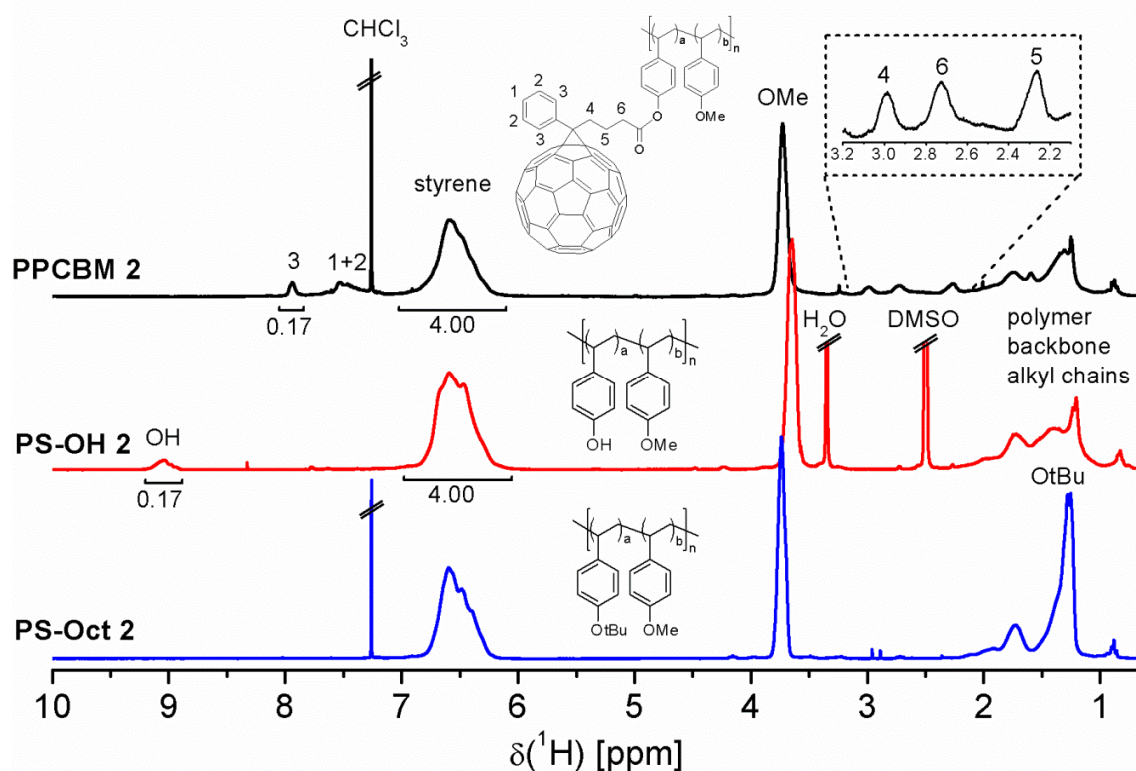


Figure 2: <sup>1</sup>H-NMR spectra of the octyl-endcapped copolymer PS-Oct 2, deprotected copolymer PS-OH 2 and the PCBM-grafted copolymer PPCBM 2.

For the final step of fullerene attachment, we favored an efficient Steglich esterification procedure, which was reported recently for polymer-analogous functionalization with PCBA by Russel *et al.*<sup>26</sup> PCBA can easily be prepared in high yields by ester hydrolysis from the commercially available PCBM.<sup>31</sup> Steglich esterification of PS-OH 1-3 with PCBA was performed at 40 °C for 72-91 h in a solvent mixture of carbon disulfide (CS<sub>2</sub>), 1,2-dichlorobenzene (*o*DCB) and acetonitrile (AcN) in the ratio 3:3:1 (v:v:v). Additional to *N,N'*-dicyclohexylcarbodiimide (DCC) and *N,N*-dimethyl-4-aminopyridine (DMAP), we further added the hydrochloride of DMAP, abbreviated as DMAP·HCl. This reagent can act as a proton source, which is supposed to enhance the yield of esterification by suppression of the side product formation of the *N*-acylurea.<sup>32</sup> An important aspect for fullerene grafting is the monomer ratio in the copolymers, since this parameter determines the maximum PCBM content of the copolymers. With increasing molar fraction of HS, the solubility of the obtained PCBM-grafted copolymers is diminished. While polymers with 30 (PPCBM 1) and 37 wt% PCBM (PPCBM 2) are well soluble in chloroform, 51 wt% PCBM (PPCBM 3) shows only limited solubility in chloroform, but good solubility in chlorobenzene (CB) and *o*DCB. The copolymer with 64 wt% PCBM (PPCBM 4) already precipitated during the esterification due to its high PCBM load. PPCBM 4 then could only be redissolved in *o*DCB at 100 °C. In consequence, the maximum content of PCBM for solution processable copolymers was determined to be 64 wt%. The corresponding monomer ratio was HS:MS = 26:74 and the number of repeating units HS:MS = 11:34.

According to the <sup>1</sup>H-NMR spectrum in Figure 2, all relevant proton signals which belong to the polymer backbone and the pendant PCBM are clearly evident. The fine structure of the multiplet signals arising from the methylene protons of PCBM (signals 4, 5 and 6 in Figure 2) show the typical polymer-related broadening. We calculated the efficiency of the Steglich esterification from <sup>1</sup>H-NMR spectroscopy and MALDI-TOF MS. According to this, the grafting process was incomplete for the copolymers PPCBM 1-3, achieving 56 to 67% esterification of the available HS units. In contrast, PPCBM 4 was fully derivatized with PCBA. In the series of PPCBM 1-4, the concentration of PCBM increases considerably while the overall molecular weight of the polymer backbone decreases. As a result, there is statistically one PCBM molecule for every 15, 10, 6 and 4 repeating units of the PCBM-

grafted copolymers PPCBM 1-4. Apparently, steric hindrance regarding the bulky fullerene molecules is not the only limiting factor for polymer-analogous grafting. The difference in grafting yield can also be attributed to the differences in dilution of HS units (different monomer ratios) as well as the used solvent mixture, which may not be ideal for the desired high fullerene grafting. The SEC traces of the PCBM-grafted copolymers PPCBM 1-3 in CB (Figure 1b) shift only marginally to higher molar masses compared to the precursor polymers PS-Az 1-3. This finding seems contradictory to the significant mass increase, which was evidenced by the MALDI-TOF mass spectra shown in Figure S2. However, this observation is mostly attributed to a contractile effect of intrachain interaction of fullerenes, leading to a reduced hydrodynamic volume.<sup>17</sup> PPCBM 4 is not soluble in chlorobenzene and could not be characterized by SEC.

## Characterization

One of the most important parameters to be determined regarding fullerene polymers is the exact amount of covalently attached PCBM molecules. We have employed several complementary methods such as MALDI-TOF MS, <sup>1</sup>H-NMR spectroscopy, thermogravimetric analysis (TGA) and quantitative UV-vis spectroscopy to determine the PCBM content (Table 2).

Table 2: PCBM weight content  $f_{\text{PCBM}}$  of PPCBM 1-4 determined by various methods. Calculated values  $f_{\text{PCBM,theor.}}$  refer to a degree of 100% grafting of the available 4-hydroxystyrene repeating units and represent the maximum theoretical PCBM weight content possible.

Polymer	PCBM content [wt%]				
	theor.	MALDI	<sup>1</sup> H-NMR	TGA	UV-Vis
<b>PPCBM 1</b>	40	30	27	44	32
<b>PPCBM 2</b>	52	37	38	52	42
<b>PPCBM 3</b>	63	51	51	56	45
<b>PPCBM 4</b>	63	64	64	63	53

Analysis of the MALDI-TOF mass spectra give the mass differences  $\Delta M$  between PPCBM 1-4 and their corresponding precursors PS-OH 1-3 that are 6.9, 6.0, 6.6 and 11.4 kDa, respectively (Figure S2). This approximately equals to 8, 7, 7 and 13 grafted PCBA molecules per chain. Accordingly, the content of pendant PCBM increases considerably as the molecular weight of the precursor copolymer is strongly reduced. The PCBM content  $f_{\text{PCBM}}$  was calculated as  $f_{\text{PCBM}} = \Delta M / M_p$ , with  $M_p$  as peak maximum of the molecular weight distribution of the PCBM-grafted copolymers PPCBM 1-4 obtained by MALDI-TOF MS. These results are in good agreement with the values calculated from  $^1\text{H-NMR}$  data.

A wide-spread method to determine  $f_{\text{PCBM}}$  is TGA.<sup>17</sup> Since the thermal decomposition of PCBM under nitrogen atmosphere is restricted to the loss of the tethered phenyl-butyric acid at about 395 °C, the remaining char is roughly 90 wt%. Thus, the PCBM content of PPCBM 1-4 can be estimated from the char, as the polystyrene backbone is expected to decompose almost completely above 395 °C (Figure S3). However, the precision of this method is restricted, because the residual char content is often too high. This effect is attributed to cross-linking during heating which hinders a neat thermal decomposition.<sup>21</sup> Consequently, the calculated values are generally overestimated. As an alternative method, quantitative UV-vis spectroscopy in solution is well described in literature for the precise determination of the molar or weight content of polymer-bound chromophores<sup>33</sup> and fullerenes.<sup>25</sup> The PCBM content is calculated by the ratio of the extinction coefficients of PPCBM 1-4 and pristine PCBM as  $f_{\text{PCBM}} = \varepsilon_{\text{Polymer}} / \varepsilon_{\text{PCBM}} \cdot 100 \text{ wt}\%$  at the absorption maximum  $\lambda_{\text{max}}$  (Figure S4). The obtained values  $f_{\text{PCBM}}$  deviate from MALDI-TOF MS and NMR values in particular for high fullerene loading. This might be due to interaction of the fullerene moieties in the polymer and in consequence a change in the molar extinction coefficients compared to pure PCBM. To conclude, the PCBM content was most accurately determined by MALDI-TOF mass spectra, which are consistent with NMR analysis. The other methods show partially significant deviations and thus are neglected for any further considerations.

To determine whether the properties of PCBM are affected by the incorporation into the precursor polymer we conducted UV-Vis measurements of PPCBM 1-4. Their absorption

spectrum is dominated by the prominent fullerene absorption bands at 258 nm ( $\epsilon_{258 \text{ nm}} = 0.0703 \text{ mLmg}^{-1} \text{ cm}^{-1}$ ) and 328 nm (Figure S5). Since pristine PCBM exhibits exactly the same absorption bands, the optical properties were not influenced by the covalent attachment to the copolymers.

Further, we studied the electrochemical characteristics by cyclic voltammetry (CV) measurements of PPCBM 1-3 (Figure 3). PPCBM 1-3 undergo three reversible reductions up to -2.0 V, very similar to pure PCBM. The lowest unoccupied molecular orbital (LUMO) levels were calculated based on the onset reduction potential  $E_{\text{red}}$  using the following equation:  $E_{\text{LUMO}} = -e(E_{\text{red}} + 4.71 \text{ V})$ .<sup>34</sup> While the LUMO level of PCBM was determined as -3.82 eV, it is -3.79 eV for PPCBM 1 and -3.80 eV for PPCBM 2 and PPCBM 3. The negligible deviations lie within the range of measurement error, thus, the attachment of PCBM to the polymer backbone does not influence the LUMO level.

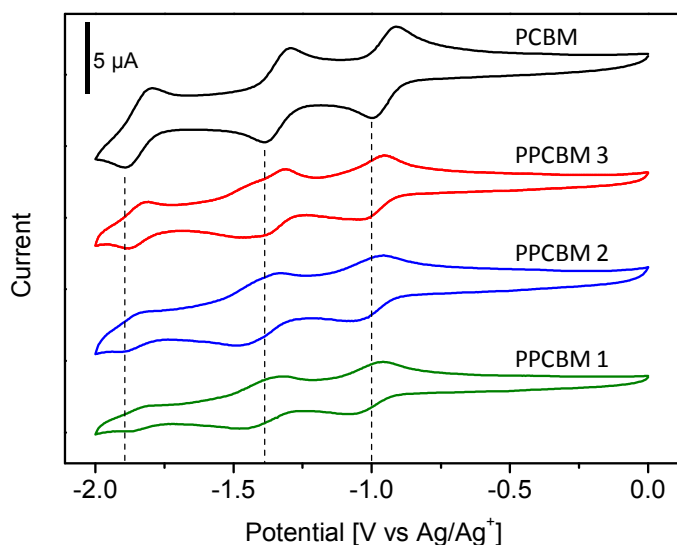


Figure 3: Cyclic voltammetry curves of PCBM-grafted copolymers and pristine PCBM measured at  $50 \text{ mV s}^{-1}$  in *o*DCB:AcN 5:1 (v:v) with 0.1 mM TBAPF<sub>6</sub>. The potential is given in volt using Ag/AgNO<sub>3</sub> as reference electrode.

The thermal behavior of the synthesized polymers was investigated using differential scanning calorimetry (DSC, Figure S6). Here, PS-OH 1-3 revealed a glass transition temperature  $T_g$  in the range of 93-95 °C, which is similar to poly(styrene). The grafting of 30, 37 and 51 wt% of PCBM onto the polymers leads both to a strong signal broadening and a

temperature shift of  $T_g$  up to 144 , 167 and 189 °C for PPCBM 1-3, respectively. This considerable decrease of molecular mobility is attributed to the sterical hindrance by the attached fullerene moieties and to the strong intermolecular interaction between the fullerenes.<sup>13,35</sup>

### Bulk electron mobility

We investigated the bulk electron mobility  $\mu_e$  of PPCBM 1-3 in comparison to blends of precursor polymer PS-OH 1 and PCBM. PPCBM 4 was not included in this study, since the degree of grafting deviates significantly from the other polymers, making the comparability difficult. We used the space-charge limited current (SCLC) method, as it enables the study of charge carrier mobility across the bulk in thin films.<sup>36</sup> The electrodes ITO/PEDOT:PSS and Ca/Al were selected to avoid any injection limited current. The active layer of the SCLC devices was prepared by blade-coating from *o*DCB at 70 °C of either PCBM-grafted copolymers or blends of PS-OH 1 and PCBM in different compositions ranging from 30 to 50 wt% PCBM. Finally, the electron mobility  $\mu_e$  can be extracted from the obtained current-voltage ( $J$ - $V$ ) curves and the Mott-Gurney equation (see experimental part for details). The  $J$ - $V$  characteristics of PPCBM 1-3 and the corresponding blends are depicted in Figure 4a. To check the thickness scaling of the SCLC, the  $J$ - $V$  curves of each material with varied active layer thickness were measured (Figure S7-S8). Within the experimental error, the electron mobility is found to be constant for each thickness. In general, the PCBM-grafted copolymers PPCBM 1-3 and the blends exhibit different electron transport values depending on the PCBM content (Figure 7b). The blend devices show an exponential increase in electron mobility with increasing PCBM content. However, even blends with 50 wt% of PCBM exhibit low mobility ( $\mu_e=8\cdot 10^{-5} \text{ cm}^2\text{V}^{-1}\text{s}^{-1}$ ) compared to pristine PCBM ( $\mu_e = 4\cdot 10^{-3} \text{ cm}^2\text{V}^{-1}\text{s}^{-1}$ ) that is two orders of magnitude higher (Figure 7c). In contrast, the PCBM-grafted copolymers show a different trend in mobility. Here, the mobility is first increasing with PCBM content and then reaches an optimum of  $1\cdot 10^{-4} \text{ cm}^2\text{V}^{-1}\text{s}^{-1}$  for PPCBM 2 with 37 wt% of grafted PCBM. Above this value, the mobility is slightly diminishing for PPCBM 3 containing 51 wt% of PCBM. Remarkably, the pendant fullerene polymers show considerable better electron mobility compared to the blends for a PCBM content below 50 wt%. Despite their low fullerene content, PPCBM 1-3 maintain reasonable charge

transport properties in reference to pristine PCBM. PPCBM 1 with 30 wt% of incorporated PCBM exhibits a three orders of magnitude higher mobility than the respective blend, which only can be understood in terms of an enhanced charge percolation in pendant fullerenes than in blend systems.

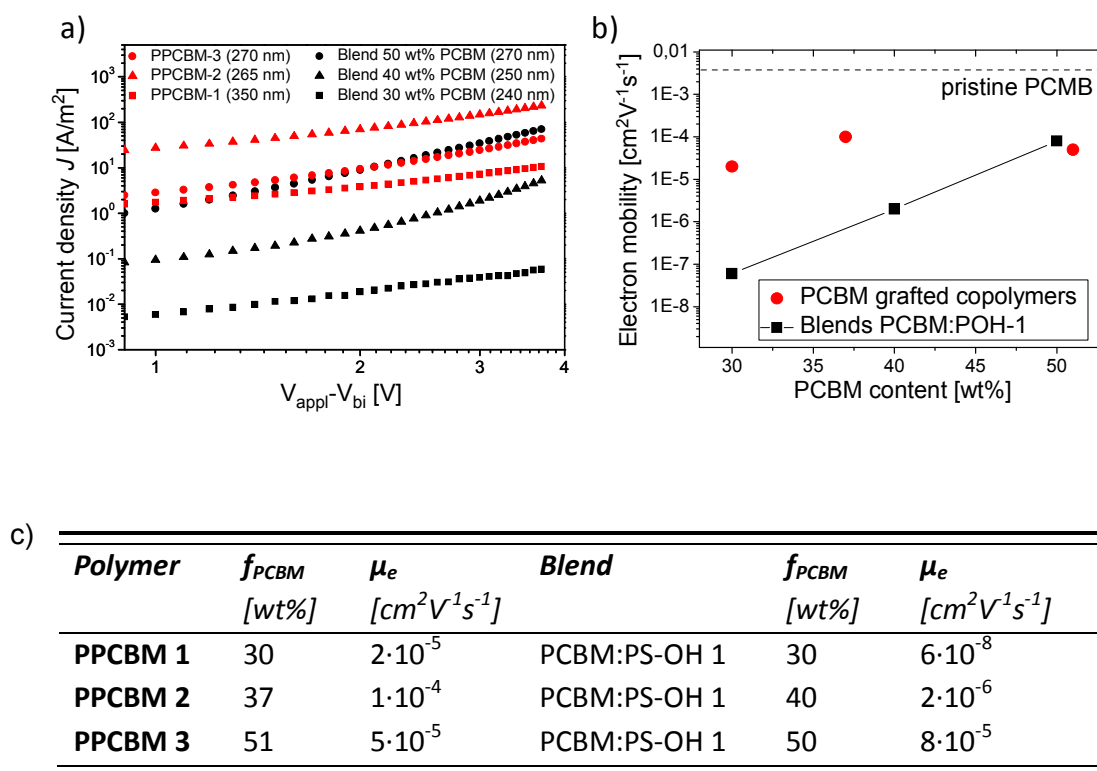


Figure 4: SCLC measurement of the PCBM-grafted copolymers PPCBM 1-3 in comparison to the blends showing (a) the  $J$ - $V$  curves with active layer thickness given in brackets, (b,c) the average electron mobility  $\mu_e$  in reference to pristine PCBM. The mobility of PCBM was determined to be  $4 \cdot 10^{-3} \text{ cm}^2 \text{ V}^{-1} \text{ s}^{-1}$ .

### Film morphology

The previous findings regarding charge transport require a correlation with structural properties. Therefore the film morphology of the SCLC devices was investigated after the initial SCLC characterization. As shown in the AFM topography images in Figure 5a, the films of PPCBM 1-3 are throughout smooth and featureless independent of the PCBM content. This indicates an effective suppression of fullerene aggregation realized by covalent

attachment to the polymer backbone. At the same time, the blend films of PCBM and PS-OH 1 are heterogeneous and strongly dominated by PCBM aggregates (Figure 5a). With increasing weight fraction of PCBM both number and size of the aggregates is growing. The fullerene aggregate size is increasing from 60-70 nm for 40 wt% to 100-110 nm for 50 wt% of PCBM in the blends. It is generally known that the formation of fullerene nanocrystals is thermodynamically favored in fullerene-polymer blends.<sup>5</sup> However, at 30 wt% PCBM a homogeneous film without aggregates was observed indicating finely dispersed fullerenes or very small aggregates. Thus, charge transport in blends is strongly dependent on fullerene content and perhaps on aggregate size. High electron mobility requires sufficient percolation pathways, therefore high PCBM contents facilitate electron transport by an increasing number of aggregates which are in close proximity. Conversely, the mobility is very low for a small PCBM content, when the phase separated fullerene aggregates are isolated from each other. In strong contrast to that, the PCBM-grafted copolymers PPCBM 1-3 do not show any aggregates and hence, enable charge percolation via homogeneously distributed fullerene molecules. Even for a low PCBM content the distance between the fullerene molecules is apparently close enough to allow efficient charge carrier percolation through the bulk.

Further powder X-ray diffraction (PXRD) studies fully support the previous findings. We collected the material as powder from films which were cast from *o*DCB at 70 °C, similar to the SCLC device preparation, and investigated the structure with a Guinier diffraction system. The blend of PCBM:PS-OH 1 with 50 wt% PCBM shows a characteristic reflection at 9.62° additional to the amorphous scattering (Figure 5b). This distinct reflection indicates the existence of polycrystalline PCBM aggregates in the amorphous polymer matrix and hence, is consistent with the AFM results. Upon annealing of PS-OH 1 above  $T_g$  at 140 °C for 3 h, the intensity of the crystalline reflections increased significantly. Since the diffusion of PCBM molecules is promoted during the annealing process, the crystallinity and size of the PCBM aggregates can grow. Consequently, both the overall crystalline fraction in the blend is increasing and the reflections get sharper. In contrast, the PCBM-grafted copolymer PPCBM 3 remains completely amorphous even after annealing for 3 h. These results are again consistent with the AFM measurements and clearly demonstrate that the covalent attachment of PCBM to the polymer entirely suppresses the aggregation of the fullerenes.

Furthermore, the high thermodynamic stability of the bulk morphology of the PCBM-grafted copolymers compared to standard small molecule acceptor materials is very promising for long living photovoltaic devices.

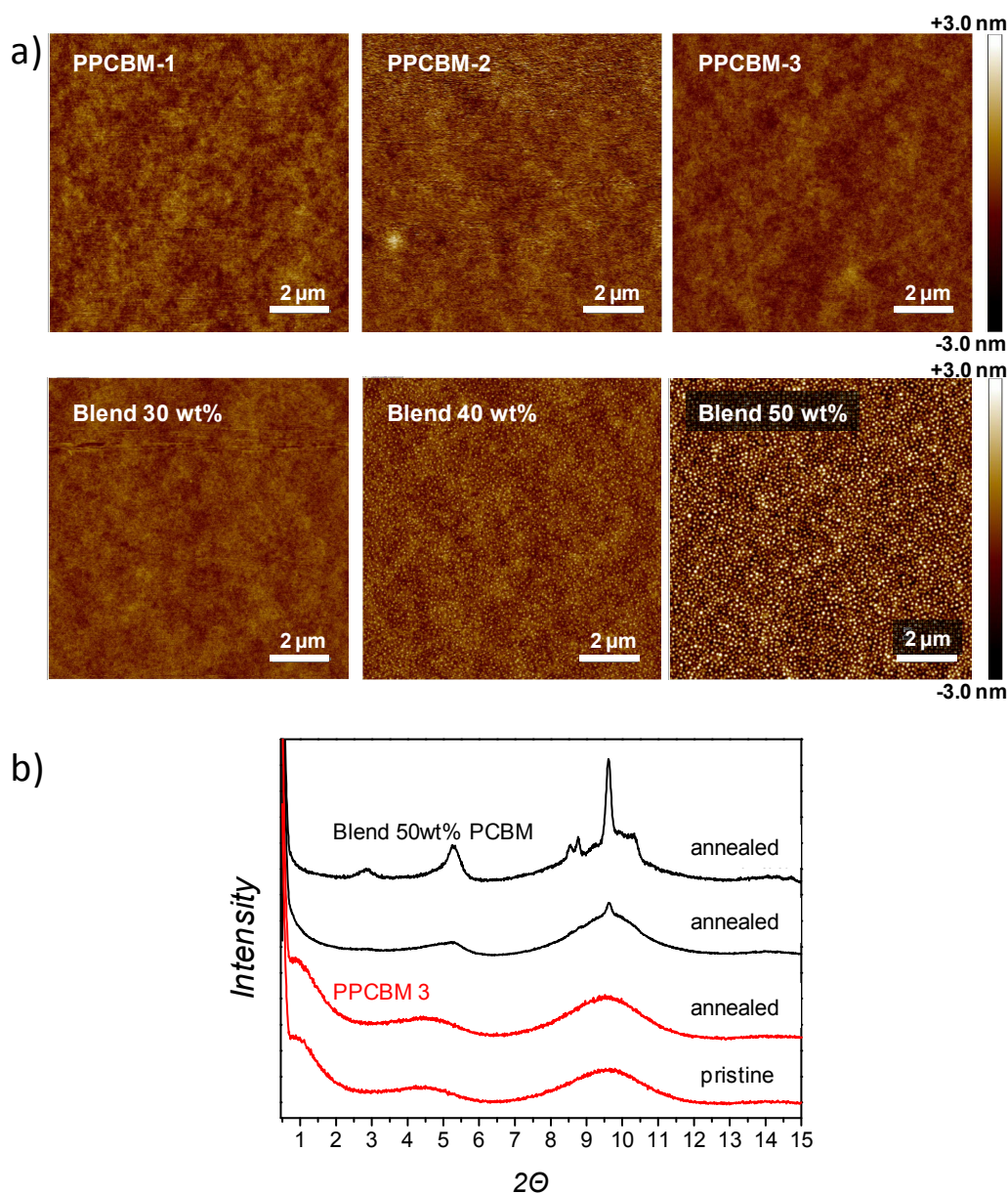


Figure 5: Morphological investigation of PPCBM 1-3 and the blends showing (a) AFM topography images of the films on devices prepared for SCLC measurements and (b) powder X-ray diffraction curves of PPCBM 3 and the corresponding blend.

## Conclusions

We have presented a successful synthesis strategy towards well-soluble fullerene side chain polymers with high PCBM contents between 30 and 64 wt%. Both grafting density and PCBM content could easily be tuned by the monomer ratio in the precursor copolymers. The resulting PCBM-grafted copolymers exhibit low polydispersity and no cross-linking owing to the controlled PCBM grafting by Steglich esterification. The acceptor polymers retain the optical and electrochemical properties of the incorporated PCBM independently of their fullerene weight fraction. Electron transport characteristics derived from SCLC show a maximum electron mobility  $\mu_e$  of  $1 \cdot 10^{-4} \text{ cm}^2 \text{ V}^{-1} \text{ s}^{-1}$  for 37 wt% of incorporated PCBM. Despite their low fullerene content, the acceptor polymers exhibit exceptional high charge transport in reference to blend systems and pure PCBM with  $4 \cdot 10^{-3} \text{ cm}^2 \text{ V}^{-1} \text{ s}^{-1}$ . The blends of PCBM and precursor polymer are outperformed regarding the electron mobility up to several orders of magnitude in particular for low PCBM contents. Charge transport in these blend systems relies on nanocrystal formation and is improved with an increasing PCBM content. This may be of disadvantage for obtaining a well-defined, nanostructured morphology in BHJ solar cells. Here, the PCBM-grafted copolymers which exhibit no structural order while maintaining good electron mobility can be of great advantage. In future, the presented acceptor polymer concept can be extended to a variety of fullerene derivatives and donor-acceptor block copolymers.

## Experimental

*Chemicals:* The reagents for the following synthetic procedures were purchased from different suppliers and used as received, if not stated otherwise. *Sigma-Aldrich:* 3-Chloropropanol, sodium azide, 4-dimethylaminopyridine, *N,N'*-dicyclohexylcarbodiimide, 4-methoxystyrene, 4-*tert*-butoxystyrene, 2-2'-azobisisobutyronitrile, 1-octyne, copper(I) iodide, *N,N,N',N',N''*-pentamethyldiethylenetriamine, anhydrous sodium sulfate, sodium hydrogencarbonate, basic and neutral alumina. *abcr:* 2-(((Dodecylthio)carbonothioyl)thio)-2-methylpropanoic acid. *Solenne BV (Groningen, Netherlands):* Phenyl- $\text{C}_{61}$ -butyric acid methyl ester (PCBM, purity 99 %). Solvents were either distilled at atmospheric pressure utilizing

appropriate desiccants or purchased in *p.a.* (pro analysi) grade. Commercially available anhydrous solvents were purchased from Sigma Aldrich and Acros in sealed bottles with mole sieve. Prior to polymerization, 4-methoxystyrene (MS) and 4-tert-butoxystyrene (BS) were passed through a column of basic alumina to remove the inhibitor and stored at -18 °C. DMAP·HCl was prepared by addition of 37 wt% HCl dropwise to a solution of DMAP in THF. The precipitated solid was collected by filtration, washed with THF and dried under vacuum at RT. The stock solution of 0.07 M CuI/PMDETA in THF was prepared according to a literature procedure<sup>37</sup> and stored at 5 °C under argon. The chain transfer agent (CTA) 3-azidopropyl-2-(((dodecylthio)carbonothioyl)thio)-2-methylpropanoate was prepared following a published synthesis route<sup>27</sup>. Phenyl-C<sub>61</sub>-butyric acid (PCBA) was also prepared according to a published synthesis protocol<sup>31</sup>.

*Instrumentation:* All <sup>1</sup>H-NMR spectra were measured with a Bruker Avance AC250 spectrometer at 300 MHz. The obtained spectra were calibrated to the corresponding residual solvent peak (CDCl<sub>3</sub> δ=7.26 ppm, DMSO-D<sub>6</sub> δ=2.50 ppm). Chemical shifts are given in ppm, coupling constants in Hertz. Ultraviolet-visible (UV-Vis) spectra were recorded on a Hitachi U-3000 spectrophotometer using quartz cuvettes with a path length of 1 cm. Fourier transform infrared (FTIR) spectra were recorded from solids on a Perkin Elmer Spectrum 100 FTIR spectrometer in attenuated total reflection (ATR) mode. Thermal gravimetry analysis (TGA) experiments were performed under continuous N<sub>2</sub> stream using a Mettler Toledo TGA/SDTA 851. The measurement range was 30-800 °C with a heating rate of 10 K/min. The determined decomposition temperatures  $T_{dec}$  are onset temperatures. Differential scanning calorimetry (DSC) experiments were carried out on a Perkin Elmer Diamond DSC with a heating rate of 10 K/min under N<sub>2</sub> atmosphere. From each sample three cycles were measured. Glass transition ( $T_g$ ) are given as half step temperature. Size exclusion chromatography (SEC) with stabilized THF as eluent was performed using a Waters 515-HPLC pump at a flow rate of 0.5 mL/min. A guard column (Varian, 50x0.75 cm, ResiPore, particle size 3 μm) and two separation columns (Varian, 300x0.75 cm, ResiPore, particle size 3 μm) are connected in series with a Waters UV detector at 254 nm and 486 nm calibrated in relation to polystyrene standards. 1,2-dichlorobenzene (*o*DCB) was used as an internal standard. SEC with chlorobenzene (CB) as eluent were carried out at 60 °C on an Agilent

1100 using two Polymer Laboratories mixed B columns in series. The refractive index detector was calibrated in relation to polystyrene standards. Matrix assisted laser desorption ionization mass spectroscopy with time of flight detection (MALDI-TOF MS) was performed on a Bruker Reflex III using *trans*-2-(3-(4-*tert*-butylphenyl)-2-methyl-2-propenylidene)malononitrile (DCTB) as matrix and silver trifluoroacetate as cationizing salt. Solutions in either THF or *o*DCB of polymer (0.01 mg/ $\mu$ L), matrix (0.02 mg/ $\mu$ L) and salt (0.01 mg/ $\mu$ L) were mixed in the ratio 5:20:1 (v:v:v) and spotted onto the MALDI target plate. In case of *o*DCB, the MALDI target plate was dried at 40 °C for 24 h prior to the measurement. Electron-only devices for space-charge limited current (SCLC) measurements were fabricated using the following device structure: glass/ITO/PEDOT:PSS/active layer/Ca/Al. Commercial ITO coated glass substrates with a sheet resistance of 13 Ohms per sq (Lumtec) were cleaned using the following sequence in an ultrasonic bath: detergent, water, acetone and 2-propanol. After ozone treatment of the substrates for 10 min, PEDOT:PSS was spin-coated on the ITO surface and dried at 130 °C for 30 min. All following steps were carried out under N<sub>2</sub> atmosphere with water and oxygen levels  $\leq 0.1$  ppm. After cooling the substrate, the polymer layer was blade coated from *o*DCB solutions at 70 °C. The substrates were then put in a thermal evaporation chamber to evaporate the top electrode (30 nm Ca/ 100 nm Al) under high vacuum ( $1 \cdot 10^{-6}$  mbar) through a shadow mask (active area 4 mm<sup>2</sup>). The current-voltage characteristics of the devices were measured using a Keithley 2420 (*J-V*) Digital SourceMeter at 25 °C. The electron mobility  $\mu_e$  was extracted from the obtained *J-V* curves using the following equation<sup>38</sup>,

$$J = \frac{9}{8} \epsilon_r \epsilon_0 \mu \frac{V^2}{L^3}$$

where *J* is the current density,  $\epsilon_r$  the dielectric constant ( $\approx 3$  for organic semiconductors<sup>39</sup>),  $\epsilon_0$  the permittivity of free space,  $\mu$  the charge carrier mobility, *V* the voltage and *L* the active layer thickness. Voltage *V* is a corrected value  $V = V_{\text{appl}} - V_{\text{built-in}}$ , resulting from the differences in work function of the calcium and ITO/PEDOT:PSS contacts ( $\approx 2.2$  eV). Film thicknesses were determined on a Dektak ST surface profilometer. Atomic force microscopy (AFM) was applied on the SCLC devices using a Veeco Dimension Icon with Nanoscope V controller, in tapping mode. The used cantilevers were NSC15/AIBS from Mikromasch.

Cyclic voltammetry experiments were carried out at 25 °C in a mixture of 1,2-dichlorobenzene and acetonitrile 5:1 (v:v) containing 0.1 M tetrabutylammonium hexafluorophosphate (TBAPF<sub>6</sub>) as the conducting electrolyte. Reduction potentials were measured with a glassy carbon disk electrode as the working electrode versus Ag/AgCl as the reference electrode. Powder X-ray analysis (PXRD) was carried out with a Huber/Seifert Iso-Debyeflex 3003, using a Guinier diffractometer system (Cu K<sub>α</sub>: 1.5418 Å) with a sealed tube for temperature dependent measurements.

*General synthetic procedure for PS-Az 1-3:* 4-Methoxystyrene (MS) and 4-tert-butoxystyrene (BS) were added to a 10 mL schlenk tube under argon. The chain transfer agent (CTA) 3-azidopropyl-2-(((dodecylthio)carbonothioyl)thio)-2-methyl-propano-ate and 2-2'-azobisisobutyronitrile (AIBN) were each separately dissolved in 500 μL of dry toluene. To guarantee exact equivalents of both reagents, the recalculated amounts of these solutions were added to the reaction flask. The overall volume of dry toluene was filled up to the given amount. Then the reaction mixture was degassed by four freeze, pump and thaw cycles and polymerization was started in a preheated oil bath at 80 °C. Samples were taken periodically by syringe to monitor the monomer conversion *via* <sup>1</sup>H-NMR spectroscopy. When the desired monomer conversion was reached, the polymerization was quenched by cooling the solution rapidly to 0 °C in an ice bath and exposition to air. The resulting polymer was isolated by precipitation twice into 300 mL methanol and drying under vacuum.

*Synthesis of PS-Az 1:* MS (4.377 g, 32.62 mmol, 253 equ.), BS (0.500 g, 2.84 mmol, 22 equ.), CTA (57.8 mg, 0.129 mmol, 1 equ.) and AIBN (4.2 mg, 0.026 mmol, 0.2 equ.) were used for polymerization in 3 mL toluene. After 27.5 h the monomer conversion was 48 % and the polymerization was stopped. Yield: 1.876 g of a pale yellow solid. The monomer ratio MS:BS was 90:10 in mol% (<sup>1</sup>H-NMR).  $M_n = 12.3$  kg/mol,  $M_w/M_n = 1.11$  (THF),  $M_n = 12.7$  kg/mol,  $M_w/M_n = 1.37$  (CB). <sup>1</sup>H-NMR (300 MHz, CDCl<sub>3</sub>, δ): 6.85-6.15 (br m, 4(a+b)·H, H<sub>ar</sub>), 3.85-3.62 (br s, 3b·H, H<sub>OMe</sub>), 2.20-1.10 (br m, H<sub>backbone</sub>, H<sub>tBu</sub>, H<sub>CTA</sub>).

*Synthesis of PS-Az 2:* MS (4.314 g, 32.15 mmol, 149 equ.), BS (1.000 g, 5.67 mmol, 26 equ.), CTA (96.4 mg, 0.215 mmol, 1 equ.) and AIBN (7.1 mg, 0.043 mmol, 0.2 equ.) were used for polymerization in 4 mL toluene. After 8.5 h the monomer conversion was 46 % and

the polymerization was stopped. Yield: 2.114 g of a pale yellow solid. Monomer ratio MS:BS was 83:17 in mol% ( $^1\text{H-NMR}$ ).  $M_n = 9.0$  kg/mol,  $M_w/M_n = 1.11$  (THF),  $M_n = 10.0$  kg/mol,  $M_w/M_n = 1.18$ .  $^1\text{H-NMR}$  (300 MHz,  $\text{CDCl}_3$ ,  $\delta$ ): 6.85-6.15 (br m, 4(a+b)·H,  $\text{H}_{\text{ar}}$ ), 3.85-3.62 (br s, 3b·H,  $\text{H}_{\text{OMe}}$ ), 2.20-1.10 (br m,  $\text{H}_{\text{backbone}}$ ,  $\text{H}_{\text{OtBu}}$ ,  $\text{H}_{\text{CTA}}$ ).

*Synthesis of PS-Az 3:* MS (3.823 g, 28.49 mmol, 88 equ.), BS (1.500 g, 8.51 mmol, 26 equ.), CTA (144.6 mg, 0.323 mmol, 1 equ.) and AIBN (10.6 mg, 0.065 mmol, 0.2 equ.) were used for polymerization in 2 mL toluene. After 5.0 h the monomer conversion was 46 % and the polymerization was stopped. Yield: 2.090 g of a pale yellow solid. Monomer ratio MS:BS was 74:26 in mol% ( $^1\text{H-NMR}$ ).  $M_n = 9.0$  kg/mol,  $M_w/M_n = 1.11$  (THF),  $M_n = 6.9$  kg/mol,  $M_w/M_n = 1.14$ .  $^1\text{H-NMR}$  (300 MHz,  $\text{CDCl}_3$ ,  $\delta$ ): 6.85-6.15 (br m, 4(a+b)·H,  $\text{H}_{\text{ar}}$ ), 3.85-3.62 (br s, 3b·H,  $\text{H}_{\text{OMe}}$ ), 2.20-1.10 (br m,  $\text{H}_{\text{backbone}}$ ,  $\text{H}_{\text{OtBu}}$ ,  $\text{H}_{\text{CTA}}$ ).

*General synthetic procedure for PS-Oct 1-3:* A dry Schlenk flask was charged with 1.20 g (1 equ.) of PS-Az under argon atmosphere and dissolved in 70 mL of dry THF. After 10 equ. of 1-octyne was added, the reaction mixture was purged with argon for 25 min. Then, 0.23 equ. of a 0.07 M CuI/PMDETA stock solution were added *via* a syringe and stirred for 24 h at RT. The reaction mixture was passed through a column of neutral aluminium oxide to remove the catalyst. The obtained polymer was isolated by precipitation twice into 500 mL methanol and drying under vacuum.

*Synthesis of PS-Oct 1:* The reaction yielded 1.284 g of a pale yellow solid.  $^1\text{H-NMR}$  (300 MHz,  $\text{CDCl}_3$ ,  $\delta$ ): 6.85-6.15 (br m, 4(a+b)·H,  $\text{H}_{\text{ar}}$ ), 3.85-3.62 (br s, 3b·H,  $\text{H}_{\text{OMe}}$ ), 2.20-1.10 (br m,  $\text{H}_{\text{backbone}}$ ,  $\text{H}_{\text{OtBu}}$ ,  $\text{H}_{\text{CTA}}$ ,  $\text{H}_{\text{Octyl}}$ ).

*Synthesis of PS-Oct 2:* The reaction yielded 1.034 g of a pale yellow solid.  $M_n = 9.1$  kg/mol,  $M_w/M_n = 1.10$  (THF),  $^1\text{H-NMR}$  (300 MHz,  $\text{CDCl}_3$ ,  $\delta$ ): 6.85-6.15 (br m, 4(a+b)·H,  $\text{H}_{\text{ar}}$ ), 3.85-3.62 (br s, 3b·H,  $\text{H}_{\text{OMe}}$ ), 2.20-1.10 (br m,  $\text{H}_{\text{backbone}}$ ,  $\text{H}_{\text{OtBu}}$ ,  $\text{H}_{\text{CTA}}$ ,  $\text{H}_{\text{Octyl}}$ ).

*Synthesis of PS-Oct 3:* The reaction yielded 1.10 g of a pale yellow solid.  $M_n = 6.0$  kg/mol,  $M_w/M_n = 1.08$  (THF),  $^1\text{H-NMR}$  (300 MHz,  $\text{CDCl}_3$ ,  $\delta$ ): 6.85-6.15 (br m, 4(a+b)·H,  $\text{H}_{\text{ar}}$ ), 3.85-3.62 (br s, 3b·H,  $\text{H}_{\text{OMe}}$ ), 2.20-1.10 (br m,  $\text{H}_{\text{backbone}}$ ,  $\text{H}_{\text{OtBu}}$ ,  $\text{H}_{\text{CTA}}$ ,  $\text{H}_{\text{Oct}}$ ).

*General synthetic procedure for PS-OH 1-3:* A round bottom flask was charged with PS-Oct and dissolved in 100 mL THF for every 1.0 g of polymer. 12 mL of concentrated hydrochloric acid (37 wt%) for every 1.0 g of polymer was added dropwise *via* a syringe. After purging the reaction mixture with argon for 20 min, it was stirred at 35 °C for 22 h. All volatile components were removed under reduced pressure. The hydrolyzed polymer was isolated by precipitation twice into 500 mL water and freeze-drying from 1,4-dioxane.

*Synthesis of PS-OH 1:*  $M_n = 9.3$  kg/mol,  $M_w/M_n = 1.29$ ,  $M_n = 16.0$  kg/mol,  $M_p = 16.6$  kg/mol (MALDI-TOF MS),  $^1\text{H-NMR}$  (300 MHz, DMSO- $D_6$ ,  $\delta$ ): 9.20-8.90 (br, a·H, OH), 6.95-6.10 (br m, 4(a+b)·H,  $H_{ar}$ ), 3.80-3.50 (br s, 3b·H,  $H_{OMe}$ ), 2.20-1.10 (br m,  $H_{backbone}$ ,  $H_{CTA}$ ,  $H_{Octyl}$ ).  $T_{dec,1} = 204$  °C,  $T_{dec,2} = 388$  °C,  $T_g = 95$  °C.

*Synthesis of PS-OH 2:*  $M_n = 7.9$  kg/mol,  $M_w/M_n = 1.17$ ,  $M_n = 10.2$  kg/mol,  $M_p = 10.1$  kg/mol (MALDI-TOF MS).  $^1\text{H-NMR}$  (300 MHz, DMSO- $D_6$ ,  $\delta$ ): 9.23-8.88 (br, a·H, OH), 6.85-6.15 (br m, 4(a+b)·H,  $H_{ar}$ ), 3.85-3.42 (br s, 3b·H,  $H_{OMe}$ ), 2.20-1.05 (br m,  $H_{backbone}$ ,  $H_{CTA}$ ,  $H_{Octyl}$ ).  $T_{dec,1} = 191$  °C,  $T_{dec,2} = 385$  °C,  $T_g = 95$  °C.

*Synthesis of PS-OH 3:*  $M_n = 5.3$  kg/mol,  $M_w/M_n = 1.10$ ,  $M_n = 6.3$  kg/mol,  $M_p = 6.4$  kg/mol (MALDI-TOF MS).  $^1\text{H-NMR}$  (300 MHz, DMSO- $D_6$ ,  $\delta$ ): 9.20-8.90 (br, a·H, OH), 6.85-6.15 (br m, 4(a+b)·H,  $H_{ar}$ ), 3.80-3.53 (br s, 3b·H,  $H_{OMe}$ ), 2.20-1.00 (br m,  $H_{backbone}$ ,  $H_{CTA}$ ,  $H_{Octyl}$ ).  $T_{dec,1} = 191$  °C,  $T_{dec,2} = 384$  °C,  $T_g = 95$  °C.

*General synthetic procedure of PPCBM 1-4:* A 500 ml schlenk flask was charged with PS-OH (1 equ. of 4-hydroxystyrene), PCBA (1.15 equ.), DMAP (3 equ.) and DMAP·HCl (2 equ.). The flask was degassed under high vacuum and backfilled with argon twice. 100 mL of dry *o*DCB:CS<sub>2</sub>:AcN (3:3:1/v:v:v) was added and stirred vigorously for 45 min at RT. In a separate 50mL schlenk flask under argon, DCC (7 equ.) was dissolved in 16.5 mL of the same solvent mixture. Then the DCC solution was added dropwise to the reaction mixture, which was stirred at 40 °C for 3-4 days. After removal of the solvents under reduced pressure, the crude product was redissolved in *o*DCB and filtered. For polymer purification the filtrate was precipitated twice into 800 ml methanol from first *o*DCB and second chloroform. To remove soluble fullerene derivatives, the polymer was precipitated from

chloroform into 800 mL of a toluene:methanol mixture (1:1 for PPCBM 1, 2:1 for PPCBM 2, 3:1 for PPCBM 3) and dried under high vacuum.

*Synthesis of PPCBM 1:*  $M_n = 17.2$  kg/mol,  $M_w/M_n = 1.27$  (CB),  $M_n = 35.1$  kg/mol,  $M_{p,1} = 22.9$  kg/mol,  $M_{p,2} = 45.2$  kg/mol (MALDI-TOF MS).  $^1\text{H-NMR}$  (300 MHz,  $\text{CDCl}_3$ ,  $\delta$ ): 8.00-7.87 (br m, 2a·H, *Ph*-( $\text{CH}_2$ )<sub>3</sub>-COOR), 7.70-7.30 (br m, 3a·H, *Ph*-( $\text{CH}_2$ )<sub>3</sub>-COOR), 6.90-6.10 (br m, 4(a+b)·H,  $\text{H}_{\text{ar}}$ ), 3.90-3.55 (br s, 3b·H,  $\text{H}_{\text{OMe}}$ ), 3.06-2.92 (br m, 2a·H, *Ph-CH*<sub>2</sub>-*CH*<sub>2</sub>-*CH*<sub>2</sub>-COOR), 2.81-2.66 (br m, 2a·H, *Ph-CH*<sub>2</sub>-*CH*<sub>2</sub>-*CH*<sub>2</sub>-COOR), 2.32-2.20 (br m, 2a·H, *Ph-CH*<sub>2</sub>-*CH*<sub>2</sub>-*CH*<sub>2</sub>-COOR), 2.20-0.8 (br m,  $\text{H}_{\text{backbone}}$ ,  $\text{H}_{\text{CTA}}$ ,  $\text{H}_{\text{Octyl}}$ ).  $T_{\text{dec},1} = 180\text{--}190$  °C,  $T_{\text{dec},2} = 395$  °C.

*Synthesis of PPCBM 2:*  $M_n = 11.6$  kg/mol,  $M_w/M_n = 1.21$ ,  $M_n = 25.8$  kg/mol,  $M_{p,1} = 16.1$  kg/mol (MALDI-TOF MS).  $^1\text{H-NMR}$  (300 MHz,  $\text{CDCl}_3$ ,  $\delta$ ): 8.00-7.87 (br m, 2a·H, *Ph*-( $\text{CH}_2$ )<sub>3</sub>-COOR), 7.70-7.30 (br m, 3a·H, *Ph*-( $\text{CH}_2$ )<sub>3</sub>-COOR), 6.90-6.10 (br m, 4(a+b)·H,  $\text{H}_{\text{ar}}$ ), 3.90-3.55 (br s, 3b·H,  $\text{H}_{\text{OMe}}$ ), 3.06-2.90 (br m, 2a·H, *Ph-CH*<sub>2</sub>-*CH*<sub>2</sub>-*CH*<sub>2</sub>-COOR), 2.81-2.63 (br m, 2a·H, *Ph-CH*<sub>2</sub>-*CH*<sub>2</sub>-*CH*<sub>2</sub>-COOR), 2.37-2.18 (br m, 2a·H, *Ph-CH*<sub>2</sub>-*CH*<sub>2</sub>-*CH*<sub>2</sub>-COOR), 2.10-0.8 (br m,  $\text{H}_{\text{backbone}}$ ,  $\text{H}_{\text{CTA}}$ ,  $\text{H}_{\text{Octyl}}$ ).  $T_{\text{dec},1} = 184$  °C,  $T_{\text{dec},2} = 391$  °C.

*Synthesis of PPCBM 3 and PPCBM 4:*  $M_n = 7.6$  kg/mol,  $M_w/M_n = 1.21$  (CB),  $M_n = 19.6$  kg/mol,  $M_{p,1} = 13.0$  kg/mol,  $M_{p,2} = 26.6$  kg/mol (MALDI-TOF MS).  $^1\text{H-NMR}$  (300 MHz, *o*DCB-*D*<sub>4</sub>,  $\delta$ ): 7.80-7.67 (br m, 2a·H, *Ph-C*-( $\text{CH}_2$ )<sub>3</sub>-COOR), 7.32-7.05 (br m, 3a·H, *Ph-C*-( $\text{CH}_2$ )<sub>3</sub>-COOR), 6.65-6.00 (br m, 4(a+b)·H,  $\text{H}_{\text{ar}}$ ), 3.55-3.27 (br s, 3b·H,  $\text{H}_{\text{OMe}}$ ), 2.84-2.68 (br m, 2a·H, *Ph-C-CH*<sub>2</sub>-*CH*<sub>2</sub>-*CH*<sub>2</sub>-COOR), 2.56-2.38 (br m, 2a·H, *Ph-C-CH*<sub>2</sub>-*CH*<sub>2</sub>-*CH*<sub>2</sub>-COOR), 2.19-2.01 (br m, 2a·H, *Ph-C-CH*<sub>2</sub>-*CH*<sub>2</sub>-*CH*<sub>2</sub>-COOR), 1.95-0.55 (br m,  $\text{H}_{\text{backbone}}$ ,  $\text{H}_{\text{CTA}}$ ,  $\text{H}_{\text{Octyl}}$ ).  $T_{\text{dec},1} = 180$  °C,  $T_{\text{dec},2} = 382$  °C.

The large amount of solid residues in the reaction flask after synthesis of PPCBM 3 was collected (198 mg) and dissolved by stirring for 3 h at 100 °C in *o*DCB. The polymer PPCBM 4 was isolated by precipitation into 400 mL toluene:methanol (5:2/v:v) and then 400 mL methanol. Yield: 78 mg of a deep brown solid.  $M_n = 25.2$  kg/mol,  $M_{p,1} = 17.8$  kg/mol,  $M_{p,2} = 35.0$  kg/mol (MALDI-TOF MS).  $^1\text{H-NMR}$  (300 MHz, *o*DCB-*D*<sub>4</sub>,  $\delta$ ): 7.82-7.65 (br m, 2a·H, *Ph-C*-( $\text{CH}_2$ )<sub>3</sub>-COOR), 7.37-7.04 (br m, 3a·H, *Ph-C*-( $\text{CH}_2$ )<sub>3</sub>-COOR), 6.65-6.00 (br m,

4(a+b)·H, H<sub>ar</sub>), 3.58-3.23 (br s, 3b·H, H<sub>OMe</sub>), 2.85-2.70 (br m, 2a·H, Ph-C-CH<sub>2</sub>-CH<sub>2</sub>-CH<sub>2</sub>-COOR), 2.57-2.38 (br m, 2a·H, Ph-C-CH<sub>2</sub>-CH<sub>2</sub>-CH<sub>2</sub>-COOR), 2.19-2.01 (br m, 2a·H, Ph-C-CH<sub>2</sub>-CH<sub>2</sub>-CH<sub>2</sub>-COOR), 1.95-0.55 (br m, H<sub>backbone</sub>, H<sub>CTA</sub>, H<sub>Octyl</sub>).  $T_{\text{dec},1} = 180\text{--}190\text{ }^{\circ}\text{C}$ ,  $T_{\text{dec},2} = 386\text{ }^{\circ}\text{C}$ .

## Acknowledgments

The authors thank the Elite Network Bavaria and Merck Chemicals Ltd. for support. We also kindly acknowledge DFG (SPP1355) for financial support of this project.

## References

- (1) N. S. Sariciftci, L. Smilowitz, a J. Heeger, F. Wudl, *Science* **1992**, *258*, 1474–6.
- (2) B. C. Thompson, J. M. J. Fréchet, *Angew. Chem. Int. Ed.* **2008**, *47*, 58–77.
- (3) W. Ma, C. Yang, X. Gong, K. Lee, a J. Heeger, *Adv. Funct. Mater.* **2005**, *15*, 1617–1622.
- (4) Z. He, C. Zhong, X. Huang, W.-Y. Wong, H. Wu, L. Chen, S. Su, Y. Cao, *Adv. Mater.* **2011**, *23*, 4636–43.
- (5) X. Yang, J. K. van Duren, R. A. Janssen, M. A. Michels, J. Loos, *Macromolecules* **2004**, *37*, 2151–2158.
- (6) X. Yang, J. Loos, S. C. Veenstra, W. J. H. Verhees, M. M. Wienk, J. M. Kroon, M. a J. Michels, R. a J. Janssen, *Nano Lett.* **2005**, *5*, 579–83.
- (7) T. Savenije, J. Kroeze, M. Wienk, J. Kroon, J. Warman, *Phys. Rev. B* **2004**, *69*, 1–11.
- (8) E. von Hauff, J. Parisi, V. Dyakonov, *J. Appl. Phys.* **2006**, *100*, 043702.
- (9) V. D. Mihailetschi, H. X. Xie, B. de Boer, L. J. a. Koster, P. W. M. Blom, *Adv. Funct. Mater.* **2006**, *16*, 699–708.
- (10) V. D. Mihailetschi, J. K. J. van Duren, P. W. M. Blom, J. C. Hummelen, R. a. J. Janssen, J. M. Kroon, M. T. Rispens, W. J. H. Verhees, M. M. Wienk, *Adv. Funct. Mater.* **2003**, *13*, 43–46.

- 
- (11) M. T. Rispens, A. Meetsma, R. Rittberger, C. J. Brabec, N. S. Sariciftci, J. C. Hummelen, *Chem. Commun.* **2003**, 2116–8.
- (12) G. Adamopoulos, T. Heiser, U. Giovanella, S. Ouldsaad, K. Vandewetering, C. Brochon, T. Zorba, K. Paraskevopoulos, G. Hadziioannou, *Thin Solid Films* **2006**, 511–512, 371–376.
- (13) L. Perrin, A. Nourdine, E. Planes, C. Carrot, N. Alberola, L. Flandin, *J. Polym. Sci. B Pol. Phys.* **2012**, doi: 10.1002/polb.23206.
- (14) M. Eo, S. Lee, M. H. Park, M. H. Lee, S. Yoo, Y. Do, *Macromol. Rapid Commun.* **2012**, 33, 1119–25.
- (15) N. Zhang, S. Schricker, F. Wudl, M. Prato, *Chem. Mater.* **1995**, 7, 441–442.
- (16) J. Kim, M. H. Yun, J. Lee, J. Y. Kim, F. Wudl, C. Yang, *Chem. Commun.* **2011**, 47, 3078–80.
- (17) U. Stalmach, B. de Boer, C. Videlot, P. F. van Hutten, G. Hadziioannou, *J. Am. Chem. Soc.* **2000**, 122, 5464–5472.
- (18) C. J. Hawker, *Macromolecules* **1994**, 27, 4836–4837.
- (19) M. H. van der Veen, B. de Boer, U. Stalmach, K. I. van de Wetering, G. Hadziioannou, M. H. Van Der Veen, B. De Boer, K. I. Van De Wetering, *Macromolecules* **2004**, 37, 3673–3684.
- (20) B. Liu, C. E. Bunker, Y.-P. Sun, *Chem. Commun.* **1996**, 1241.
- [21] C. Yang, J. K. Lee, A. J. Heeger, F. Wudl, *J. Mater. Chem.* **2009**, 19, 5416–5423.
- (22) L. Dai, A. Mau, H. Griesser, T. Spurling, *J. Phys. Chem.* **1995**, 99, 17302–17304.
- (23) M. Heuken, H. Komber, B. Voit, *Macromol. Chem. Phys.* **2012**, 213, 97–107.
- (24) S. Miyanishi, Y. Zhang, K. Tajima, K. Hashimoto, *Chem. Commun.* **2010**, 46, 6723–6725.
- (25) X.-H. Dong, W.-B. Zhang, Y. Li, M. Huang, S. Zhang, R. P. Quirk, S. Z. D. Cheng, *Polym. Chem.* **2012**, 3, 124–134.
- (26) J. U. Lee, A. Cirpan, T. Emrick, P. Russell, W. Ho, T. P. Russell, W. H. Jo, *J. Mater. Chem.* **2009**, 19, 1483.
- (27) S. R. Gondi, A. P. Vogt, B. S. Sumerlin, *Macromolecules* **2007**, 40, 474–481.

- (28) W. H. Binder, R. Sachsenhofer, *Macromol. Rapid Commun.* **2007**, *28*, 15–54.
- (29) E. Lieber, C. N. R. Rao, T. Chao, C. Hoffman, *Anal. Chem.* **1957**, *29*, 916–918.
- (30) C. Barner-Kowollik, Ed., *Handbook of RAFT Polymerization*, Wiley-VCH, Weinheim, Germany, **2008**.
- (31) J. C. Hummelen, B. W. Knight, F. LePeq, F. Wudl, J. Yao, C. L. Wilkins, *J. Org. Chem.* **1995**, *60*, 532–538.
- (32) E. P. Boden, G. E. Keck, *J. Org. Chem.* **1985**, *50*, 2394–2395.
- (33) M. Thelakkat, P. Pösch, H. W. Schmidt, *Macromolecules* **2001**, *34*, 7441–7447.
- (34) Y. He, G. Zhao, B. Peng, Y. Li, *Adv. Funct. Mater.* **2010**, *20*, 3383–3389.
- (35) C. J. Hawker, *Macromolecules* **1994**, *27*, 4836–4837.
- (36) V. Mihailetschi, J. Wildeman, P. Blom, *Phys. Rev. Lett.* **2005**, *94*, 1–4.
- (37) A. S. Lang, M. Thelakkat, *Polym. Chem.* **2011**, *2*, 2213.
- (38) P. Blom, M. Vissenberg, *Mater. Sci. Eng.* **2000**, *27*, 53–94.
- (39) C. Goh, R. J. Kline, M. D. McGehee, E. N. Kadnikova, J. M. J. Fréchet, *Appl. Phys. Lett.* **2005**, *86*, 122110.

## Supporting Information

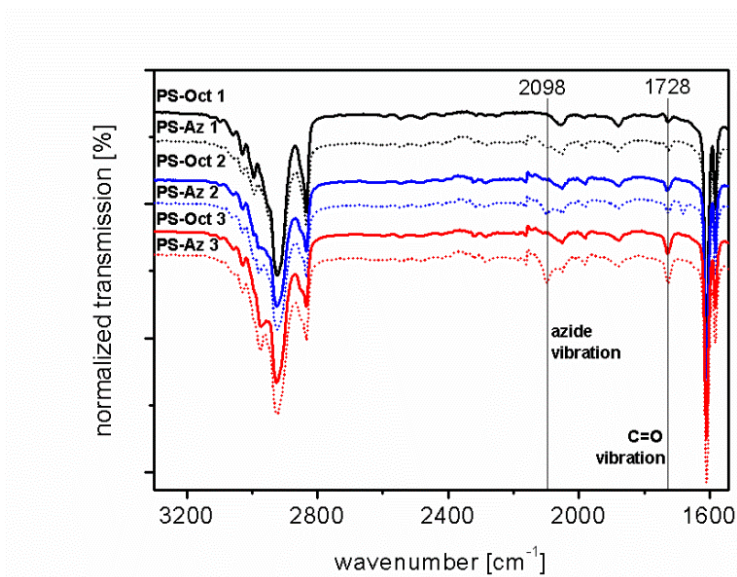


Figure S1: Magnified portion of the FTIR spectra of octyl end-capped polymers PS-Oct 1, PS-Oct 2 and PS-Oct 3 (solid lines) and their respective precursor copolymers PS-Az 1, PS-Az 2 and PS-Az 3 (dotted lines) with terminal azide groups. The azide vibration band at  $\nu = 2098 \text{ cm}^{-1}$  of the copolymers PS-Az 1, PS-Az 2 and PS-Az 3 disappears completely after the 1,3-dipolar cycloaddition (click reaction) with 1-octyne, since a triazole ring is formed. This gives evidence for a quantitative conversion of the azide end groups. Besides, the intensity of the end group dependent IR bands at  $2098 \text{ cm}^{-1}$  and  $1728 \text{ cm}^{-1}$  (C=O stretching band of carboxylic acid ester) correlates with the chain length in the expected indirect proportional manner due to normalization of all FTIR spectra to the polymer backbone signals.

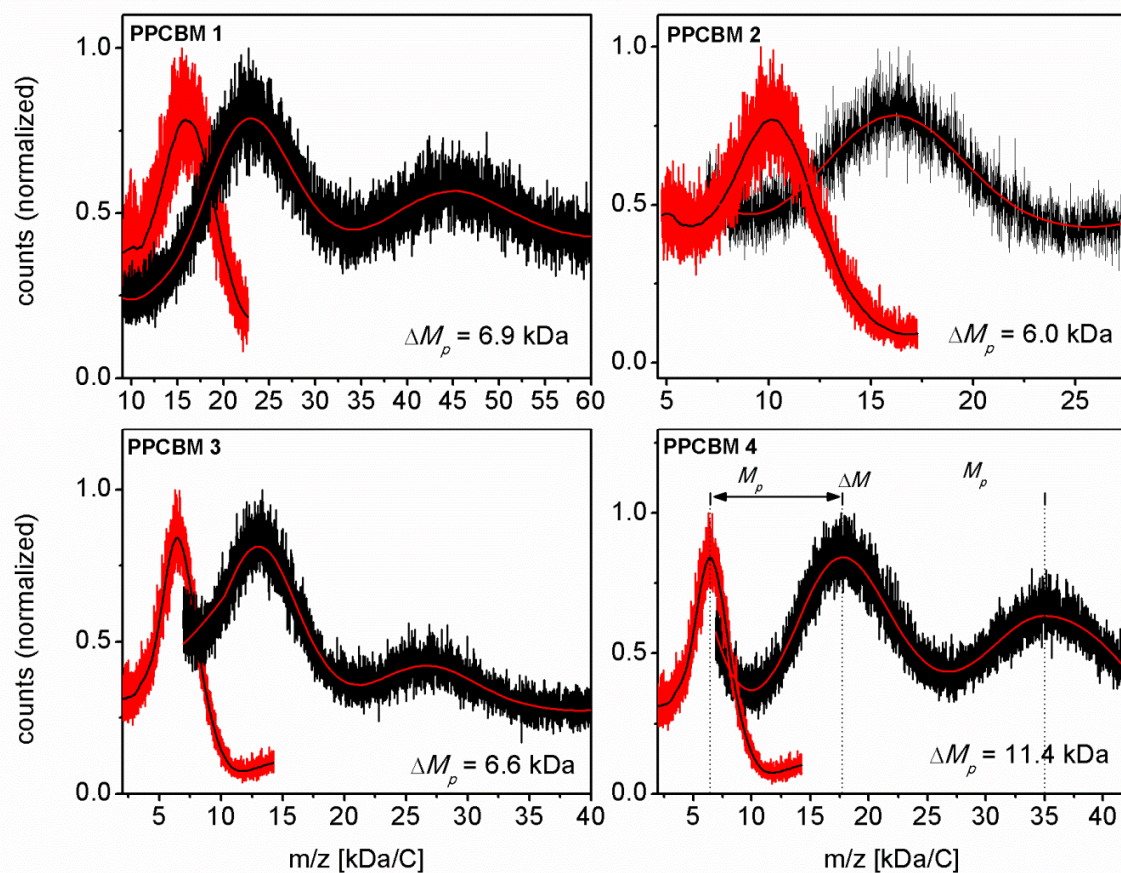


Figure S2: MALDI-TOF mass spectra of PCBM-grafted copolymers PPCBM 1-4 (black signal) and their corresponding precursor copolymers PS-OH 1-3 (red signal). As depicted for PPCBM 4, the PCBM content  $f_{\text{PCBM}}$  was determined from the mass difference  $\Delta M$  of the peak maxima. All mass spectra were smoothed for clarity due to the low signal-to-noise ratio.

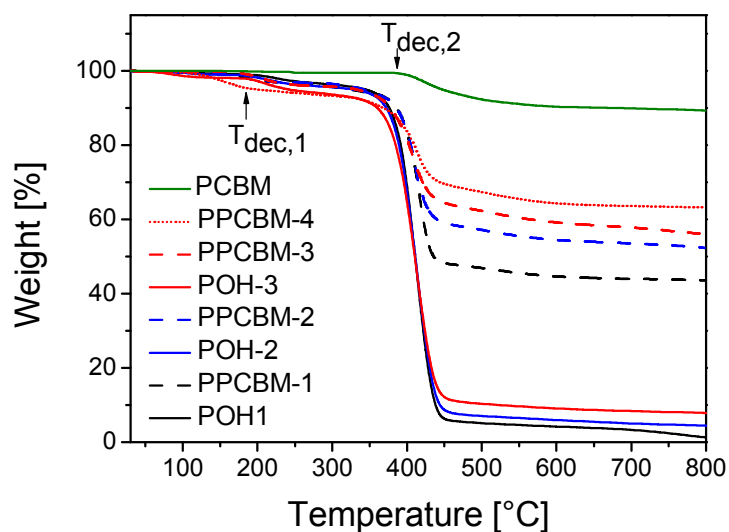


Figure S3: TGA weight loss curves (for heating under  $N_2$  atmosphere) of PCBM-grafted copolymers PPCBM 1-4, their corresponding precursor copolymers PS-OH 1-3 and pristine PCBM as reference. The copolymers show two decomposition processes at  $T_{dec,1} \approx 180-190^\circ C$ , which is related to the trithiocarbonate decomposition, and  $T_{dec,2} \approx 390^\circ C$ , which arises from the polymer backbone decomposition. Since degradation of PCBM is only marginal above  $400^\circ C$ , the residual char of the PCBM-grafted copolymers indicates the PCBM weight content, but is usually overestimated.

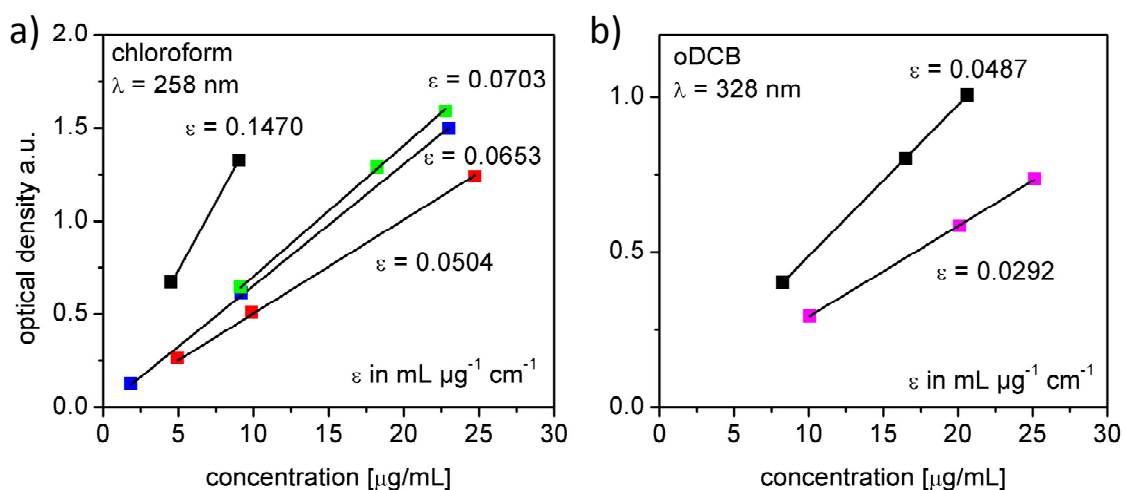


Figure S4: Quantitative UV-vis measurements for the determination of extinction coefficient  $\epsilon$ . A) PCBM (black), PPCBM 1 (red), PPCBM 2 (blue) and PPCBM 3 (green) in chloroform. b) PCBM (black) and PPCBM 4 (magenta) measured in oDCB. According to the law of Lambert-Beer, the extinction coefficient  $\epsilon$  can be extracted from the slope of the linear fits. The ratio  $\epsilon_{\text{polymer}}/\epsilon_{\text{PCBM}}$  gives the PCBM weight content of the PCBM-grafted copolymers, but is usually underestimated for high contents.

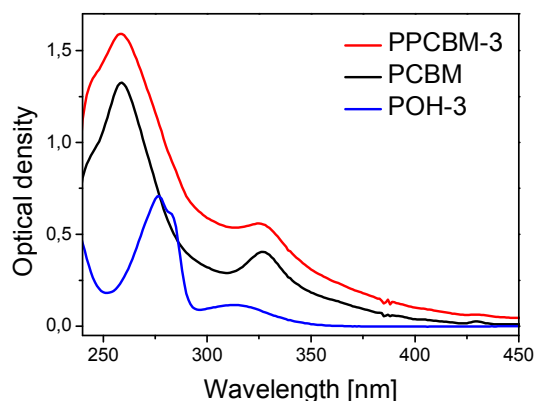


Figure S5: UV-Vis absorption spectra of PCBM (9.04  $\mu\text{g/mL}$ ), PS-OH 3 (62.88  $\mu\text{g/mL}$ ) and PPCBM 3 (22.79  $\mu\text{g/mL}$ ). The PCBM-grafted copolymer PPCBM 3 exhibits the same optical features as PCBM, i.e. two absorption bands at 258 nm ( $\epsilon_{258\text{ nm}} = 0.0703\text{ mL mg}^{-1}\text{ cm}^{-1}$ ) and 328 nm. Hence, the optical properties of PCBM are not affected by the covalent attachment to the polymer backbone.

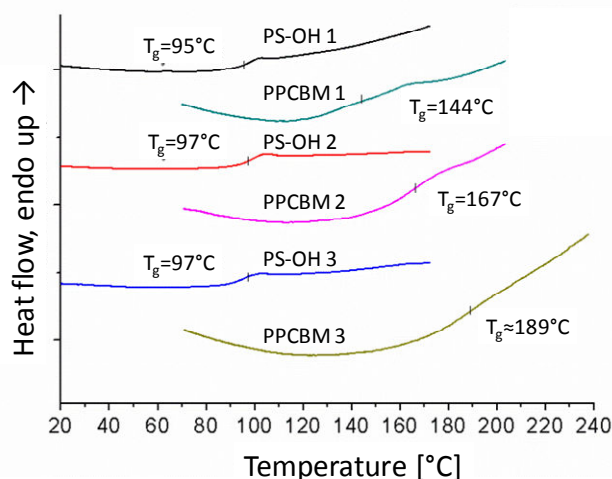


Figure S6: DSC curves (second heating cycle) of PCBM-grafted copolymers PPCBM 1-3 and the corresponding precursor copolymers PS-OH 1-3. The precursor copolymers exhibit a typical glass transition at  $T_g \approx 95\text{--}97\text{ }^\circ\text{C}$ , whereas the glass transition of PCBM-grafted copolymers is shifted considerably towards higher temperatures. With increasing PCBM content of 30 wt% (PPCBM 1), 37 wt% (PPCBM 2) and 51 wt% (PPCBM 3), the  $T_g$  step is broadening and increasing to 144  $^\circ\text{C}$ , 167  $^\circ\text{C}$  and about 189  $^\circ\text{C}$ , respectively.

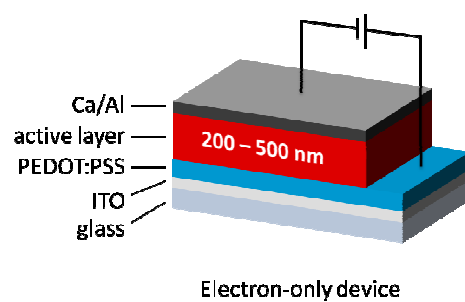


Figure S7: Device configuration for space-charge limited current (SCLC) measurements.

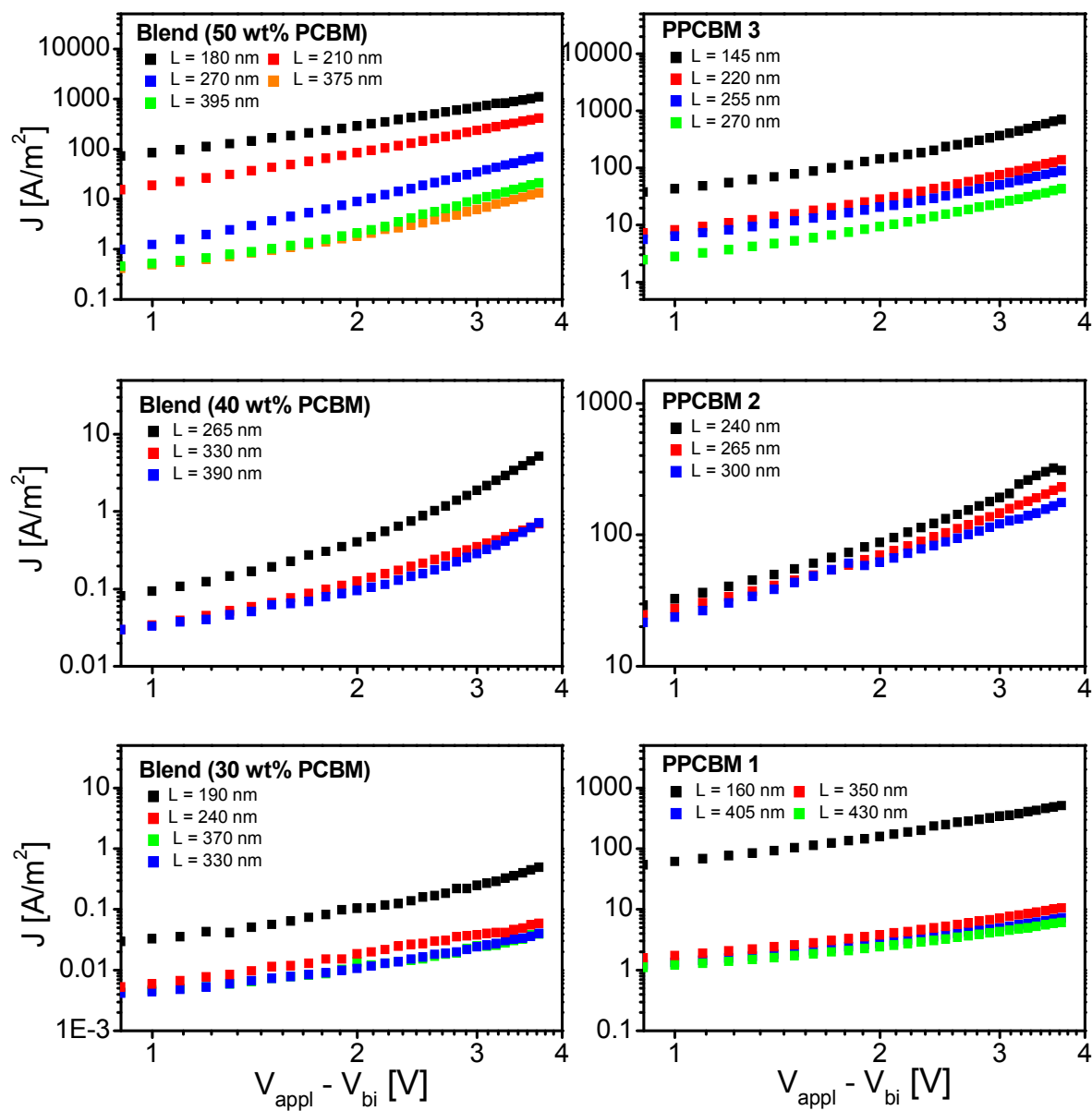


Figure S8: Current-voltage ( $J$ - $V$ ) curves from SCLC measurements of blends (PCBM:PS-OH 1) in different compositions in comparison to the synthesized PCBM-grafted copolymers PPCBM 1-3. A series of devices with varying film thickness  $L$  was measured for each compound.

## 8. Annex: Perylene bisimide Blend Solar Cells: Influence of Substituents on Blend Morphology and Device Performance

*Mathis-Andreas Muth<sup>a,b</sup>, André Wicklein<sup>a</sup>, Helga Wietasch<sup>a</sup>, William Mitchell<sup>b</sup>, Steven Tierney<sup>b</sup>, Miguel Carrasco-Orozco<sup>b</sup> and Mukundan Thelakkat<sup>a\*</sup>*

[a] Prof. Dr. Mukundan Thelakkat, Applied Functional Polymers, Department of Macromolecular Chemistry I, University of Bayreuth, Universitaetsstr.30, 95440 Bayreuth (Germany)

[b] Dr. Miguel Carrasco-Orozco, Merck Chemicals Ltd., Chilworth Technical Centre, University Parkway, Southampton SO16 7QD (UK)

\*corresponding author: mukundan.thelakkat@uni-bayreuth.de

This manuscript contains experimental data on blend morphology and devices performance of Polymer:PBI solar cells. The work presented here is strongly related to Chapter 3 and can be considered as starting point for further investigations.

## Introduction

Organic bulk heterojunction (BHJ) solar cells typically consist of an electron donor (p-type) polymer and an electron acceptor (n-type) small molecule, such as PCBM, as active layer.<sup>1</sup> To achieve high power conversion efficiencies (PCE), the main focus of research to date was on optimizing the p-type polymers, whilst keeping PCBM as acceptor. However, alternative n-type materials could provide additional versatility for the choice of donor materials in order to find more donor:acceptor combinations with suitable energy levels. In addition, light absorption of PCBM in the visible range is comparatively poor. Hence, new organic acceptors which can fulfill all necessary parameters for high performance OPV, such as light harvesting, charge transfer, charge transport and thermal, chemical and photostability are required. Perylene bisimides (PBI) derivatives are a relevant class of n-type semiconductors due to their relatively high electron affinity and strong visible light absorption, combined with good photochemical and thermal stability.<sup>2</sup> Even though it was shown that PBIs can be better electron acceptors than PCBM with respect to charge photogeneration,<sup>3</sup> their performance in solar cells is still significantly lower. Bimolecular recombination due to a finely dispersed PBI derivative in a p-type polymer matrix on the one hand and suppressed charge transfer for a highly aggregated PBI on the other hand have been reported as two possible loss mechanisms in PBI solar cells.<sup>4</sup> Thus, morphology of PBI thin films and corresponding blends with p-type materials needs to be studied and controlled. Aggregation and crystallinity in PBI thin films is primarily driven by  $\pi$ - $\pi$  interaction of aromatic perylene cores. Several approaches to control PBI crystal growth have been reported including thermal and solvent-vapor annealing, as well as optimization of coating solvents.<sup>5, 6</sup> Modifications of the chemical structure of PBI were also demonstrated to hinder aggregation and improve PCE of photovoltaic devices, when alkyl substituents were not only employed at the imide positions (*N*-substitution), but also attached to the perylene core (bay-substitution).<sup>7</sup> However, in contrast to *N*-substitution, bay-substitution is usually accompanied by changes in optical and electrochemical properties.<sup>8</sup> Furthermore, the majority of PBI based solar cells reported to date, utilize P3HT as p-type material. In this case, the crystallization of P3HT, which is known to be crucial for high PCE in OPV cells,<sup>9</sup> was observed to be inhibited in presence of PBI,<sup>7</sup> indicating that rather amorphous p-type polymers might be more suitable in combination with PBIs. Herein, we report novel blend systems for organic photovoltaic

(OPV) cells consisting of n-type PBI small molecules and a p-type low band gap copolymer and correlate blend morphology with devices performance.

## Results and Discussion

In an earlier comparative study, we investigated optical and electronic properties, as well as crystalline structure of three unymmetrical PBIs. The results encouraged us to test these materials in solar cell devices. In the following we compare photovoltaic devices and blend morphology of each n-type PBI small molecule in combination with a p-type low band gap copolymer. The chemical structures of all compounds are depicted in Figure 1a. The solubilizing side groups of the PBI acceptor material are systematically changed from hydrophobic alkyl chains to hydrophilic oligoethylenglycol (OEG) chains. In all cases an unsymmetrical *N*-substitution pattern with one linear and one branched *N*-substituent is employed. Since the energy levels of all three materials are similar, testing these materials in solar cell devices allows for a comparative study of side chain effects on morphology and device performance. The HOMO and LUMO values measured by cyclic voltammetry and electron mobilities of pristine PBI films determined by SCLC measurements, are listed in Table 1. A detailed study of the mobility of pristine and annealed PBI films can be found in Chapter 3. As donor material we chose a well soluble copolymer consisting of benzodithiophene, benzothiadiazole and thiophene units (Figure 1a). The benzodithiophene moiety is decorated with two ethyl hexyl chains and the benzothiadiazole carries two octyloxy substituents to give good solubility in common organic solvents. The polymer has a molecular weight of  $M_n=30000 \text{ gmol}^{-1}$  and a PDI of 1.8. HOMO and LUMO energy levels were determined as 5.3 eV and 3.6 eV, respectively, resulting in a band-gap of 1.7 eV. A hole mobility of  $3 \cdot 10^{-4} \text{ cm}^2\text{V}^{-1}\text{s}^{-1}$  was measured in SCLC hole-only devices (Table 1). Solar cells with this polymer in combination with a series of fullerene based acceptors were subject of Chapter 6. In Literature several similar copolymers were reported.<sup>10, 11</sup>

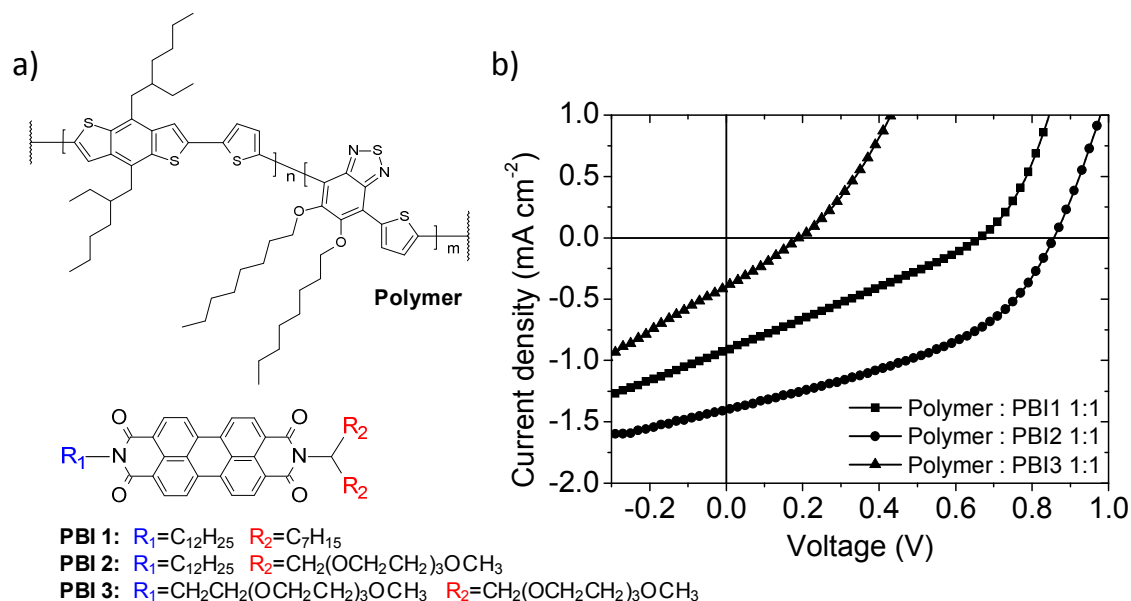


Figure 1: a) Structure formula of the low band gap copolymer and the three Perylene bisimides (PBI) derivatives and b)  $J$ - $V$  characteristics of photovoltaic cells thereof under AM1.5 solar irradiation (1 sun).

Table 1: HOMO and LUMO energy levels, determined from cyclic voltammetry, electron mobility  $\mu_e$  of pristine PBI films and hole mobility  $\mu_h$  of the polymer, measured by SCLC single carrier devices.

Compound	HOMO [eV]	LUMO [eV]	$\mu_e$ (pristine) [ $cm^2V^{-1}s^{-1}$ ]	$\mu_h$ [ $cm^2V^{-1}s^{-1}$ ]
<b>PBI 1</b>	6.0	3.8	$3 \cdot 10^{-5}$	-
<b>PBI 2</b>	6.0	3.8	$2 \cdot 10^{-5}$	-
<b>PBI 3</b>	6.0	3.8	$6 \cdot 10^{-5}$	-
<b>Polymer</b>	5.3	3.6	-	$3 \cdot 10^{-4}$

BHJ photovoltaic devices were fabricated using a standard OPV device architecture with an ITO/PEDOT:PSS bottom contact and a calcium/aluminum top contact. The active layers were applied using a doctor blade technique to give ca. 100 nm thin films (see Experimental Section for details). Blend systems consisting of a Polymer:PBI ratio of 1:1 (wt) coated from 1,2-dichlorobenzene (*o*DCB) solutions were tested for PBI 1, PBI 2 and PBI 3. The current density – voltage ( $J$ - $V$ ) characteristics of the devices under AM1.5 solar illumination (1sun)

are shown in Figure 1b. The curves presented are representative for up to 10 OPV cells measured for each blend. We observe that PBI 2 as acceptor material outperforms both PBI 1 and PBI 3 with the highest short circuit current density ( $J_{SC}$ ) and open circuit voltage ( $V_{OC}$ ) and fill factor (FF) (see Table 2) resulting in a power conversion efficiency (PCE) of 0.51 %. In comparison, the blend consisting of PBI 1 shows significantly lower  $J_{SC}$ ,  $V_{OC}$  and FF and a PCE of 0.19 %, whereas almost no photovoltaic properties could be observed for blends with PBI 3 (PCE=0.02 %). The corresponding series resistance ( $R_S$ ) and parallel resistance ( $R_{SH}$ ) values of the devices are also given in Table 2. It is evident that  $R_S$  is lowest and  $R_{SH}$  highest for the Polymer:PBI 2 blend, which is consistent with the best performance observed.

To understand these findings, blend morphologies were investigated with atomic force microscopy (AFM). Topography images are shown in Figure 2. A featureless and smooth film is obtained for the blend of Polymer:PBI 1 (Figure 2a). This suggests a highly intermixed blend system of PBI 1 with the Polymer, both possessing alkyl chains as solubilizing groups and therefore similar polarity. For the PBI 2 system, an increased surface roughness is detected in the AFM image in Figure 2b, which indicates that domain sizes of pure PBI or Polymer have increased. In other words, the blend of PBI 2 having alkyl and OEG substituents exhibits a more pronounced phase separation, which can be attributed to hydrophobic-hydrophilic interactions of the PBI and Polymer upon drying of the film. In Figure 2c a very coarse and non-homogeneous surface of Polymer:PBI 3 blend illustrates that donor and acceptor material in this system are likely to be completely phase separated. During the film drying process, PBI 3 with only OEG substituents seems to segregate from the Polymer, resulting in large domains of PBI 3 and Polymer aggregates. A clear trend of increasing phase separation of the Polymer:PBI blends was observed, when PBI alkyl side groups were replaced with OEG substituents. Trying to explain the different device performances of these blends, we assume that various loss mechanisms are competing, depending on the morphology. Greenham and co-workers reported for a blend of F8BT and an asymmetrical *N*-substituted PBI, that if the PBI molecules are finely dispersed in the polymer matrix, fast bimolecular charge recombination is an important loss mechanism.<sup>4</sup> Bimolecular recombination caused by poor percolation pathways for charge carriers and/or low charge carrier mobility might be the limiting factor for the Polymer:PBI 1 blend. For the

PBI 3 blend system with coarse blend morphology and highly aggregated perylene domains, a different loss mechanism seems plausible. It was demonstrated that intermolecular state formation in large PBI domains is restricting efficient charge transfer.<sup>4</sup> Due to the worse device performance of PBI 3 compared to PBI 1, this effect appears to be more crucial. In the case of Polymer:PBI 2 blends, comparatively small, but distinct domain sizes support the assumption, that a balance between intermixed blend and aggregated PBI domains gives the best device efficiencies in combination with this polymer. However, domains sizes of this blend system are still significantly larger than 10-20 nm, which is generally required for efficient charge generation because of the limited exciton diffusion length.<sup>12</sup> The SEM cross section image in Figure 3 shows coarse features along the cross-section of the film and visualizes large domains of phase separated PBI 2 and Polymer with domain sizes of up to hundred nanometers.

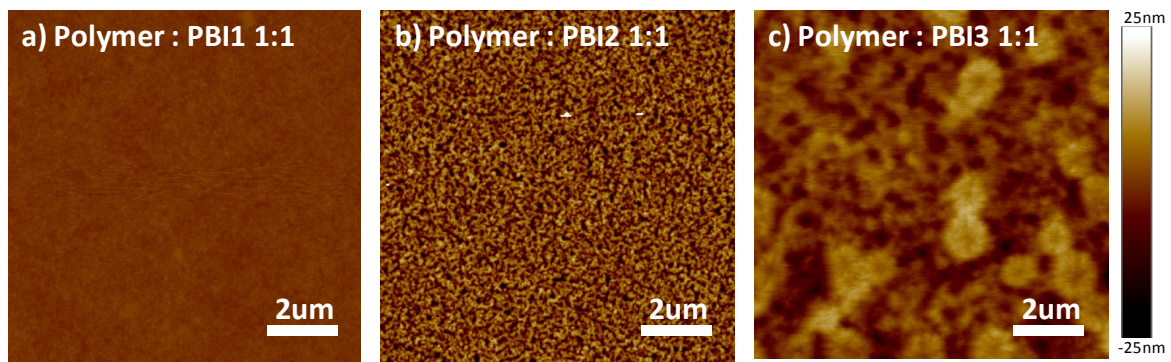


Figure 2: AFM Topography images obtained in Tapping Mode for a) Polymer:PBI 1, b) Polymer:PBI 2 and c) Polymer:PBI 3 blends.

Table 2: Solar cell parameters obtained from J-V curves under AM1.5 conditions;  $R_S$  and  $R_{SH}$  represent series and parallel resistance, respectively.

Blend	$J_{sc}$ [mA·cm <sup>-2</sup> ]	$V_{oc}$ [mV]	FF [%]	PCE [%]	$R_S$ [Ωcm <sup>2</sup> ]	$R_{SH}$ [Ωcm <sup>2</sup> ]
Polymer:PBI 1 (1:1)	-0.9	670	31	0.19	148	806
Polymer:PBI 2 (1:1)	-1.4	860	42	0.51	117	1351
Polymer:PBI 3 (1:1)	-0.4	200	27	0.02	247	562

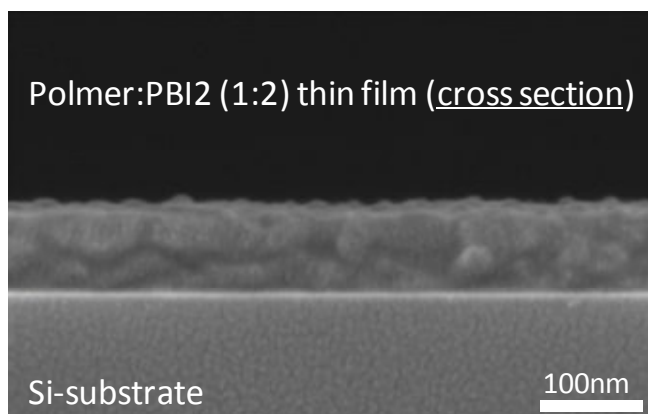


Figure 3: SEM cross-section image of a Polymer:PBI 2 (ratio 1:2) 100nm thin film on a silicon substrate; after freeze-fracturing of the film, the sample was coated with 2 nm of platinum.

As demonstrated for the PBI derivatives in Chapter 3, electron mobility can be improved by thermal annealing. The device performance of the Polymer:PBI blends however decreased upon thermal annealing, which indicates that the blend morphology is unstable. Even though in general high charge carrier mobilities are desirable in OPV blends, the negative impact of annealing on morphology seems to be more crucial in this case. To achieve better PCE, both domain sizes and device stability have to be optimized, which is beyond the scope of this paper. The comparison of the three PBIs demonstrates that in BHJ solar cells, the blend morphology is of great importance. Even though PBI 3 showed high electron mobilities, the OPV cell gave poor efficiency due to the unfavorable, macrophase separated morphology.

For the further optimization of these solar cell devices, two approaches are feasible. One can either optimize the Polymer:PBI 1 blend to induce phase separation and charge percolation or tune phase separation in the Polymer:PBI 2 blend. In the following, the optimization of the blend ratio of the Polymer:PBI 2 system is discussed. First, the evolution of the morphology with increasing PBI 2 content was monitored by AFM. Six different Polymer:PBI 2 blend ratios ranging from 2:1 to 1:2.5 were tested. The morphology is clearly determined by the PBI aggregation, which is demonstrated in AFM topography and phase images shown in Figure 4 and Figure 5. Surface roughness as well as phase separation of the blend increases with increasing PBI 2 content.  $J-V$  curves of all Polymer:PBI 2 cells and the corresponding devices parameter are given in Figure 6 and Table 3.  $V_{OC}$  is constantly high for Polmyer:PBI 2 blend ratios from 2:1 to 1:1.5. For higher PBI 2 contents,  $V_{OC}$  is decreasing.

Interestingly, the FF constantly increases with increasing PBI 2 content from 34 % to 49 %, which is mainly due to improved series resistance  $R_S$  of the devices (Table 3). Since all devices were fabricated under similar conditions, the changes in  $R_S$  are due to changes in the active layer. Better electron transport due to the increasing electron transporting PBI 2 content on the one hand and changes in the blend morphology on the other hand can potentially both account for the improved  $R_S$  values. No clear trend of the parallel resistance  $R_{SH}$  was observed.  $R_{SH}$  values are high compared to PBI 1 and PBI 3 blend devices (see Table 2) and range between  $1351 \Omega\text{cm}^2$  and  $2128 \Omega\text{cm}^2$ . With increasingly phase separated donor and acceptor materials however, efficient charge transfer is more and more deterred. Thus even though a high PBI 2 content is necessary to achieve low  $R_S$  and better transport, the crystallization is strongly pronounced here and the morphology is unfavorable for an efficient solar cell. The fundamental question here is how to suppress the coarse phase separation for a high PBI 2 content, which seems to be required for good charge transport in these blends. Hence, the optimum performance with the highest  $J_{SC}$  is found at a Polymer:PBI 2 ratio of  $1:1.5$  yielding a PCE of 0.6 %. Here, a balance between good charge transport and morphology is reached.

Table 3: Solar cell parameters obtained from J-V curves under AM1.5 (1sun) conditions for various Polymer:PBI 2 blend ratios;  $R_S$  and  $R_{SH}$  represent series and parallel resistance, respectively.

<i>Blend</i>	$J_{sc}$ [mA·cm <sup>-2</sup> ]	$V_{oc}$ [mV]	<i>FF</i> [%]	<i>PCE</i> [%]	$R_S$ [ $\Omega\text{cm}^2$ ]	$R_{SH}$ [ $\Omega\text{cm}^2$ ]
<b>Polymer:PBI 2 2:1</b>	-0.8	860	34	0.25	180	1639
<b>Polymer:PBI 2 1.5:1</b>	-1.0	860	36	0.32	128	1429
<b>Polymer:PBI 2 1:1</b>	-1.4	860	42	0.51	117	1351
<b>Polymer:PBI 2 1:1.5</b>	-1.6	860	44	0.60	117	1408
<b>Polymer:PBI 2 1:2</b>	-1.3	840	47	0.53	110	1818
<b>Polymer:PBI 2 1:2.5</b>	-1.2	810	49	0.46	90	2128

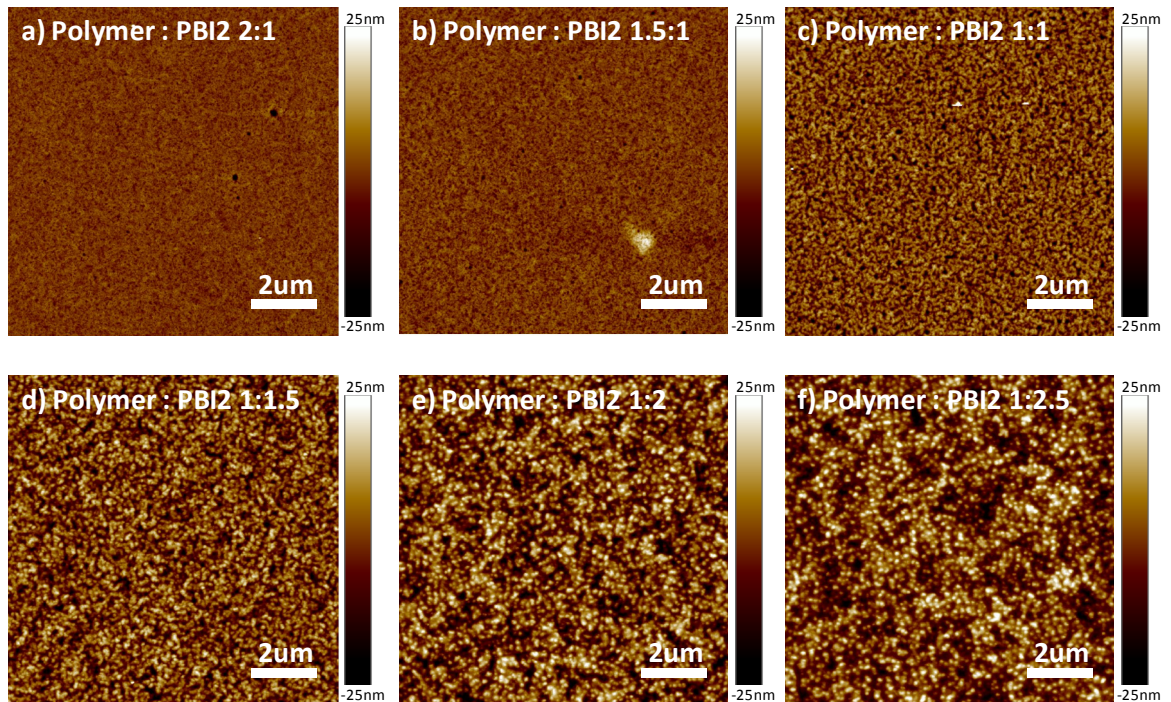


Figure 4: AFM topography images obtained in Tapping Mode for different Polymer:PBI 2 blend ratios showing increased surface roughness and aggregation with increasing PBI 2 content.

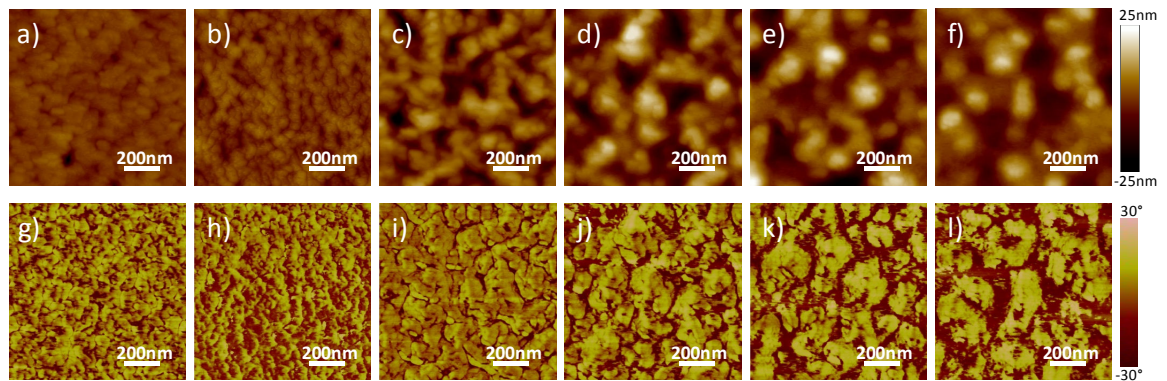


Figure 5: AFM topography (a-f) and phase images (g-l) in Tapping Mode for different Polymer:PBI 2 blend ratios, which are 2:1 (a,g), 1.5:1 (b,h), 1:1 (c,i), 1:1.5 (d,j), 1:2 (e,k) and 1:2.5 (f,l); the scan size is 1 $\mu$ m x 1 $\mu$ m; both topography and phase image show an increased phases separated blend with increasing PBI 2 content.

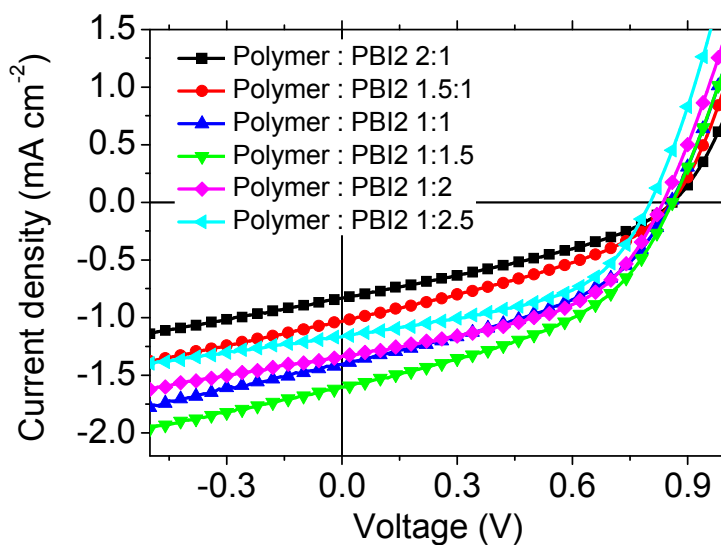


Figure 6: J-V characteristics of Polymer:PBI2 solar cells with varied blend ratio under AM1.5 solar irradiation (1 sun).

## Conclusion and Outlook

Ultimately, we were able to show that interactions of side groups of acceptor and donor in OPV blends have great influence on the resulting blend morphology. Hydrophobic-hydrophilic interaction of the substituents can be used to tune the blend morphology from highly intermixed blends to macro phase separated systems, which was shown by AFM measurements. Even though the device performance could be improved by choosing suitable substituents and altering the blend ratio, the PCEs were all comparatively low. The comparison of PBI 2 and PBI 3 demonstrates that even though the materials exhibit similar electron mobilities and crystallinity in thin films (as discussed in Chapter 3), solar cell efficiency was significantly better for PBI 2 with 0.51 % compared to PBI 3 with 0.02 %. Hence, the combination of donor and acceptor material needs to be carefully adjusted in order to obtain a suitable OPV blend. An optimized blend ratio of Polymer:PBI2 1:1.5 gave a PCE of 0.60 %. The devices suffer from high  $R_s$  and low  $J_{sc}$  and FF, which indicates fundamental recombination losses in these devices.

## Experimental Section

*Chemicals:* The synthesis route to obtain unsymmetrical *N*-substituted PBIs is described elsewhere.<sup>13</sup> Polymer was provided by Merck Chemicals Ltd.. 1,2-dichlorobenzene (*o*DCB) (anhydrous with crown cap, 99%) was purchased from Sigma-Aldrich. Blends were prepared by dissolving the materials in *o*DCB with the respective blend ratio (wt). PEDOT:PSS (Clevios P VP Al 4083) was purchased from Heraeus.

*Instrumentation:* Atomic force microscopy was performed on a Veeco Dimension Icon with Nanoscope V controller, in Tapping Mode. The used cantilevers were NSC15/AlBS from Mikromasch. Film thicknesses were determined on an Alphastep 500 surface profilometer. Scanning Electron Microscopy cross-sections: samples were prepared by coating the active layer on a silicon wafer and subsequent breaking of the wafer under liquid nitrogen to obtain smooth cross-sections and avoid damage of the film. The samples were coated with a 2 nm layer of platinum using a Cressington 208HR sputter coater. SEM measurements were performed with a Zeiss LEO 1530 (FE-SEM) with Schottky-field emission cathode and in-lens detector. For cyclic voltammetry experiments of the PBI small molecules, a conventional three-electrode assembly using a Ag/AgNO<sub>3</sub> reference electrode was used. CH<sub>2</sub>Cl<sub>2</sub> containing 0.1 M Tetrabutylammonium hexafluorophosphate was used as solvent. All measurements were carried out under N<sub>2</sub> atmosphere at a scan rate of 50 mVs<sup>-1</sup> at 25 °C and all redox potentials were calibrated to ferrocene/ferrocenium couple (Fc/Fc<sup>+</sup>). CV of the polymer was recorded on a Princeton Applied Research VersaSTAT 4 Potentiostat/Galvanostat 108 using platinum electrodes at a scan rate of 50 mVs<sup>-1</sup> at 25 °C and a Ag/Ag<sup>+</sup> (0.10 M of AgNO<sub>3</sub> in acetonitrile) reference electrode in a anhydrous and nitrogen-saturated solution of 0.1 M of tetrabutylammonium tetrafluoroborate in acetonitrile. Oxidation potential (E<sub>ox</sub><sup>1/2</sup>) of ferrocene is 0.08-0.11 V versus Ag/Ag<sup>+</sup>, and 0.41 V versus SCE. The HOMO and LUMO energy levels were determined from the oxidation and reduction onset of the second scan from CV data taking into account the SCE level at -4.7 eV.

*Photovoltaic device preparation:* OPV cells were fabricated using a standard device architecture: glass/ITO/PEDOT:PSS/Active Layer/Ca/Al. Commercial ITO coated glass substrates with a sheet resistance of 13 Ohms per sq (Lumtec) were cleaned using following

sequence in an ultrasonic bath: detergent, water, acetone and 2-propanol. After ozone treatment of the substrates for 5 min, PEDOT:PSS was spin-coated on the ITO surface and dried at 130 °C for 30 min under nitrogen atmosphere. All following steps were carried out under nitrogen atmosphere with water and oxygen levels  $\leq 0.1$  ppm. After cooling the substrate, the active layer was blade coated at 70 °C from 1,2-dichlorobenzene solution on an Erichsen Coatmaster 509MC. The substrates were then put in a thermal evaporation chamber to evaporate the top electrodes (30 nm Ca/ 100 nm Al) under high vacuum ( $1 \cdot 10^{-6}$  mbar) through a shadow mask (active area 4 mm<sup>2</sup>). The current-voltage characteristics of the devices were measured using a Keithley 2420 (I-V) Digital SourceMeter at 25 °C under AM1.5 solar irradiation (1000 Wm<sup>-2</sup>).

*SCLC single carrier devices* were fabricated using the following structure: glass/ITO/PEDOT:PSS/Active Layer/Ca/Al for electron-only devices and glass/ITO/PEDOT:PSS/Active Layer/Au for hole-only devices. Commercial ITO coated glass substrates with a sheet resistance of 13 Ohms per sq (Lumtec) were cleaned using following sequence in an ultrasonic bath: detergent, water, acetone and 2-propanol. After ozone treatment of the substrates for 5 min, PEDOT:PSS was spin-coated on the ITO surface and dried at 130 °C for 30 min. All following steps were carried out under nitrogen atmosphere with water and oxygen levels  $\leq 0.1$  ppm. After cooling the substrate, the active layer was blade coated from chloroform solutions. The substrates were then put in a thermal evaporation chamber to evaporate the top electrodes (30 nm Ca/ 100 nm Al for electron-only devices and 60 nm Au for hole-only devices) under high vacuum ( $1 \cdot 10^{-6}$  mbar) through a shadow mask (active area 4 mm<sup>2</sup>). The current-voltage characteristics of the devices were measured using a Keithley 2420 (I-V) Digital SourceMeter at 25 °C.

## References

- (1) Li, G.; Zhu, R.; Yang, Y., *Nature Photonics* **2012**, 6, (3), 153-161.
- (2) Zhan, X.; Facchetti, A.; Barlow, S.; Marks, T. J.; Ratner, M. A.; Wasielewski, M. R.; Marder, S. R., *Advanced Materials* **2011**, 23, (2), 268-284.

- 
- (3) Shoae, S.; An, Z.; Zhang, X.; Barlow, S.; Marder, S. R.; Duffy, W.; Heaney, M.; McCulloch, I.; Durrant, J. R., *Chemical Communications* **2009**, (36), 5445-5447.
  - (4) Howard, I. A.; Laquai, F. d. r.; Keivanidis, P. E.; Friend, R. H.; Greenham, N. C., *The Journal of Physical Chemistry C* **2009**, *113*, (50), 21225-21232.
  - (5) Guo, X.; Bu, L.; Zhao, Y.; Xie, Z.; Geng, Y.; Wang, L., *Thin Solid Films* **2009**, *517*, (16), 4654-4657.
  - (6) Hüttner, S.; Sommer, M.; Chiche, A.; Krausch, G.; Steiner, U.; Thelakkat, M., *Soft Matter* **2009**, *5*, (21), 4206-4211.
  - (7) Kamm, V.; Battagliarin, G.; Howard, I. A.; Pisula, W.; Mavrinskiy, A.; Li, C.; Müllen, K.; Laquai, F., *Advanced Energy Materials* **2011**, *1*, (2), 297-302.
  - (8) Langhals, H.; Demmig, S.; Huber, H., *Spectrochimica Acta Part A: Molecular Spectroscopy* **1988**, *44*, (11), 1189-1193.
  - (9) Yang, X.; Loos, J.; Veenstra, S. C.; Verhees, W. J. H.; Wienk, M. M.; Kroon, J. M.; Michels, M. A. J.; Janssen, R. A. J., *Nano Letters* **2005**, *5*, (4), 579-583.
  - (10) Zhou, H.; Yang, L.; Price, S. C.; Knight, K. J.; You, W., *Angewandte Chemie International Edition* **2010**, *49*, (43), 7992-7995.
  - (11) Ding, P.; Zou, Y.; Chu, C.-C.; Xiao, D.; Hsu, C.-S., *Journal of Applied Polymer Science* **2012**, *125*, (5), 3936-3945.
  - (12) Clarke, T. M.; Durrant, J. R., *Chemical Reviews* **2010**, *110*, (11), 6736-6767.
  - (13) Wicklein, A.; Lang, A.; Muth, M.; Thelakkat, M., *Journal of the American Chemical Society* **2009**, *131*, (40), 14442-14453.



## List of Publications

Lang, A.-S.; **Muth, M.-A.**; Heinrich, C. D.; Carasco-Orozco, M.; Thelakkat, M.: “Pendant Perylene Polymers with High Electron Mobility” *Journal of Polymer Science: Polymer Physics* DOI: 10.1002/polb.23357.

**Muth, M.-A.**; Carrasco-Orozco, M.; Thelakkat, M.: “Liquid-Crystalline Perylene Diester Polymers with Tunable Charge-Carrier Mobility” *Advanced Functional Materials* **2011**, *21*(23), 4510-4518.

Wicklein, A.; **Muth, M.-A.**; Thelakkat, M.: “Room Temperature Liquid Crystalline Perylene Diester Benzimidazoles with Extended Absorption” *Journal of Materials Chemistry* **2010**, *20*(39), 8646-8652.

Wicklein, A.; Lang, A.; **Muth, M.-A.**; Thelakkat, M.: “Swallow Tail Substituted Liquid Crystalline Perylene Bisimides: Synthesis and Thermotropic Properties” *Journal of the American Chemical Society* **2009**, *131* (40), 14442-14453.



## Danksagung / Acknowledgment

An dieser Stelle möchte ich mich bei allen bedanken, die durch ihre Unterstützung zum Gelingen dieser Arbeit beigetragen haben.

Meinem Doktorvater, Prof. Dr. Mukundan Thelakkat, danke ich herzlich für die Ermöglichung und die Betreuung des Projektes. Trotz der Distanz Bayreuth-Southampton habe ich bei ihm immer ein offenes Ohr gefunden. Hilfreichen Anregungen und motivierende Gespräche gaben meiner Forschung wertvolle Impulse. Danke auch, dass ich an internationalen Konferenzen und Tagungen teilnehmen durfte.

Special thanks goes to Merck Chemicals Ltd. in Southampton / United Kingdom for making the project possible in this way. Thanks to Dr. Frank Meyer who was responsible for funding of the project and enabled the co-operation between Merck and the University of Bayreuth. I'd also like to thank Merck for providing me with a brand new laboratory, desk space and high-tech instruments and measurement equipment in Southampton. Many thanks to my supervisor from Merck's side, Dr. Miguel Carrasco-Orozco, for the great support and interest in my work. I also thank the whole OPV physics and chemistry team for help and support with various measurement techniques, fruitful discussions and supplying me with new semiconductor polymers.

Herzlichen Dank auch an Gaurav Kumar Gupta und Prof. Dr. Thomas Thurn-Albrecht von der Universität Halle-Wittenberg, durch deren Hilfe in Sachen Röntgenmessungen und Strukturaufklärung meine Arbeit um einige interessante Ergebnisse bereichert wurde.

Meinen Kollegen in der Arbeitsgruppe Angewandte Funktionspolymere danke ich für die enge Zusammenarbeit, ohne die viele Teile dieser Arbeit nicht möglich gewesen wären. Hervorzuheben sind hierbei Dr. André Wicklein, der mir durch seine Betreuung im Vertiefungspraktikum und während der Diplomarbeit den Einstieg in die Perylenchemie beschert, und auch die Synthese von Perylenbisimidinen ermöglicht hat. Besten Dank auch an

Dr. Andreas Lang und Martin Hufnagel, die mir mit ihrer Synthese von verschiedenen n-typ Halbleitern hochinteressante Materialien zur Charakterisierung des Ladungstransports und der Morphologie zur Verfügung stellten. Helga Wietasch danke ich für ihre Unterstützung, die gute Atmosphäre im 583 und ihre Nachsicht mit der „lila Seuche“. Vielen Dank auch an alle aktuellen und ehemaligen „Afupos“ für lustige Kochabende und musikalische Höhepunkte beim traditionellen Adventssingen.

Ein herzliches Dankeschön geht auch an alle Mitarbeiter des Lehrstuhles MC1, die mir in den letzten Jahren durch ihre Hilfsbereitschaft unterstützt haben. Danke Petra Weiß für alles Organisatorische und Martina Heider für die Einweisung am REM. Danke auch allen Freunden und Kollegen für gemeinsame Aktivitäten wie z.B. Skiurlaube und ausgedehnte Grillabende.

Bei allen Freunden, die ich während meiner Zeit in Bayreuth und Southampton kennen gelernt habe, möchte ich mich für die schöne Zeit und die vielen gemeinsamen Erlebnisse bedanken.

Ein lieber Gruß geht auch an meine Familie, bei der ich mich für die Unterstützung und den Rückhalt, den ich in all den Jahren erfahren habe, bedanken möchte.

Zu guter Letzt ‚un beso muy fuerte‘ an Laura, die mir durch ihre verständnisvolle Art, wertvolle Ratschläge und Motivation sehr geholfen und die nötige Kraft gegeben hat.

## Erklärung

Hiermit erkläre ich, dass ich die vorliegende Arbeit selbständig verfasst, und keine anderen als die von mir angegebenen Quellen und Hilfsmitteln verwendet habe.

Ferner erkläre ich, dass ich weder anderweitig mit oder ohne Erfolg versucht habe, diese Dissertation einzureichen, noch eine gleichartige Doktorprüfung an einer anderen Hochschule endgültig nicht bestanden habe.

Bayreuth, den 08.03.2013

Mathis-Andreas Muth